

Syracuse University

**SURFACE**

---

Physics - Dissertations

College of Arts and Sciences

---

2011

## **Bioenergetics and dynamics of ciliary responses and systems biology of phototaxis in *Chlamydomonas reinhardtii***

Suphatra Adulrattananuwat  
*Syracuse University*

Follow this and additional works at: [https://surface.syr.edu/phy\\_etd](https://surface.syr.edu/phy_etd)



Part of the [Physics Commons](#)

---

### **Recommended Citation**

Adulrattananuwat, Suphatra, "Bioenergetics and dynamics of ciliary responses and systems biology of phototaxis in *Chlamydomonas reinhardtii*" (2011). *Physics - Dissertations*. 111.  
[https://surface.syr.edu/phy\\_etd/111](https://surface.syr.edu/phy_etd/111)

This Dissertation is brought to you for free and open access by the College of Arts and Sciences at SURFACE. It has been accepted for inclusion in Physics - Dissertations by an authorized administrator of SURFACE. For more information, please contact [surface@syr.edu](mailto:surface@syr.edu).

## Abstract

The goal of this dissertation is to understand how a eukaryotic cell makes decisions. *Chlamydomonas reinhardtii*, a biciliated unicellular green alga, is used as our model organism. This organism has the ability to track the light using its photoreceptor called rhodopsin, which overlays the eyespot. The organism makes decisions to swim toward, away from, perpendicular to or to ignore the light using its slender arm-like structures called cilia. It can integrate several external inputs such as ion concentration and light intensity, and then process this information to adjust the steering of its cilia corresponding to its environment.

We investigated how red light (670 nm) influences cell behavior. Most studies were done with a single cell held on a micropipette making it possible to observe the cilia behavior over a long time. The cell is illuminated with near-infrared light (peak at 870 nm) to avoid photoreceptor excitation. Ciliary movement is monitored using a quadrant photodiode detector (Chapter 2). Interpreted ciliary behavior parameters are the beating frequency (BF) and the stroke velocity (SV). Pulse stimuli were used to stimulate the mutant strain 806 (*agg1*), a negatively phototactic cell, whose beating frequency is in the same range as wild type. The “step-up” red light from the dark increases the beating frequency as an exponential function,  $y(t) = a[1 - \exp(-t/b)]$ , where  $y$  is a beating frequency,  $a$  is an amplitude and  $b$  is a time constant. On the other hand, the “step-down” red light drops the beating frequency transiently and recovers to its normal beating frequency of about 50 Hz in about 10 s. The 40 s duration pulse gave the maximum transient drop of the beating frequency. Using multi-sinusoidal red-light stimuli, I compared the behavior of the double mutant (*cpc1-2*) relative to the single mutant 806

(*cpc1-2* was backcrossed to strain 806 so it is a single mutant with respect to 806). The mutant misses the part of the central-pair complex containing the enolase enzyme, one of the ciliary glycolytic enzymes that produces ATP in the cilia. Under a high constant-intensity of red light, the BF fluctuation is less than 2%. In the dark, BF of *cpc1-2* is about 30 Hz which is lower than 806 probably due to less ATP being available. However, BF can be increased to the 806 level of 50 Hz by exposure to red light. A simple hypothesis is that red-light photosynthesis of the chloroplast makes ATP more available in the cell. In any case, sinusoidal red-light response of *cpc1-2* shows that part of the early signal processing is approximately linear. In this case, cells respond to a decrease in light intensity by differentiating the red light signal. Our hypothesis is that the cell creates this signal to avoid futile usage of ATP. The transfer function describing this step is,  $G(s) = a * s * e^{-\tau s}$  where  $\tau = 0.40$  sec. In addition to this linear part, both strains have non-linear or approximately full-wave rectified signal processing of another red light created signal with a simple delay in time described by the transfer function,  $G(s) = a * e^{-\tau_{strain} s}$  where  $\tau_{806} = 1.18$  sec and  $\tau_{cpc1-2} = 0.37$  sec. The longer delay time of 806 is likely due to the slow conversion of 3-phosphoglycerate (3PG) to adenosine triphosphate (ATP), in the glycolytic pathway, which is absent in the mutant. We hypothesize that the slow synthesis is due to the positive Gibbs free energy of two steps in the ciliary glycolytic pathway between 3PG and production of ATP and pyruvate. Furthermore, the beating frequency of red-light sinusoidal responses is stabilized by negative feedback. However, in the frequency range from 10 to 100 Hz in both strains that stabilizing negative feedback becomes positive and the BF jumps to a new state.

In addition, I also studied how external ion concentration such as  $\text{Ca}^{2+}$ ,  $\text{H}^+$ , and  $\text{K}^+$  and red light affect phototaxis of positively and negatively-phototactic cells (1117 and 806 respectively). I have tracked a cell population using the cell-tracking system for 10 s after stimulating them with green light (Chapter 4). Increasing  $[\text{Ca}^{2+}]_{\text{ext}}$  with a red light background enhances the motion of cells in the same and the opposite direction respectively according to cells' phototactic behavior under normal condition (pCa4 and pH 6.8). Increasing the pH tends to induce cells to move away from the light while increasing the  $[\text{K}^+]_{\text{ext}}$  gave the opposite results. Changing external ion concentration such as  $\text{H}^+$  and  $\text{K}^+$  affects the cell's membrane potential. Changing  $\text{Ca}^{2+}$  concentration affects both membrane potential and likely triggers internal signaling proteins such as  $\text{IP}_3$  and cAMP. Therefore, we hypothesize that cells may integrate these and potentially other signals to decide its phototaxis.

Finally, I developed a technique that can be used to measure changes of the electric field across the plasma membrane of the cell in response to rhodopsin excitation. Rhodopsin excitation is thought to cause transmembrane ion influxes resulting in changes in the electric field across the plasma membrane. These electric field signals are then sensed in the cilia to enable phototactic steering of the cell (Chapter 5).

BIOENERGETICS AND DYNAMICS OF CILIARY  
RESPONSES AND SYSTEMS BIOLOGY OF  
PHOTOTAXIS IN  
*CHLAMYDOMONAS REINHARDTII*

by

Suphatra Adulrattananuwat  
M.Sc. Chulalongkorn University, 2003  
B.Sc. Prince of Songkhla University, 1998

DISSERTATION

Submitted in partial fulfillment of the requirements for  
the degree of Doctor of Philosophy in Physics  
in the Graduate School of Syracuse University

May 2011

Approved by  
Professor Kenneth Foster

Copyright 2011 by Suphatra Adulrattananuwat

All rights reserved.

# TABLE OF CONTENTS

<b>List of Figures</b>	<b>x</b>
<b>List of Tables</b>	<b>xv</b>
<b>Acknowledgements</b>	<b>xvi</b>
<b>Chapter 1 Introduction</b>	<b>1</b>
<b>Chapter 2 The Opto-Electric Detector</b>	<b>6</b>
2.1 Introduction.....	6
2.2 Ciliary motility observation techniques.....	7
2.2.1 Holding a single cell.....	7
2.2.2 Illuminating the cilia.....	8
2.2.3 Observing ciliary motility and signal processing.....	10
2.2.4 Stimulating the cell.....	12
2.3 Designing the 2 <sup>nd</sup> generation of electro-optical detector.....	14
2.3.1 The 1 <sup>st</sup> stage: the operation amplifier (op-amp) current to voltage converter.....	14
2.3.2 The 2 <sup>nd</sup> stage: the 1 <sup>st</sup> -order high-pass filter.....	16
2.3.3 The 3 <sup>rd</sup> stage: the 2 <sup>nd</sup> -order Butterworth low-pass filter.....	16
2.3.4 The last stage: the instrumentation Amplifier (INA101HP).....	17
2.3.5 Pin connections of the electro-optical detector system.....	18
2.4 Data analysis.....	20
2.4.1 Removal of low frequency and DC drift from recorded data.....	22
2.4.2 Beating-frequency analysis.....	23

2.4.3	Stroke-velocity analysis.....	24
2.5	Creating a stimulus file.....	25
2.6	Future improvements and suggestions.....	27
<b>Chapter 3 Red light effects on ciliary motility</b>		<b>28</b>
3.1	Introduction.....	28
3.1.1	How does each compartment function?.....	30
3.1.2	The relationship between mutants (806 and <i>cpc1-2</i> strain) and wild-type.....	48
3.1.3	How does red light play a role in system function?.....	50
3.1.4	How can we interpret a relationship between input and output?..	51
3.2	Results and Discussions.....	57
3.2.1	Continuous red and 2.5-second-duration pulse of green-light responses of 806 strain.....	57
3.2.2	Duration-pulse responses of 806 strain.....	59
	• 5 second-duration pulse responses.....	59
	• 40 second-duration pulse responses.....	59
	• Comparison of beating-frequency responses between 5 and 40 second-duration pulse.....	64
	• 5 to 160 second-duration pulse responses.....	65
3.2.3	Besting frequency change in the dark and under DC red light...	67
3.2.4	Multi-sinusoidal responses at the low frequency range from 0.006 to 1 Hz of both 806 and <i>cpc1-2</i> strain to red light.....	71

3.2.5	Multi-sinusoidal responses at the high frequency range from 2 to 100 Hz of both 806 and <i>cpc1-2</i> strain to red light at 15 W/m <sup>2</sup> ...	88
3.3	Conclusions.....	94
<b>Chapter 4 Effects of external ion concentrations and red light on phototaxis</b>		<b>97</b>
4.1	Introduction.....	97
4.1.1	Change of extracellular ion concentration.....	100
4.1.2	Red light as a background light.....	110
4.1.3	Signaling pathway.....	110
4.2	Methods and materials.....	113
4.2.1	Cell preparation.....	113
4.2.2	Free Calcium medium preparation.....	113
4.2.3	Free proton medium preparation.....	114
4.2.4	Cell tracking machine.....	115
4.2.5	Data collection and analysis.....	115
4.3	Results and discussions.....	116
4.3.1	Varying external free calcium ion concentration.....	117
4.3.2	Varying external free hydronium ion concentration.....	122
4.3.3	Varying external free potassium ion concentration.....	124
4.3.4	Varying red-light intensity 633 nm.....	125
4.4	Conclusions.....	130
<b>Chapter 5 The electric field technique</b>		<b>132</b>
5.1	Introduction.....	132

5.2	Characteristics of the voltage-sensitive dye di-8-butyle-amino-naphthyl-ethylenepyridinium-propyl-sulfonate (di-8-ANEPPS).....	135
5.3	Methods and measurements.....	137
5.3.1	Staining Method.....	138
5.3.2	Experimental Setup.....	140
5.3.3	Operating the Ciliary Monitoring Program.....	143
5.4	Results and Discussions.....	146
5.5	Conclusions.....	149
	<b>Chapter 6 Summary and conclusions</b>	<b>151</b>
	<b>Appendix A: Infrared Emitting Diode (TSFF5200)</b>	<b>154</b>
	<b>Appendix B: Dual Low Noise Precision <i>Difet</i> OPERATIONAL AMPLIFIER</b>	<b>157</b>
	<b>Appendix C: Universal Active Filter (UAF42)</b>	<b>166</b>
	<b>Appendix D: Instrumental Amplifier (INA101HP)</b>	<b>172</b>
	<b>Appendix E: Ciliary monitoring program to maneuver both cilia on 2D plane using LabView</b>	<b>178</b>
	<b>Bibliography</b>	<b>179</b>
	<b>Biographical data</b>	<b>196</b>

## LIST OF FIGURES

1.1	An example of <i>C. reinhardtii</i> 's TEM images.....	1
1.2	Diagram of <i>Chlamydomonas</i> cell showing multiple positions of its two cilia..	2
1.3	The number of gene families of <i>Chlamydomonas</i> , human, and <i>Arabidopsis</i> .	2
2.1	Diagram of the holding needle method of a single cell.....	9
2.2	The absorption spectra of <i>Chlamydomonas reinhardtii</i> 's photoreceptors.....	9
2.3	Normalized response magnitude of the electro-optical detector.....	12
2.4	Schematic diagram of ciliary monitoring system.....	13
2.5	The circuit diagram of one-quadrant of the electro-optical quadrant detector.	15
2.6	The example of raw data before and after adding the DC adjust potentiometer to the INA101HP Instrumentation Amplifier.....	18
2.7	Diagram of holding position on the quadrant photodiode.....	21
2.8	Graphs represent the step stimulus pattern.....	26
3.1	Schematic representation of electron transfer and energetic pathway.....	30
3.2	The Calvin cycle.....	32
3.3	Activation of Fructose biphosphatase ferredoxin:Thioredoxin reductase.....	33
3.4	The glycolytic pathway and its standard Gibbs free energy ( $\Delta G'^{\circ}$ ) in kJ/mol.	34
3.5	The number of ATP molecules synthesized by the glycolysis, the Krebs cycle, and the electron transport Chain.....	36
3.6	Transport proteins along mitochondria membrane and their regulations.....	36
3.7	Theoretical relationship between ATP synthesis rate ( $J_p$ ) and driving force ( $n \Delta \tilde{\mu}_{H^+} - (-\Delta G_p)$ ).....	37

3.8	Regulations of the Krebs cycle.....	38
3.9	The mitochondrial electron transport chain.....	39
3.10	Show interconnections of mitochondria to photosynthesis.....	41
3.11	Show a relationship between ATP, ADP, and ATP/ADP ratio and light intensity.....	41
3.12	Show the interconnection between chloroplast and mitochondria through redox Messages.....	42
3.13	<i>C. reinhardtii</i> cells' cilium in a cross-section view and a side view.....	43
3.14	A dynein, its binding conformation, and configuration.....	44
3.15	Adenylate kinase (AK) shuttle.....	46
3.16	ATP transportation through the glycolytic network.....	47
3.17	Cross-section of <i>C. reinhardtii</i> 's axonemes in wild-type and <i>cpc1-2</i> mutant..	49
3.18	Graph shows a relationship between inversion of beating frequency and ATP concentration.....	50
3.19	The example of the second-order lag response to the step stimulus.....	54
3.20	Bode plot of the second-order lag system.....	56
3.21	Effects of continuous red light and 2.5 second pulse-duration green light on beating frequency responses.....	58
3.22	The 5 second-step red light effects on the beat frequency and stroke velocity.	60
3.23	The BF responses of the 40 second duration-pulse stimulus.....	61
3.24	The BF change (%) and its fitted transfer function.....	63
3.25	The Stroke velocity change (SV)(%) due to the 40 second pulse duration.....	64
3.26	Area of the “step-down” responses under the BF in the dark.....	65

3.27	The BF change (%) of various pulse-duration stimuli.....	66
3.28	A sample of raw data and the beating frequency of 806 strain in the dark.....	68
3.29	The BF of 806 strain at various red-light intensities and in the dark.....	69
3.30	A sample of raw data and the beating frequency of <i>cpc1-2</i> strain in the dark.....	70
3.31	The 806 BF responses of the multi-sinusoidal red light at various intensities.....	72
3.32	The smoothed BF responses of the multi-sinusoidal red light.....	73
3.33	The 806 BF change in percentage at red-light intensity of 15 W/m <sup>2</sup> .....	74
3.34	Bode plot of the 806 BF responses to the multi-sinusoidal stimulus.....	75
3.35	Diagram shows a possibility of total cell-signal processing function to Multi-sinusoidal stimulus.....	76
3.36	Predicted BF change (%) from two transfer functions.....	77
3.37	The 806 SV responses of the multi-sinusoidal red light.....	78
3.38	The interpreted ciliary movement.....	79
3.39	Bode plot of the 806 SV responses to the multi-sinusoidal stimulus.....	80
3.40	The <i>cpc1-2</i> BF responses of the multi-sinusoidal red light.....	83
3.41	Bode plot of the <i>cpc1-2</i> BF response to the multi-sinusoidal stimulus.....	84
3.42	The <i>cpc1-2</i> SV responses of the multi-sinusoidal red light.....	86
3.43	Bode plot of the <i>cpc1-2</i> SV responses to the multi-sinusoidal stimulus.....	87
3.44	The 806 BF and SV responses to the multi-sinusoidal red-light stimulus within the frequency range from 2 to 100Hz.....	89
3.45	The <i>cpc1-2</i> BF and SV responses to the multi-sinusoidal red-light stimulus	

	within the frequency range from 2 to 10 Hz.....	91
3.46	Bode plot of the <i>cpc1-2</i> BF and SV responses within the frequency range from 0.01 to 10 Hz.....	92
4.1	Driving forces of $K^+$ , $H^+$ and $Ca^{2+}$ .....	103
4.2	Photocurrent response of <i>C. reinhardtii</i> on the extracellular $Ca^{2+}$ .....	106
4.3	The calcium dependence of photocurrent (PC).....	106
4.4	Show the action spectra of the rhodopsin.....	107
4.5	Photocurrents of oocytes expressed with the ChR2.....	109
4.6	The effect of pH and $K^+$ on the membrane potential.....	109
4.7	The electric current of 1117 strain.....	112
4.8	Net displacement response vs. light intensity at 500 nm of 806 strain grown in NMM medium at different $Ca^{2+}$ concentrations .....	119
4.9	Net displacement response vs. light intensity at 500 nm of 806 strain grown in HSM medium at different $Ca^{2+}$ concentrations .....	119
4.10	Net displacement response vs. light intensity at 500 nm of 1117 strain grown in NMM medium at different $Ca^{2+}$ concentrations .....	121
4.11	Net displacement response vs. light intensity at 500 nm of 1117 strain grown in HSM medium at different $Ca^{2+}$ concentrations.....	121
4.12	Net displacement response vs. light intensity of 806 in different pH.....	123
4.13	Net displacement response vs. light intensity of 1117 in different pH.....	123
4.14	Net displacement response vs. light intensity of 806 strain in different potassium concentrations.....	124
4.15	Net displacement response vs. light intensity of 1117 strain	

	in different potassium concentrations.....	125
4.16	Net displacement response vs. green-light intensity of 806 strain with various red-light intensities in pCa 4 and pCa 5.....	127
4.17	Net displacement response vs. green-light intensity of 806 strain with various red-light intensities in pCa 6 and pCa 7.....	128
4.18	Net displacement response vs. green-light intensity of 1117 strain with various red-light intensities in pCa 4, pCa 5 and pCa 6.....	129
5.1	The rhodopsin excitation scheme.....	132
5.2	The example of relationship among rhodopsin receptor, ion exchange, membrane potential and ciliary motility on the cell-wall-deficient mutant....	133
5.3	The structure and its spectra of the voltage-sensitive dye, di-8-butyl-amino-naphthyl-ethylenepyridinium-propyl-sulfonate.....	136
5.4	The excitation wavelength of the di-8-Anepps and the rhodopsin.....	137
5.5	Protocol for loading the di-8-ANEPPS dye to the cell.....	139
5.6	The electric field measurement setup.....	143
5.7	An inside view of the sample box and the Plano-Convex lenses.....	144
5.8	Schematic of the electric field measurement.....	144
5.9	The laser light stimulus patterns.....	145
5.10	An example of a loaded single cell with the fluorescence dye.....	146
5.11	A recorded signal of different dye concentrations from a Lock-in Amplifier with 600 V supplied to the photomultiplier.....	147
5.12	Lock-in amplifier signals of cells loaded with 8 $\mu$ M dye.....	148

## LIST OF TABLES

2.1	Pin connection description for the acquisition signal.....	19
2.2	Pin connections between the output board and the modulating driver.....	19
2.3	A step stimulus sample.....	26
3.1	The elements of transfer function.....	52
4.1	Intracellular concentration of cAMP in <i>C. reinhardtii</i> .....	99
4.2	Show calcium concentrations, amount of chelators and CaCl <sub>2</sub> for each expected free calcium medium.....	114
4.3	The effects of the ionic concentrations and the red light in both 806 and 1117 strain.....	131
5.1	Pin connections between Lock-in Amplifier and analog input board.....	142

## ACKNOWLEDGEMENTS

I would here like to express my thanks to everyone from the bottom of my hearts for helping me through my doctoral degree including writing this thesis and supporting me in some ways or the other. Firstly, thank you to my advisor, Professor Kenneth Foster, for his support, encouragement, and guidance. He has been very kind to me. Also thanks to my co-advisor, research assistant professor Jurepan Saranak, for guidance on cell culture techniques, discussion on cell behaviors, and importantly talking to me about living in USA. Thank to all of my committee for reviewing the dissertation and providing meaningful ideas and comments.

I am indebted to all my colleagues Keith Josef, Ned Tuck, Taviare Hawkins, and Ganesh Srinivasan for providing me their helps such as setting up equipments, advising on the experiments, and software and hardware problems. Without them, I could take me a lot longer to finish this thesis. I am really appreciated their helps.

Designing and building the instrument can be harder and slower without helps from Charles Brown. Thank you for your helps. Special thank also to Daniel Kirkpatrick for his advising and helps for the computer issues, Lou Buda for maintaining the clean room where we keep the cell culture and Lester Schmutzler for finding me the tools that I needed in the workshop.

I would like to have a special thank to all of my friends and family for loving, supporting and encouraging me. I would not have a wonderful life without all of them. Specially thanks to the Development and Promotion of Science and Technology Talents Project (DPST) Scholarship, Thailand for giving me an opportunity and supporting me financially since I was an undergraduate student.

# Chapter 1

## Introduction

---

*Chlamydomonas reinhardtii*, a green alga, has components commonly found in animals such as a pair of cilia, arm-like structures, for swimming and rhodopsin receptors for sensing light and components found in plants such as a chloroplast for harvesting light energy. See Figure 1.1 for transmission electron microscopy (TEM) images of *C. reinhardtii*'s and Figure 1.2 for its diagram with its movement direction. Its genome database revealed that it shares about 40% of its genes with humans and 60% of its genes with plants (Merchant et al., 2007). Figure 1.3 shows the number of *C. reinhardtii*, human and *Arabidopsis*' gene families. This cell is studied widely in many fields including medicine, biotechnology, bioenergetics, and environmental engineering. It has multiple advantages as a model organism such as being easy to grow and to handle, the availability of mutants and systematic screening methods, and available techniques in molecular and genetic analysis (Harris, 2001). Furthermore, it is a unicellular cell, thus, its signaling network is much simpler than that of multi-cellular organisms.

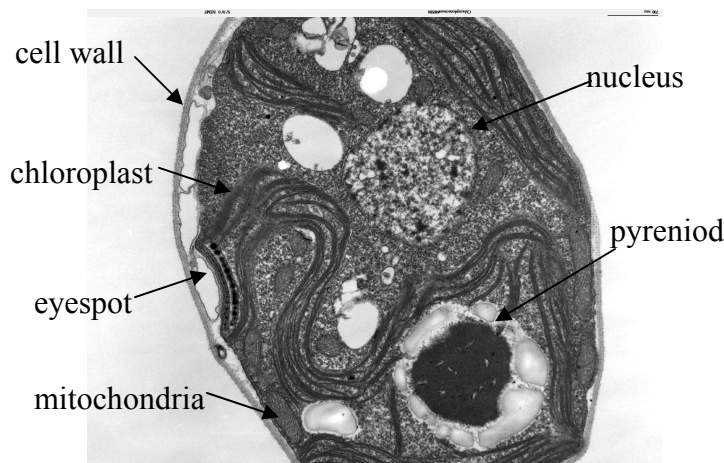


Figure 1.1. Show TEM images of *C. reinhardtii* (Smith et al., 2001). The cell comprises of basic organelles that are the characteristics of plants: chloroplast and animals: cilia (not shown).

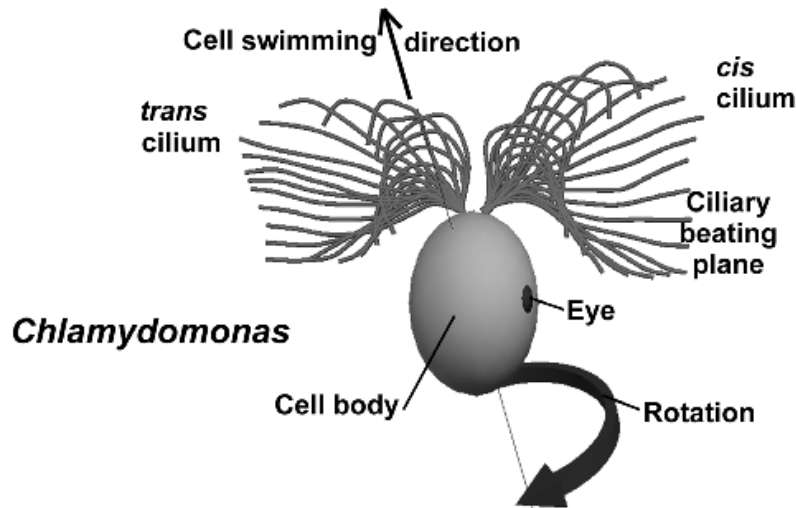


Figure 1.2. Diagram of *Chlamydomonas* cell showing multiple positions of its two cilia (Foster et al., 2006). It uses the eye to scan the light while rotating itself about 2 Hz. Once it detects the light, it adjusts its position according to the light direction using the cilia. Similar cilia's structures are found in various human organs such as the lung to repel dust and bacteria, the kidney to measure fluid flow, and in sperm to propel itself. Therefore, defective cilia can lead to diseases or malfunction in these organs (Fliegeauf et al., 2007).

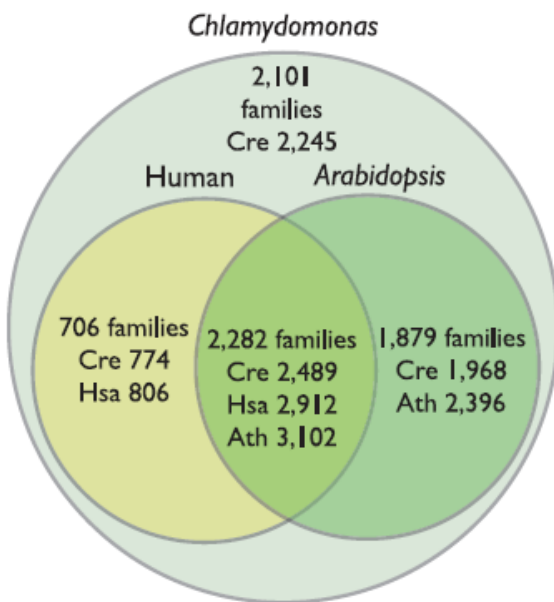


Figure 1.3. *Chlamydomonas* shares gene families with both animals (as represented by humans) and plants (*Arabidopsis*) (Merchant et al., 2007). Cre, Hsa, and Ath are *Chlamydomonas reinhardtii*, *Homo sapiens*, and *Arabidopsis thaliana* respectively. The family numbers mean the protein families and other figures are the numbers of proteins in each species.

This cell has an ability to process multiple inputs such as light intensity and ion concentration and adjust its responses such as ciliary motility and phototaxis. In this dissertation, I tried to understand the signaling pathway that controls some of these responses. Josef and colleagues (2005b; 2005a; 2006) intensively investigated how the green light (peak at 543 nm) affected its ciliary beating using a quadrant photo-detector to measure the beating of the cilia of a single cell held on a micropipette tip. He discovered that red light altered ciliary beating and proposed that red light could affect phototaxis (Josef, 2005). This idea supported the early finding by Takahashi and Watanabe (1993) that red light could reverse the direction of phototaxis.

I used the same method as Josef et al. (2005a; 2005b), however, the detector was improved to detect ciliary beating frequencies over a wider frequency range to make it useful to study slow ciliary beating mutants (Chapter 2). I used this improved quadrant photo-diode detector to investigate further how the red light affects ciliary beating in the *806* strain which is negatively phototactic, but otherwise similar to wild-type, and the *cpc1-2* strain which is a strain that was back-crossed to the *806* and in addition misses the C1b part of the central-pair complex, which enables ATP production in the cilia through the glycolytic enzyme, enolase (Zhang and Mitchell, 2004; Mitchell et al., 2005) (Chapter 3). Even though *C. reinhardtii* is just a single cell organism, its signaling network is nevertheless complicated. We are trying to understand how this organism integrates responses to external stimuli using its chloroplast, mitochondria, ciliary, and cytoplasmic compartments. This is in contrast to most of the prior efforts which have concentrated on a single component.

Signaling pathways of each compartment individually have been widely studied, but their dynamics on the sub-second time scale have remained under investigated. Their pathways link to each other either by chemical molecules such as ATP/ADP, 3-Phosphoglycerate (3PG), and Triose phosphate (Triose-P) or by electrical signals through ion exchanges. Thus, a change in one compartment can initiate changes in the others.

We modulated the light absorption of the chloroplast by modulating the light intensity. We measured its ciliary beating frequency (BF) *in vivo* as an indirect measure of the ATP concentration. According to Zhang and Mitchell (2004), if everything else is held constant, the BF is monotonically related to the ATP level via the Michaelis-Menton equation. We compared the BF of both 806 and *cpc1-2*. The mutant *cpc1-2* can not utilize 3-phosphoglycerate (3PG) to make ATP (Mitchell et al., 2005). Consequently, the overall availability of pyruvate and ATP concentration is less than the 806 especially in the ciliary compartment. Without ATP molecules, dynein arms, the motors that drive ciliary beating, within cilia are starved for ATP. However, the *cpc1-2* mutant has proved valuable in learning about the role of ATP in the cilia and conveniently the fluctuation of the BF is less making it possible to better resolve details of response.

In Chapter 4, the external factors affecting phototaxis of both positive and negative phototactic cell (1117 and 806 respectively) are discussed. I perturbed a cell population by changing external ion concentrations such as  $\text{Ca}^{2+}$ ,  $\text{H}^{+}$  and  $\text{K}^{+}$  and/or adding red light background illumination (peak at 633 nm). Cell movement was tracked by using in-house cell tracking software.

Finally, I developed and setup electric field measurements in order to measure changes of electric field across the plasma membrane (Chapter 5). This change is due to

rhodopsin excitation. The earliest signal detected for phototaxis is the electric current due to  $\text{Ca}^{2+}$  and  $\text{H}^+$  influx through its eyespot where rhodopsin receptors are located (Harz and Hegemann, 1991; Ehlenbeck et al., 2002). This signal is believed to distribute electrically along the plasma membrane and control ciliary motility. No one has measured the electric field before in *Chlamydomonas*. This method uses the di-8-Anepps dye which intercalates into the cell's plasma membrane. Due to the Stark Effect, which shifts both the absorption and fluorescent spectra as a function of the electric field, it is possible to have a measure of the electric field by recording the emitted fluorescent light intensity as the cells are stimulated by rapid alternation between two different light absorption wavelengths.

# Chapter 2

## The Opto-Electric Detector

---

### 2.1 Introduction

*Chlamydomonas*, a free-living unicellular alga, is used as our model for a single eukaryotic cell. It is self-sufficient with numerous biochemical processes within itself. Each of these processes is connected by networks that facilitate the whole system to perform efficiently. In order to understand how the cell regulates these networks, we have chosen to perturb the cell with light, change its environment and observe its ciliary motility or beating as an integrated response of swimming behavioral system. Since light is easily regulated, it is the perfect stimulus for this purpose. In order to monitor the ciliary beating, we have used the same method as Josef et al. (2005a; 2005 b), but we improved both its hardware and software in order to expand its applications. We have used a quadrant photodiode detector to monitor a single cell held on a micropipette in real time. The data from this method is easy to analysis and rich with extractable parameters such as beating frequency (the number of completed beating cycles per second) and stroke velocity (the root mean square of detected signal) and the setup itself is relatively inexpensive. In addition to the detector, the cilia are illuminated with the Near Infra-Red (NIR) light in order to avoid activation of photoreceptors. Therefore, the ciliary control response is closest to the response in its normal environment. This chapter addresses why we chose this system, how we combined several techniques to monitor ciliary beating,

how we designed the electro-optical detector, how we improved the stimulus signal, and finally how we now process and analyze the detected signal.

## **2.2 Ciliary motility observation techniques**

A variety of techniques such as holding and monitoring techniques has been used previously to observe the ciliary motility of either a freely swimming cell or the ciliary beating of a held cell. In the case of a freely swimming cell, the ciliary motility parameters can be obtained by indirect and direct methods. An example of an indirect method is the use of high-speed cinematography where the ciliary motility is monitored with a high-speed camera and recorded on film. Its ciliary beating frequency was derived from the cell motion's oscillating path due to the relationship of ciliary breast stroke and the back and forth motion during swimming (Racey et al., 1981). This method is only practical to track a cell for a short period of time. Therefore observing a held cell is more appropriate to monitor ciliary beating for a longer period of time. Several techniques to be described below have been combined in order to observe the ciliary beating of a single cell.

### *2.2.1 Holding a single cell (Wratten, 1994)*

In order to hold a moving cell in place, the easiest method is to use polylysine or concanavalin A (conA) as a glue to attach a cell on a cover slide. Again this method does not work for monitoring a long period of time due to the weakness of glue compared to the cell strength. Furthermore, this method can restrict the ciliary movement since the cilia beat just above the attached surface. Two additional methods are the holding needle and the suction micropipette (Rüffer and Nultsch, 1987) methods. For the holding needle method, the cell liquid sample is dropped into the chamber that has a glass-needle on the

bottom. The cell sticks on to the glass-needle by penetrating or pressing again its membrane. This method can damage the cell (Figure 2.1). On the other hand, the suction micropipette method using an open-end micropipette is less invasive since it can hold a single cell by applying a negative pressure without breaking through the cell membrane. The suction micropipette has been used by Ruffer and Nultsch (1987), then Holland et al. (1997) and Josef et al. (2005a; 2005b). We have used the same procedure as Josef et al. (2005a; 2005b). Cells were grown in a High Salt Medium-agar plate (HSM) for 3 to 7 days under a constant  $10 \text{ W/m}^2$  fluorescent light. Later they were transferred and shaken under the same light condition at 120 rpm in a nitrogen-deficient minimal medium (NMM) with  $0.1 \text{ mM CaCl}_2$  for 3 to 4 hours in order to induce cells to become gametes and lengthen cilia. Before starting an experiment, they were adapted in the dark for at least 30 minutes. The suction micropipette captured a single cell and was maneuvered by a micro-manipulator to get the cilia on the optical observing plane.

### 2.2.2 *Illuminating the cilia* (Josef et al., 2006)

In addition to the holding technique, choosing a light source to illuminate the cilia is also important because the cell has different types of receptors such as chlorophyll a and b, carotenoids, phytochromes and rhodopsins which can be excited at difference wavelengths. These receptors spread throughout the cell body. See the photoreceptor spectra on Figure 2.2 A and B. According to their spectra, Holland and colleagues (1997) introduced the use of infra-red LEDs as light sources to observe the ciliary beating without photoreceptor excitation. We have used an infrared diode array (an eleven-IR LED array connected circularly, peak at 870 nm, GaAIAs Double Hetero, model TSFF5200 from Vishay Intertechnology, Malvern, MA. See Appendix A) that we have

powered either with a pulsed or constant current generator. The IR diode array was pulsed with a forward current of 600 mA for 2 ms at about 50 Hz (a normal beating progression of a wild type cell). This pulsed source was used in order to position both cilia in the optical plane of the Nikon 1.43-1.20 NA oil-immersion dark-field condenser. After the cell was properly positioned, we switched the pulsed current generator to the 70-mA constant-current generator to provide stable illumination for recording the ciliary beating behaviors.

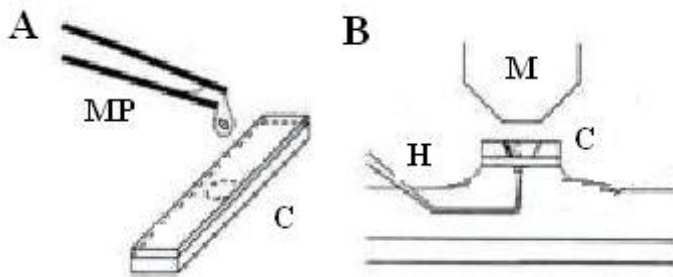


Figure 2.1. Diagram of the holding needle method where A: cell samples held by micropipette (MP) are dropped on a chamber (C). B: the hole on the bottom

allows a sharp glass needle (H) to expose to the cell samples and hook on a single cell. The ciliary motility can be monitored under microscope. This image is modified from Wratten (1994).

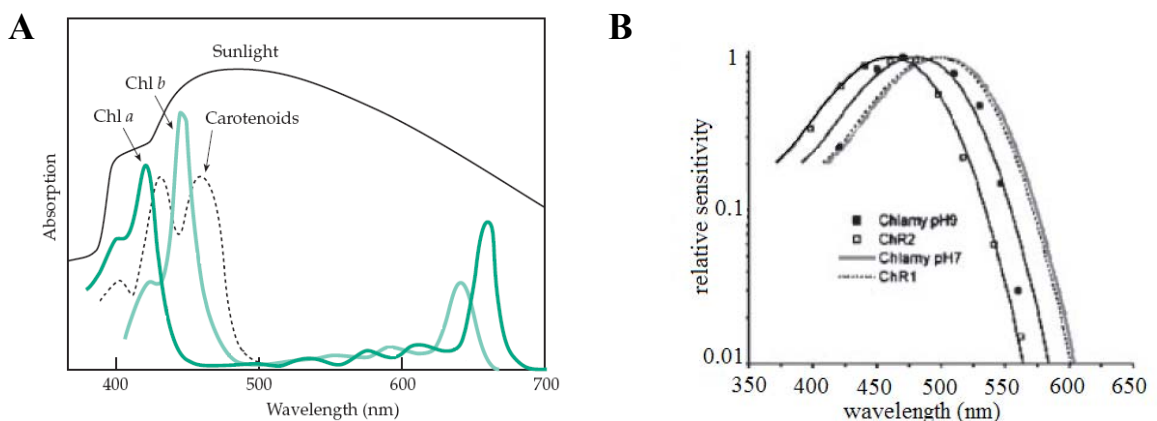


Figure 2.2. The absorption spectra of *Chlamydomonas reinhardtii* photoreceptors including chlorophylls and carotenoids in the chloroplasts (A: absorption spectra are

modified from Metzler and Metzler (2001) and two *Chlamydomonas* rhodopsins 1 and 2 (ChR1 and ChR2). B: The ChR1 and ChR2 action spectra are measured from the inward current expressed in oocytes at pH<sub>o</sub> 5.5 and -40 mV for ChR1 (Nagel et al., 2002) and pH<sub>o</sub> 7.6 and -100 mV for ChR2 (Nagel et al., 2003). The *C. reinhardtii* strain CW2 cells were used to measure their action spectra from the photocurrent at pH 7 (Ehlenbeck et al., 2002) and pH 9 (Nagel et al., 2003).

### 2.2.3 *Observing ciliary motility and signal processing*

The illuminated cilia can be observed by using the stroboscope which was first introduced by Gray (1929). This method captured the ciliary-beating frequency by synchronizing it with a strobe light. Later several research groups used the similar technique such as flash photomicroscopy (Rüffer and Nultsch. 1987; 1990; 1991; 1995; 1997) and an electronic photodetector (Smyth and Berg, 1982; Josef et al., 2005b) for monitoring ciliary motility. We have used a quadrant photodiode detector to monitor the ciliary movement through the Nikon Eclipse E600FN microscope (Nikon, Melville, NY) with the Nikon CFI 60x/1.00W Fluor DIC water immersion objective lenses (Josef et al., 2005b). To improve our signal from the dark field of NIR illuminated cilia, we reduce the scattered light from the cell body by using a blocking pin and use a NIR video camera for adjusting the position of the cilia. Once cilia are in the optical focused plane of the microscope, we switch the light path to the quadrant-photodiode detector.

The electronic photodetector has an advantage of fast signal processing. Josef (1994) and Josef et al. (2005b) built the 1<sup>st</sup> generation of the electro-optical detector. The operating system written in Pascal language had with a signal sampling interval of 0.25 ms. His electro-optical detector's circuit and system had several disadvantages. First of

all, it was designed to have a narrow bandwidth response which he claimed is to be between 20 and 80 Hz (Josef, 1994). However, it actually could not detect beating frequencies below 30 Hz. Thus it could not be used to study mutant cells with low beating frequencies (see the detector response spectrum on Figure 2.3). Second, some electrical components were obsolete. Therefore they were not only hard to find, but also expensive to get. Third, even though the temporal resolution of 0.25 ms was sufficient at that time, we improved this resolution to 0.078 ms in order to study at the higher resolution needed for studying of white-noise responses. Fourth, the software had a limited amount of data length per file (about 30 minutes) which we extended to record for hours depending on the computer speed and storage. This allows us to use this system to record a continuous effect of some stimulus such as white noise of the red light. Finally, the stimulus file had to be created into an ASCII code whose numbers of characters are limited.

We have upgraded the hardware with a new optical detector (or the 2<sup>nd</sup> generation electro-optical detector) and two PCI data acquisition boards (See section 2.3.) One of the boards, the 64-channel, 16-bit PCI digital I/O lab board (PDL-DIO 64 ST, United Electric Industries, Walpole, MA) has been used to modulate the polychromatic modulator system (the MOD.nc driver and the AOTF.nc acoustic tunable filter, AA Opto-Electronic Company: Quanta Tech, New York, NY) which controls the laser light. The other board is the 150 kS/s, 16-bit, 1/2/4/8 gains, 16SE/8DI A/D PCI multifunction board (PD2\_MF 16-150/16H, United Electric Industries, Walpole, MA) for recording the data from the electro-optical detector. (Note: see Table 2.1 for the pin connection between the electro-

optical detector and the PD2\_MF 16-150/16H input board, and Table 2.2 for the PDL-DIO 64ST output board and the AA.MOD.nC driver)

### 2.2.4 Stimulating the cell

We have used the 0.98-mm (in core diameter) fiber-optic strand (Edmund Optics NT-534) as a guiding light pipe from a 7-mW, 670-nm diode laser (LDCU12/1197 New Focus 9884, Power Technology Inc. Alexander, AR) and a 1.0-mW 543-nm Helium-Neon laser (Research Electro-Optics, Inc., Boulder, CO) to stimulate the cell as described by Josef et al. (2005a; 2005b; 2006). The laser has several advantages such as a wide range of light intensity and a narrow wavelength spectrum.

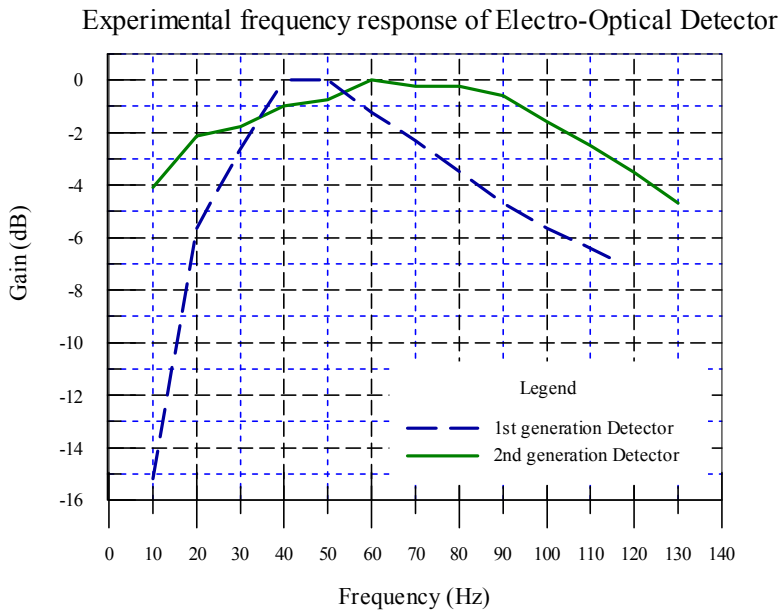


Figure 2.3. Normalized response magnitude of both the 1<sup>st</sup> and 2<sup>nd</sup> generation electro-optical detector.

Additional to the hardware setup (Figure 2.4), we also wrote in-house programs to acquire the data with C<sup>++</sup> language programs, to monitor and position the cilia with a Labview program (See Appendix E), and to analyze data with built in functions of MATLAB.

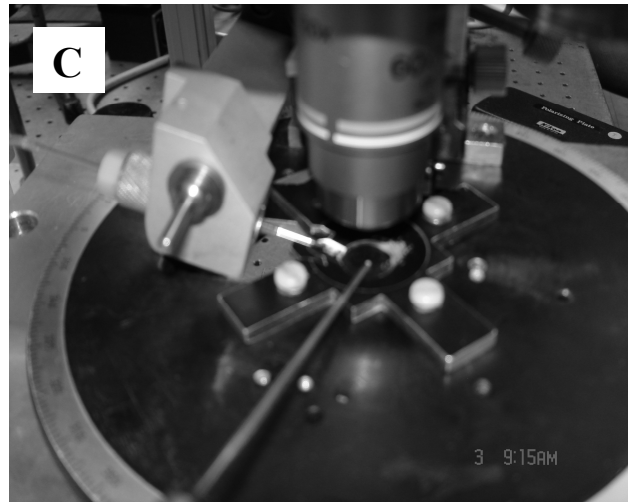
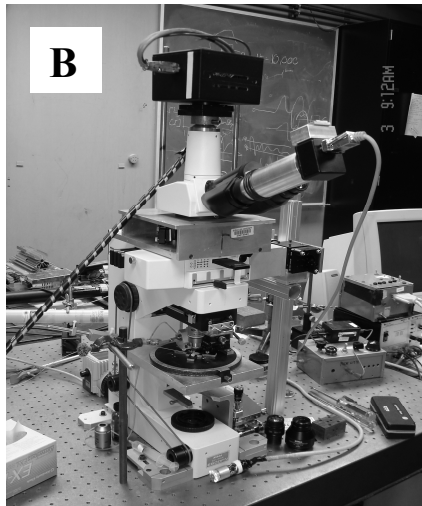
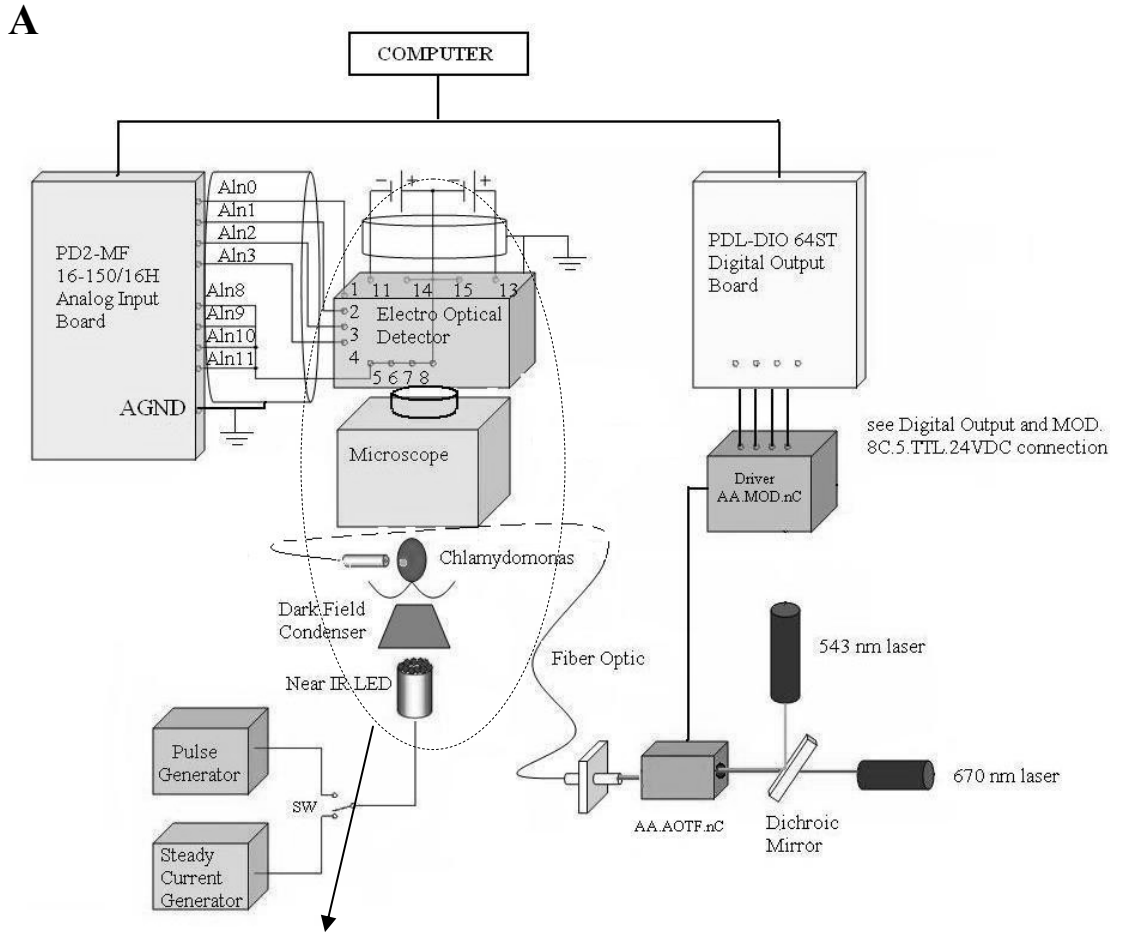


Figure 2.4. Schematic diagram of ciliary monitoring system (A) and an overall view of the microscope set up (B). Figure C shows a close up of the micropipette, the cell chamber, the fiber optic and the 60X water-immersion objective lens (C).

## 2.3 Design of the 2<sup>nd</sup> generation of electro-optical detector

The object was to rebuild the Electro-Optical detector with a band pass of 10-100 Hz based on Josef's designs and suggestions (1994). See Figure 2.5 for circuit diagram.

The circuit is divided into 4 stages as follows.

### 2.3.1 *The 1<sup>st</sup> stage: the operation amplifier (op-amp) current to voltage converter*

The quadrant-photodiode array (s1557, Hamamatsu USA, Bridgewater, NJ) converts incident light energy (800 to 1000 nm) to current proportional to the number of electron-hole pairs between the P and N layers created by the incident photon. This current, in the order of pico-amps, is carried by a Teflon shielded wire as recommended by the Burr-Brown data sheet to reduce noise. Further more, an operation amplifier current-voltage converter circuit was used to reduce both the internal and external noise and amplify the current. This circuit consists of the operational amplifier (OPA2111, Burr-Brown Corp., USA. See Appendix B.), a 300 MΩ feedback resistance ( $R_f$ ) and bias resistor, a 1 pF capacitor ( $C_f$ ) to eliminate gain peaking in the high frequency range from  $f_1 = 177 \text{ Hz}$  to  $f_2 = 531 \text{ Hz}$  (See equations 2.1 and 2.2), and the 0.1 μF capacitor was used to reduce noise (Figure. 2.5 Convert I to V stage). The 1<sup>st</sup>-stage has a gain of  $3 \times 10^8$  and its gain peaking elimination was calculated as the following:

$$f_1 = \frac{1}{2\pi R_f (C_f + C_j)} = 177 \text{ Hz} \quad 2.1)$$

$$f_2 = \frac{1}{2\pi C_f R_f} = 531 \text{ Hz} \quad 2.2)$$

where  $C_j = \text{photodiode capacitor} = 2 \text{ pF}$

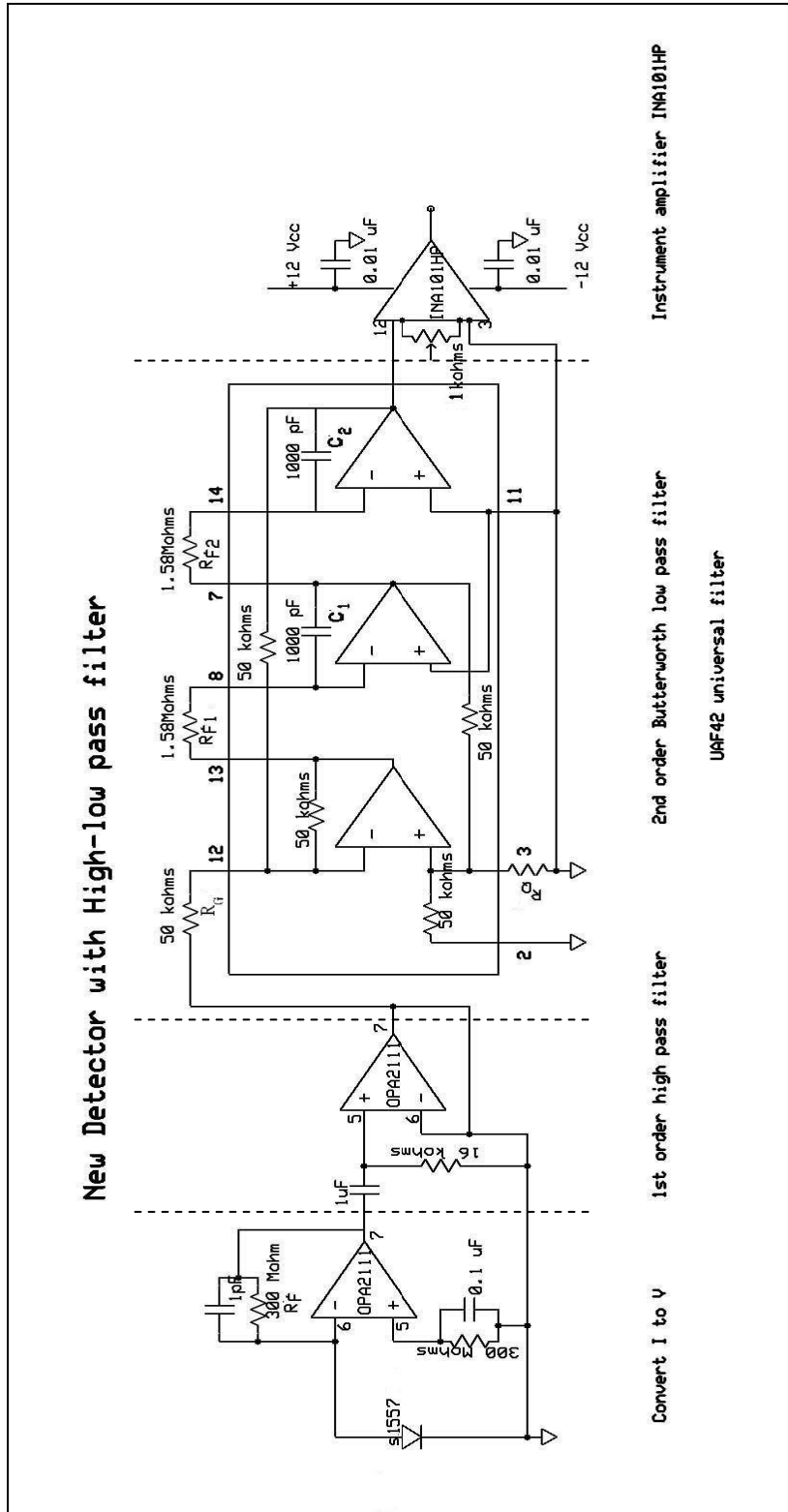


Figure 2.5. Show the circuit diagram of one-quadrant of the electro-optical quadrant detector. It is composed of five functional parts which are the photodiode array (s1557 circular quadrant photodiode array, Hamamatsu, Bridgewater, NJ), the current to voltage converter, the high pass filter, the low pass filter (UAF42 universal filter, Burr-Brown, USA), and the instrument amplifier (INA101HP, Burr-Brown, USA).

### 2.3.2 The 2<sup>nd</sup>-stage: the 1<sup>st</sup>-order high-pass filter

The 1<sup>st</sup>-order high-pass filter allows signals > 10 Hz to pass. From Johnson et al.

(1980), the capacitor and the resistor for this high pass filter are  $C = \frac{10}{f_c} = \frac{10}{10} = 1 \mu F$

and  $R = \frac{1}{\omega_0 C} = \frac{1}{2\pi f_c C} = 16 k\Omega$  respectively, where  $f_c$  is the cut off frequency. In

addition to their value, we chose polystyrene capacitors for their less noise.

### 2.3.3 The 3<sup>rd</sup>-stage: the 2<sup>nd</sup>-order Butterworth low-pass filter (UAF42 universal Filter, Texas Instrument, USA)

This stage allows signals < 100 Hz to pass. From UAF42 datasheet (See Appendix C), the low pass transfer function is

$$\frac{V_o(s)}{V_i(s)} = \frac{A_{LP} \omega_n^2}{s^2 + s\omega_n / Q + \omega_n^2} \quad 2.3)$$

where  $\omega_n^2 = \frac{R_2}{R_1 R_{F1} R_{F2} C_1 C_2}$  2.4)

$$A_{LP} = \frac{R_1}{R_G} \quad 2.5)$$

$$Q = \left(1 + \frac{R_4}{R_Q}\right) \left(\frac{1}{\frac{1}{R_1} + \frac{1}{R_2} + \frac{1}{R_G}}\right) \left(\frac{R_{F1} C_1}{R_1 R_2 R_{F2} C_2}\right)^{1/2} \quad 2.6)$$

According to “A Handbook of Active Filter” by Johnson et al. (1980), the constant Q is equal to 0.707 for the second-order Butterworth low-pass filter. In order to design the low-pass frequency filter at 100 Hz, we calculated the required component values according to the above equations and the existing component values within the UAF42 universal filter. We used the above equations to find the  $R_{F1}$  and  $R_{F2}$  by substituting

these parameters,  $f_n = 100 \text{ Hz}$ ,  $C_1 = C_2 = 1000 \text{ pF}$ ,  $R_1 = R_2 = 50 \text{ k}\Omega$  (See in Appendix C for their location in the circuit), into the equation 2.4.

$$\omega_n^2 = \frac{R_2}{R_1 R_{F1} R_{F2} C_1 C_2} \Rightarrow (2\pi f_n)^2 = \frac{50 \text{ k}\Omega}{50 \text{ k}\Omega R_{F1} R_{F2} (1000 \text{ pF})^2}$$

$$R_{F1} R_{F2} = 2.5 \times 10^{12} \Omega^2 \quad 2.7)$$

with the designed gain ( $A_{LP}$ ) of 1, we obtained  $R_G = R_1 = 50 \text{ k}\Omega$ .

Then we substituted the equation 2.6 and 2.7 with the following constants,  $Q = 0.707$ ,  $R_1 = R_2 = R_4 = R_G = 50 \text{ k}\Omega$ , and  $C_1 = C_2$ , and we had

$$Q = \left(1 + \frac{R_4}{R_Q}\right) \left(\frac{1}{\frac{1}{R_1} + \frac{1}{R_2} + \frac{1}{R_G}}\right) \left(\frac{R_{F1} C_1}{R_1 R_2 R_{F2} C_2}\right)^{1/2}$$

$$0.707 = \left(1 + \frac{50 \text{ k}\Omega}{50 \text{ k}\Omega}\right) \left(\frac{1}{\frac{1}{50 \text{ k}\Omega} + \frac{1}{50 \text{ k}\Omega} + \frac{1}{50 \text{ k}\Omega}}\right) \left(\frac{R_{F1}}{(50 \text{ k}\Omega)^2 R_{F2}}\right)^{1/2}$$

$$\frac{R_{F1}}{R_{F2}} = 1.125 \Rightarrow R_{F1} \approx R_{F2} \quad 2.8)$$

Finally substituting equation (2.7) into (2.8), we obtained the resistor values of

$R_{F1} = R_{F2} = 1.58 \text{ M}\Omega$  for the 2<sup>nd</sup>-order low pass filter.

#### 2.3.4 The last stage: the instrumentation Amplifier (INA101HP)

The potentiometer adjusts the signal gain and the average experimental value.

Experimentally, we adjusted its external gain setting resistor ( $R_G$ ) to about  $88 \Omega$ . As a result, the signal gain (See Appendix D for the INA101HP data sheet)

is  $G = 1 + \frac{40 \text{ k}\Omega}{R_G} = 455$ . Additional to the gain potentiometer, we also added the  $100 \text{ k}\Omega$

off-set potentiometer between Pin 6 and Pin 7 of the INA101HP in order to get rid of the

DC offset of the analog signal which was causing clipping of the signal. Figure 2.6 is the example of before and after adding the offset potentiometer.

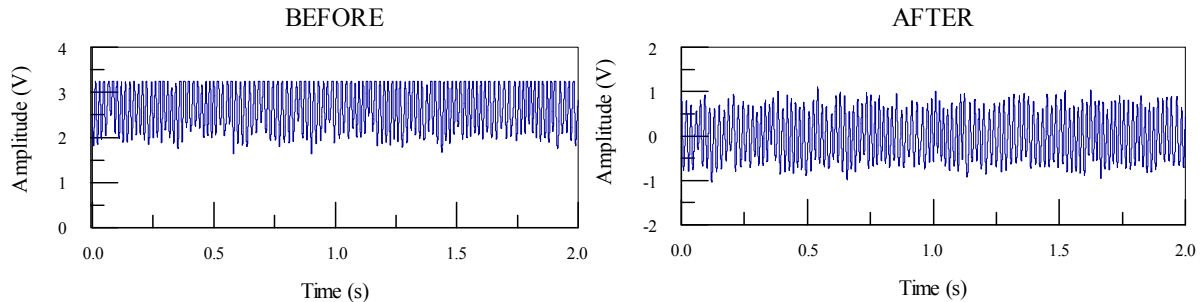
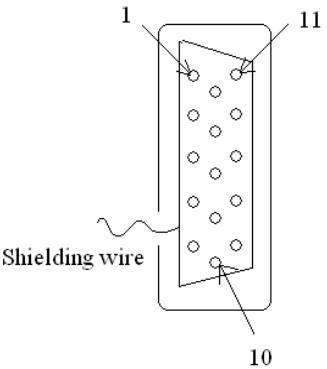


Figure 2.6. Show the example of raw data before and after adding the DC adjustable potentiometer to the INA101HP Instrumentation Amplifier.

### *2.3.5 Pin connections of the electro-optical detector system*

Since we have to detect small current signals in the frequency range of 60 Hz, the detector system requires a proper ground and a DC power supply that does not interfere with the recorded signal. A Golf Cart DC battery is an inexpensive solution for a  $\pm 12V$  power supply without 60-Hz ripple. Besides the DC supply, we have also used a shielded cable to connect between the input board (PD2\_MF 16-150/16H) and the detector box. Furthermore, we carefully grounded the detector circuit with an external ground as described in Table 2.1. These actions reduced the external noises from acquired signal.

Pin	Signal Name	Wire color
1	Channel 1	White
2	Channel 2	Green
3	Channel 3	Red
4	Channel 4	Blue
5	Ground	Black
6	Ground	Black
7	Ground	Black
8	Ground	Black
9	-	-
10	-	-
11	-12 volts	Blue
12	-	-
13	+12 volts	Red
14	Ground	White
15	Ground	Green
Shielding wire	Ground to the back of CPU computer	Bare wire



The diagram shows a vertical 15-pin connector. Pin 1 is at the top left, pin 11 is at the top right, and pin 10 is at the bottom right. A wavy line labeled 'Shielding wire' is connected to the back of the connector.

Table 2.1. Pin connection description for the acquisition signal from the output pins of the electro-optical detector to the PD2\_MF 16-150/16H input board.

Besides these, we also have the pin connections between the output board (PDL-DIO 64ST) and the polychromatic modulator system (the AA.MOD.nc driver) (Table 2.2)

Modulator Pin	Channel name on PDL DIO 64ST
6	DIO22
7	DIO21
8	DIO20
9	DIO19
10	DIO18
11	DIO17
12	DIO16
13	DGND (red)
14,15,16	Ground
24,25,26	+ 24 DC

Table 2.2. Pin connections between the output board and the modulating driver.

## 2.4 Data analysis

The quadrant photodiode tracks the light intensity corresponding to ciliary positions as see in Figure 2.7 A. The channel 1 and 2,  $Q_1$  and  $Q_2$ , represent the *trans*-cilium signal while the channel 3 and 4,  $Q_3$  and  $Q_4$ , represent the *cis*-cilium signal (Figure 2.7 B and C). This light energy is converted to the electrical voltage signal, called the raw data, into the range between a few millivolts and a few volts. Even with carefully grounding the detector system, all the noise on the signal cannot be eliminated. In order to reduce this noise, we filtered the raw data according to section 2.4.1.

The filtered signals are subsequently analyzed into several derived parameters, for example beating frequency and stroke velocity. Sections 2.4.2 and 2.4.3 show how the beating frequency (BF: the number of beating cycle per second) and the stroke velocity (SV: the root mean square of the signal) were determined respectively. MATLAB was used to filter and derive these parameters.

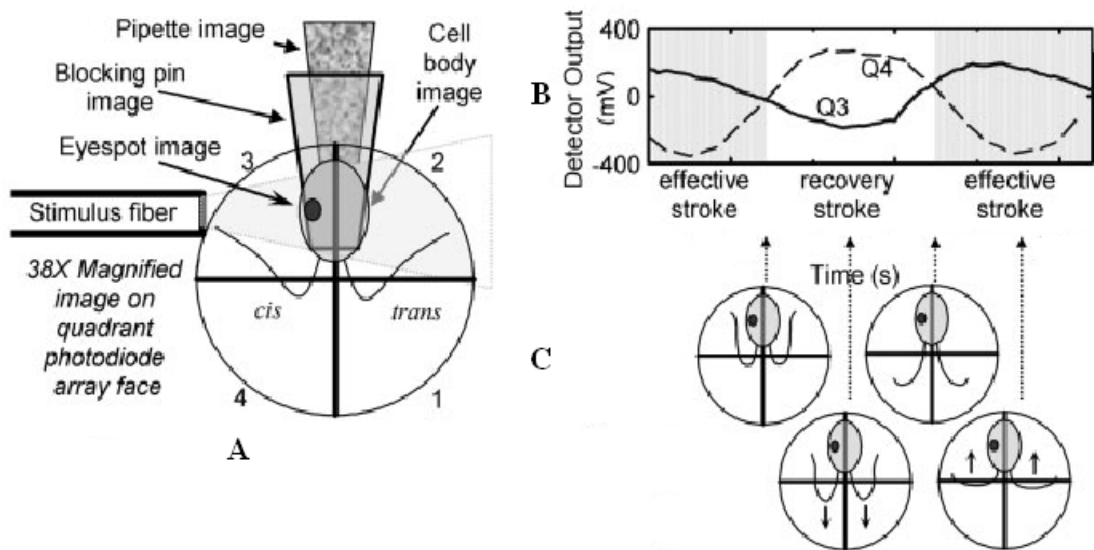
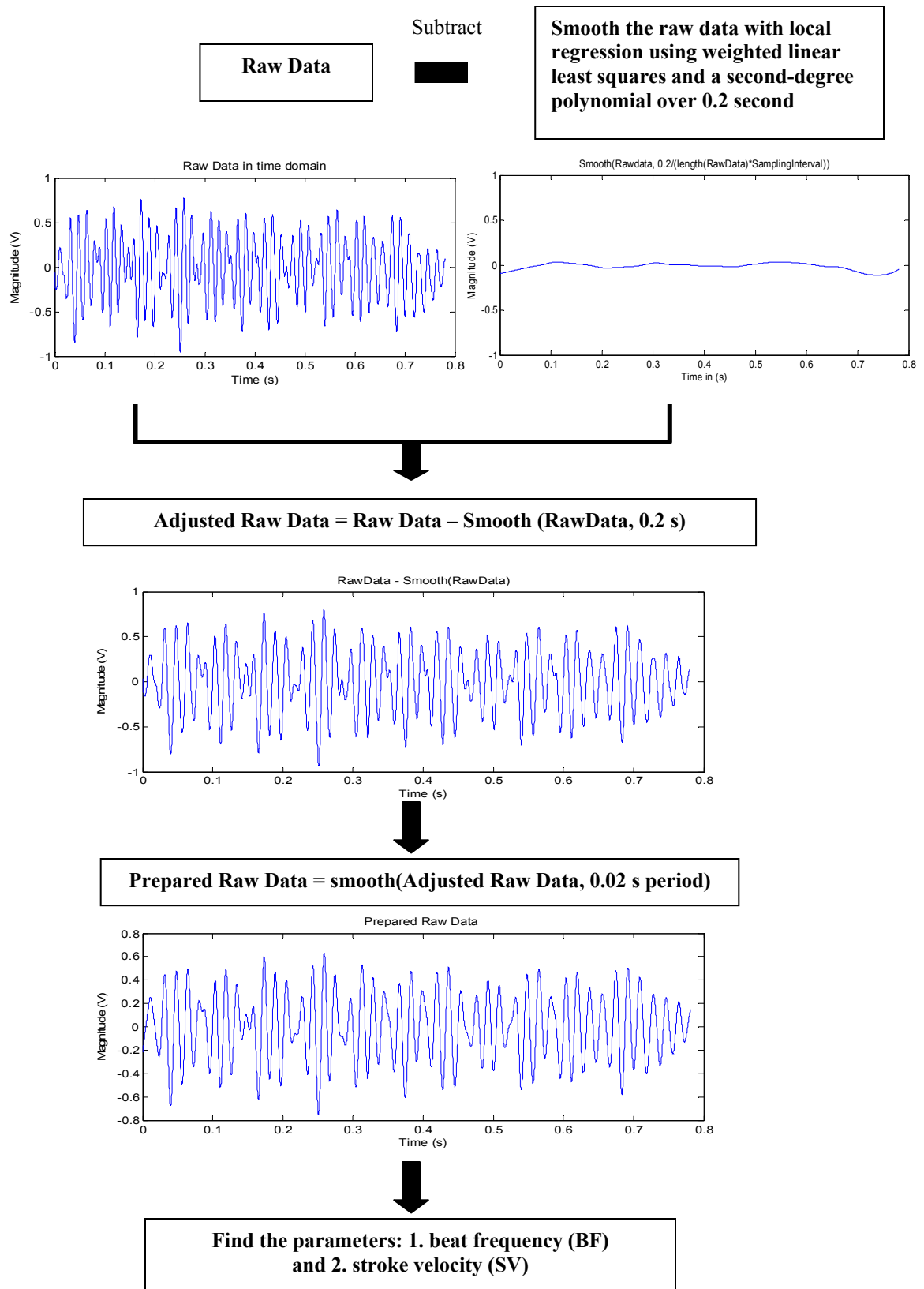


Figure 2.7. Signal diagram. A: shows the position of cell image on the quadrant photodiode detector. The single cell is held on a micropipette and light scattered by the cell body was reduced by a blocking pin in the optical relay box. B: the detector output signal represents the change of light intensity in channel Q3 and Q4 where the effective stroke is the ciliary motion from maximal anterior position to maximal posterior position and the recovery stroke is the opposite motion. C: the actual ciliary beating corresponds to the electrical signal in B. Figures are from Josef et al. (2005a; 2005b.)

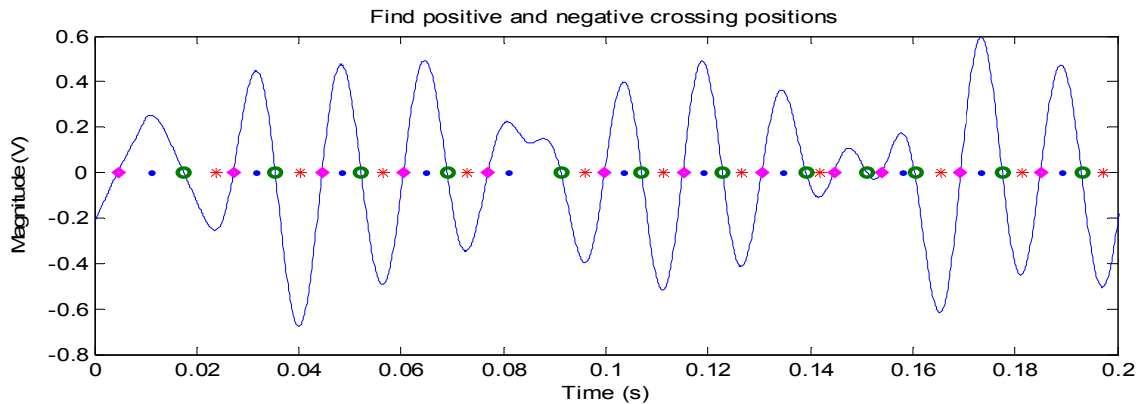
### 2.4.1 Removal of low frequency and DC drift from recorded data



## 2.4.2 Beating frequency analysis

1. Find beat frequency response

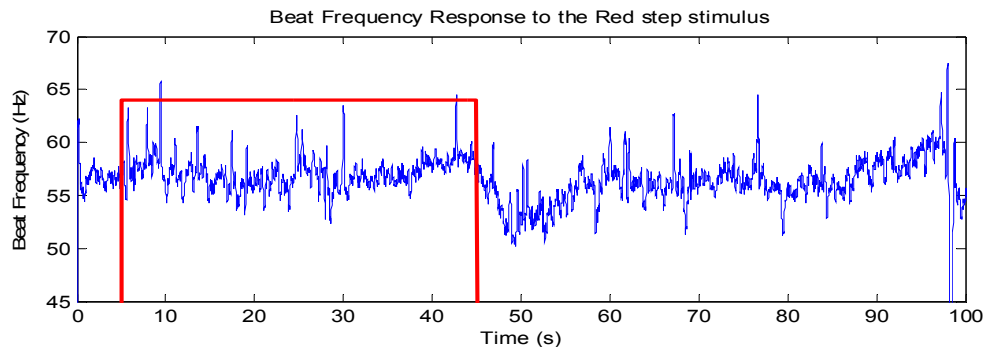
Find maximum (max), minimum (min), positive (pc) and negative crossing (nc) indexes within time period of 0.01 second which is a half period of 50 Hz. (an average ciliary beating frequency)



Beat frequency (BF) between two minimum indexes  
 $= 1 / \{(\min[i+1] - \min[i]) * \text{sampling interval}\}$  and so on

Resample BF response at the same rate as stimulus sampling frequency

BF response = median[BF\_min, BF\_max, BF\_pc, BF\_nc]

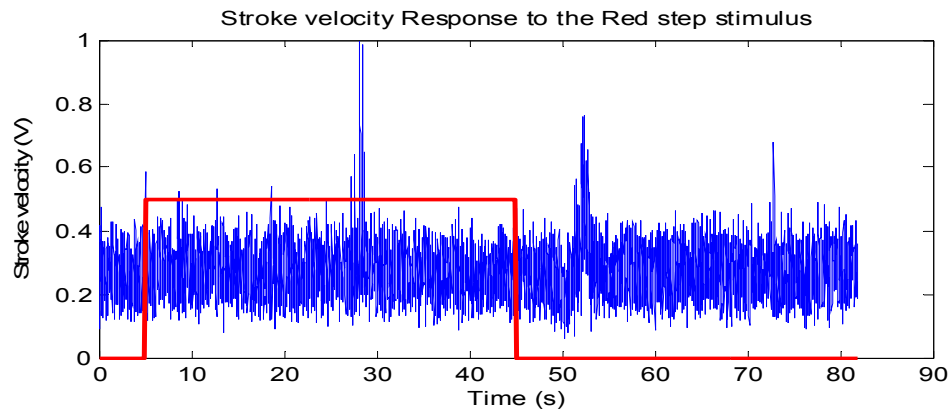
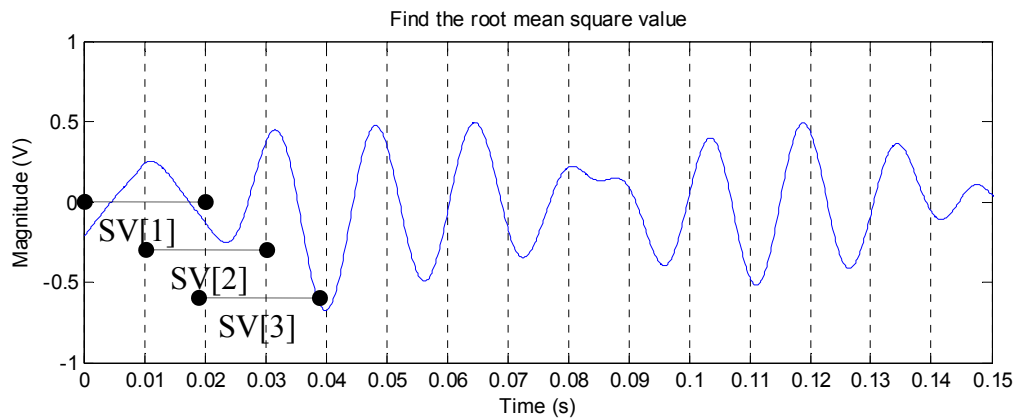


### 2.4.3 Stroke-velocity analysis

2. Find stroke velocity response (SV)



Find the root mean square value over the window size of  $2 \times$  stimulus sampling interval and move to the next by half of window size. For example, stimulus sampling interval is 0.01 s. The window size is 0.02 s.



## 2.5 Creating a stimulus file

We have used in-house C<sup>++</sup> programs (c:\ciliary monitor\Experiment-stream.dsw) to control both the input and output data acquisition with the same acquiring rate. The maximum rate is at 12.8 kHz or 78.25  $\mu$ s per sample. Therefore, creating the stimulus file (\*.stm) has to consider this rate corresponding to others parameters such as the sampling frequency rate (fs), the number of levels per sample (NI), the number of samples (Ns), and the number of repeated stimulus (n) (Table 2.3 A stimulus sample file (\*.stm)). Moreover, there are some constraints that have to be taken into account as the following:

1. The Pulse Width Modulator (PWM) frequency rate =  $fs * NI \leq 12800$   
(the sampling frequency rate \* the number of levels per sample where fs is an integer and NI is a base 2 number for example 2, 4, 8, 16, 32, 64, and 128)
2.  $NI * Ns * n = integer * 4096$   
(Ns and n are integer. Due to the in-house software has the 4096 data point per frame, the stimulus data point has to fill this frame. Otherwise it will automatically turn on another stimulus channel if you set up for two stimulus channels)
3. An empty line between stimulus parameters and stimulus pattern
4. Stimulus pattern can be created by using the Notepad, Psiplot or Matlab program. For example, step stimulus which starts with “0” level or dark for 0.5 s and 32 levels of 64 maximum levels or 50% light intensity for 0.5 s as see on Figure 2.8.

Stimulus value	Description			
100	Sampling frequency of each sample in Hz = fs			
64	stimulus parameters			
100		Number of levels per sample = NI		
16		Number of samples = Ns		
	Number of repeats = n			
	Empty line			
0	stimulus pattern			
0		Total 50 samples (sampling at $1/fs = 0.01$ s) of "0" value which means no light		
.			and total of 50 samples *NI levels = 3200 levels (sampling at $1/(fs*NI) = 0.00015625$ s)	
.				is proportional to light intensity
.				
32				
32				
32				
.				
.				

Table 2.3. A step stimulus sample where the light is "Off" for 0.5 s and "On" for 0.5 s at 50% light intensity. The PWM rate is 0.0001526 and data acquisition rate is 0.01s.

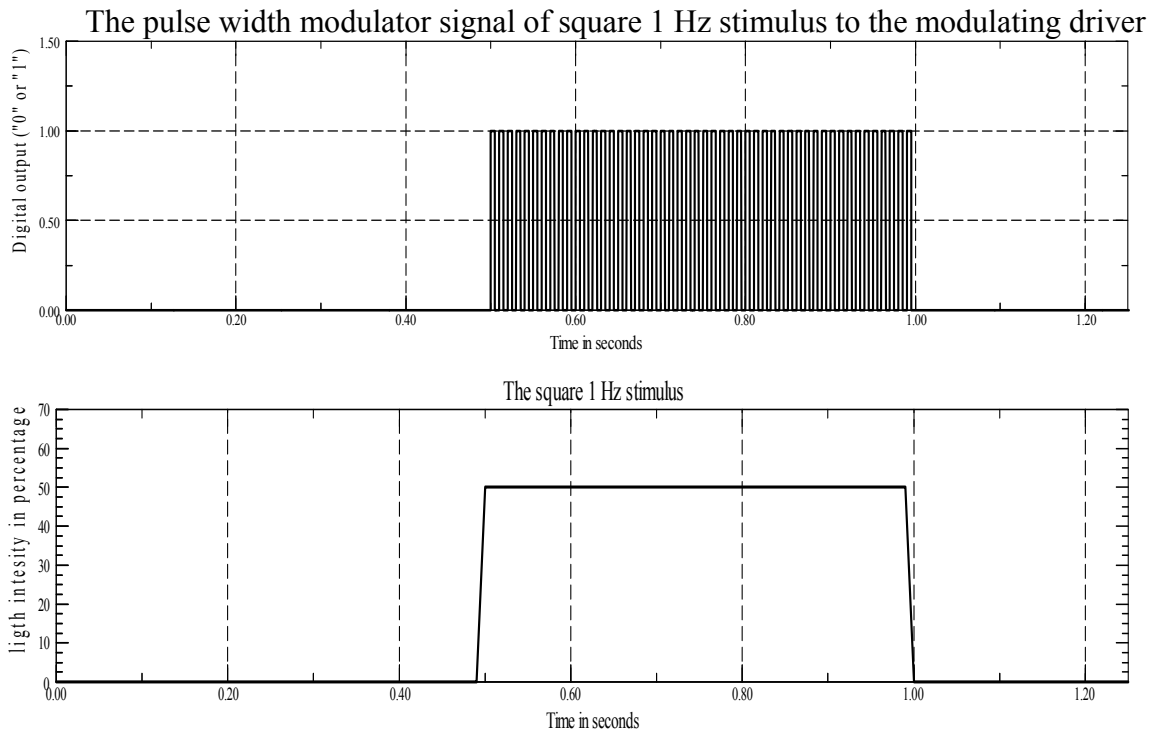


Figure 2.8. Graphs represent the step stimulus pattern according to table 2.3.

## 2.6 Future improvements and suggestions

2.6.1 The optical tweezers technique could be used to hold a single cell in place instead of micropipette. It would allow control and monitor the suction force that can affect the cell body's mechanoreceptors (Yoshimura 1998) and may change the ciliary motility. While the beating frequencies can easily be determined by the oscillation of the cell body, this method has the distinct disadvantage that the cilia may not be observed distinguishably since cell orientation is not fixed. In addition, the eye may not be stably stimulated.

2.6.2 If the mechanical micro-manipulator is still being used, it should be redesigned to be more stable for a manual manipulation or use a damped hydraulic manipulator to reduce the unsteady force from hand manipulation. A computer controlled manipulator is also another possibility.

2.6.3 More powerful NIR LED could increase the light intensity and increase the signal-to-noise ratio.

2.6.4 To observe the cells, the electro-optical detector could be supplemented by a high sensitive digital camera to record ciliary beating with higher spatial and time resolution.

2.6.5 The collected data files are large. For example, the data recorded at the sampling frequency of 50 Hz for 131,072 levels of 4 channels filled about 150 Mbytes. The file size can be reduced by assigning new variable types through out the acquisition program.

2.6.3 Acquiring and analyzing programs are not automatic. Improvements in the computer program could shorten the experimental and analytical time.

# Chapter 3

## Red light effects on ciliary motility

---

### 3.1 Introduction

*C. reinhardtii* has several photoreceptors including cryptochrome-like proteins for light-dark cycle (Reisdorph and Small, 2004), phototropins for cell division and differentiation (Weissig and Beck, 1991), rhodopsins for phototaxis (Foster et al., 1984), a phytochrome-like receptor (Petridou et al., 1997) (Mittag et al., 2005 claim there is no physiological and biochemical evidence) and chlorophylls for photosynthesis. These receptors are sensitive to blue light. However, the rhodopsins are also sensitive to green light while the chlorophylls and the phytochrome-like receptor are sensitive to red and red/far-red light respectively. In this chapter, we study how red light plays a role in ciliary motility rather than green light or rhodopsin excitation.

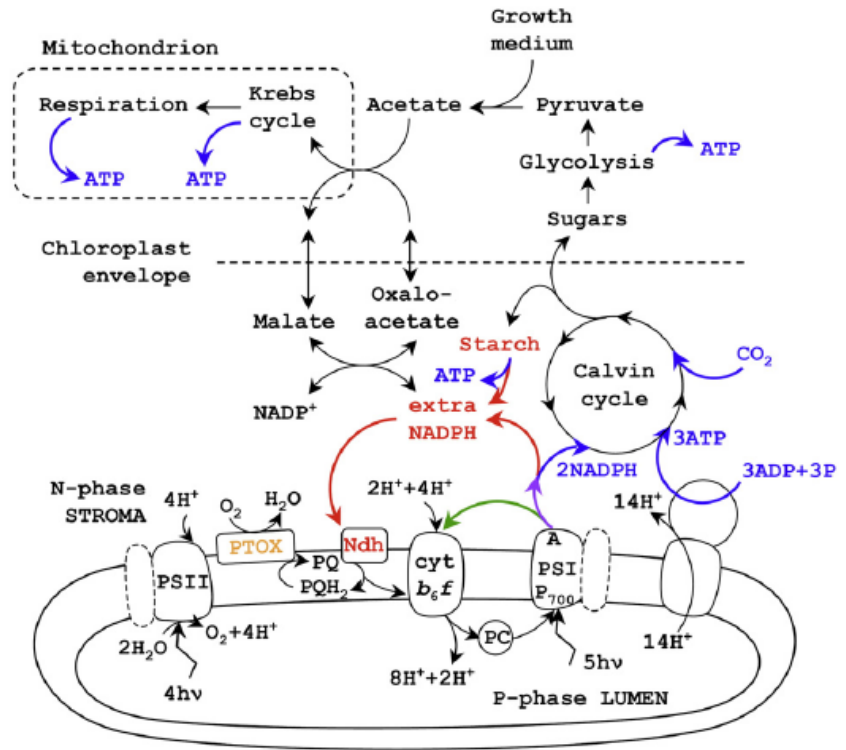
Unlike higher plants, no *C. reinhardtii* gene has so far been identified that shows homology to phytochrome or red/far-red light sensitive photoreceptor (Mittag et al., 2005). However, a specific far-red phytochrome with absorption peak between 710 and 730 nm is reported (Petridou et al., 1997) and phytochromes have been identified in other green algae (Haupt et al., 1976; Morand et al., 1993). Red light possibly stimulates chlorophylls in photosynthesis since the spectra of photosystem I and photosystem II (PSI and PSII) have maximal absorption at about 700 nm and 680 nm respectively. In addition, a blockage of electron transfer between PSI and PSII using 3-(3, 4-dichlorophenyl)-1,1-dimethylurea (DCMU) decreased red light effect ( $\lambda > 620$  nm) on

the reversal sign of phototaxis (Takahashi and Watanabe, 1993). Therefore, the red light (peak at 670 nm) we have used for stimulation could be stimulating chlorophylls. The first red light report was the reset of circadian clock in cell wall-less mutant, *CW15* by 660 nm-red light (Kondo et al., 1991). Red light or photosynthesis was thought not involved in phototaxis (Stavis and Hirschberg, 1973; Nultsch and Häder, 1979), however, Takahashi and Watanabe (1993) demonstrated that red light or photosynthesis (wavelength > 620 nm) reversed the phototactic direction of *C. reinhardtii*, positively phototactic strain *I37c*. Josef (2005) also reported that red light (peak at 670 nm) increased the beating frequency and decreased the stroke velocity. Therefore, he suggested that it could affect the green light signaling pathway. Red light can eventually reduce or inhibit green light responses under specific conditions (see Figure 3.21 for results and more explanation in discussions).

We investigated red light effects on the ciliary beating of the *806* (similar to wild-type with respect to red light effects based on beating frequency) and *cpc1-2* strain by stimulating them with different red-light temporal patterns including pulse stimuli from 5 to 160 s and multi-sinusoidal stimuli at discrete frequencies from 0.006 to 100 Hz. Sensed red light forms the cell system input while the beating frequency (BF) and stroke velocity (SV) of the cilia are cell system outputs. We try to understand the signaling pathway that controls ciliary beating and its interconnection among cellular compartments including the chloroplast, mitochondrial, cytoplasmic, and ciliary compartments by finding the relationships between input (as measured the modulated red light) and output (the behavior of the cilia). Figure 3.1 show a diagram of how each compartment connects electrically and chemically. Although chemical reactions of each

compartment and interconnections among them are known by studying isolated compartments (Harris, 1995), how they might work dynamically together as a system needs further clarification. Using red light stimuli and observing ciliary responses (Chapter 2 method) allow us to reveal how this system may function as a whole dynamically on the sub-second time scale.

Figure 3.1. Schematic representation of electron transfer and energetic pathway among cellular compartments: chloroplast, mitochondria, and cytoplasm (Alric et al., 2010).



### 3.1.1 How does each compartment function?

- Chloroplast (Metzler and Metzler, 2001; Harris, 1995)

Photosynthesis in the chloroplast is carried out with two main absorption centers, photosystem I and II (PSI and PSII). Each of these centers has the absorption pigments, chlorophyll a (Chl a), chlorophyll b (Chl b) and carotenoids. A spinach chloroplast has 160, 70, and 48 molecules of Chl a, Chl b and carotenoids respectively. The greatest absorption wavelength is 678 nm from Chl a (See its spectra on Figure 2.2 A). We used

the 670 nm-laser light to stimulate the cell which is close to its maximum absorption wavelength. The electrons are transferred from Chls and converted to a membrane gradient driving a production of energy molecules such as ATP and NADPH. These molecules are used as fuel to further drive the Calvin cycle (Figure 3.2) producing sugar and dihydroxyacetone phosphate (DHAP) by fixing carbon dioxide molecules. The DHAP molecules are transported to the cytoplasm by its antiporters or translocators (dihydroxyacetone phosphate (DHAP)-P<sub>i</sub> antiporter exchanging P<sub>i</sub>). Later DHAP molecules are converted to 3-phosphoglycerate (3PG) by the glycolytic pathway in the cytoplasm (Figure 3.4). 3PG molecules are found through out the cell body and the ciliary compartment. The final product of the glycolytic pathway is pyruvate.

*Chlamydomonas* which is analogous to a C<sub>4</sub> plant is also able to exchange malate for pyruvate. Most chloroplast ATP and NADPH molecules from light absorption centers are reused within the Calvin cycle. Therefore light energy is likely converted to chemical energy as organic molecules (sugars), the starting materials for metabolic pathways of other compartments (Campbell 1996).

The transportation rate of this sugar depends on its concentration within the chloroplast, [DHAP]<sub>chl</sub>, and the concentration of cytoplasm phosphate, [P<sub>i</sub>]<sub>cyt</sub>. If [P<sub>i</sub>]<sub>cyt</sub> is high or a cell continuously demands ATP, DHAP-P<sub>i</sub> will increase its export rate. If it is low, DHAP-P<sub>i</sub> does not have enough [P<sub>i</sub>]<sub>cyt</sub> to exchange for DHAP, therefore, it is converted and stored temporarily as starch. The electron transfer pathway, the Calvin cycle and the DHAP-P<sub>i</sub> antiporter communicate among themselves through their available products or supplies. For instance, limitations of ATP and NADPH from electron transfer pathway under low light intensity reduces the [DHAP]<sub>chl</sub>. On the other

hand, ATP and NADPH is in excess under high light intensity, however, CO<sub>2</sub> is limited by the respiration pathway. Therefore, [DHAP]<sub>chl</sub> also reduces and less [DHAP]<sub>chl</sub> is exported to the cytoplasm. Besides these regulators, light can affect indirectly the enzymes not in equilibrium such as fructose-1, 6-biphosphatase through the ferredoxin:thioredoxin reductase and **riburose bisphosphate carboxylate** (Rubisco) through ion movements (H<sup>+</sup> and Mg<sup>2+</sup>).

The “step-up” light activates ferredoxin:thioredoxin reductase and consequently activates several carbon metabolism enzymes such as fructose-1, 6-biphosphatases (FBPase) through reducing sulfide bridge and activating enzymes (See Figure 3.2 Fructose-1, 6-biphosphatase in the Calvin cycle and Figure 3.3 activation diagram of ferredoxin:thioredoxin reductase pathway). Light activates the carbon fixation and produces sugar molecules as its end products; nevertheless, it can also inhibit the pathway through PSII inhibition if the light intensity is too high.

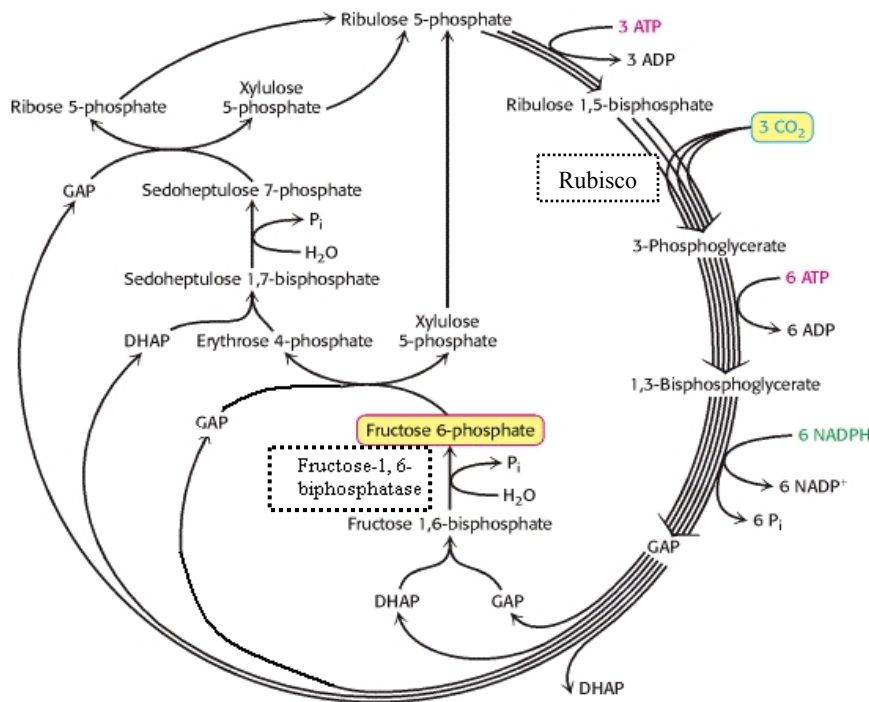


Figure 3.2. Calvin cycle is a metabolic pathway that fixes carbon dioxide (CO<sub>2</sub>) and releases a product in the form of a sugar (DHAP: 3 carbon molecules) (modified from Berg et al., 2002)

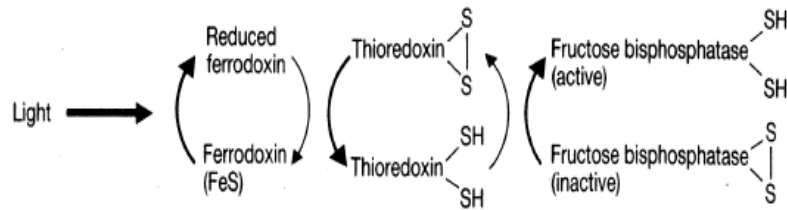
Figure 3.3. Activation

of Fructose

bisphosphatase by

ferredoxin: thioredoxin

reductase (Harris,



For the “step-down” response, no electrons are transferred within the light reaction center and consequently the concentrations of ATP and NADPH are reduced, removing fuel for the Calvin cycle. If the Calvin cycle continued in the dark, then critical reduction of substrates such as ATP, NADPH, and Ribose 5-phosphate would be used up and when light is turned on again, the Calvin cycle would take some time to produce these substrates.

- Cytoplasm (Nelson and Cox, 2000)

Various molecules from other compartments are released into the cytoplasm compartment. They interact and then diffuse throughout the cell. Several chemical reactions happen within this compartment including glycolysis (Figure 3.4). Here DHAP from the chloroplast is converted to 3-phosphoglycerate (3GP) as well as pyruvate. 3PG molecules travel to the ciliary compartment where they are the secondary energy source to make ATP for ciliary motion (Mitchell et al., 2005). Pyruvate is imported into mitochondria as an initial substrate for the citric cycle or Krebs cycle (more details in mitochondria section). The direction of chemical reactions in glycolysis pathway depends on its Gibbs free energy (G). Gibbs free energy measures the amount of energy to do work under constant temperature and pressure. Its change ( $\Delta G$ ) can be calculated from the change of heat content, called enthalpy or H, and entropy or S, of chemical reaction at

constant temperature. In other words,  $\Delta G = \Delta H - T\Delta S$ . If  $\Delta G < 0$ , the reaction occurs spontaneously. While  $\Delta G=0$ , the reaction is in equilibrium. If  $\Delta G > 0$ , the reaction is less preferred, but may occur slowly if a subsequent step has  $\Delta G < 0$ .

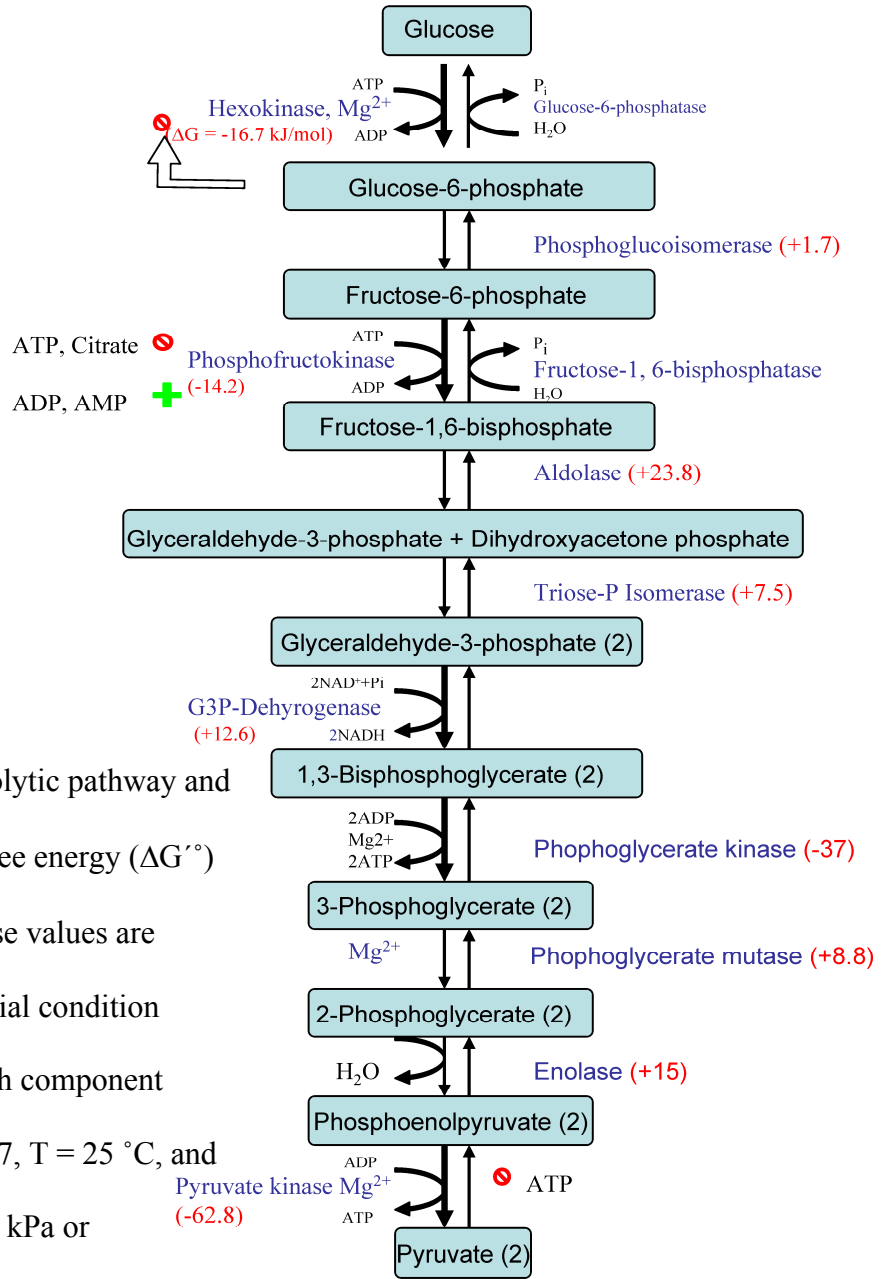


Figure 3.4. the glycolytic pathway and its standard Gibbs free energy ( $\Delta G^{\circ}$ ) in kJ/mol. Note: these values are calculated under initial condition concentration of each component being 1.0 M at pH= 7, T = 25 °C, and Pressure (P) = 101.3 kPa or 1 atm (Nelson and Cox, 2000).

Several enzymes in the glycolytic pathway such as hexokinase, phosphofruktokinase, and pyruvate kinase are considered as irreversible enzymes and

regulated either directly or indirectly through their products. The inhibitors of these enzymes are glucose 6-phosphate for hexokinase, phosphoenolpyruvate (PEP) for phosphofruktokinase (PFK), and ATP for both PFK and pyruvate kinase. In the other hand, PFK is able to be reactivated by ADP and AMP (See Figure 3.4).

- Mitochondria (Harris, 1995)

Mitochondria play multiple functions including metabolite synthesis, redox potential maintenance, apoptosis (programmed cell death), ion regulations such as  $\text{Ca}^{2+}$  homeostasis, and, last but not least, are a main energy resource (Saks, 2007). In this chapter, we consider how mitochondria interact with other compartments by light regulation. In order to make energy molecules, mitochondria import pyruvate molecules as primary substrates through their symporters with protons for their Krebs cycle. The mitochondrial electron transport chain (METC) converts pyruvate to reducing equivalents (Nicotinamide adenine dinucleotide or NADH). The METC and oxidative phosphorylation can make up to 34 ATP molecules (Figure 3.5). The main ATP production of a cell is from mitochondria. Various transport proteins including  $\text{Ca}^{2+}$  uniport,  $\text{Ca}^{2+}/\text{Na}^{+}$  exchanger, Malate/Citrate exchanger, and adenine nucleotide translocator (ANT) are found along the mitochondrial membrane (Figure 3.6). Regulations of METC depend on the proton motive force ( $\Delta p$ ) consisting of membrane potential ( $\Delta \psi$ ) and proton gradient ( $\Delta \text{pH}$ ). In addition to proton motive force, regulation of import of ADP and export of ATP through the voltage-dependent anion channel (VDAC) and the adenosine nucleotide translocator (ANT) respectively also play important roles in ATP synthesis (Murphy et al., 2005).

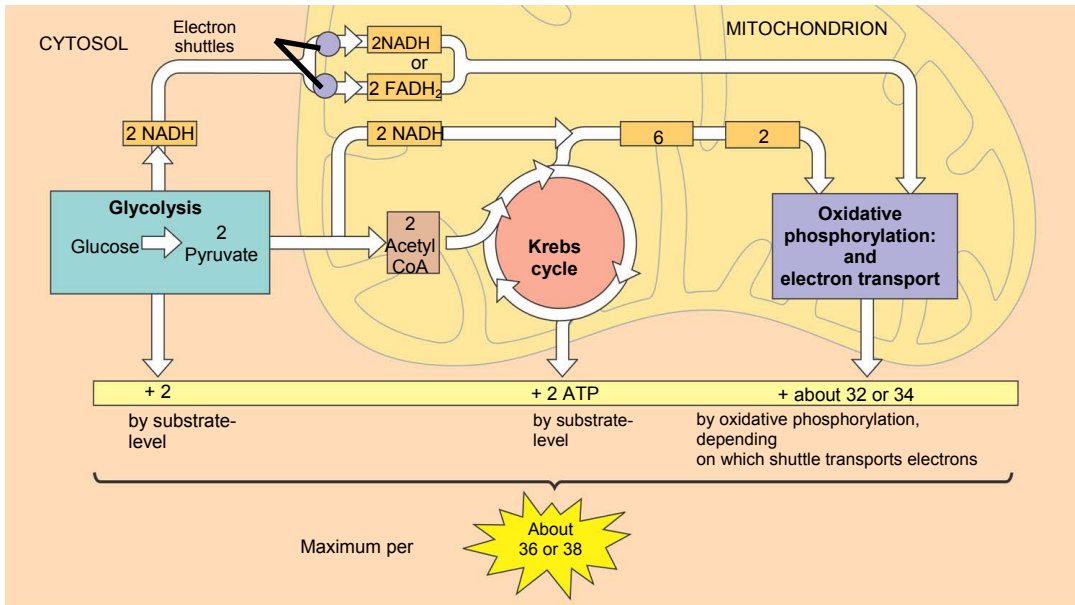


Figure 3.5. The number of ATP molecules synthesized by glycolysis, Krebs cycle, and ETC (Campbell and Reece, 2009)

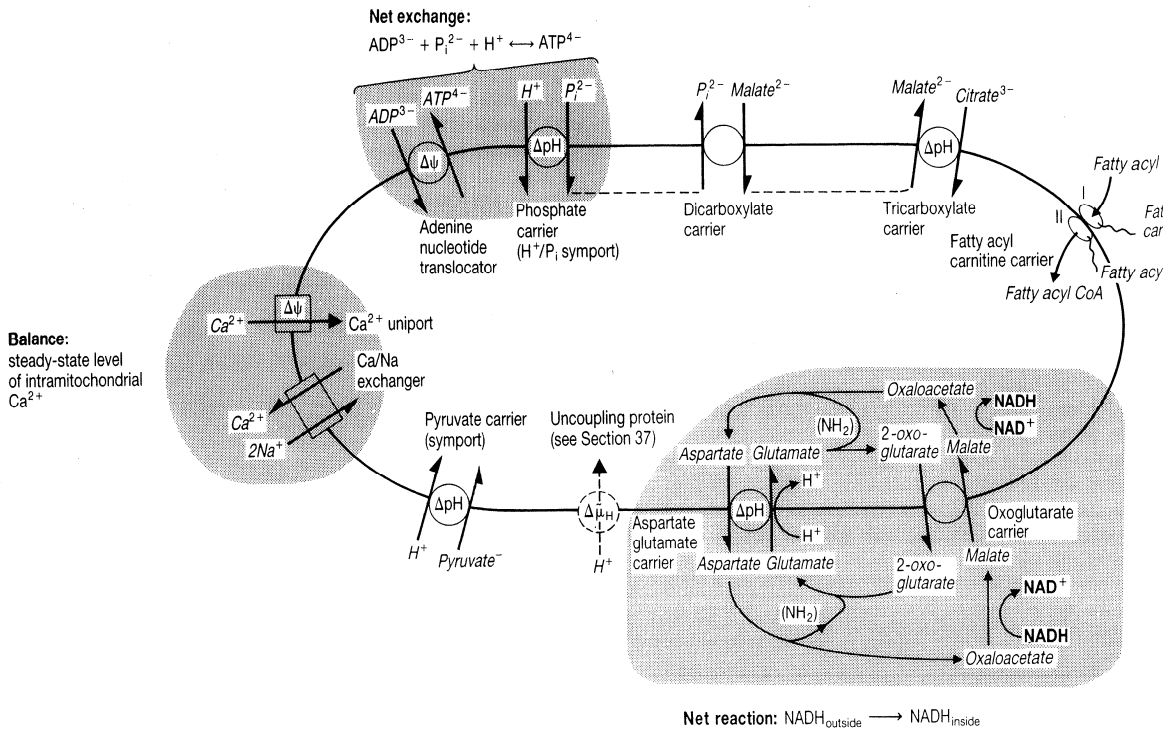


Figure 3.6. Transport proteins along mitochondria membrane and their regulations (Harris, 1995).

If we consider the control of ATP synthesis thermodynamically without including NADH and other effects, we could explain the relationship between ATP synthesis rate ( $J_p$ ) and driving force which is the difference between electrochemical gradient ( $n \Delta \tilde{\mu}_{H^+}$ ) and required energy for ATP hydrolysis ( $-\Delta G_p$ ). Their relationship can be divided into 4 regions (Figure 3.7):

- Region I: the ATP synthesis reaches its maximum threshold. Increasing the proton force will not change the ATP synthetic rate.
- Region II: the slope area where increasing the proton force also increases the ATP synthesis
- Region III: in order to create the ATP molecules, electron chain needs about 3 protons. Therefore, it could slow down the ATP synthesis rate if the proton force is low.
- Region IV: lacking of proton force could drive the system in opposite direction. In this case, ATP is hydrolyzed instead of synthesis.

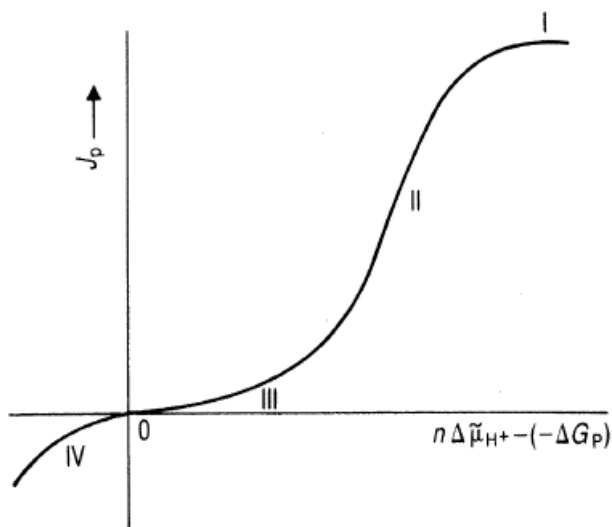


Figure 3.7 Theoretical relationship between ATP synthesis rate ( $J_p$ ) and driving force ( $n \Delta \tilde{\mu}_{H^+} - (-\Delta G_p)$ ) where  $n$  = the number of protons are required for ATP synthesis (Harris, 1995).

An amount of ATP could be regulated either through its Krebs cycle or electron chain transport (ETC) through its substrates, products, ions and enzymes. See Figure 3.8 and 3.9. The Krebs cycle in mitochondria and the glycolysis in cytoplasm coordinately make energy molecules, ATP. The glycolytic pathway in the cytoplasm converts glucose molecules to pyruvate as it needs. The mitochondria then imports for its Krebs cycle.

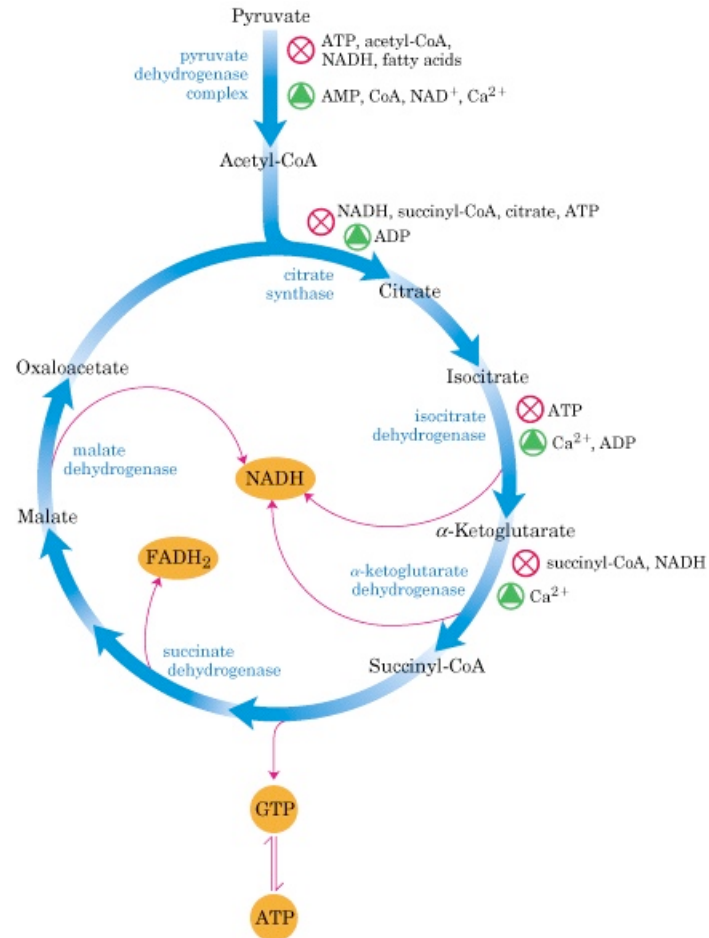


Figure 3.8. Regulation of Krebs cycle by available substrates, accumulating products, and allosteric feedback of enzymes (Nelson and Cox, 2000).

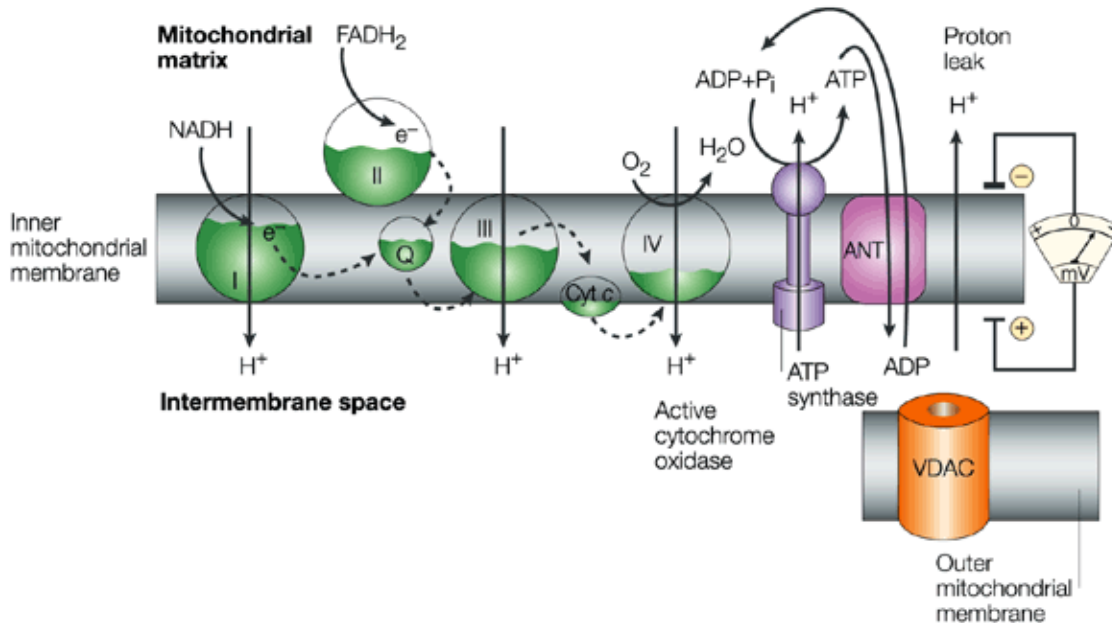


Figure 3.9. Mitochondrial electron transport chain utilizes reducing equivalents  $\text{FADH}_2$  and  $\text{NADH}_2$  to create proton gradient and membrane potential along its inner membrane or proton motive force. The proton motive force drives ATPsynthase to make ATP within the mitochondria matrix. In order to transport ATP molecules to the cytoplasm compartment, mitochondria use the adenosine nucleotide translocator (ANT) to exchange  $\text{ATP}^{4-}$  with  $\text{ADP}^{3-}$  in 1:1 ratio (Moncada and Erusalimsky, 2002).

A highly relevant question for our study is “How do mitochondria operate when there is active photosynthesis?” Light suppressed the mitochondrial pyruvate dehydrogenase complex (mtPDC) in pea leaf (Budde and Randall, 1990; Gemel and Randall, 1992). The mtPDC is an irreversible enzyme that catalyzes pyruvate to Acetyl-CoA for Krebs cycle (Figure 3.8). Suppression of mtPDC, therefore, decreases Acetyl-CoA and leads to low amount of reducing equivalents ( $\text{NADH}$  and  $\text{FADH}_2$ ) producing by the mitochondria. Besides slowing down of Krebs cycle causing from mtPDC, a high  $\text{NAD(P)H/NAD(P)}^+$  ratio from the photorespiration Gly decarboxylation also inhibits

several enzymes in Krebs cycle and slows down its function (Siedow and Day, 2000; Tcherkez et al., 2005).

Several reports suggest that photosynthesis needs mitochondria to function optimally (Kromer and Heldt, 1991; Kromer et al., 1993). During photosynthesis, mitochondria can produce NADH by oxidizing glycine to serine in  $C_3$  plant (Gemel and Randall, 1992) and assimilate  $CO_2$  by using the malate-oxaloacetate shuttle (Forti et al., 2003). However, mitochondria may be playing a relatively minor role during photosynthesis, although a very significant role in the dark. In the absence of light the mitochondria appear to provide the bulk of ATP synthesis and higher ATP/ADP ratio, as seen by the much higher [ADP] level when mitochondria are knocked out (Figure 3.10).

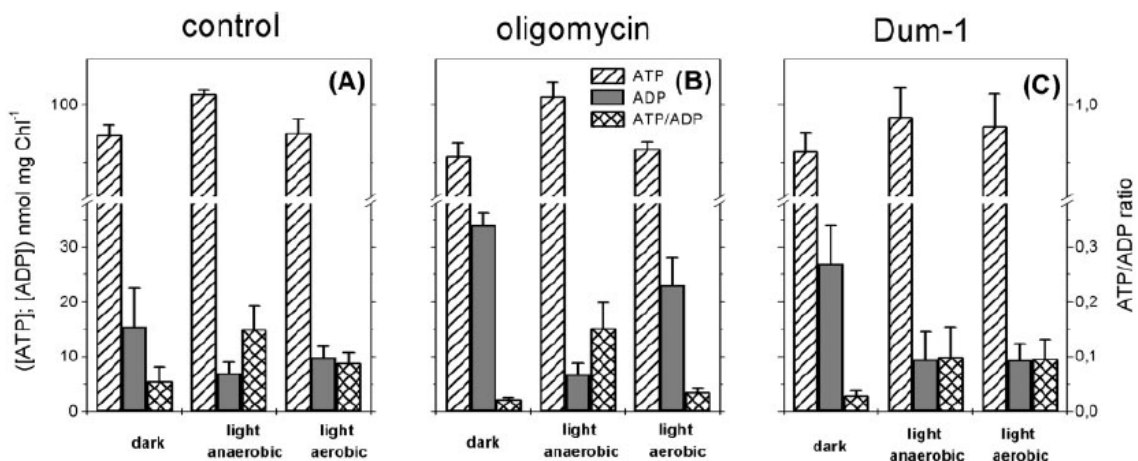


Figure 3.10. Show the steady state contributions of mitochondria to photosynthesis by measuring cellular [ATP], [ADP], and ATP/ADP ratio of *C. reinhardtii*. (A: wild type under control condition, B: blocked electron transfer of MT by oligomycin, and C: mutant lacking electron transport chain) at different conditions: dark, light anaerobic and light aerobic (Forti et al., 2003). Note: Light intensity was  $24 \mu E m^{-2} s^{-1}$ .

In the light the chloroplast synthesis of ATP appears to take over as blocking

mitochondrial activity in the light by the electron transfer blocker, oligomycin, or by the defective electron transfer in mitochondria mutant, DUM-1 has little affect. Further the [ATP]/[ADP] ratio increases with increased levels of illumination compared to in the dark (Figure 3.11). Note that the [ATP] level does not change very much whether mitochondria or photosynthesis is active.

Figure 3.11. Show the relationship between [ATP], [ADP], and [ATP]/[ADP] ratio and light intensity (Forti et al., 2003).

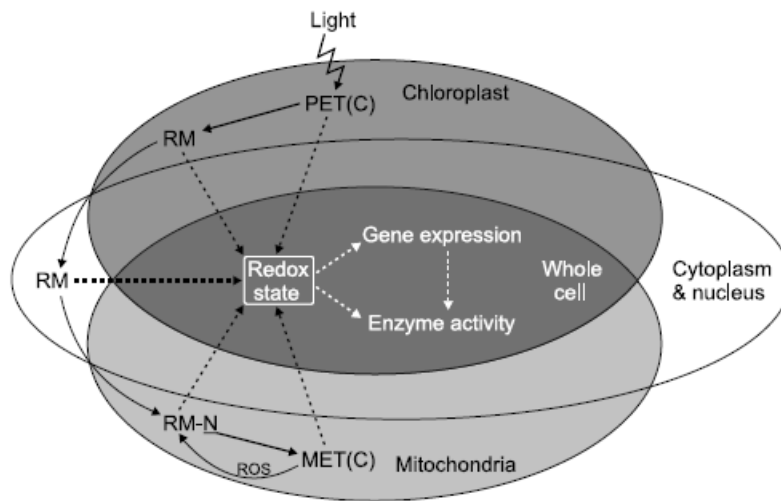
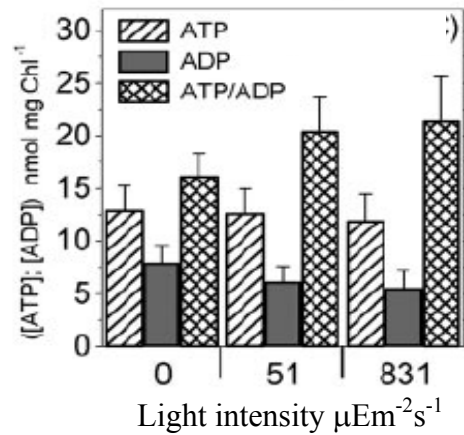


Figure 3.12. Show the interconnection between chloroplast and mitochondria through redox messages (Lis and Atteia, 2004). PET(C) = Photosynthetic Electron Transfer (Chain), RM = Redox Message molecules, RM-N = RM-NAD(P)H, MET (C) = Mitochondrial Electron Transfer (Chain), and ROS = Reactive Oxygen Species.

Another part of light regulation in the mitochondria is the redox messages (Figure 3.12). Several redox messages such as thioredoxins or Trxs are found on the mitochondrial inner membrane and intermembrane space (Michelet et al., 2009).

- Cilia

*C. reinhardtii*'s cilium (Figure 3.13 A) has a 9+2 axonemal structure or 9 doublet microtubules (A- and B-tubules) linked by nexins (elastic proteins) and 2 singlet microtubules at the center, called the central pair (Figure 3.13 B). There are 11 inner-dynein arms (IDAs) (Kagami and Kamiya, 1992; Yagi et al., 2009) every 96 nm attached to each doublet microtubule and 1 outer dynein arm (ODA) every 24 nm (King and Kamiya, 2009) (Figure 3.13C). These dynein arms or ATPase motors walk along adjacent doublet microtubules to cause the doublets to slide relative to each other and leads to axonemal bending (Figure 3.14) provided the axoneme is attached at one end or otherwise held along its length.

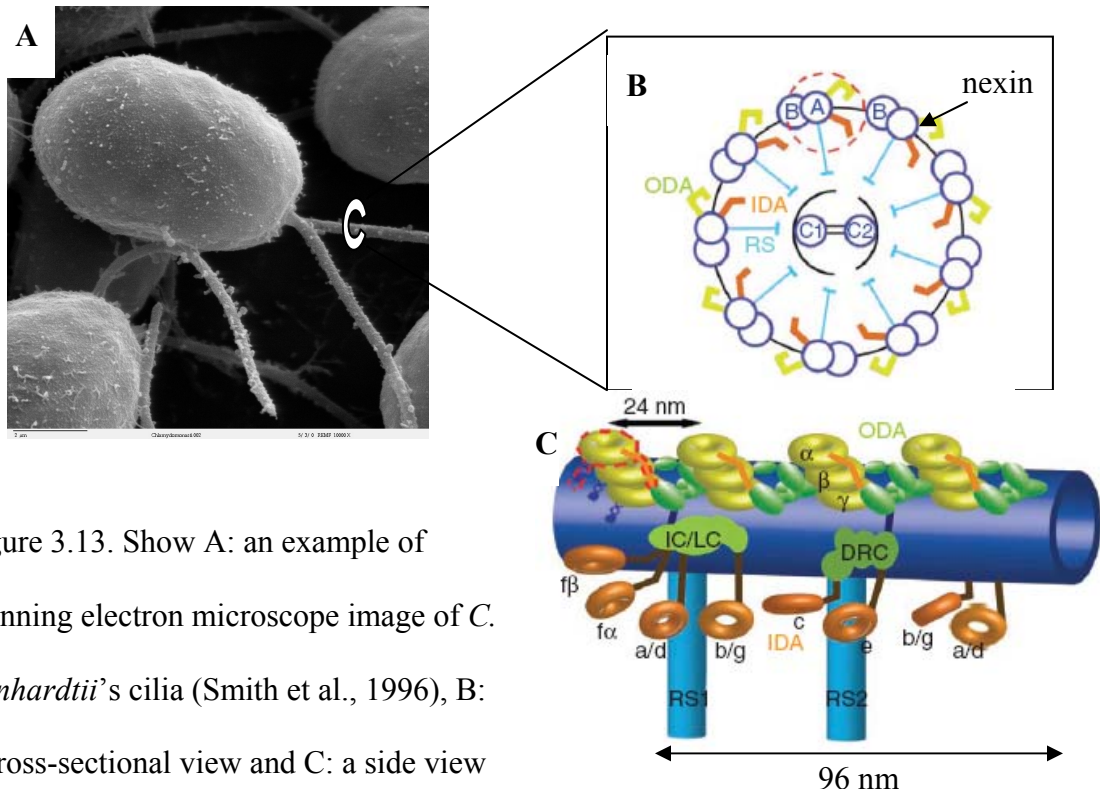


Figure 3.13. Show A: an example of scanning electron microscope image of *C. reinhardtii*'s cilia (Smith et al., 1996), B: a cross-sectional view and C: a side view

of an A-tubule. Cilium's major structure consists of inner and outer dynein arms (IDA and ODA, respectively), nexins (also called the dynein regulatory complex (DRC)), central pair (C1 and C2), and radial spokes (RS). RS links doublets to the central pair. Inner dynein arms can be divided into dynein I1 (or f with its subunit  $\alpha$  and  $\beta$ ), I2 including a, c, d, and e, and other unknowns. Note images B and C are from Movassagh et al., (2010).

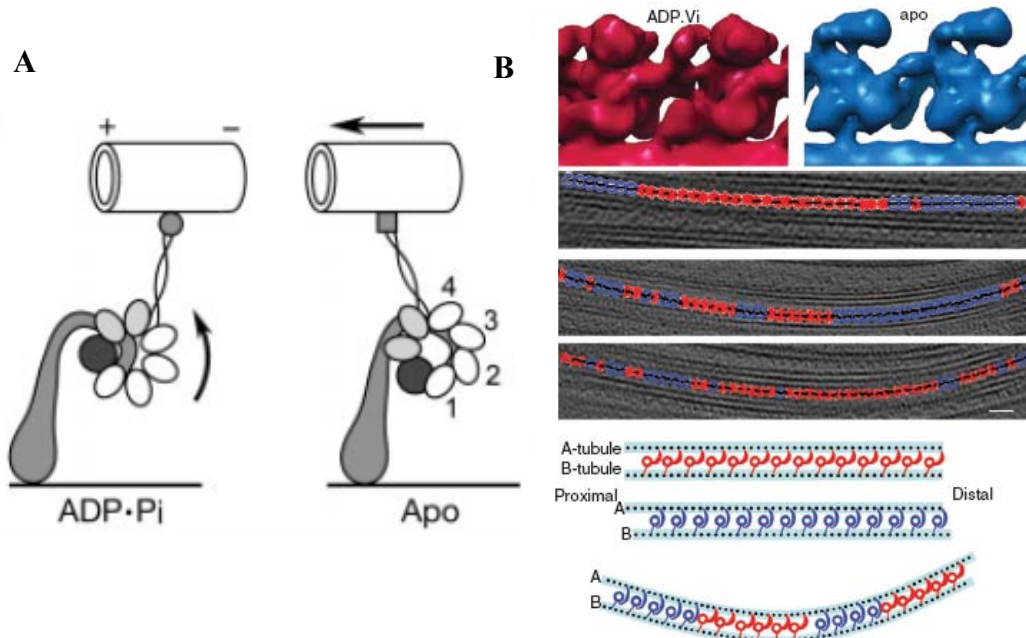


Figure 3.14. A: A dynein forms a fixed conformation when it binds to ATP or ADP•Pi and creates a power stroke releasing ADP turning into an apo-state or post-power-stroke conformation (Burgess et al., 2003). B: Shows configurations of binding and unbinding of dyneins on doublet microtubules. How this relates to a bending mechanism is still unknown (Movassagh et al., 2010).

Lacking outer dynein arms (*oda* mutants) decreases swimming velocity to about 34% in *oda1* mutant (missing outer arm, ODA-DC) compared to wild-type *l37c* ( $136.0 \pm 12.0 \mu\text{m/s}$  (Yagi et al., 2005)). Lacking inner dynein arms (*ida* mutants) decreases swimming velocity to about 56% in *ida1* (missing I1 or f subunit), *ida4* (missing a, c, and d) and *ida5* (missing a, c, d, and e) mutants (Yagi et al., 2005). Reduction of swimming velocity in *oda* mutants is caused by decreasing of its beating frequency while in *ida* mutants it is caused by reduction in the angle of its waveform bending (Brokaw and Kamiya, 1987; Kamiya et al., 1991; Yagi et al., 2005). Besides this, *oda* mutants also

lack the abilities to swim backwards or symmetrically in a ciliary beat pattern (Kamiya and Okamoto, 1985; Mitchell and Rosenbaum, 1985).

In order to meet the continuous need for energy of intracellular compartments, energy is distributed by phosphotransfer networks. The primary energy source is the mitochondria. Phosphotransfer networks use enzymes creatine kinase, adenylate kinase, and glycolytic kinase to communicate metabolic signals among mitochondria and cellular ATPases (Saks, 2007). *C. reinhardtii* does not have creatine kinase or a phosphocreatine shuttle like mammals for ATP transport. Instead, it uses adenylate kinase (AK) which converts 2ADP to ATP and AMP, a reaction also found in mammals (Cao et al., 2006). AK is anchored near the outer arm dyneins by associated outer-dynein arm proteins, called *Oda5* and *Oda10* (Wirschell et al., 2004). Since outer dynein arms are the main generators to provide power to swim in high viscosities (Brokaw, 1994), having AK nearby would be advantageous to meet the extra energy needs of outer dynein arms. In addition to the cilia compartment, AK has been found all over the cell including in the mitochondrial matrix and intermediate space, cytoplasm, cell membrane, and chloroplast. AK enables sensitivity to small changes of ATP creating AMP which is used as a signal potentially low ATP levels to other organelles within cells. Via the AK chain, AMP is thought to give a feedback response from cilia to MT (Dzeja et al., 2007). See Figure 3.15 for AK shuttle between mitochondria and outer arm dyneins.

In order to transfer high energy molecules such as ATP to remote ATP utilization sites such as along cilia, ATP is converted to ADP and high-energy phosphoryls such as 1, 3-Bisphosphoglycerate (1-3 bisP-G), 3-phosphoglycerate (3-P-G), 2-phosphoglycerate (2-P-G) and phosphoenolpyruvate (PEP) through glycolytic networks with different

enzymes such as phosphoglycerate kinase (PGK), phosphoglycerate mutase (PGM), enolase (ENO), and pyruvate kinase (PK). See Figure 3.16.

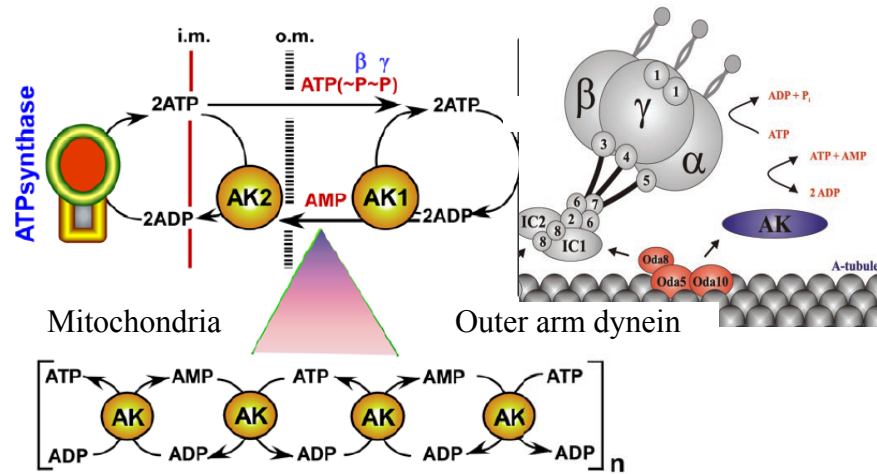


Figure 3.15. Show the adenylate kinase (AK) shuttle that facilitates ATP transport from generation site (mitochondria) to utilization site such as outer arm dynein. Figure is modified from Dzeja and Terzic (2009) and Wirschell and colleagues (2004).

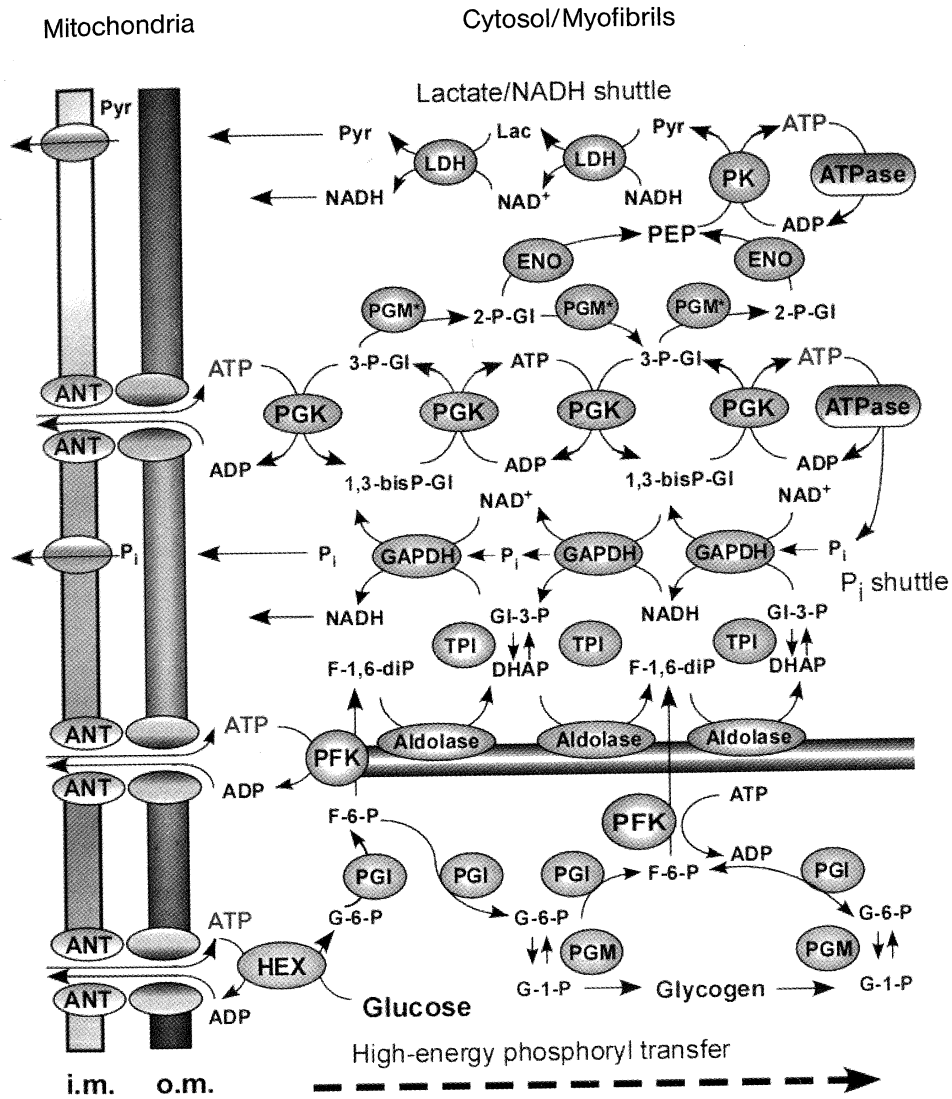


Figure 3.16. ATP molecules transport through the glycolytic network between mitochondria and the cytosol (Dzeja et al., 2007).

### 3.1.2 *The relationship between strain 806, the *cpc1-2* mutant, and wild-type*

Both the 806 and *cpc1-2* strain have negative phototaxis. Strain 806 has similar beating frequency (~ 50 to 60 Hz) as wild-type, 1117, which is positively phototactic, but 806 has 6 times less [cAMP] in the dark and 4 times less under red light (Boonyareth et al., 2009). *Cpc1-2* was backcrossed to the 806 strain by David R. Mitchell, Department of cell and Developmental Biology, SUNY Upstate Medical University, NY. The ciliary structure of 806 is like wild-type (Figure 3.17 A) compared to *cpc1-2* (Figure 3.17 B). *Cpc1-2* strain is missing C1b part of the central pair complex (CPC-1b) and its beating frequency is about 37 Hz under weakly illuminated or unilluminated conditions (Zhang and Mitchell, 2004) (62-74% of wild type). During forward-swimming (asymmetric, breast stroke or ciliary) waveforms, the CPC-1b or C1b complex is on the side associated with doublets 7-8 in a principal bend and with doublets 3-4 in a reverse bend (Mitchell, 2003). In both cases this is on the side opposite to the active dyneins forming the principal or reverse bend. One of *cpc1* conserved domains is homologous to the adenylate kinase domain which converts ADP to ATP and lacking of this subunit was conjectured to be the cause of lower [ATP] availability and lower ciliary beating frequency (Zhang and Mitchell, 2004). In order to test whether reduced [ATP] is responsible for the lower beating frequency, Zhang and Mitchell (2004) reactivated a permeabilized cell model consisting of the demembrated cilium of *cpc1* with a saturating ATP concentration (1 mM) and the beating frequency recovered to almost the same level as wild-type. Beating frequency is the number of cycles that the cilia beat in one second and in the absence of other factors changing it is related to the ATP availability (Kamiya and Okamoto, 1985;

Mitchell and Rosenbaum, 1985). Beating frequency response (BF) relates to ATP concentration in the ciliary compartment through the Michaelis-Menten equation:

$$\frac{1}{BF} = \frac{K_m}{BF_{\max} [ATP]} + \frac{1}{BF_{\max}}$$

where  $K_m$  is the ATP concentration at which the half of

$BF_{\max}$  is achieved (Figure 3.18).

In 2005, Mitchell et al. showed that the AK activity was normal in *cpc1-2* and demonstrated that an additional ATP source missing in *cpc1-2* is from the ciliary glycolytic enzyme (Figure 3.4), enolase, which is an essential enzyme in the pathway converting ADP to ATP. As already noted enolase and possibly the entire glycolytic pathway, which increases the ATP concentration to the dynein ATPases, is always present on the inactive side of the bending cilium. If we use the diffusion coefficient (D) of  $64 \mu\text{m}^2/\text{s}$  (Takao and Kamimura, 2008) for ATP and use the one-dimension diffusion equation ( $x^2 = 2Dt$ ,  $x \approx \pi \cdot \text{radius of cilium (100 nm)}$ ) to estimate the delay time (t) for ATP to diffuse to the opposite side it likely range from 1 ms to several ms depending on the openness and viscosity of the diffusion path. This delay time could play a significant role in the ciliary beating cycle.

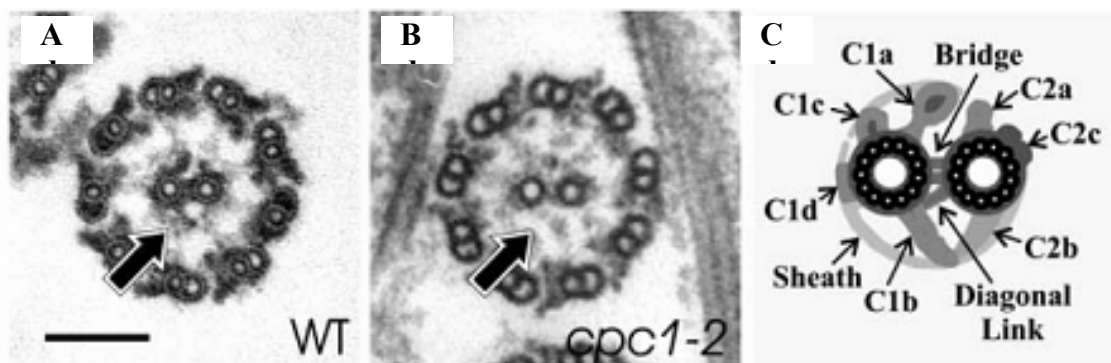


Figure 3.17. Cross-section of *C. reinhardtii*'s axonemes in wild-type (A), *cpc1-2* mutant (B), and diagram showing different components of central pair structure (C) (Zhang and Mitchell, 2004).

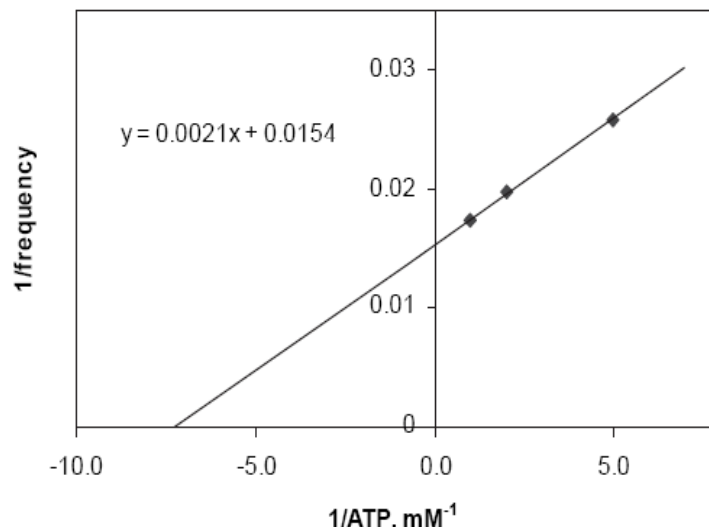


Figure 3.18. Show an example of a relationship between inversion of beating frequency (y) and ATP concentration (x) in wild-type axonemes with beating frequency maximum at 64.9 Hz and  $K_m$  is 0.14 mM ATP (Zhang and Mitchell, 2004). This relationship shows that the ATP concentration of the wild-type cilium is about 1.2 mM, whereas only about 0.2 mM in *cpc1-2*.

### 3.1.3 How does red light play a role in system function?

As already previously discussed in the introductory sections, red light stimulates photosynthesis in the chloroplast since red light is absorbed its wavelength by its chlorophylls. Therefore, red light could induce the production of DHAP or later Triose-phosphate (See Figure 3.1 as sugar and Figure 3.2 as DHAP). Triose-phosphate molecules are then converted to 3PG which is a substrate for making ATP in the glycolytic pathway in both the cytoplasm and the ciliary compartment. This could increase the ATP/ADP ratio in total. During illumination, ATP production is controlled by the chloroplast rather than by the mitochondria because blockage of mitochondrial electron chain by oligomycin and using DUM-1 mutant (lacking of electron transport

chain mutant) did not affect an increase of ATP/ADP ratio comparing to its dark condition (Figure 3.10).

ATP molecules from either glycolytic pathway in cytoplasm or MT diffuse or are transported by the AK shuttle to the ciliary compartment. Since the ciliary compartment also has the required part of the glycolytic pathway, the 3PG molecules can also be converted to ATP within the ciliary compartment. Therefore, the ciliary compartment has at least three sources of ATP energy supplies: from mitochondria, the glycolytic pathway in the cytoplasm or the ciliary compartment. The pyruvate, an end product of the glycolytic pathway, may go back to the mitochondria to report ATP usage within the ciliary compartment.

### 3.1.4 *How can we interpret the relationship between input and output? (Murrill, 1967)*

A cell responds to specific frequencies of stimulation. We interpret its response using the transfer function that explains the output system frequency response to both magnitude and phase of the input stimuli. The transfer function is the Laplace transform of the output divided by the Laplace transform of the input,  $Y(s)/X(s)$

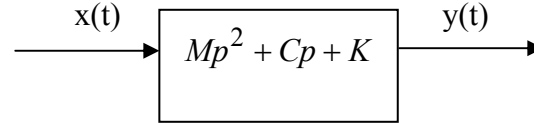
or  $\int_0^{\infty} y(t)e^{-st} dt / \int_0^{\infty} x(t)e^{-st} dt$ . Finding the transfer function allows us to understand the

system characteristics and we may use this information to predict the ciliary responses (beating frequency (BF) and stroke velocity (SV)) and describe how the system processes external stimuli such as light. For example, if the differential equation in Equation 3.1 describes the BF response  $y(t)$  to the stimulus  $x(t)$ , we can write the transfer function as

Equation 3.2. 
$$(Mp^2 + Cp + K)x(t) = y(t) \tag{3.1}$$

where  $p = \frac{d}{dt}$ ,  $x(t)$  = input signal in time,  $y(t)$  = output signal in time and  $M, C, K$  = constant

or redraw as the following diagram and can be converted to



$$\text{Transfer function } G(s) \text{ or } \frac{Y(s)}{X(s)} = Ms^2 + Cs + K \quad (3.2)$$

where  $s$  is the Laplace transform variable

Some basic elements of transfer functions and equivalent differential equations are listed in Table 3.1 and their Bode plots are in the appendix 3.1.

Element	Differential equation	Transfer function
Gain	$y(t) = Kx(t)$	$K$
First-order lag	$y(t) = \frac{K}{1 + \tau p} x(t)$	$\frac{K}{1 + \tau s}$
First-order lead	$y(t) = K(1 + \tau p)x(t)$	$K(1 + \tau s)$
Second-order lag	$y(t) = \frac{K\omega_n^2}{p^2 + 2\zeta\omega_n p + \omega_n^2} x(t)$	$\frac{K\omega_n^2}{s^2 + 2\zeta\omega_n s + \omega_n^2}$
Second-order lead	$y(t) = \frac{K(p^2 + 2\zeta\omega_n p + \omega_n^2)}{\omega_n^2} x(t)$	$\frac{K(s^2 + 2\zeta\omega_n s + \omega_n^2)}{\omega_n^2}$
Integrator	$y(t) = \frac{K}{p} x(t)$	$\frac{K}{s}$
Differentiator	$y(t) = Kpx(t)$	$Ks$
Delay time	$y(t) = Kx(t) \quad t \geq t_0$ $y(t) = 0 \quad t < t_0$	$Ke^{-t_0 s}$

Table 3.1. The elements of transfer function where  $\tau$  is time constant,  $\zeta$  is damping ratio, and  $\omega_n$  is natural frequency. For the system identification, the parameters such as  $K, \tau, \zeta,$  and  $\omega_n$  of transfer functions can be identified by using both time response and

frequency response of an output or a BF response. In this chapter, we use the time response of step stimulus and the frequency response of multi-sinusoidal stimulus to find these parameters.

- Time response of step stimulus

A time response is the change of response to the input in time. If the response is the first-order lag system, the transfer function is  $\frac{K}{1 + \tau s}$ . K is the gain of the response which equals to steady state of response amplitude divided by step stimulus amplitude (a unit value for simplification).  $\tau$  is the time constant where the output response reaches 63% of its steady amplitude.

If the response is the second-order lag system (see Figure 3.19), we can find its damping ratio ( $\zeta$ ) and its natural frequency ( $\omega_n$ ) in Equation 3.3 as the following.

$$Y(s) = G(s)X(s) = \left( \frac{K\omega_n^2}{s^2 + 2\zeta\omega_n s + \omega_n^2} \right) X(s) \quad (3.3)$$

where  $OverShoot \text{ or } \frac{D_1}{D_2} = e^{-\pi\zeta / \sqrt{1-\zeta^2}}$

$$\omega_n = \frac{2\pi / T_d}{\sqrt{1-\zeta^2}}$$

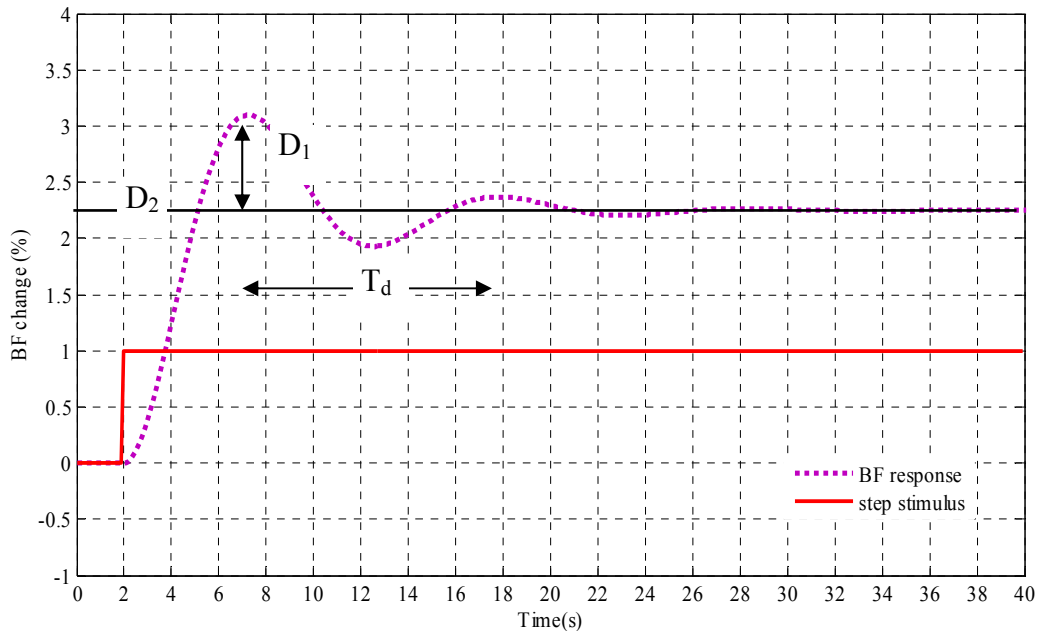


Figure 3.19. An example of a second-order lag response to a step stimulus.  $D_1$  is the overshoot amplitude over the steady state,  $D_2$  is the steady state amplitude, and  $T_d$  is the period of damping oscillation.

- Frequency response of multi-sinusoidal stimulus

The frequency response comprises the magnitude and the phase response with respect to the input wave. We stimulated the cell with a sinusoidal wave at different frequencies in order to get a frequency response of the system. If the system is linear, the output will be the sinusoidal wave with differences in amplitude, phase or both. For system identification, we do not know the system components but we know the frequency response which can be used to identify the order of system and find the system differential equation. If the system shows a complex frequency response, the basic elements of transfer function (Table 3.1) can be combined to create a complex differential equation. We can match the frequency response to Bode plots of transfer function (appendix 3.1) and determine the type of the system. For example, if our system has the

frequency response as in Figure 3.20, its pattern is the same as the second-order lag system according to the Bode plot of transfer function. Therefore, we can describe the system with the transfer function as Equation 3.3 and determine its parameters by the following.

- ⇒ Natural frequency ( $\omega_n = 2\pi f_n$ ) by finding the frequency at the intersection of high-frequency and low-frequency asymptote
- ⇒ Damping ratio ( $\zeta$ ) by fitting the constant value (less than one for underdamped system) numerically to the magnitude and phase response. The transition from one asymptote to the other depends on  $\zeta$ .
- ⇒ Gain (K) by multiplying a constant to the transfer function to match the output steady amplitude. For simplification, we use the unit value for the input amplitude.

The order of the system is identified by the slope of magnitude response vs. frequency in logarithm scale. If it is positive, there is a zero or a numerator in transfer function. When it is negative, the transfer function has a pole. The slope value identifies the number of poles and zeroes of transfer function. For example, the high frequency asymptote has a slope of -2 or -40 dB per decade and the low frequency asymptote has a slope of 0. The transfer function will have two poles (denominator) and no zero (numerator) as show in Equation 3.4 or the second-order lag element as in Equation 3.3.

$$G(s) = \frac{K}{(s + a)(s + b)} \quad (3.4)$$

Once we found the parameters, we can fit the magnitude and phase response of the second-order lag system as the following equations (Murrill 1967).

$$Magnitude = \frac{1}{\sqrt{\left[1 - \left(\frac{f}{f_n}\right)^2\right]^2 + \left(2\zeta \frac{f}{f_n}\right)^2}} \quad (3.5)$$

$$phase = -\tan^{-1} \frac{2\zeta \frac{f}{f_n}}{1 - \left(\frac{f}{f_n}\right)^2} \quad (3.6)$$

Note: if  $f = f_n$ , there is a discontinuity and its *corrected phase* =  $-\pi + phase$  .

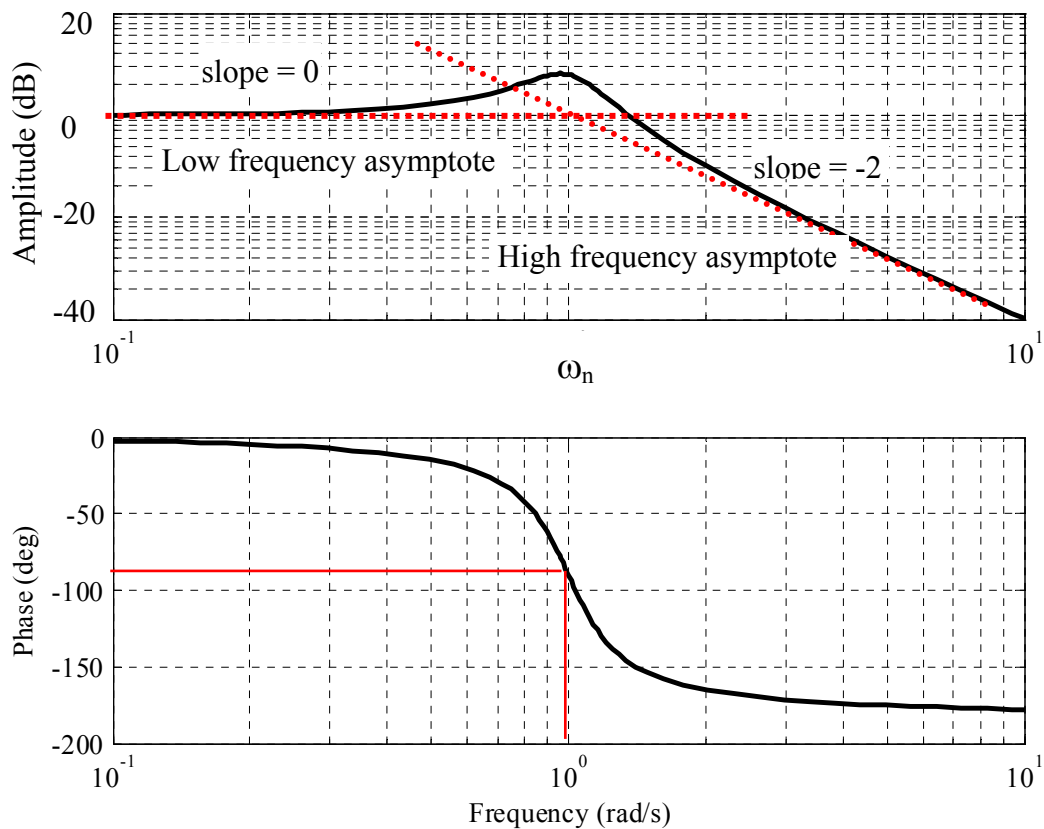


Figure 3.20. A Bode plot of second-order lag system with natural frequency,  $\omega_n$  and damping ratio,  $\zeta$ . Its phase response is stable at -180 degree for second-order where as -90 degree for the first-order system.

## 3.2 Results and Discussions

We monitored *C. reinhardtii*'s ciliary motility (806 strain) by changing the red-light pattern and its intensity. First of all, we simultaneously stimulated the cell with both red (670 nm) and green light (543 nm) to confirm their interactions on ciliary motility by using a 2.5s pulse of green light and continuous red light. The red light probably stimulates chlorophylls while the green light stimulates rhodopsin receptors that regulate the phototactic response. We then investigated further how only red light affects ciliary motility using various pulse-duration stimuli from 5 to 160 seconds and the multi-sinusoidal stimuli with frequency from 0.0065 to 100 Hz. Finally, we used the *cpc1-2* strain to investigate the effect of red light with multi-sinusoidal stimuli and compared its results with the 806 strain.

### 3.2.1 *Continuous red and 2.5-second-duration pulse of green light responses of 806 strain*

Stimulating the cell with green light will trigger the rhodopsin receptor. This signal controls ciliary motility of both the *cis*- and *trans*-cilium and leads to the phototactic response (Josef et al., 2005a). Figure 3.21 A shows an example of beating frequency change in percentage of the *cis*-cilium due to green light only. The beating frequency had only a small reduction on the “step-up”. On the other hand, its “step down” beating frequency drops transiently about 20% from its baseline. This beating frequency response is similar to one for green light response patterns reported by Josef et al. (2005a) in which there is a small change or no change on the “step-up” response and a transient change on the “step-down” response. The added red light did not affect the beating-frequency responses to green light on the “step-up” stimulus at any intensity. On the other hand, the

transient change of beating frequency to the “step-down” green stimulus was reduced from 20% to less than 10% from its baseline at the 182 mW/m<sup>2</sup> red-light intensity (Figure 3.21 B). Therefore, red light decreases the transient change on the “step-down” green-light response at 20% red-light intensity. The amplitude of transient change seems to recover at 50% and 100% red-light intensity but still less than one of green-light response (see Figure 3.21 C and D). The results suggest that red light reduces green-light effects on beating frequency. Therefore, red light plays a role in ciliary motility where it may affect the phototaxis of green-light stimulus.

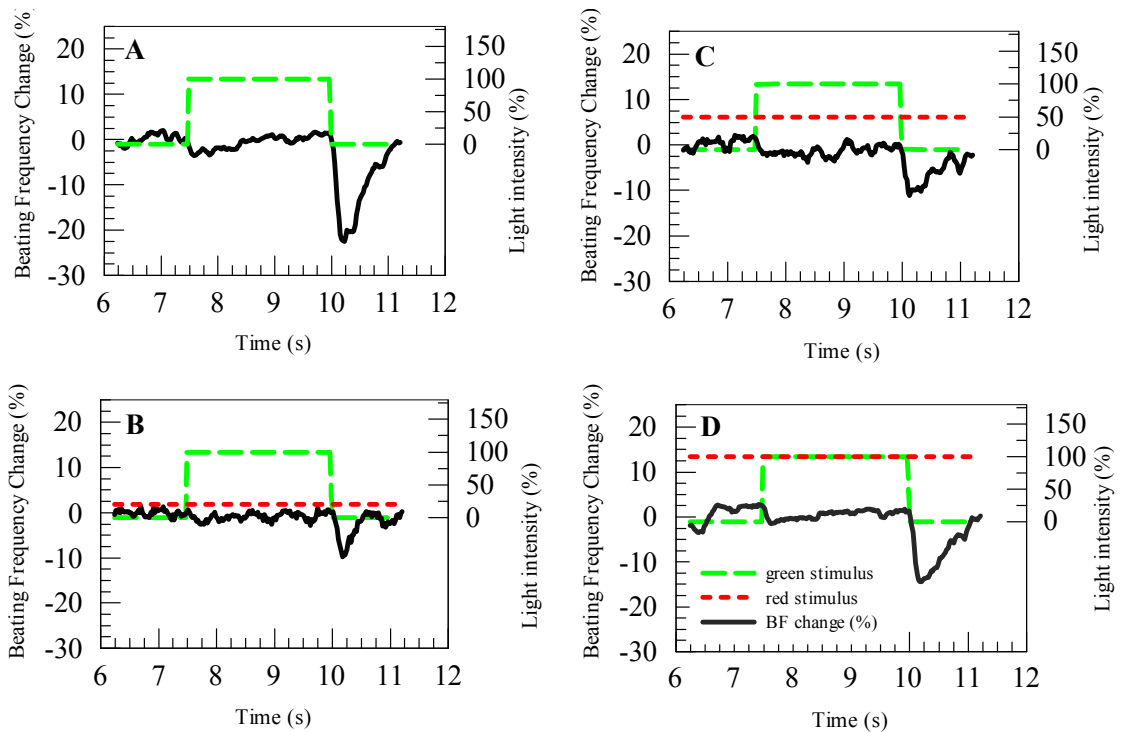


Figure 3.21. Effects of continuous red light on the BF response to a 2.5 second pulse-duration green light. A-D: 806 strain was stimulated with 100% green light intensity for 2.5 seconds from the dark (100% intensity equals to 5.26 mW/m<sup>2</sup>) and red light 20%, 50%, and 100% was added to B, C, and D respectively. 20%, 50%, and 100% red light intensity equals to 182, 469, and 921 mW/m<sup>2</sup>.

### 3.2.2 *Duration-pulse responses of 806 strain*

- 5 second-duration pulse responses

The beating frequency (BF) is about 50-60 Hz in the dark at 20 °C. From dark, 5 seconds pulses of red light from 1.3 to 192 W/m<sup>2</sup> increases the cell's beating frequency about 1 to 3 % respectively as seen in Figure 3.22 A. The BF responses do not have a shape like the applied pulse, but that of a differentiated pulse. The BF response needs more than 5 seconds to adjust to reach its stable state for the “step-up” red light from the dark. The higher the red light intensity, the greater the amplitude of BF response is. The differentiated responses are explicitly seen in Figure 3.46 A for the BF response. These results suggest that the cell differentiates the input signal or it detects the change of its input or environment. For stroke velocity responses (SV), they are a negative response compared to the BF positive response and even more negative with increasing of red-light intensity and also may be differentiated although the weakness of the signal makes conclusions difficult (See Figure 3.22B). The situation is more clearly seen later in Fig. 3.46B in which it is clear that the SV response is not differentiated.

- 40 second duration-pulse responses

With a longer exposure duration of red light, the BF change at the “step-up” response increases about 1 to 3% from the dark which is about the same change as observed in the 5 second-pulse responses. The data was recorded under the light intensity from 1.3 to 50 W/m<sup>2</sup> (Figure 3.23 A). The “step-up” responses are fitted to an exponential function with two constants, a and b, on Equation 3.5. See its fitted curve on Figure 3.23 B.

$$y(t) = a[1 - \exp(-t/b)] \text{ or } y(s) = \frac{a}{bs^2 + s} \quad (3.5)$$

where  $a = 0.77 * \log_{10}(I/I_0)$ ,  $b = -0.27 * \log_{10}(I/I_0)$ , and  $I_0 = 0.0005 \text{ W/m}^2$

These two constants linearly depend on the log of red light intensity as seen on Figure 3.23 C. The higher the red light intensity, the higher the ‘a’ constant or the steady state value and the lower the ‘b’ constant or faster steady state is reached.

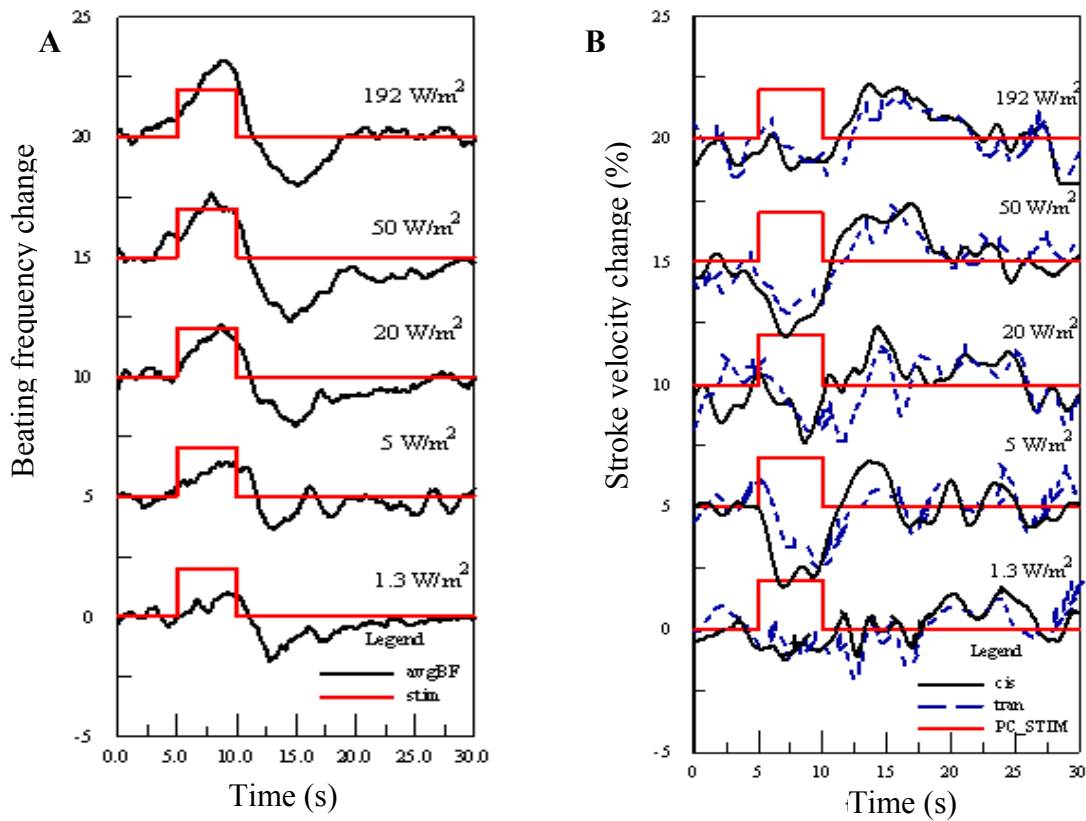


Figure 3.22. The 5 second-step red light effects on the beat frequency (A) and stroke velocity (B) in real time. The red line or the lighter color line is the stimulus. There is no difference between the BF of *cis*- and *trans*-cilium to the red light. The data are an average of 16 repetitions at 30 s intervals. The baselines of both BF and SV change are added by 0, 5, 10, 15, and 20 percents starting from  $1.3 \text{ W/m}^2$  to  $192 \text{ W/m}^2$  in order to compare their amplitudes on the same graph.

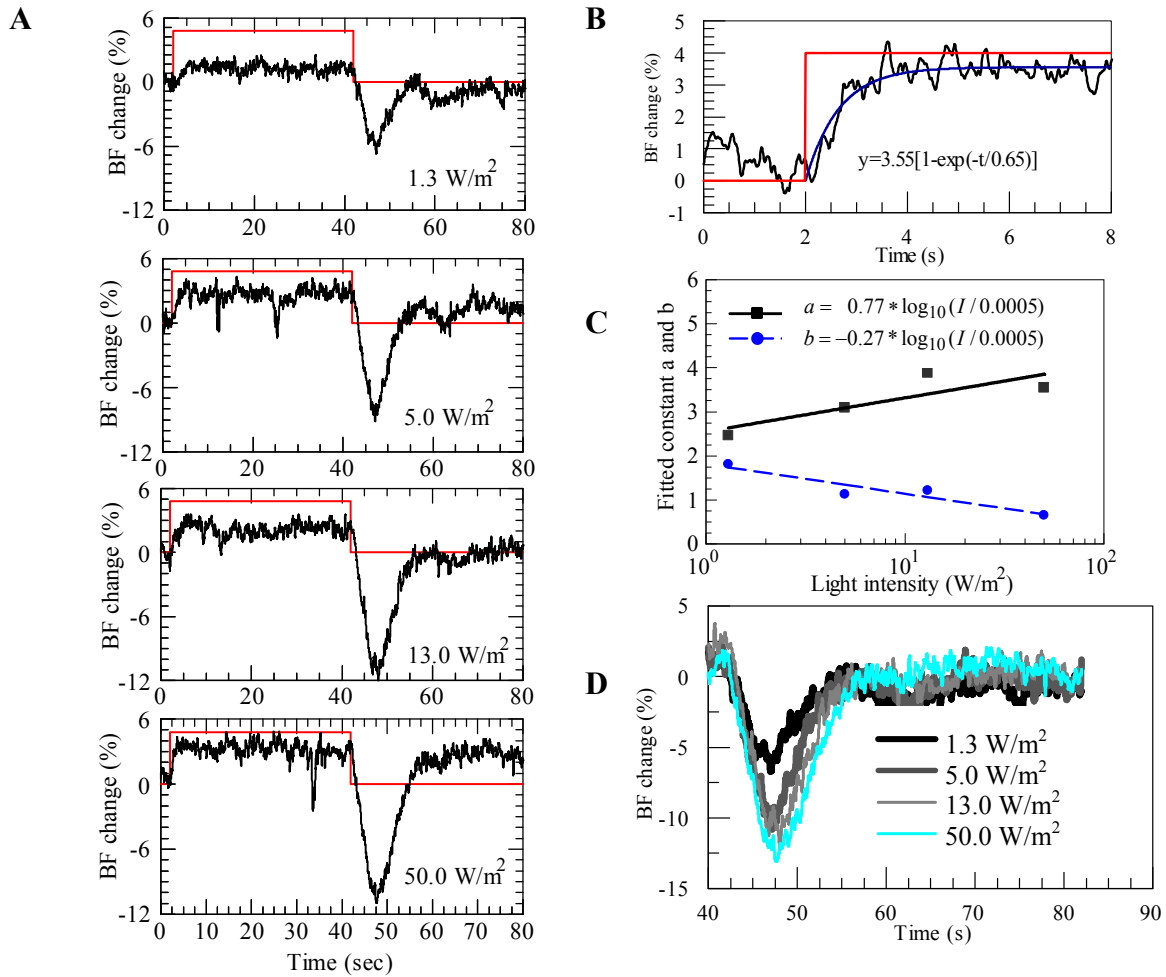


Figure 3.23. The beat frequency responses of the 40 second duration-pulse stimulus under the red light where A: the beating frequency (BF) change in percentage with various intensity (Note: the base line of each graph is about 50 Hz and they are the same at each light intensity before the “step-up” responses), B: the “step-up” response of 50 W/m<sup>2</sup> is fitted to the exponential function on Equation 3.5, C: the graph shows the relationship between the constant a (b) and the intensity, and D: the “step-down” responses of BF at various light intensity.

The BF change in Figure 3.23 B seems to be fit by a first-order lag system since the beating frequency increases immediately after the “ON” signal and there is no damping response before it reaches the steady state. The time constant ( $\tau$ ) is the same as the parameter “b” in the Equation 3.5. It measures the total time for the system to adjust to its input (the time at 63% change of its steady magnitude).

At the “step-up” response of BF change to 13 W/m<sup>2</sup> in Figure 3.23 A, BF change (%) oscillates around a steady state (Figure 3.24). Therefore, we fitted this result with the second-order lag transfer function as in Equation 3.3 and the following is the transfer function (Equation 3.6) that describes the “step-up” response with the natural frequency

( $\omega_n$ ) equals to  $\frac{2\pi}{T_d} = \frac{2\pi}{10} = 0.63 \text{ rad / s}$  or 0.1 Hz and the damping ratio ( $\zeta$ ) is

$$\zeta = \frac{-\ln(D_1 / D_2)}{\sqrt{\pi^2 + \ln^2(D_1 / D_2)}} = \frac{-\ln(0.85 / 2.25)}{\sqrt{\pi^2 + \ln^2(0.85 / 2.25)}} = 0.30$$

By substituting these parameters into Equation 3.3, we got

$$G(s) = \frac{2.25 * 0.39}{s^2 + 0.38s + 0.39} \quad (3.6)$$

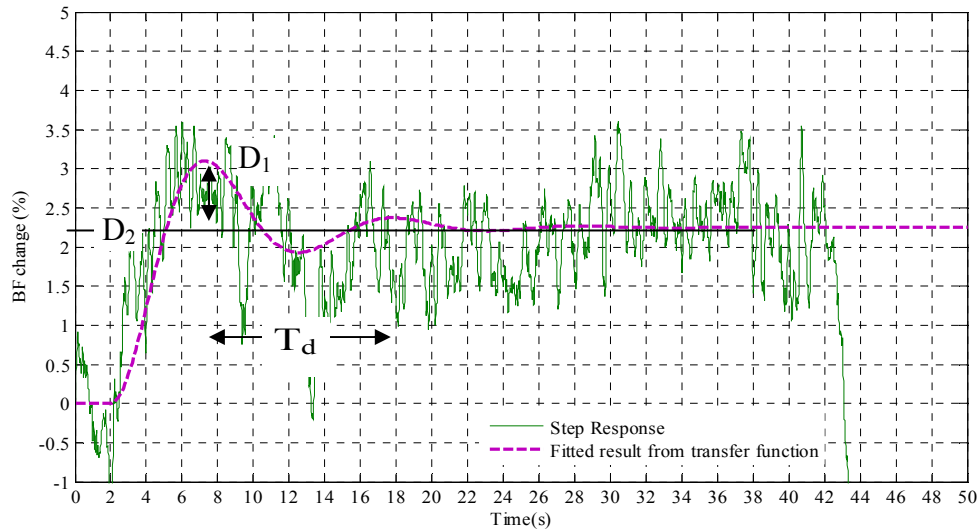


Figure 3.24. BF change (%) in time is fitted to the output results from the transfer function of second-order lag system.  $T_d$  is the oscillation period,  $D_1$  is the overshoot amplitude and  $D_2$  is the steady amplitude. Note: this is the zoom-in version of Figure 3.23 A at red-light intensity of  $13.0 \text{ W/m}^2$ .

On the other hand, the “step-down” responses of BF transiently decrease and they are lower than the baseline from 5 to 12.5 %. The higher the red light intensity, the greater the magnitude of the BF drops. See Figure 3.23 D. The BF response needs about 15 seconds to recover to its baseline level after the red light is turned off which means the supply materials (or potentially signals) or molecules such as ATP needs this much time to return to their normal concentrations.

Stroke-velocity (SV) changes are in the opposite direction of response to beating-frequency (BF) changes caused by the red light stimulation. This implies that SV and BF have separate controllers. They also are noisier than the BF changes as seen in Figure 3.25. Red light stimulation reduces the stroke velocity of both cilia. Its change is only 2.5 to 4 % from its baseline. There is no consistent difference between *cis*- and *trans*-cilium responses to red light.

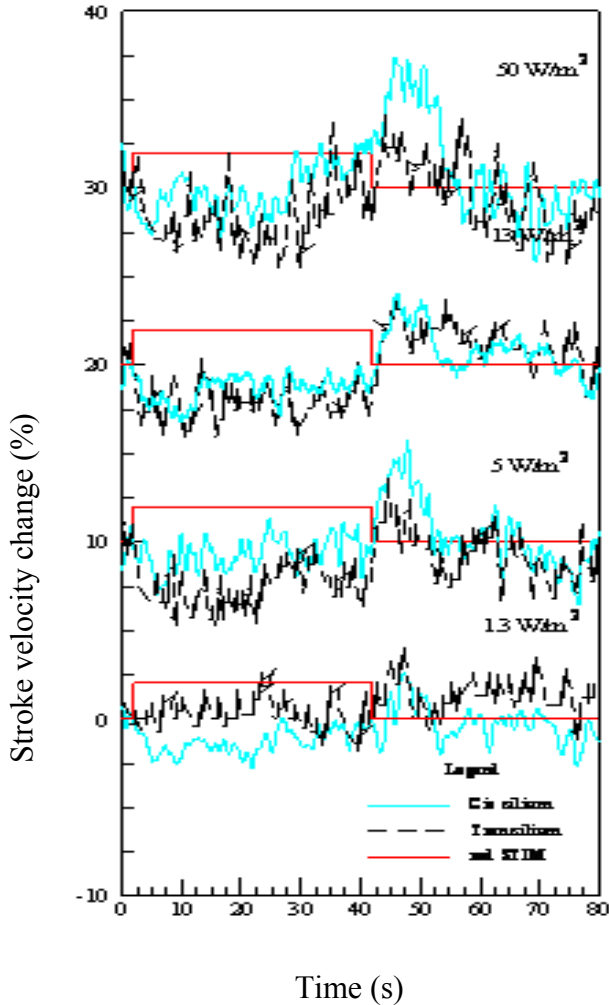


Figure 3.25. Stroke velocity change (SV) in percentage due to the 40 second pulse duration of red light at various intensities ranging from 1.3 to 50 W/m<sup>2</sup> after the dark. The baselines are added by 0%, 10%, 20%, and 30% stroke velocity change according to an increase of light intensity from 1.3, 5, 13, and 50 W/m<sup>2</sup> respectively.

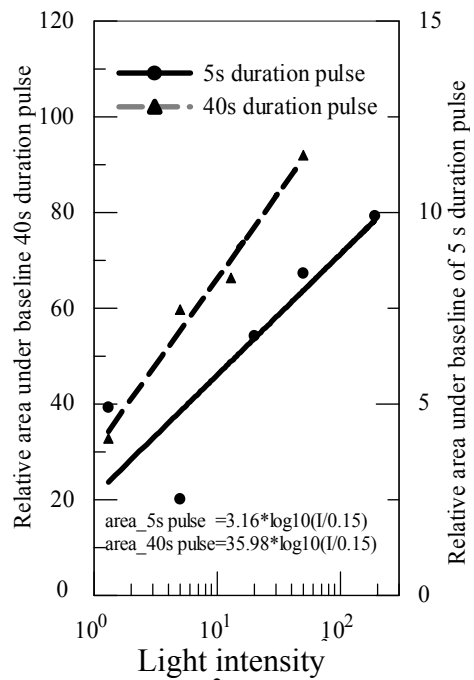
- Comparison of beating-frequency responses between 5 and 40 second-duration pulse

The areas of the “step-down” response under the base line of BF change of both 5 and 40 second duration pulse depend linearly on the logarithm of light intensity as seen in Figure 3.26. The 40 second-step BF responses have a higher area the base line than the 5 second-step BF responses by about 12 times. The longer the stimulus is on, the larger the area under its baseline. A hypothesis would be that the red light suppresses a signal pathway (or a source of a necessary metabolite) that regulates (or is needed to maintain) the beating frequency. The longer the cell has been exposed to red light, the more the

pathway (or metabolite) is suppressed. These records show that red light affects the beating frequency and have an interconnected pathway linking to the green-light signaling pathway or the phototactic pathway. Since red light is absorbed by chlorophylls, one of possible pathway would be the energy pathway (ATP). However, there may be unknown parameters in signaling pathway that could contribute to this suppression.

Increasing the “step-up” duration of red light from 5 to 40 s (8 times) increases the response area approximately proportionally (35.98/3.16 or 11.4 times).

Figure 3.26. Area of the “step-down” responses under the BF in the dark or the base line of both 5 and 40 second-step red light stimulus.



- 5 to 160 second-duration pulse responses

Besides the 5 and 40 second-pulse duration stimulus, we also monitored the beating frequency change at other durations at the “step-up” stimuli including 10, 20, 80 and 160 second-step. See Figure 3.27 A. At the longer duration pulse (80-160 second), the beating frequency fluctuates where the red light is continuously turned on. The “step-down” responses transiently drop with the sinusoidal shapes as 5 and 40 second-pulse-duration stimulus. For duration of stimuli greater than 40 second, the transient change of

the beating frequency is reduced (Figure 3.27 B). This implied that some slow adaptation to the red light has occurred. As a result, the area under the base line of BF change is the highest at the 40 second-duration-pulse stimulus.

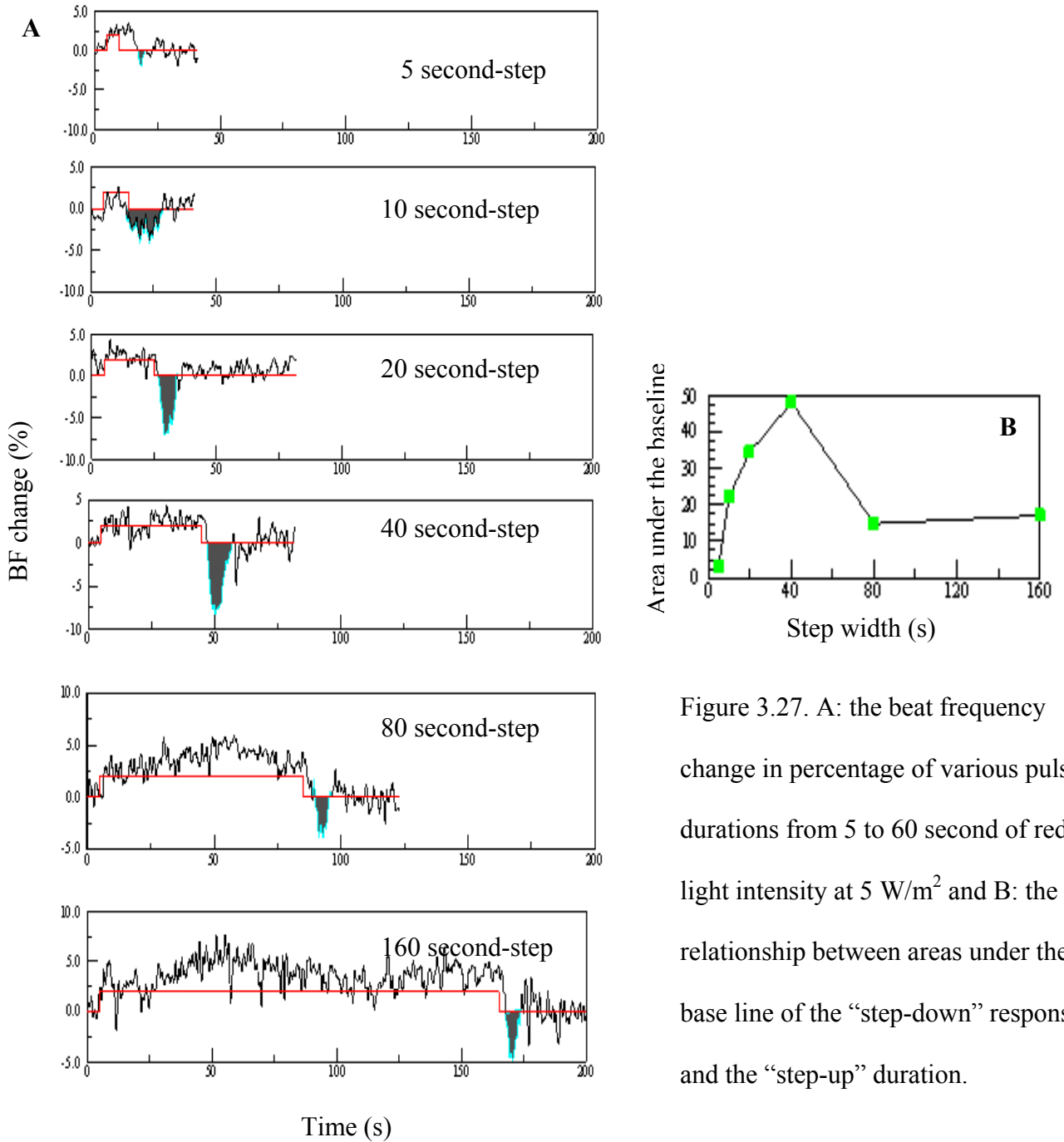


Figure 3.27. A: the beat frequency change in percentage of various pulse durations from 5 to 60 second of red light intensity at  $5 \text{ W/m}^2$  and B: the relationship between areas under the base line of the “step-down” response and the “step-up” duration.

### 3.2.3 *Beating frequency change in the dark and under DC red light*

- 806 strain

A sample of the raw signal recorded by the quadrant electro-optical detector in the dark is shown in Figure 3.28 A. The respective beating frequency is shown in Figure 3.28 B. The average beating frequency of 806 cells in the dark and before the cell sees a red light stimulus ( $0 \text{ W/m}^2$  in Figure 3.39 B) is about  $57 \pm 8 \text{ Hz}$  (average BF  $\pm$  its standard deviation). Once the cell saw the red light at different intensities from 2.6 to  $33 \text{ W/m}^2$  for 20 minutes, its ciliary movement was recorded in the dark for 16 seconds (Figure 3.39 A). The average BF in the dark after red-light stimulation at  $33 \text{ W/m}^2$  is subsequently reduced to about  $52 \pm 7 \text{ Hz}$  (See Figure 3.29 B). Although the average beating frequency in the dark is reduced, its standard deviation does not really change.

We varied the DC red light intensity with optical density filters (OD) including 1.8, 1.2, 0.6, and no OD corresponding to 2.6, 6, 15, and  $33 \text{ W/m}^2$  respectively. The beating frequency fluctuates between 30 to 70 Hz under DC red light. The higher the red light intensity, the lesser the fluctuation of beating frequency is. The average BF at 15 and  $33 \text{ W/m}^2$  is about 50 Hz. The cell held its rate of beating at this frequency. See Figure 3.29 A.

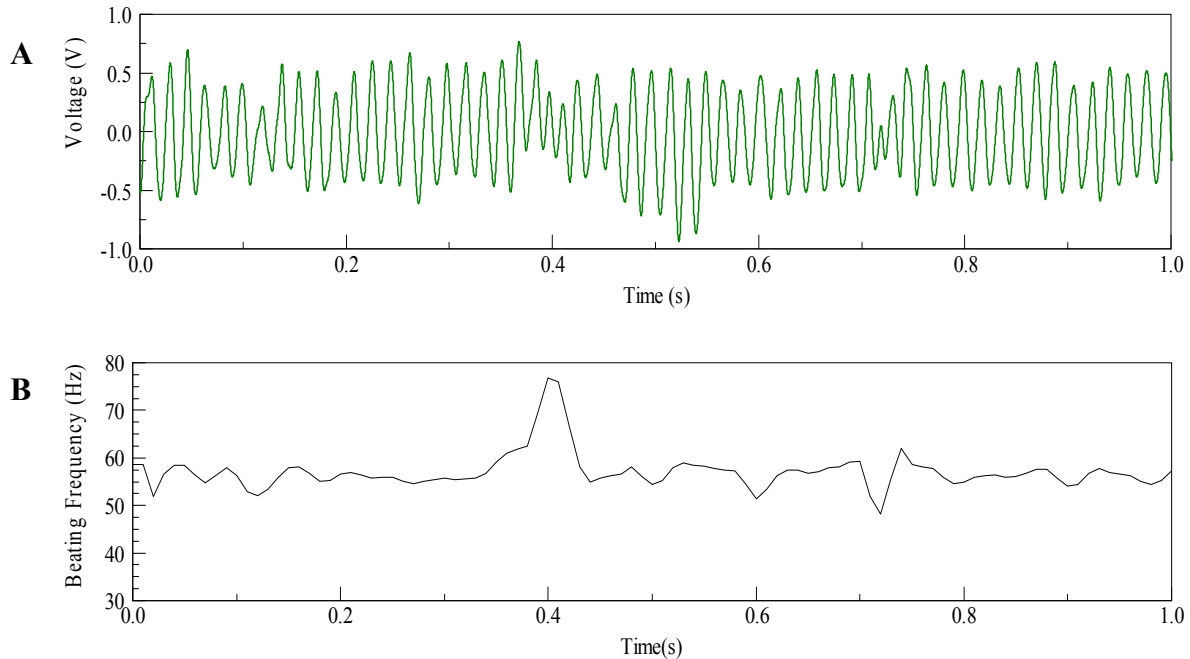


Figure 3.28. A sample of real-time recording data from the quadrant electro-optical detector (A) is converted to the beating frequency (B) of 806 cells in the dark. Note: the relatively smooth oscillation of the voltage signal gives a smooth beating pattern.

A cell must maintain the beating frequency at this level through a feedback mechanism with a controlling variable of beating frequency such as the ATP level. This feedback mechanism could be regulating how the dyneins use the ATP molecules. Feedback control could be at the mitochondria and/or chloroplast. A possible feedback control is as follows: at high light intensities, chloroplasts are activated to make more sugar molecules (DHAP or triose-phosphate). The DHAP is converted to 3PG and then pyruvate by the glycolytic pathway in the cytoplasm compartment (Figure 3.4). Since there is already a high ATP concentration within the cell, further increase of ATP concentration could inhibit the pyruvate production by inhibiting the glycolytic enzymes such as phosphofructokinase and pyruvate kinase (Figure 3.4). With a limited availability of pyruvate, mitochondria should produce less amount of ATP. An alternative possibility,

mitochondria could theoretically reach a steady state (Region I in Figure 3.7) where further increase of hydronium ions by usage of reducing equivalences would not increase the ATP synthetic rate because it reaches the maximum ATP turnover rate due to kinetic limitation such as availability of ADP level.

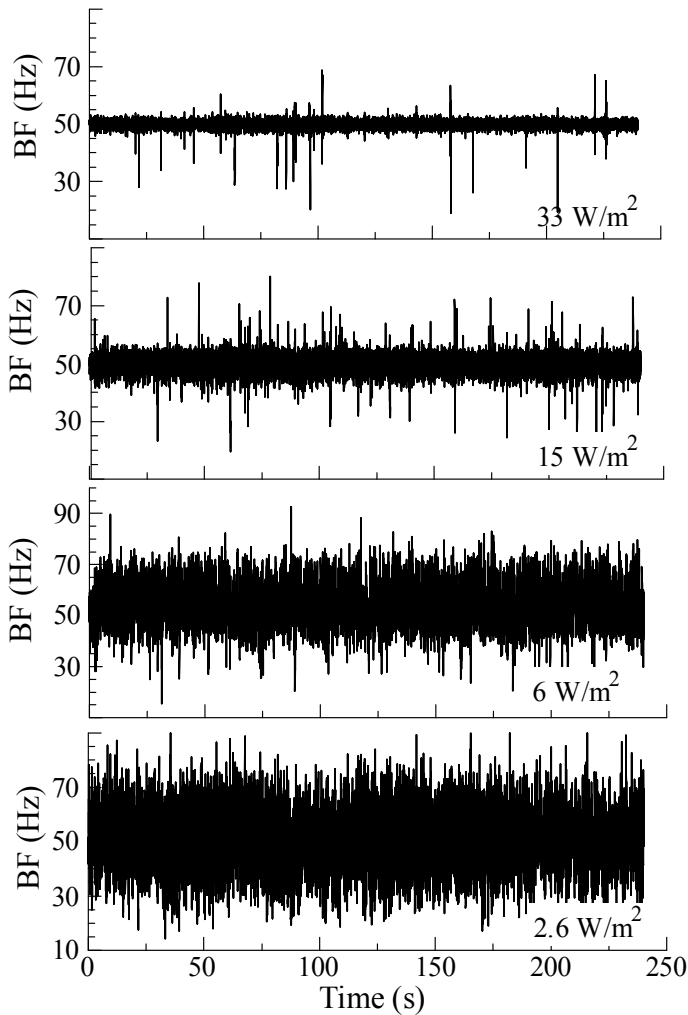
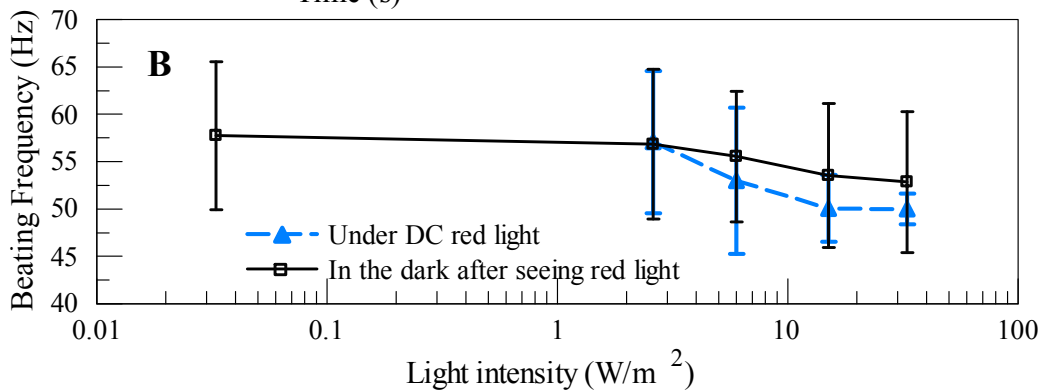


Figure 3.29. A: the ciliary beating frequency of 806 strain under DC red light at different intensity from 2.6 to 33  $\text{W}/\text{m}^2$  and B: the relationship between ciliary beating frequency and red light intensity both in the dark after seeing red light (solid line) and under DC red light (dash line). Note: In the dark, the cell previously saw red light at different intensities for 20 minutes.



- *Cpcl-2* strain

In the dark ciliary beating of *cpcl-2* cells (Figure 3.30 A) is less regular or smooth and slower than that of *806* (Figure 3.28 A). Its beating frequency is about  $32 \pm 9$  Hz (Figure 3.30 B). Surprisingly the beating frequency increases to 50 Hz under DC red light (Figure 3.30 C). Its standard deviation or its fluctuation under DC red light is even less compare to that of *806* as seen in Figure 3.29 B.

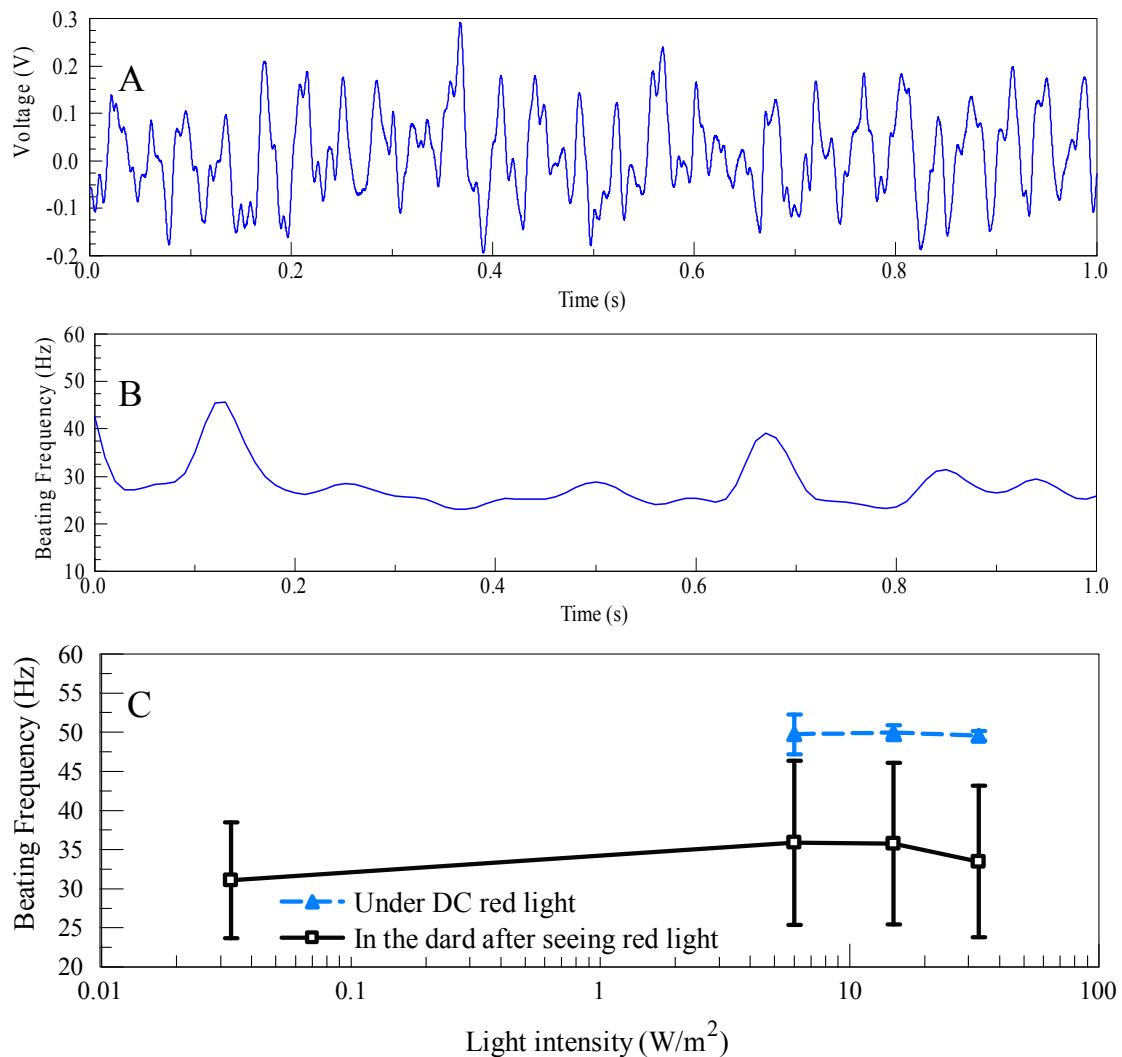


Figure 3.30. A sample of real-time recording data from the quadrant electro-optical detector (A) showing the relative irregular beating frequency of *cpcl-2* is converted to the beating frequency (B) of *cpcl-2* cells in the dark. The beating frequency responses

both in the dark after seeing the red light and in the DC red light of *cpc1-2* cells are compared (C).

### 3.2.4 *Multi-sinusoidal responses at the low-frequency range from 0.006 to 1 Hz of both the 806 and cpc1-2 strains to red light*

- 806 strain

#### A. Beating frequency at various intensities

We stimulated the cell with sine waves at different frequencies from 0.006 to 1.1 Hz while maintaining a constant average red light at the 50% level. Over a whole sine wave, the average light intensity was always at the 50% level. This stimulus pattern made it easy for us to identify a response delay. The stimulus pattern and BF responses at various intensities are shown in Figure 3.31 A-C. The beating-frequency responses (BF response) fluctuate more at lower red-light intensities.

The examples of smoothed beating frequency response from 0.015 to 0.052 Hz at three different intensities are in Figure 3.32. At  $2.6 \text{ W/m}^2$ , the BF responses seem to decrease if the intensity changes from 50% to 0% at the negative peak of the sine wave (Figure 3.32 A). At  $6 \text{ W/m}^2$  (1.2 OD), the BF responses have the same sine-wave pattern as the stimulus in the frequency range of 0.015 to 0.040 Hz (Figure 3.32 B). Otherwise, the beating frequency responses to the negative peak of the sine wave, called the negative response, is rectified having the same shape as the positive response (the BF response of the positive peak of sine wave) when the stimulus frequency is faster than 0.04 Hz (Figure 3.32 C). However the magnitude of the negative responses is not as high as the positive responses. Finally at  $15 \text{ W/m}^2$  (0.6 OD, Figure 3.32 D), the BF responses show clearly the double peak rectified responses where either increasing (50% to 100%) or

decreasing of stimulus intensity (50% to 0%) also increases the beating frequency (See Figure 3.32 D.)

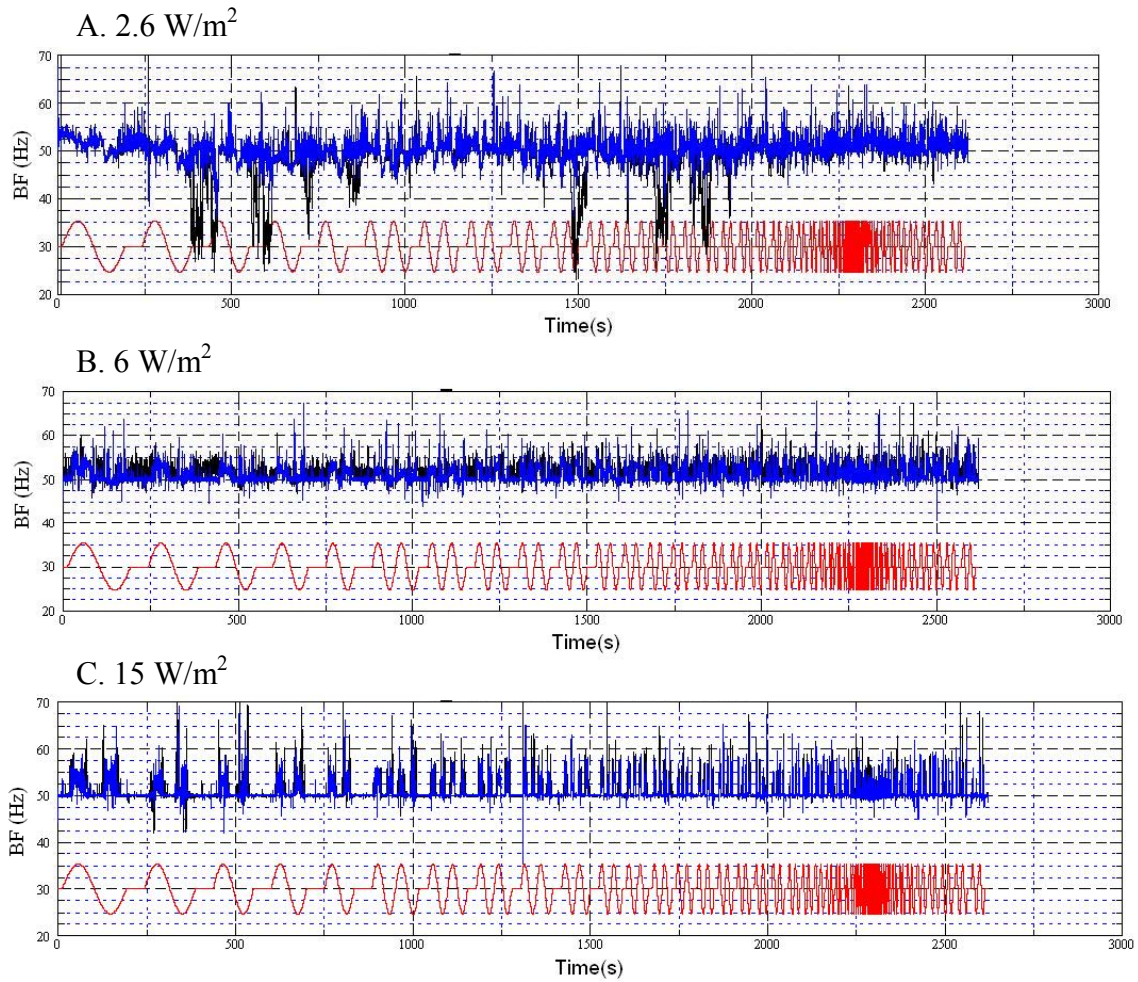


Figure 3.31. Beating-frequency responses of the 806 strain to multi-sinusoidal red light at maximum light intensity at  $2.6 \text{ (A)}$ ,  $6 \text{ (B)}$  and  $15 \text{ W/m}^2 \text{ (C)}$ .

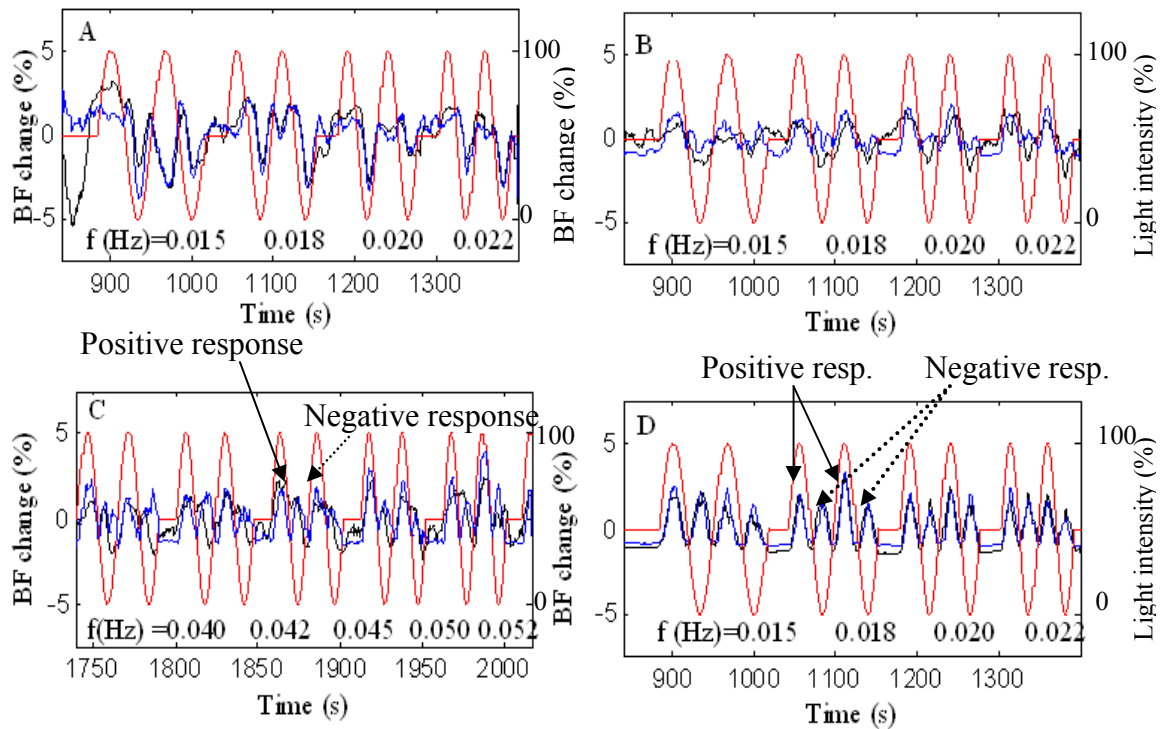


Figure 3.32. Showing smooth beating frequency responses of the 806 strain to multi-sinusoidal red light stimulus at various frequencies from 0.015 to 0.052 Hz. Three levels of 100% light intensities that are used for these data are A)  $2.6 \text{ W/m}^2$ , B) and C)  $6 \text{ W/m}^2$ , and D)  $15 \text{ W/m}^2$ .

We chose the  $15 \text{ W/m}^2$  BF response to quantify the phase and magnitudes because these responses have less noise than those obtained at lower intensities. In Figure 3.33, Figure 3.32 C has been magnified to show BF response to each frequency. The BF increases when the red light intensity either higher or lower than about 25% from the stimulus baseline (50% light intensity). The records show that the BF is tightly controlled during the periods in between the sinusoidal stimuli.

#### B. Magnitude and phase response of BF at $15 \text{ W/m}^2$

A portion of the BF response is not linear because it is not a sine wave like the stimulus but is a rectified response. Hence, we divided the BF responses into positive and negative

responses according to the responses being due to the positive or negative peak of stimulus sine wave respectively (See Figure 3.32). The magnitude responses and shifted phases from the stimulus wave at each frequency were plotted in Figure 3.34 A and B respectively. Note a shorter delay in the negative response compared to the positive response becomes apparent at high frequencies

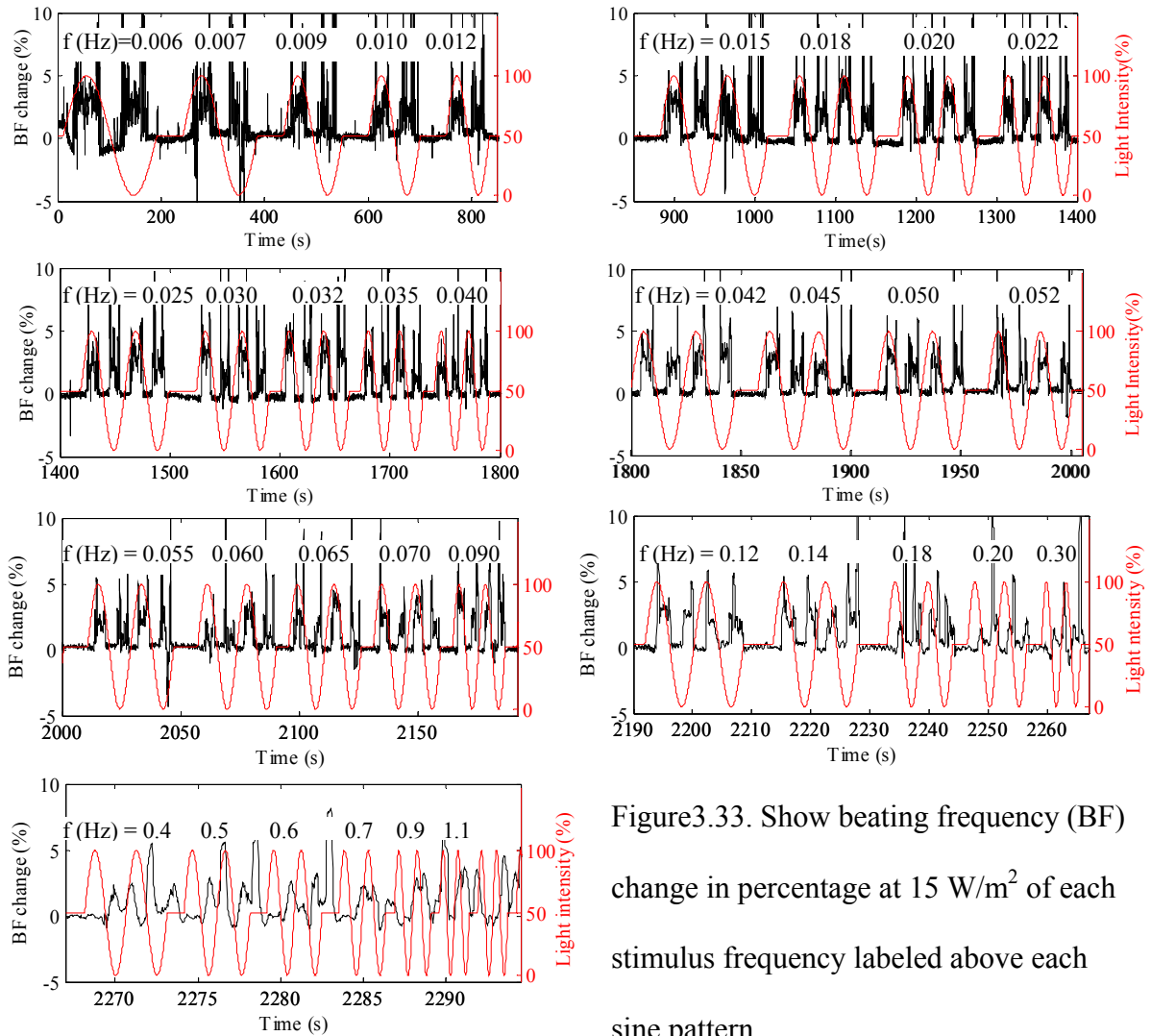


Figure 3.33. Show beating frequency (BF) change in percentage at  $15 \text{ W/m}^2$  of each stimulus frequency labeled above each sine pattern.

Magnitude of positive and negative responses has a flat slope until at least 0.6 Hz as seen on Figure 3.34 A1 and 0.1 Hz as seen on Figure 3.34 A2 respectively. There may be something additional happening above 0.6 Hz for positive responses and 0.1 Hz for negative responses. The magnitude response of *806* is less noise than the one of *cpc1-2*. In any case, we simply estimated the system with the delay time transfer function. The delay time is the time that the system needs to transport the product or to generate a system change. Therefore we estimated that the transfer function to be the Equation 3.7 for the BF positive response and the Equation 3.8 for the BF negative response.

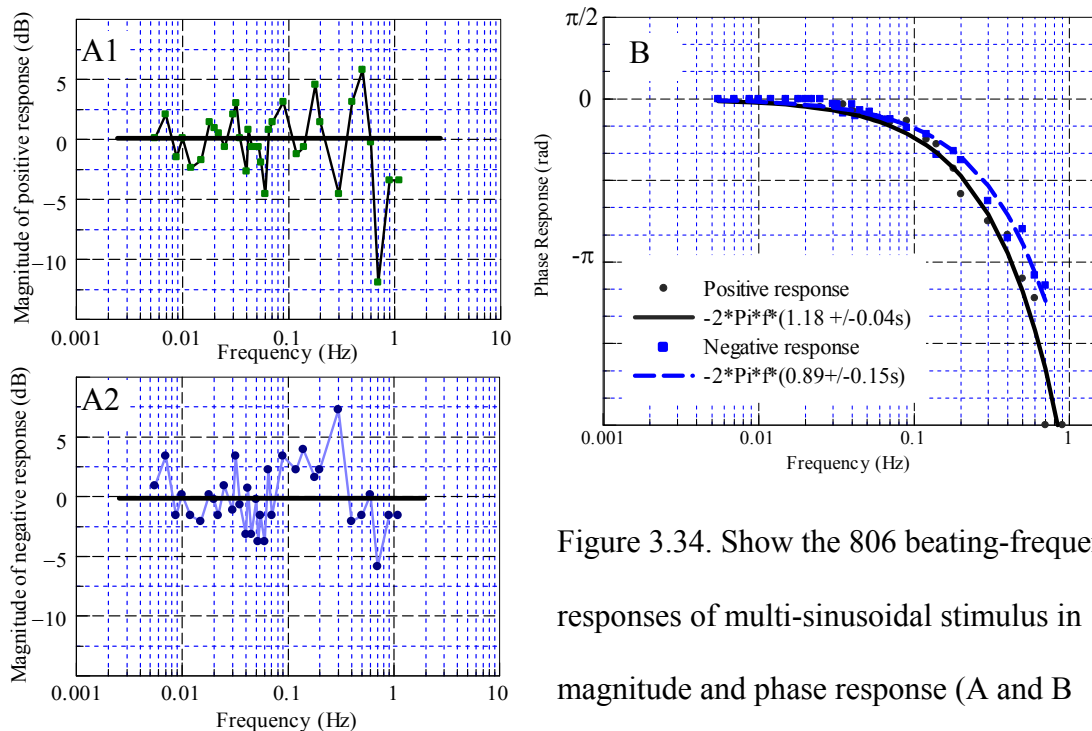


Figure 3.34. Show the 806 beating-frequency responses of multi-sinusoidal stimulus in magnitude and phase response (A and B respectively) or Bode plot. Their positive (B: solid line) and negative phase-response peak (B: dash line) were fitted to the delay-time transfer function (See Table 3.1) based on their Bode plot. The fitted transfer functions have the delay time with a constant time of  $1.18 \pm 0.04$  s for the positive response and  $0.89 \pm 0.15$  s for the negative response.

$$G_+(s) = K_+ e^{-\tau s} = K_+ e^{-1.18s} \quad (3.7)$$

where  $K_+$  is the gain and the fitted time constant has a standard deviation of 0.04 s

$$G_-(s) = K_- e^{-\tau s} = K_- e^{-0.89s} \quad (3.8)$$

where  $K_-$  is the gain and the fitted time constant has a standard deviation of 0.15s.

We combined both negative and positive transfer functions as on Figure 3.35 to explain the multi-sinusoidal BF response. Its fitted results are compared to the BF response on Figure 3.36.

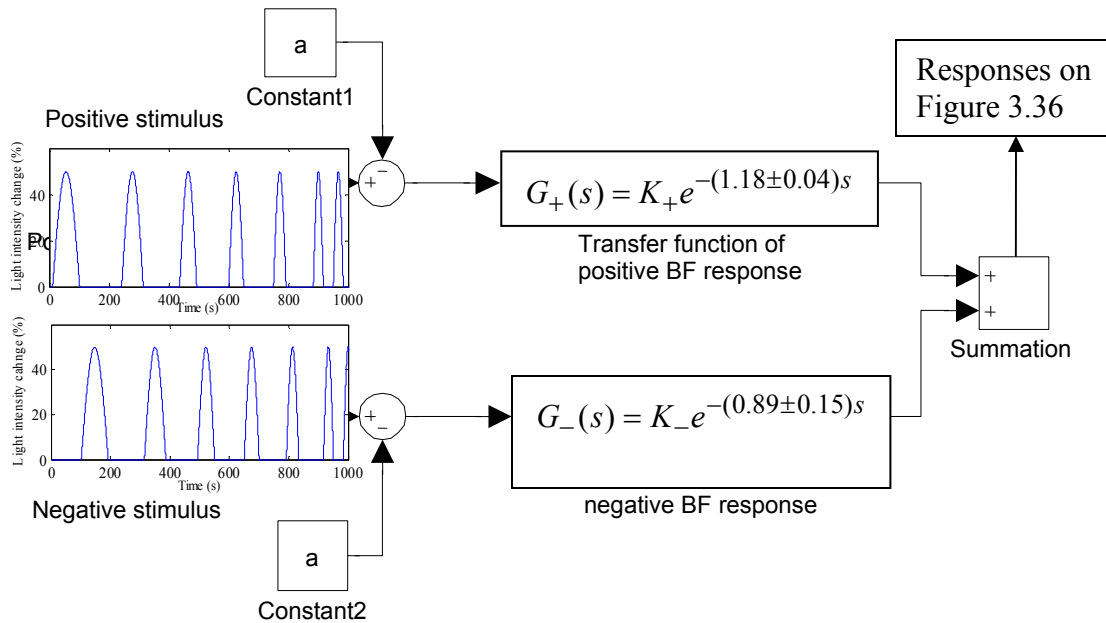


Figure 3.35. The diagram shows a possibility of total cell-signal processing function using separated transfer functions of positive and negative responses ( $G_+$  and  $G_-$ ). The light intensity change (%) is from its baseline at 50% or  $7.5 \text{ W/m}^2$  and the constant a is the threshold level that the cell responds to sinusoidal intensity change about 70% from the DC base line.

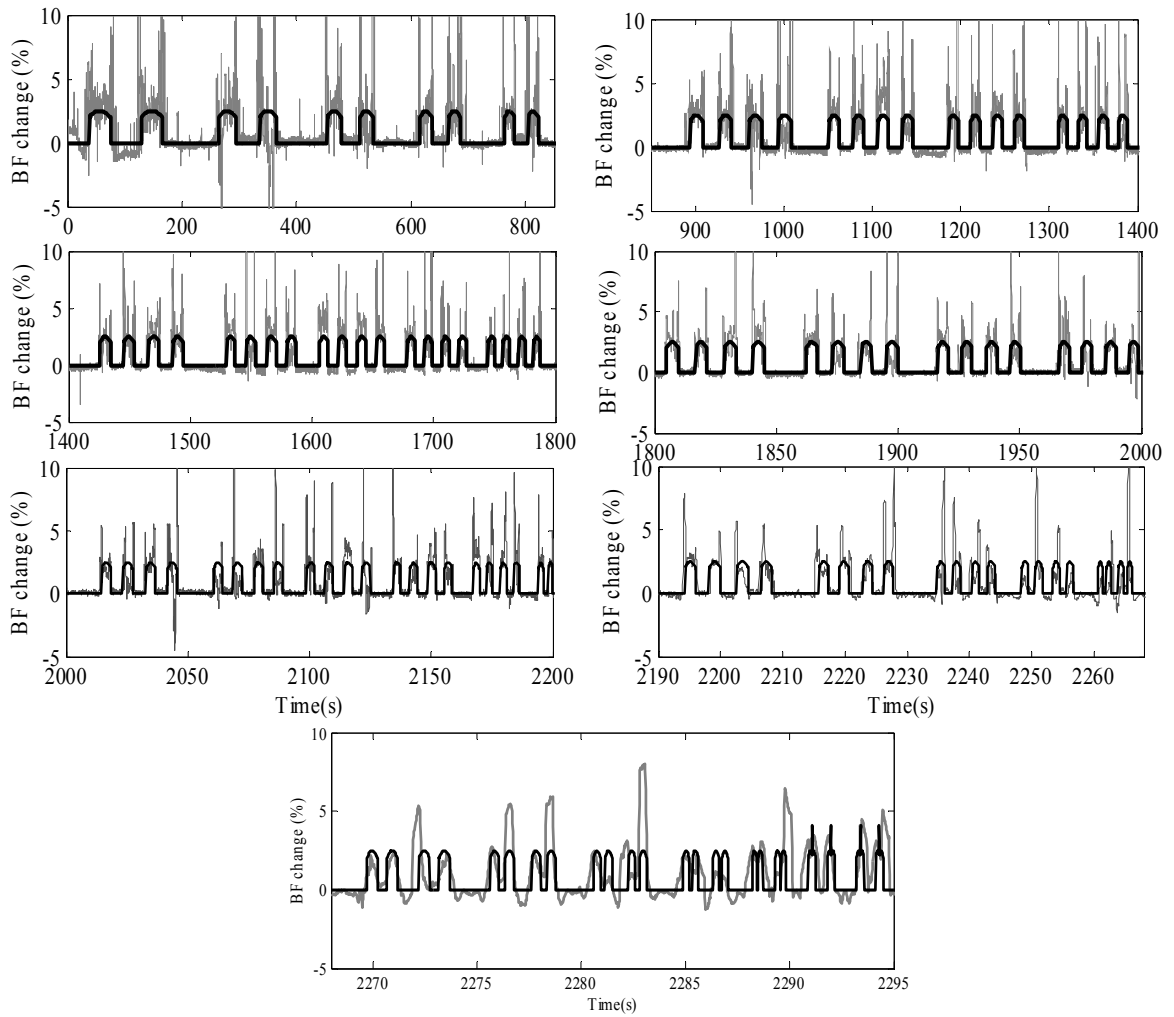


Figure 3.36. Predicted responses from two delay-time transfer functions as seen on Figure 3.35 are compared to BF responses at different frequency (Figure 3.33).

### C. Stroke-velocity response

The stroke-velocity responses to multi-sinusoidal red light stimuli at  $15 \text{ W/m}^2$  are opposite to the beating-frequency responses. Increasing (or decreasing) the red light intensity from 50% to 100% (or 100% to 50%) always decreases the stroke velocity. Thus regulation of the red light intensity above and below its constant level decreases the stroke velocity. The stroke-velocity response is non-linear since it does not follow the stimulus pattern. See the example of stroke velocity responses in Figure 3.37. The amplitude response of stroke velocity is about the same at all frequencies. This implies a simple delay model at the studied frequencies.

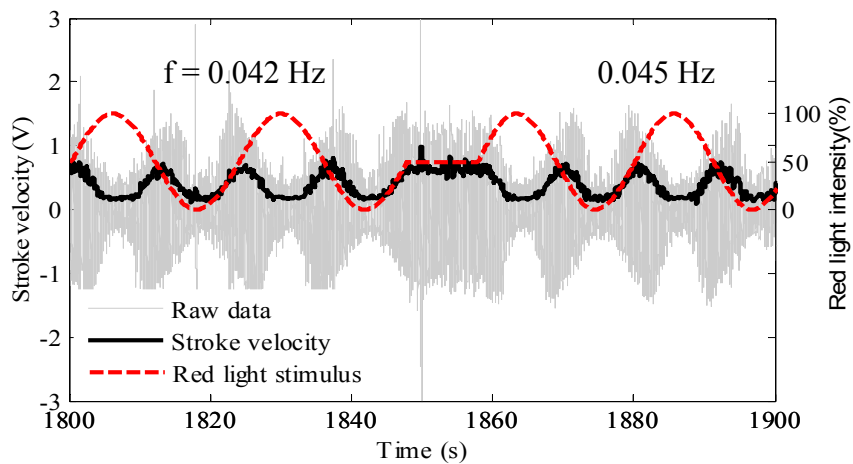


Figure 3.37. Stroke-velocity responses of *806* strain in corresponding to the multi-sinusoidal red-light stimulus at frequency 0.042 and 0.045 Hz. The raw data is the electrical signal recorded by the quadrant photodiode and it is on the same y-axis as the stroke velocity (SV).

### D. Ciliary movement

Both BF and SV responses to multi-sinusoidal red light stimuli are rectified but in the opposite direction. The BF responses increased from average responses either during

red-light intensity above or below average level (50% intensity of 15 W/m<sup>2</sup> red light) (Figure 3.33) while the SV responses decreased (Figure 3.37). From these results, we compare the average responses at 50% red-light intensity, called BF<sub>1</sub> and SV<sub>1</sub>, to the modulated responses above and below 50% red-light intensity, called BF<sub>2</sub> and SV<sub>2</sub>.

The BF response is a reciprocal of time (1/ΔT) that a cilium spends in a beating cycle and the SV response is a rate that a cilium enters or exits a quadrant detector or a cilium speed (ΔX/ΔT). From 806's results, they imply that BF<sub>1</sub> is less than BF<sub>2</sub> or the cell under the modulated red-light stimuli spent less time to complete a beating cycle (ΔT<sub>2</sub> < ΔT<sub>1</sub>). In addition to BF responses, SV responses gave us a clue that a cilium under the modulated red-light stimuli has a lower speed than under the average red-light level (SV<sub>2</sub> < SV<sub>1</sub> or ΔX<sub>2</sub>/ΔT<sub>2</sub> < ΔX<sub>1</sub>/ΔT<sub>1</sub>). Therefore, the stroke amplitude of a cilium (ΔX) is smaller under the modulated red-light stimuli than the average red-light intensity. See Figure 3.38.

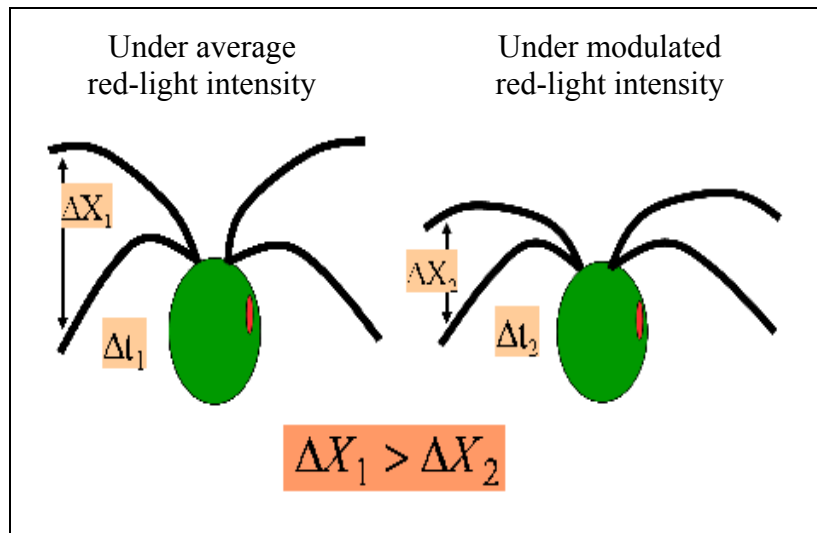


Figure 3.38 Show the interpreted ciliary movement between the average red-light intensity and the modulated red-light intensity.

### E. Magnitude and phase response of stroke velocity at 15 W/m<sup>2</sup>

The stroke response has a constant delay about 1 s for both positive and negative responses (Figure 3.39 A and B). The transfer function is a simple delay with a constant time of  $1.02 \pm 0.07$  s for positive response and  $1.01 \pm 0.28$  s for negative response. Since the stroke-velocity response is small, it is possible that the ATP usage is also low.

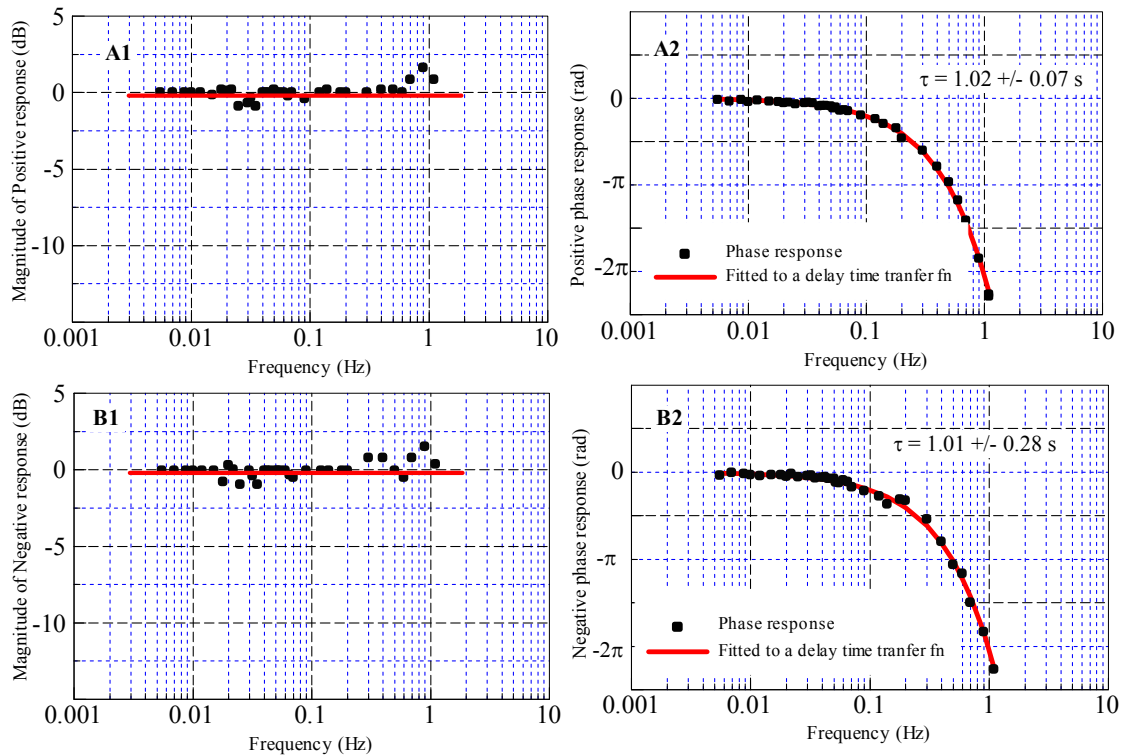


Figure 3.39. Bode plot of the 806 stroke-velocity response to multi-sinusoidal stimulus in both positive and negative peak (A and B respectively).

- *cpc1-2* strain

- A. Beating Frequency response to the red light at 15 W/m<sup>2</sup>

The beating frequency of *cpc1-2* strain is about 35 Hz in the dark which is much lower than that of 806. Mitchell and colleagues (2005) has suggested the explanation may be the lower availability of ATP due to the blockage of the ciliary glycolytic pathway. Sinusoidal-modulation of the red light in the manner already described for 806 stimulation reduces the *cpc1-2* beating frequency of both the positive and the negative changes in light intensity (Figure 3.40) in sharp contrast to the increasing seen in 806 (Figure 3.33). This dramatic change in sign of response suggests that mutation of *cpc1-2* has a strong effect in the BF response to multi-sinusoidal stimuli. Furthermore, the negative response magnitude is a lot smaller than the positive one (about 13 dB). This suggests that the enolase enzymes in the ciliary glycolytic pathway play an important role in its BF response to multi-sinusoidal stimuli. One interpretation would be that whatever causes these negative changes in BF is converted by the glycolytic pathway to positive responses as seen in strain 806.

In the dark, the *cpc1-2* cell maintains its BF response at about 35 Hz. Without the enolase enzyme synthesizing ATP in cilia, cilia must depend exclusively on cell body's energy source. Morphologically the mitochondria seem likely to be the most suitable source as they are found near the base of all cilia.

Exposing the cell to red light activates photosynthesis which converts light energy to chemical molecules such as DHAP through Calvin cycle (see section 3.11 and Figure 3.2 for more detail and pathway) or starch which can later be used as an energy source exchanging malate and oxaloacetate with mitochondria. The DHAP are then exported and

converted to 3PG molecules by glycolytic pathway in cytoplasm (see Figure 3.4 glycolytic pathway). According to BF results of both *cpc1-2* and *806*, they are both rectified but in opposite direction.

At the average 50% of red light intensity before changing a frequency of multi-sinusoidal stimuli, the *cpc1-2* maintains tightly a BF of 50 Hz, the same result as for continuous red light (Figure 3.30). Further increase of red-light intensity above the average level (50% or 15 W/m<sup>2</sup>) dropped BF response. Decrease of BF may be from the suppression of mitochondria at the higher light intensity (as hypothesized earlier for step changes in light) and lack of ability to use 3PG to make up the difference in *cpc1-2*. On the other hand, when red-light intensity decreased below 50% (or 15 W/m<sup>2</sup>), BF response also decreased below the average level but it dropped less than for the response to the positive phase of the sinusoidal stimulus. We hypothesize that a reduction of chloroplast contribution causes the decrease of BF while some recovery of the mitochondria as an alternative energy source helps maintain its amplitude. Hence both positive and negative BF responses of *cpc1-2* decreased.

The BF at red-light intensity during the positive phase of the sinusoidal stimulus (above 50% intensity) of *806* is always higher than the BF at the average intensity. Similarly the BF during the negative phase of the sinusoidal response is always higher than the BF at the average intensity given before the sinusoid. These responses are opposite to the case of *cpc1-2*. We hypothesize that in the case of *cpc1-2* the decreases in BF correspond to high levels of ADP. Hence, it could be that since ADP is a necessary substrate for ATP formation by the glycolytic pathway this ADP drives an ATP increase

with corresponding increase of BF in 806 due to utilization of 3PG corresponding to each earlier decrease seen in *cpc1-2*.

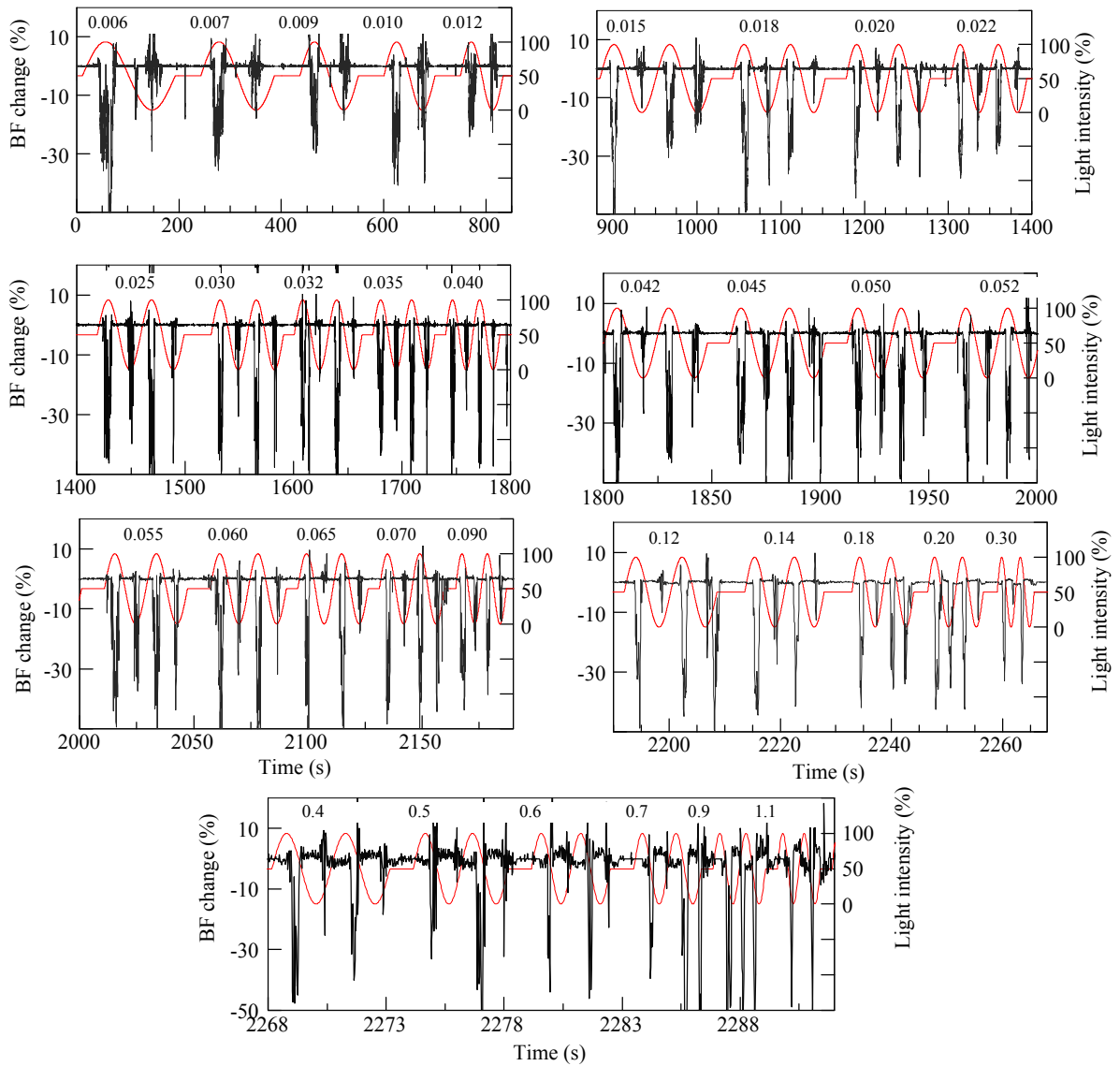


Figure 3.40. Beating-frequency responses of the *cpc1-2* cell to multi-sinusoidal red-light stimulus at  $15 \text{ W/m}^2$ . The frequency is range from 0.065 to 1.1 Hz.

## B. Magnitude and phase response of BF at 15 W/m<sup>2</sup>

We compare positive and negative response according to the responses of positive and negative peak of multi-sinusoidal stimulus respectively. The magnitude and shifted phase responses of each frequency are plotted and fitted to estimated delay-time transfer functions as in Figure 3.41. The recordings at less than 0.2 Hz give the appearance of being tightly controlled between the average intensity levels. Above 0.2 Hz, the base level becomes sinusoid with the stimulus and increases its amplitude at high frequency relative to the low frequency value.

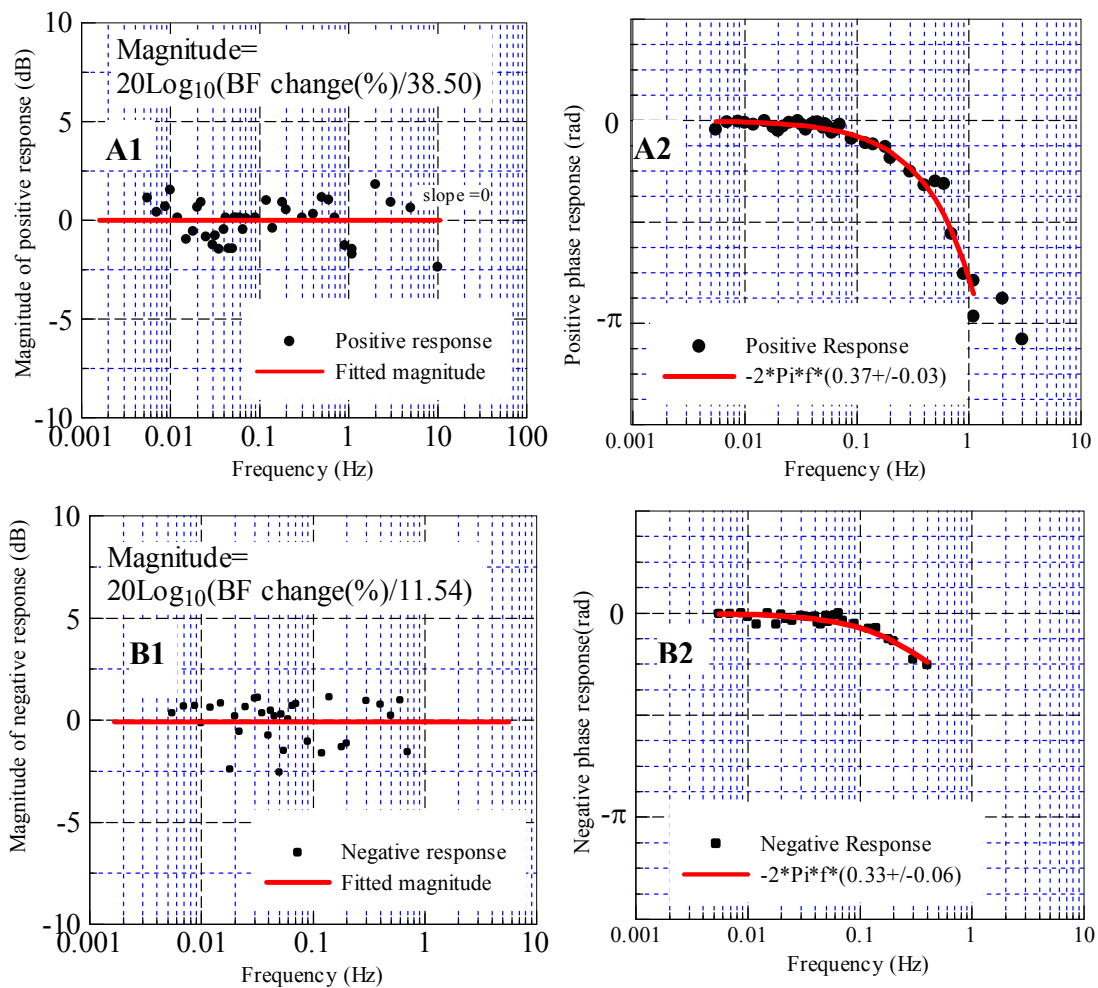


Figure 3.41. Bode plot of the *cpc1-2* BF responses to multi-sinusoidal stimulus. Its amplitude and phase responses of positive and negative responses are plot in A and B

respectively. The magnitude responses of both positive (A1) and negative (B1) peak have a flat slope but the negative one has less normalized amplitude than the positive one by about 3 times. The phase response of positive peak has a constant time of  $0.37 \pm 0.03$  s (A2) while the negative one has a constant time of  $0.33 \pm 0.06$  s (B2). The fitted plots are from the delay-time transfer function.

The magnitude response has a slope of zero suggesting a simple gain or one with a delay. The phase response can be explained by the delay function of  $-2\pi f\tau$ . Substitute this value to the delay time transfer function, we have

$$G_+(s) = K_+ e^{-(0.37 \pm 0.03)s} \quad (3.9)$$

where the constant time ( $\tau$ ) is 0.37 second with its standard deviation of 0.03 second for the positive responses. This compares to  $1.18 \pm 0.04$  s in the *806* delay.

$$G_-(s) = K_- e^{-(0.33 \pm 0.06)s} \quad (3.10)$$

where the constant time ( $\tau$ ) is 0.33 second with its standard deviation of 0.06 second for the negative response. This compares to  $0.89 \pm 0.15$  s in the *806* delay.

The two *cpc1-2* delays are within reasonable values of each other so that both may be considered to have the same delay.

### C. Stroke-velocity response (SV)

Stroke-velocity response of the *cpc1-2* is similar to the *806* where red-light intensity above its average decreases the stroke velocity from its baseline. This suggests that the reduction of glycolytic enzyme does not affect the *cpc1-2* stroke velocity.

Furthermore, this may imply that the control of beating frequency and stroke velocity are different.

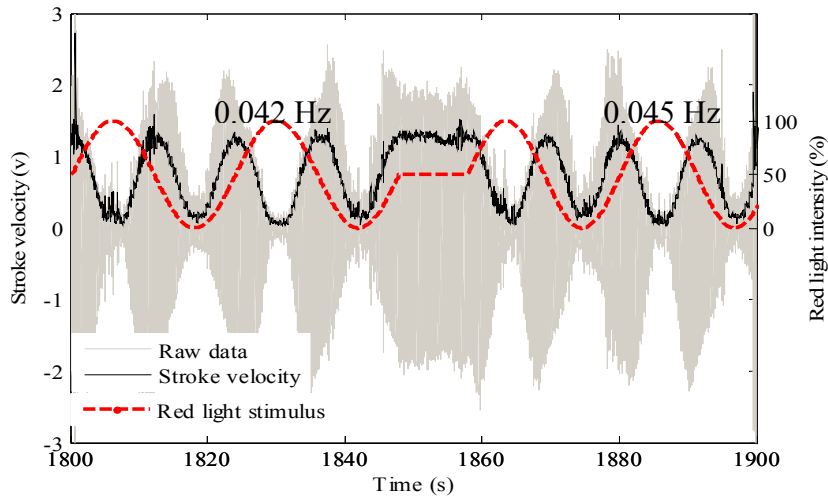


Figure 3.42. An example of stroke velocity response of *cpc1-2* strain in corresponding to the multi-sinusoidal red-light stimulus at frequency 0.042 and 0.045 Hz. The raw data is the electrical signal recorded by the quadrant photodiode and it is on the same y-axis as the stroke velocity (SV).

#### D. Magnitude and phase response of stroke velocity (SV) at $15 \text{ W/m}^2$

Stroke-velocity response has a constant delay about 0.36 s for positive responses and 0.34 s for negative responses (see Figure 3.43). The transfer function that describes its frequency response is a simple delay transfer function since its amplitude is independent from frequency.

There are no difference in a delay time between BF and SV response in both strains so they may be related in some ways. The delay time of *806* strain is about 1.01 to 1.18 s and one of *cpc1-2* strain is about 0.33 to 0.37 s. SV responses have the same delay in both positive and negative in both strain. The positive response of BF has a delay time longer than the negative one by about 0.29 s for the *806* strain versus by 0.04 s for the *cpc1-2*. This delay time possibly arises on the ATP regulation in the ciliary compartment because the *cpc1-2* which has a reduction of ATP in the ciliary compartment shows only a small delay between positive and negative response. Therefore, the negative and

positive change of light intensity could be regulated at different time scale within the ciliary compartment.

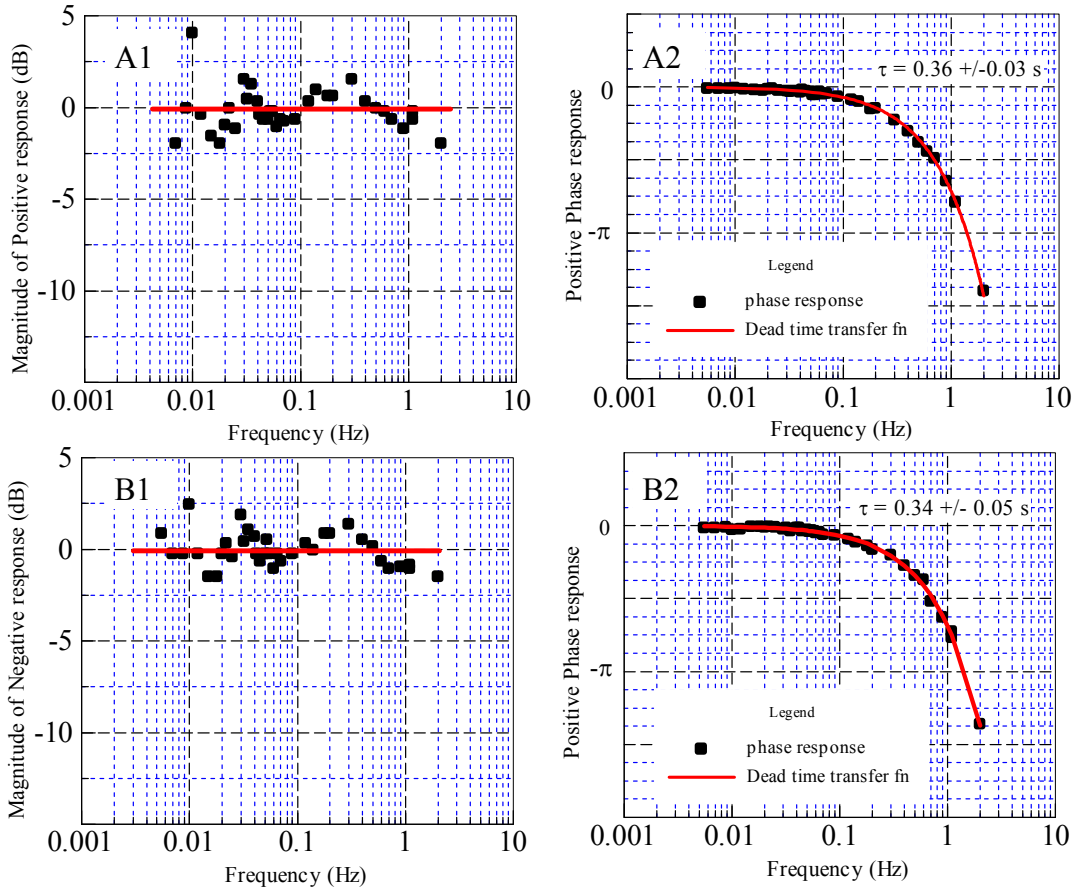


Figure 3.43. Bode plot of the *cpc-1* stroke-velocity response at each frequency of multi-sinusoidal stimulus to both positive and negative peak (A and B respectively). The fitted delay times of transfer function are about  $0.36 \pm 0.03$  s (fitted delay time  $\pm$  SD.) for positive and  $0.34 \pm 0.05$  s for negative response.

In *cpc1-2*, the beating frequency and the stroke velocity decrease when the light intensity is maximum or minimum whereas the *806* (wild-type, WT) strain similarly decreases its stroke velocity as does *cpc1-2* and it increases its beating frequency when the light intensity is maximum and minimum.

### 3.2.5 *Multi-sinusoidal responses at the high frequency range*

*from 2 to 100 Hz of 806 and cpc1-2 strain to red light at 15*

*W/m<sup>2</sup>*

- 806 strain

Beating Frequency fluctuates around its baseline between 2 to 5 Hz of red light modulating frequency (Figure 3.44 A). However, when we further increased this frequency to 10 Hz, the BF starts to decrease about 50% below its normal condition or baseline. These beating frequency responses are opposite and more dramatic to one at the lower frequencies as previously seen in Figure 3.33. At the low frequencies (below 2 Hz) of red light stimulus, the beating frequency increases when red light intensity increases and its percent change is below 5%. In contrast to the low frequency, beating frequency could drop to 20 Hz when red light is modulated at 20 Hz. The beating frequency recovers back to its baseline at 50 Hz and reverses its response direction to positive or increasing the beating frequency at 70 Hz and 100 Hz.

The stroke velocity decreases when red-light intensity is regulated at low frequencies (< 2 Hz). While it increases dramatically at 20 Hz, this is the same frequency as beating frequency's break down point. There is no reversed point like in the beating frequency at 70 Hz.

According to previous results, in the absence of light intensity changes the cell maintains its cilia's beating frequency and stroke velocity at very constant levels. This shows that the cell has tight control implying a negative feedback network. By having red light on the background or illuminating the cell with the continuous red light in Figure 3.29 B, the beating frequency fluctuates less. Therefore red light has an effect on this

control. By modulating red light to a frequency above 5 Hz, this negative feedback is broken down in terms of both beating frequency and stroke velocity responses. At high frequencies (> 7 Hz), the SV responses unlike the BF responses increase rather than decrease. The increase of SV responses occurs whenever the BF responses decrease, consequently the angular sweep of the cilia must be very large.

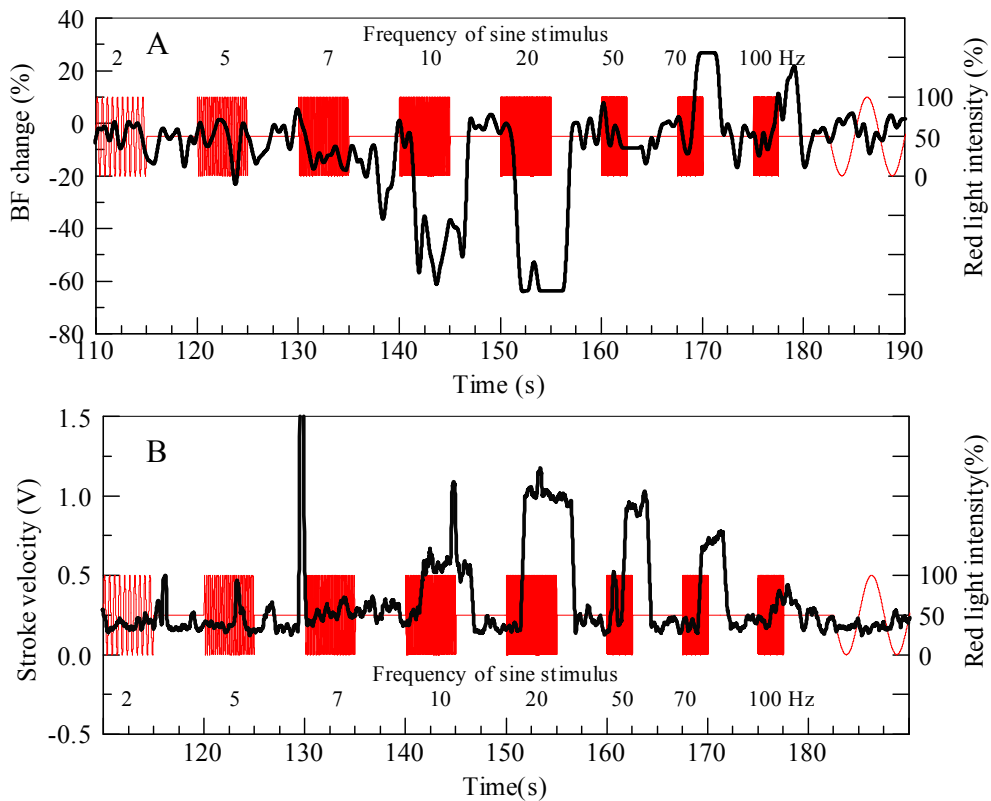


Figure 3.44. the 806 beating-frequency (A) and stroke-velocity responses (B) to multi-sinusoidal red light stimulus within the frequency range from 2 to 100 Hz.

- *cpcl-2* strain

*Cpcl-2* strain has a breakdown of negative feedback at 10 Hz which is in the same range of frequency as the 806 strain. See Figure 3.45 A for BF responses and B for SV responses. BF responses at the frequency range from 2 to 5 Hz also show a sinusoidal

pattern with a phase shift of 180 degree relative to their multi-sinusoidal stimuli and transient drops while SV responses did not have them. SV responses of *cpc1-2* strain have the same response-patterns as in 806 strain (a rectified sinusoidal signal). Therefore, the defect in *cpc1-2* strain does not affect the SV response-pattern except with respect to the time-delay (see Figure 3.43 for the time-delay). By 5 Hz, the average BF responses are suppressed as well as SV responses.

We extracted beating-frequency response of this sinusoidal response over the stimulus-frequency range from 0.3 to 10 Hz. Its Bode plot is shown as Figure 3.46 A. The magnitude response has a slope of 1 or +20 dB/decade. Its phase response starts at the positive 90 degree or  $+\pi/2$ . This is characteristic of the differentiator transfer function,

$$G(s) = Ks \quad (3.11)$$

where K is the gain.

This differentiated response has previously been observed on BF responses to short pulses of red light, see Figure 3.22 A. The SV pulse responses shown in Fig. 3.22B are much weaker and although clearly in the opposite direction from the BF responses drawing a conclusion was not possible. However, the situation is made clear in Figure 43.46B where the signal is clearly not differentiated. This tells us that the system has separate pathways for BF and SV responses.

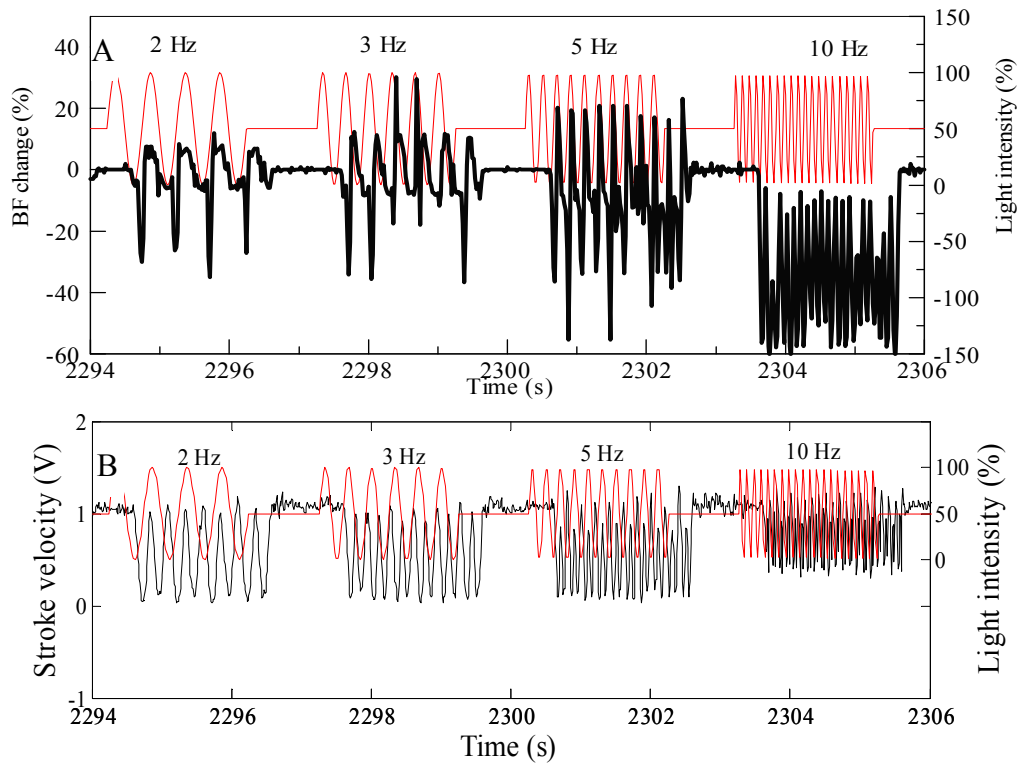


Figure 3.45. Show the *cpc1-2* beating-frequency (A) and stroke-velocity response (B) to the multi-sinusoidal red-light stimulus within the frequency range from 2 to 10 Hz.

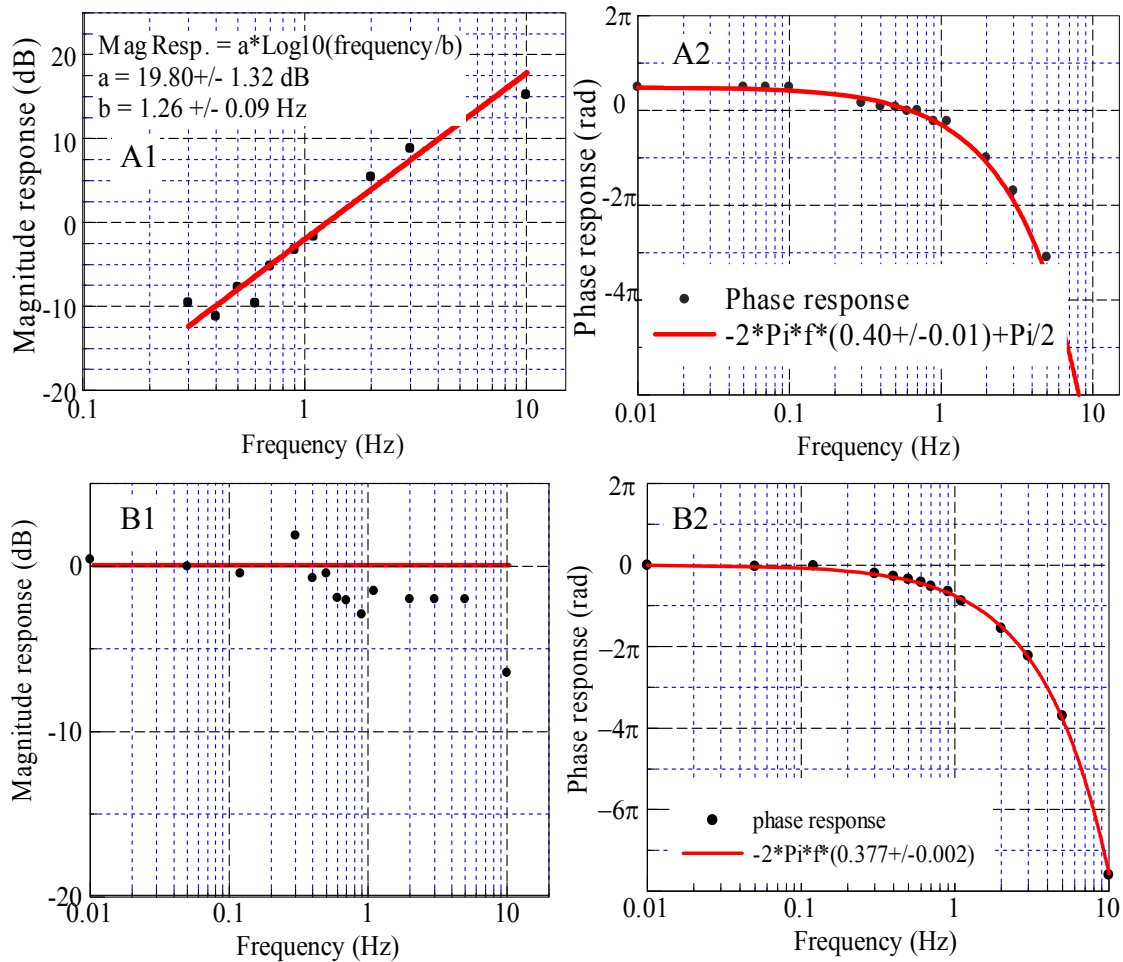


Figure 3.46. Bode plot of the *cpc-1* beating-frequency (A) and stroke-velocity (B) responses within the frequency range from 0.01 to 10 Hz.

Red light activates chlorophylls and possibly other red-light receptors such as phytochrome. The following discussions are based on the hypothesis that red light activation of chlorophylls is responsible for the observed effects. Chloroplasts convert light energy absorbed by chlorophylls into chemical molecules such as ATP, ADP, 3PG, etc. These molecules are distributed throughout cellular compartments including the chloroplast, the cytoplasm, mitochondria and ciliary compartments. According to both

*806* and *cpc1-2* results, we postulate that BF and SV responses are the results of the followings:

- i) Under a continuous (Figure 3.29B and 3.30 C) and multi-sinusoidal red-light stimulus (Figure 3.31), a cell tries to maintain its BF responses at 50 Hz. Hence, the 50 Hz is considered as a reference point in BF signaling pathway.
- ii) Since *cpc1-2* strain defects in ciliary structures and lack of ciliary glycolytic enzymes (including enolase) converting 3PG to ATP, its results is postulated to be due to parts of the signaling pathway within the cell body without the 3PG conversion to ATP in the ciliary compartment. Whereas the *806* results show how a cell processes an input signal as a total system. The Bode plots of *806* (see Figure 3.34) and *cpc1-2*'s BF responses (see Figure 3.41) provide an evidence of a simple delay time of 1.18 s and 0.37 s respectively. Therefore, the different delay time between *806* and *cpc1-2* is 0.81 s which represents a delay time possibly for synthesizing of ATP in the cilium from ADP. We hypothesize that the extra delay is a result of the positive Gibbs free energy for two steps in the conversion of 3PG to ATP within the glycolytic pathway in the ciliary compartment. See glycolytic pathways in Figure 3.4.
- iii) Both BF and SV responses of these two strains are non-linear but only the BF responses of *cpc1-2* in a frequency range from 0.3 to 10 Hz shows linear responses to multi-sinusoidal stimulus with a phase shift. Its Bode plot shows a differentiator (Figure 3.46 A). These prove that a cell differentiates the input signal. In addition to a differentiator, SV and BF responses must have separated pathways since SV responses of *cpc1-2* do not have linear

responses. To further support the idea of separated pathways or controllers of SV and BF responses, their response direction are always in an opposite direction to each other. We hypothesize that the differentiating process happens within the cell body since it is found in the *cpc1-2* results.

- iv) Using multi-sinusoidal stimuli in the frequency range from 2 to 100 Hz (see Figure 3.44), both BF and SV responses show positive and negative feedback controls that break the 50 Hz reference point.

### 3.3 Conclusions

Stimulating *C. reinhardtii* with red light (670 nm) and monitoring its ciliary motility not only allows us to understand the dynamic of bioenergetics pathway in sub-second time scale but also give us clues as to how each cell's compartment such as chloroplast, cytoplasm, mitochondria and ciliary compartment may be regulated *in vivo*. We modulated red light into different patterns: multi-sinusoidal waves and short- to long-pulse durations (5 to 160 s). Red light will affect photosynthesis in the chloroplast, but it is not the only potential target to influence. Therefore, the signals that matter are presumably linearly relative to the red light intensity. Examples could be 3PG and NADPH.

For multi-sinusoidal results, comparing the beating frequency between *806* and *cpc1-2* reveals how this organism processes red-light signal and how long it takes to respond to red light. Red light excites chlorophyll molecules in the chloroplast. According to our *cpc1-2* results on multi-sinusoidal stimuli, chloroplast differentiated and responded approximately and linearly to the sine-wave stimuli at different frequencies.

Therefore, its end products such as 3PG and NADPH should be linearly proportional to the red light intensity. The 3PG molecules can either be converted to pyruvate and ATP through the glycolytic pathway in cytoplasm or diffuse to the ciliary compartment. Pyruvate and NADPH are imported to mitochondria in order to produce energy molecules (ATP). Finding a delay time of about 400 ms (0.37 s) from *cpc1-2* transfer function suggests that a processing time is mostly due to diffusion because of the estimate for  $\text{Ca}^{++}$  diffusion being of this magnitude for this distance. The additional time delay of 800 ms is probably due to lag in synthesis of preparation of ATP. This time scale is determined by subtracting the total delay time from *806* transfer function of multi-sinusoidal stimuli (1.18 s) to the 400 ms. The 1.18 s represents the total processing time from light excitation to ATP hydrolysis within the ciliary compartment.

Even though red light is processed linearly by the chloroplast, its products can be summed to non-linear signals since beating frequency responses are full-wave rectified. Besides these, our beating frequency results at high frequency suggest that beating frequency regulation breaks down at 10 Hz, reducing BF to 20 Hz while at 70 Hz increases BF to 75 Hz. This implied at least two feedback laws that get broken, going in opposite direction. All these results were based on results in which the cell was illuminated on average with 50% red light intensity relative to the 100% range of stimulation ( $15 \text{ W/m}^2$ ).

In order to understand how this organism may process its signal from dark adaptation, we stimulated the cell with various pulse durations. The 5 second-pulse duration shows that the cell differentiated red light which agrees with our multi-sinusoidal results. By changing pulse duration from 5 to 160 s, the “step-down” of 40

second-pulse duration stimulus had the maximum drop-off amplitude. This implies that mitochondria function is suppressed at the most in this state or pulse duration. The higher the red light intensity is, the higher the drop-off amplitude. Therefore, mitochondria function is suppressed with the red light intensity. On the other hand, the “step-up” stimuli exponentially activate the chloroplast to produce metabolites that are turned into ATP with a short time constant (less than 2 second).

Finally, the beating frequency is very tightly controlled at about 50 Hz under red light compare to in the dark as indicated by the decrease of the standard deviation under red light (Figure 3.29 B and Figure 3.30 C). We also found that beating frequency responses due to multi-sinusoidal stimuli of *806* and *cpc1-2* are different while stroke velocity responses are the same. Thus, it confirms that BF and SV responses have different regulation.

# Chapter 4

## **Effects of external ion concentrations and red light on phototaxis**

---

### **4.1 Introduction**

Phototaxis, triggered by rhodopsin photoreceptors (Foster and Smyth, 1980; Foster et al., 1984; Deininger et al., 1995), is the swimming response whose direction depends on a cell's orientation relative to a light source - toward (positive phototaxis), away (negative phototaxis), or orthogonal (diaphototaxis). Phototaxis helps a cell reach a favorable light condition or to distribute itself (Pfeffer, 1904; Buder, 1917; Schaller et al., 1997). This phenomenon was formulated theoretically by Ray in 1693 who believed that a plant orientation was caused by its asymmetrical position to the differential effects of light intensity (Ray, 1693; Bendix, 1960). However, the first scientific investigations were performed by Treviranus in 1817 on zoospore movement of the green algae, *Draparnaldia*, away from broad daylight (Bendix, 1960; Treviranus, 1817). Phototactic unicellular and multicellular organisms harvest light through their photoreceptors such as chlorophylls and rhodopsin receptors. Light is used both as a signal for information and as a source of energy. Examples of its use include phototaxis, induction of enzyme activities, regulation of ion channels, and improved mating by swimming to a surface (concentrating in two dimensions) (Foster and Smyth, 1980; Togashi and Cox, 2004). Studies of phototaxis can lead either directly or indirectly to understanding how light regulates signaling processes. Even though much research has been carried out on

phototactic behaviors, how a cell decides its direction and how its mechanism works is still argued about.

The sign of phototaxis depends on many parameters such as ion concentrations (Morel-Laurens, 1987; Stavis and Hirschberg, 1973), photosynthesis (Takahashi and Watanabe, 1993), dark-adapted period (Nultsch and Throm, 1975), chemical molecules such as cAMP (Boonyareth et al., 2009), and cellular redox poise (Wakabayashi et al., 2010). Changing extracellular ion concentrations such as  $\text{Ca}^{2+}$ ,  $\text{K}^+$ , and  $\text{Na}^+$  significantly influences the phototactic response both in sign and magnitude as seen in several organisms including the unicellular flagellate *Cryptomonas* (Uematsu-Kaneda and Furuya, 1982), the marine ciliate *Fabrea salina* (Puntoni et al., 1998), *Cyanobacteria* (Moon et al., 2004), and, last but not least, our model organism, *Chlamydomonas reinhardtii*. For *C. reinhardtii*, required ions for phototaxis are  $\text{Ca}^{2+}$  and either  $\text{K}^+$  or  $\text{NH}_4^+$  (Stavis and Hirschberg, 1973).

The threshold action spectrum for the phototaxis associated electrical signal is the same as the phototactic threshold spectrum (Litvin et al., 1978; Sineshchekov, 1978; Sineshchekov and Litvin, 1988; Sineshchekov 1991). This motivated our phototactic studies to measure the electrical current (Capano, 2005) in order to explain the phototactic behaviors. Capano found that the response to the green-light sinusoidal stimuli comprises two kinds of signals: an initial electrical current (or the photocurrent, PC, which mostly is from the flow of ions in and out the eyespot region) and a second electrical current with a long delay of about 200 to 300 milliseconds. This long delay is probably from internal signaling or chemical molecules in the phototactic pathway involving cyclic adenosine monophosphate (cAMP), inositol triphosphate ( $\text{IP}_3$ ), and  $\text{Ca}^{2+}$ .

Green light activates rhodopsin receptors which cause ion influxes such as  $H^+$  and  $Ca^{2+}$ . Activated rhodopsins trigger  $IP_3$  molecules which later diffuse and bind onto endoplasmic reticulum (ER) leading to internal  $Ca^{2+}$  release to cytoplasm (Ferris and Snyder, 1992). Raising of  $[Ca^{2+}]_{cyt}$  depolarizes membrane potential and triggers the opening of voltage dependent  $Ca^{2+}$ -channels on the plasma membrane (Ferris and Snyder, 1992) and then  $K^+$ -channel. cAMP-dependent phosphorylation of  $Ca^{2+}$ -channels facilitate a delay of  $Ca^{2+}$  flow. cAMP also plays an important role in ciliary motility through cAMP-dependent protein kinase regulating dynein activities along microtubules (Howard et al., 1994). Concentration of cAMP in the positive phototactic strain, 1117, is higher than in the negative phototactic strain, 806, in all light conditions including in the dark, under green light (514 nm) and red light (674 nm). See Table 4.1. Higher cAMP concentration tends to bias cells to move toward green light (514 nm) (Boonyareth et al., 2009).

Condition	806 (negative phototaxis)	1117 (positive phototaxis)	Ratio of cAMP in 1117 to 806
	Mean $\pm$ SEM (pmol/106 cells)		
Dark	0.16 $\pm$ 0.01	0.90 $\pm$ 0.08	5.62 $\pm$ 1.03
Green light (514 nm)	0.50 $\pm$ 0.05	1.53 $\pm$ 0.05	3.06 $\pm$ 0.10
Red light (647 nm)	0.25 $\pm$ 0.03	0.99 $\pm$ 0.11	3.96 $\pm$ 0.65

Table 4.1. Intracellular concentration of cAMP in *C. reinhardtii* (Boonyareth et al., 2009).

Increasing internal signaling molecules raises the electrical current of internal chemical signal as a feedback signal when the cell responds to its environment. The ratio between the integration of the first electrical signal and the second electrical signal may

determine the sign of phototaxis. High in the later signal integration may lead to positive phototaxis. This ratio is possibly modulated by changing the external perturbation such as light intensity and its wavelength, extracellular ion concentrations such as  $\text{Ca}^{2+}$ ,  $\text{K}^+$  and  $\text{H}^+$ , and photosynthesis. This chapter reported the results of these external changes to the phototaxis triggered by green light (500 nm) of both to the 1117 (positive phototaxis) and the 806 (negative phototaxis) strains.

#### 4.1.1 *Change of extracellular ion concentration*

Under equilibrium conditions, *C. reinhardtii* maintains the difference between intracellular and extracellular ion concentrations (High in  $[\text{K}^+]_{\text{cyt}}$ , but low in  $[\text{Ca}^{2+}]_{\text{cyt}}$  and  $[\text{Na}^+]_{\text{cyt}}$  compared to extracellular ion concentration) and gives its resting membrane potential about -120 mV at pH 7.0 and  $[\text{K}^+]_{\text{ext}} = 0.1$  mM (Malhotra and Glass, 1995a). The resting membrane potential comes from the Goldman-Hodgkin-Katz (GHK) flux equation as Equation 4.1 for both monovalent and divalent ions and Equation 4.2 for resting membrane potential set by monovalent ions such as  $\text{K}^+$ ,  $\text{Na}^+$  and  $\text{Cl}^-$  (Jackson, 2006). These two equations are also called Nernst equations. The membrane potential allows the cell to sense the change of extracellular ion concentration and send the electrical signal within or among cells. In animals, the membrane potential depends mainly on  $\text{K}^+$  because the permeability of the membrane to potassium is the highest. Other ions have a slight effect.

$$V_m = \frac{kT}{q} \ln \left[ \frac{-b + \sqrt{b^2 - 4ac}}{2a} \right] \quad (4.1)$$

$$V_m = V_t \ln \left[ \frac{P_K C_{\text{ext},K} + P_{Na} C_{\text{ext},Na} + P_{Cl} C_{\text{cyt},Cl}}{P_K C_{\text{cyt},K} + P_{Na} C_{\text{cyt},Na} + P_{Cl} C_{\text{ext},Cl}} \right] \quad (4.2)$$

where  $q$  = the proton charge in Coulomb =  $1.6 \times 10^{-19}$  C

$k$  = the Boltzmann constant =  $1.38 \times 10^{-23}$  J-K<sup>-1</sup>

$T$  = temperature in Kelvin = 293 K (20 °C)

$V_t = kT/q = 25.3$  mV,  $V_m$  = resting membrane potential

$$a = 4P_j C_{ext,j} + \sum_i P_i C_{ext,i}, \quad b = \sum_i P_i (C_{ext,i} - C_{cyt,i}),$$

$$c = -4P_j C_{cyt,j} - \sum_i P_i C_{cyt,i}$$

$P_i$  and  $P_j$  = permeability of either the monovalent ion (i) or the divalent ion (j)

$C_{ext,i}$  and  $C_{cyt,i}$  = extracellular and intercellular ion concentration respectively

Under non-equilibrium conditions, charge movement is added to Equation 4.2.

The electrochemical driving force,  $\mu_i$ , depends on the resting membrane potential, the extracellular and the intercellular ion concentration. See Equation 4.3 (Modified from Ianowski and O'Donnell, 2006).

$$\mu_i = zV_m - \frac{kT}{q} \ln \frac{C_{ext,i}}{C_{cyt,i}} \quad (4.3)$$

where  $z$  is the ion valence.

The  $zV_m$  and the  $\frac{kT}{q} \ln \frac{C_{ext,i}}{C_{cyt,i}}$  are an electrostatic and a diffusion component

respectively. The balance between these two forces gives us the ion driving direction. If the  $\mu_i$  is positive, the ions efflux and oppositely for the negative value. For example, if cells are in the medium with the  $C_{ext,K} = 0.1$  mM, cells maintain the  $C_{cyt,K} = 150$  mM at the membrane potential -120 mV. The driving force can be calculated as following

$$\mu_i = (-120 \text{ mV}) - (25.3 \text{ mV}) \ln \left[ \frac{0.1 \text{ mM}}{150 \text{ mM}} \right] = -120 - (-185) = +60 \text{ mV} \quad (4.4)$$

Since the driving force is positive, the potassium ions tend to leave the cell at this condition if there is an opening of potassium channels. The driving forces are shown in Figure 4.1 (A) for potassium ion (Malhotra and Glass, 1995a) and (B) for hydronium and calcium ion. The driving forces of  $\text{Ca}^{2+}$  and  $\text{H}^+$  are approximately calculated using  $[\text{H}^+]_{\text{ext}}$  and their corresponding membrane potential from Malhotra and Glass (1995b).  $[\text{H}^+]_{\text{cyt}}$  is about pH 7 (Messerli et al., 2005; Balkos and Colman, 2007; Braun and Hegemann, 1999) and  $[\text{Ca}^{2+}]_{\text{cyt}}$  is at pCa7 at membrane potential of -120 mV (Braun and Hegemann, 1999; Bothwell et al., 2006). The driving force of  $\text{H}^+$  is high at low pH (Figure 4.1 C), but its maximum PC is at pH 7.4 for ChR1 and ChR2. This evidence demonstrated that other ions also play a role in PC amplitude (Sineshchekov et al., 2009).

Figure 4.1 raises a question of how the cell maintains its negative membrane potential since all positive charges influx. The GHK equation only explains the ion flow passively such as  $\text{K}^+$  efflux and  $\text{Cl}^-$  influx helping repolarization (a recovery from a raise of membrane potential or less negative membrane potential). In addition to a passive flow, the ATP pumps or ion pumps such as the  $\text{Na}^+/\text{K}^+$  pump and the  $\text{H}^+$ -ATPase could maintain a negative membrane potential. The  $\text{Na}^+/\text{K}^+$  pump is electrogenic as it imports 2  $\text{K}^+$  and exports 3  $\text{Na}^+$ . The vacuolar  $\text{H}^+$ -ATPase in unicellular green algae such as *Micrasterias torreyi* (Lehtonen and Saari, 2000) also helps maintain the internal pH. Other possible candidates present in the *C. reinhardtii* genome are the  $\text{Na}^+/\text{H}^+$  exchanger, the voltage-gate chloride channel (GEF1), and the light-gated proton channel (COP3) ([www.uniprot.org](http://www.uniprot.org)).

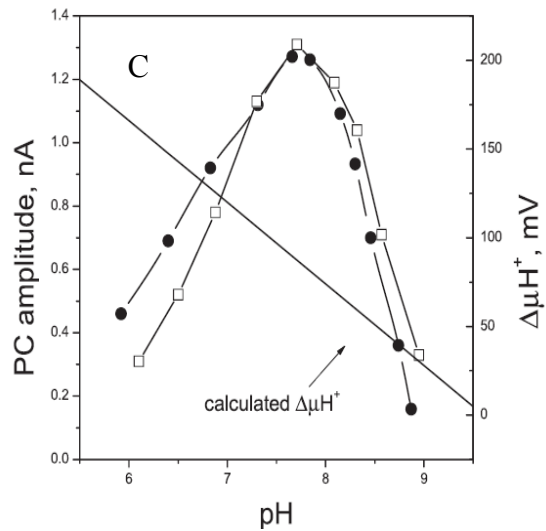
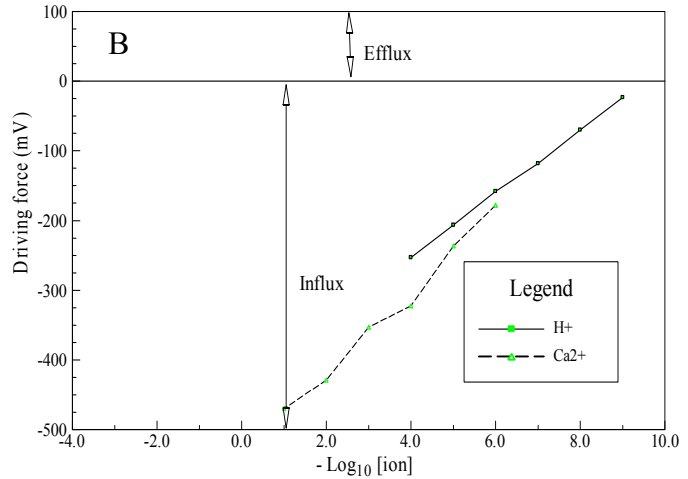
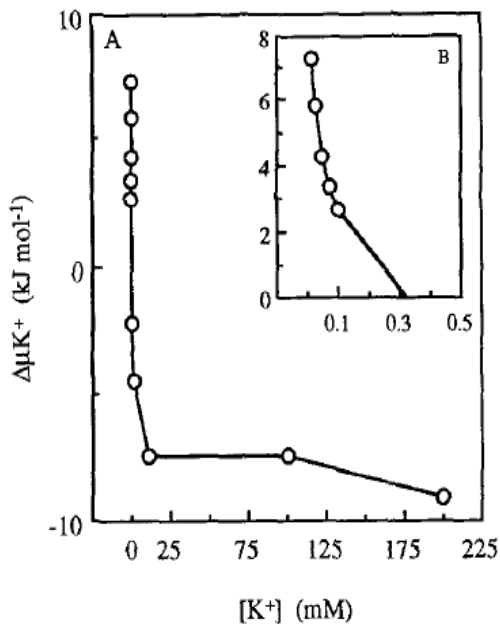


Figure 4.1. Driving forces of  $K^+$  (A),  $H^+$  and  $Ca^{2+}$  (calculated in B). Both  $H^+$  and  $Ca^+$  ions tend to flow into the cell once their channels are opened. C: The PC and  $-\Delta\mu H^+$  from the ChR1 and ChR2-enriched *C. reinhardtii* RNAi transformants (Sineshchekov et al., 2009). The filled and opened symbols are the ChR1 and the ChR2 respectively.

Note:  $1 \text{ kJ/mol} = 10 \text{ mV}$  using the Faraday constant,  $F$ , is  $96485 \text{ coulombs/mol}$ .

### Calcium

The regulation of intracellular calcium concentration make it possible for a cell to keep its concentration very low preventing its precipitation and also plays an important role in shaping the dynamics of the calcium ion as a second messenger in cell signaling (Pittman et al., 2009). Several behaviors depend on a  $Ca^{2+}$  signals such as phototaxis

(Nultsch, 1979), ciliary motility (Bessen et al., 1980), and sexual signaling (Snell et al., 1982). The  $\text{Ca}^{2+}$  concentration in the cytosol,  $[\text{Ca}^{2+}]_{\text{cyt}}$ , is in the range from  $10^{-7}$  to  $10^{-6}$  M (pCa7 to pCa6) (Braun and Hegemann, 1999; Bothwell et al., 2006; Sanders et al., 1999). If the extracellular  $\text{Ca}^{2+}$  concentration is 20mM, *C. reinhardtii* adjusted its  $[\text{Ca}^{2+}]_{\text{cyt}}$  to approximately 400 nM (Bothwell et al., 2006). A cell adjusts its  $[\text{Ca}^{2+}]_{\text{cyt}}$  in order to not only protect itself from  $\text{Ca}^{2+}$  toxicity, but also to maintain its signaling level (McAinsh and Pittman, 2009).

The change of calcium concentration is able to significantly influence the phototaxis due to the existence of  $\text{Ca}^{2+}$  channels such as the transient receptor potential (TRP) (Pazour et al., 2005) and the voltage-dependent calcium channel (VDCC) on ciliary membrane (Fujiu et al., 2009), channelrhodopsins on eyespot region (Harz and Hegemann, 1991). Rhodopsin excitation on the eyespot depolarizes its membrane and triggers the electrical signal to flagellar  $\text{Ca}^{2+}$  channels and lead to increase of  $[\text{Ca}^{2+}]_{\text{cyt}}$  and  $[\text{Ca}^{2+}]_{\text{cilia}}$ . How this  $\text{Ca}^{2+}$  influx leads to the sign of phototaxis is still under investigation. Kamiya and Witman (1984) proposed the model of dominance between the *cis*- and *trans*-cilium that determines the sign of phototaxis. They used the demembrated *C. reinhardtii*, 137 (+), and demonstrated that the alteration of *cis*-(closer to the eyespot) and *trans*-cilium depends on the  $[\text{Ca}^{2+}]_{\text{o}}$ . At  $10^{-9}$  M  $[\text{Ca}^{2+}]_{\text{o}}$ , the *cis*-cilium is dominant and the cell swam with the eye spot outside the helical path. Conversely the *trans*-cilium is dominant at  $10^{-7}$  to  $10^{-6}$  M  $[\text{Ca}^{2+}]_{\text{o}}$ . According to their conclusion on the demembrated model, the *trans*-cilium dominance leads to a turn toward a source light or positive phototaxis. However Josef and colleagues (2006) reported that the *trans*-cilium of excited 806 strain or negative phototactic strain (back cross to the wild-type, 1117), is dominant

since it has a shorter delay and a faster beating frequency than the *cis*-cilium. The conflict between these results possibly comes from the different type of strains used or inadequacy of interpretation. Nevertheless, using the non-phototactic mutant, *ptx1* supported the model of  $\text{Ca}^{2+}$  dependence in alteration of two cilia (Horst and Witman, 1993). Later, Okita et al.(2005) found that non-phototactic mutants, both *ptx1* and *lsp1*, showing no  $\text{Ca}^{2+}$  dependence on the cilium dominance actually have a weak phototaxis. Therefore, other pathways such as  $\text{H}^+$  (Ehlenbeck et al., 2002), cAMP (Habermacher and Sale, 1995), and guanosine-5'-triphosphate (GTP-) (Patel-King et al., 2002) may be a part of a phototactic pathway.

Besides the dominance between two cilia, the electrical signal pathway was detected as an early signal of the phototactic pathway. It is the earliest detected signal in phototaxis and depends on the  $[\text{Ca}^{2+}]_{\text{ext}}$  (Harz et al., 1992). The suction pipette of a single cell technique was used to measure the electrical signal shown photoreceptor current (PC) and flagellar current (FC) (as seen in Figure. 4.2) and the PC depends on the external calcium concentration as shown in Figure 4.3. The  $\text{Ca}^{2+}$  influx creates the photoreceptor current (PC) on the eyespot region and leads to a depolarization of membrane potential. If the PC reaches a threshold level, it triggers the flagellar current (FC) which seems to be a “calcium action potential” response. The action spectra of photocurrent potential generation are the same as the one for phototaxis (Figure 4.4).

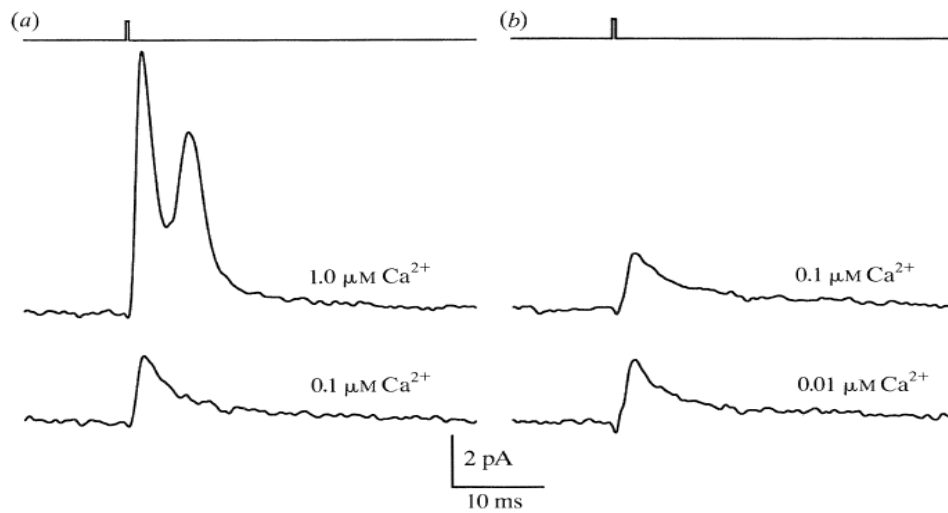


Figure 4.2. Photocurrent response of *C. reinhardtii*, cell wall-deficient mutant or CW2, depends on the extracellular calcium concentration. The transient signal happened at the  $1.0 \mu\text{M Ca}^{2+}$  which the first peak represents the photoreceptor current and the second peak represents the flagella current (a). Lowering in the extracellular  $\text{Ca}^{2+}$  concentration decreases the photocurrent

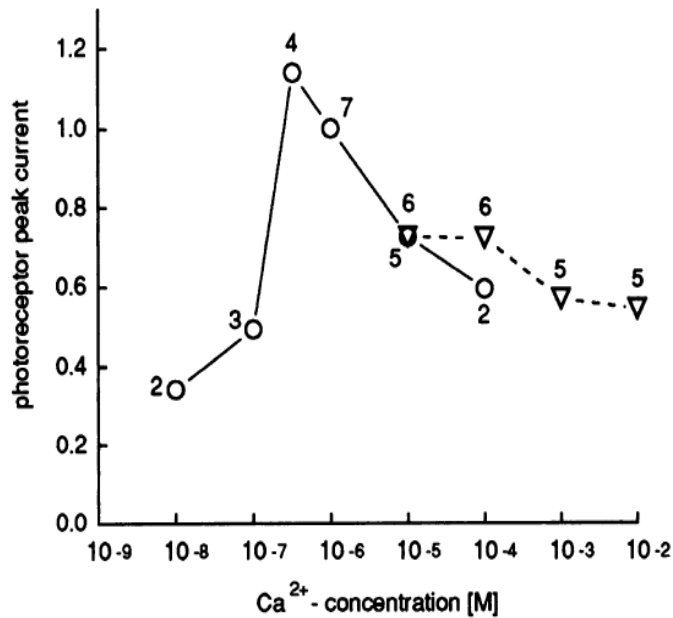


Figure 4.3. Photocurrent (PC) depends on calcium concentration by using the suction technique on the cell-wall deficient mutant, CW2. The number on each symbol represents the number of analyzed cells. Cells were prepared in different buffers: KP<sub>i</sub> (dash line) and NMG<sup>+</sup>/K<sup>+</sup> (solid line) (Holland et al., 1996).

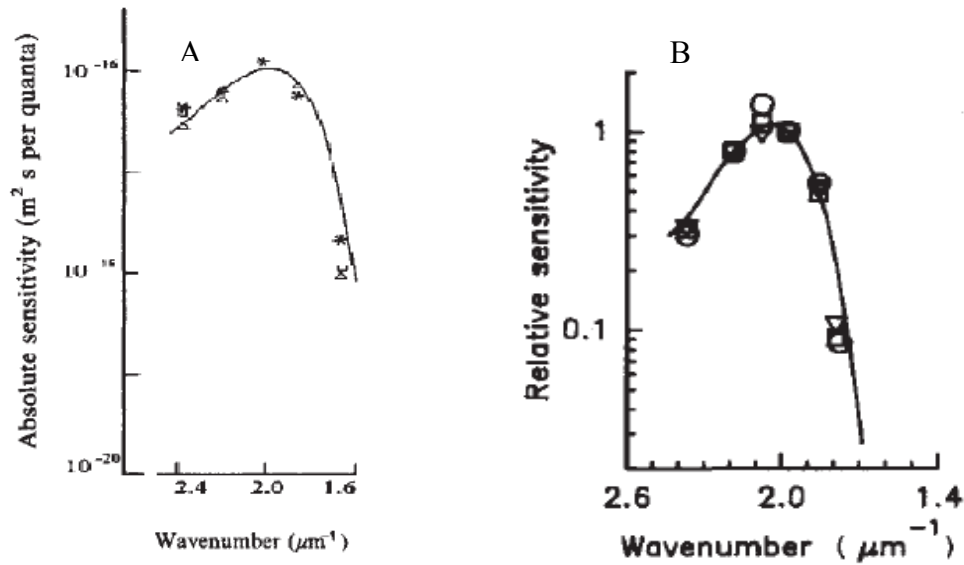


Figure 4.4. Show the action spectra of the phototaxis: Foster and colleagues (1984) (A) and the photoreceptor current, PC (B) (Harz and Hegemann, 1991).

Depolarization of membrane potential (or less negative membrane potential) is presumably the down stream pathway after the photocurrent happens in the area of the eyespot. The ion influx on the cilia membrane can further depolarize the membrane potential. However no one has reported an actual change of plasma-membrane potential due to rhodopsin excitation (Note: the suggested method to measure this change is the electric field measurement, Chapter 5). Change of  $[Ca^{2+}]_{cyt}$  influences not only organelles such as mitochondria (mt) and endoplasmic reticular (ER), but also the transport channels that work as a network and regulate local calcium concentrations within a cell.

### Hydronium

H<sup>+</sup> ions are from passive entry, ionization of water molecules, and buffering between weak acid and weak base within cells. Maintaining their concentration within narrow limits is very important since cell molecules such as peptides and proteins bind each other and themselves through multitudes of hydrogen bonds. A cell regulates  $[H^+]_{cyt}$

or  $[pH]_{\text{cyt}}$  through transmembrane transporters and its organelles such as chloroplast for photosynthesis and mitochondria for respiration. In *C. reinhardtii*,  $H^+$  ions also enter the cell through the eyespot region when the rhodopsin receptors are triggered.

A biological system usually maintains its plasma-membrane potential at a negative value. Therefore, stimulating channelrhodopsin2 proteins, for example, leads to an inward photocurrent from positive charges (Figure 4.5 A at -100 mV). On the other hand, if the cell membrane were held at a positive potential, the photocurrent would reverse its direction (Figure 4.5 A at +40 mV). Therefore, changing membrane potential affects the photocurrent. Besides the membrane potential, changing extracellular ion concentration such as  $[H^+]_{\text{ext}}$  could also affect the photocurrent. *C.reinhardtii* maintains  $[pH]_{\text{cyt}}$  at  $7.4 \pm 0.1$  (Braun and Hegemann, 1999). Decrease of  $[pH]_{\text{ext}}$  increases the proton gradient along the membrane. When light triggers an opening of these channels, more ions influx leads to a larger photocurrent at pH 5 than one at pH 7.6 or 9 (Figure 4.5 B). Pre-conditioning cells in NMM medium (pH 6.8), which is close to its  $[H^+]_{\text{cyt}}$ , should make the cells less sensitive to changes of pH and its effect on the proton motive force that drives the hydronium ion through the membrane. Therefore, under these conditions the photocurrent should come less from the hydronium proton motive force ( $\Delta\mu_{H^+} =$  change of membrane potential ( $\Delta\psi$ ) + change of pH ( $\Delta pH$ )) but mainly comes from  $\Delta\psi$ .

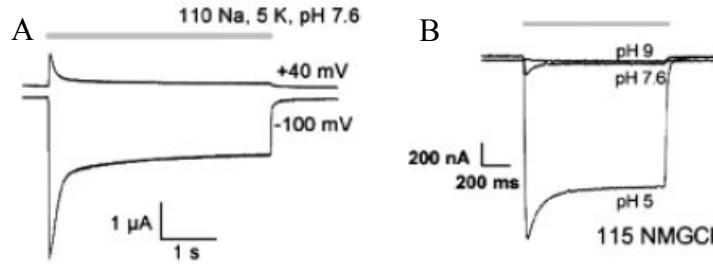


Figure 4.5. Photocurrents of oocytes expressing in ChR2-315 depend on both  $\Delta\psi$  (A) and  $\Delta\text{pH}$  (B) (Nagel et al., 2003).

### Potassium

$\text{K}^+$  is essential in several biological processes, especially protein synthesis.

Therefore, a cell maintains  $[\text{K}^+]_{\text{cyt}}$  at a high level of about 150 mM (Malhotra and Glass, 1995a; Leigh and Jones, 1984; Memon et al., 1985). In general,  $[\text{K}^+]_{\text{cyt}}$  is higher than  $[\text{K}^+]_{\text{ext}}$ . Change of the  $[\text{K}^+]_{\text{ext}}$  affects the membrane potential as seen in Figure 4.6 B. If the  $[\text{K}^+]_{\text{ext}}$  is higher than the  $[\text{K}^+]_{\text{cyt}}$ , it leads to  $\text{K}^+$  influx and depolarizes or increases the membrane potential to a less negative value.

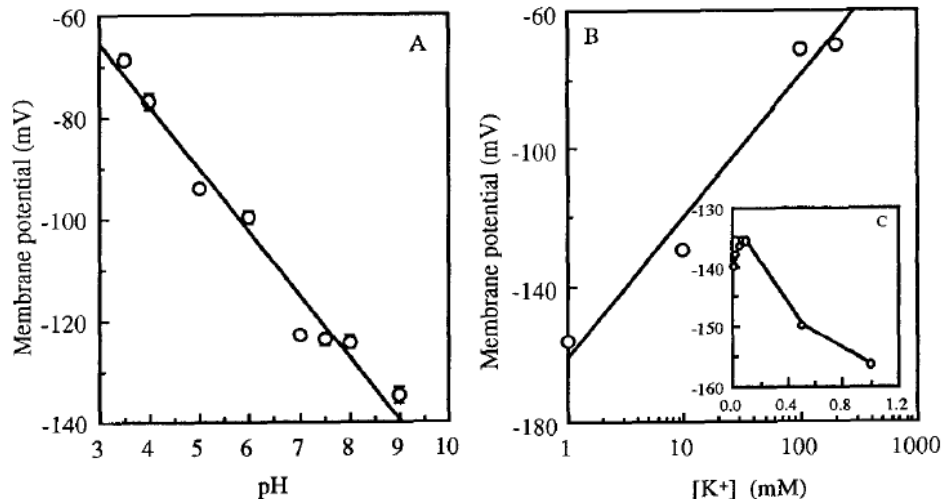


Figure 4.6. Show effects of external ion concentrations such as pH (A) and  $\text{K}^+$  (B) on the membrane potential. *Chlamydomonas reinhardtii* were grown at  $[\text{K}^+]_{\text{ext}}$  0.1 mM (Malhotra and Glass, 1995a).

### 4.1.2 *Red light as a background light*

Red light hyperpolarizes membrane potential to a more negative value (Sineshchekov, 1991; Sineshchekov and Govorunova, 1999) and it could lead to a reverse phototactic direction as seen in Takahashi and Watanabe (1993). The red light at 633 nm is absorbed mainly by the *Chlorophyll a* in the chloroplast. However, there is also evidence of a far-red phytochrome-like response and the cells are very sensitive to it (Petridou et al., 1997). While so far a red phytochrome has not been found in the *C. reinhardtii*'s genome unlike in higher plant or even other green algae, it could very well be there.

### 4.1.3 *Signaling Pathway*

The phototactic signaling pathway comprises both an electrical signal and a chemical signal (Sineshchekov et al., 2009). Green light (at 500 nm) excitation of the Channel Rhodopsin Receptors (ChRs) on the eyespot region changes the rhodopsin conformation and allows the cell membrane to exchange ions such as  $\text{Ca}^{2+}$ ,  $\text{Na}^+$ , and  $\text{K}^+$  with its environment. This process leads to a membrane depolarization sending the *first electrical signal* ( $E_1$ ) to the cilia compartment or the *photocurrent signal* ( $PC$ ) and induces  $\text{Ca}^{2+}$  influx on the cilia membrane through the  $\text{Ca}^{2+}$  voltage-dependent channels. In addition, green light excitation also activates a *chemical signal* ( $C$ ) via molecules such as  $\text{IP}_3$  found on the eyespot region to the cytoplasm. The  $\text{IP}_3$  molecules then diffuse, bind to and trigger the ER membrane to release  $\text{Ca}^{2+}$  to the cytoplasm. The increased intracellular calcium level then initiates several  $\text{Ca}^{2+}$  dependent proteins to trigger the opening of  $\text{Ca}^{2+}$  channels on the cell membrane. We consider this step as the *second electrical signal* ( $E_2$ ). Increased intracellular  $[\text{Ca}^{2+}]$  is recovered by  $\text{K}^+$  efflux or

hyperpolarization of the membrane potential and pumping  $\text{Ca}^{2+}$  out. Cells require both  $\text{Ca}^{2+}$  and  $\text{K}^+$  for phototaxis (Stavis and Hirschberg, 1973). Besides these ions, changing of pH level could also affect the phototaxis since the cell has pH homeostasis. We reported the effects of these ions to phototactic responses due to the green light stimulation. In addition to varying ion concentration, we also investigated the effect of a red light background (633nm) on phototaxis. Red light stimulates not only the chlorophyll receptors in the photosynthesis pathway which change the oxidation and reduction of NADP (Forti et al., 2003) and produce the energy molecules such as 3PG, but also change gene expression on a time scale of an hour (Petridou et al., 1997; Teramoto et al., 2006). Takahashi and Watanabe (1993) also reported that photosynthesis due to red light changed the sign of phototaxis to green light from positive phototaxis to negative phototaxis in wild-type *C. reinhardtii* 137c mt<sup>+</sup>.

All signaling pathways have their own response times. An electrical signal, of course, is faster than a chemical one. The electrical signal or photocurrent by saturating flash light is triggered in less than 50  $\mu\text{s}$  (Holland et al., 1996) and response reaches its peak within 20 ms (Ehlenbeck et al., 2002). The electrical signal sent from the eyespot to cilia compartment has a behavioral response latency of less than 1 ms (Josef et al., 2006) while the chemical signal which is a delay between the first electrical signal and the second electrical signal is several hundred milliseconds (Capano, 2005). Therefore, both electrical signaling pathways could influence the swimming direction or the sign of phototaxis. Although phototaxis has long been known, no one understands clearly the signaling pathway involved and how a cell decides its direction. Since a depolarization of cell membrane from light is proportional to the number of charges transported across cell

membrane, the integration of this electrical signal in a time period measures ion activities (Sineshchekov et al., 2009). We hypothesize that *the sign of phototaxis comes from a comparison between the integration of the first and the second electrical signal*. The higher the integration of the second electrical signal, the more a cell biases to a positive direction. Since the positive phototactic strain or wild-type, 1117, has a higher integration of the second electrical signal than the negative phototactic strain, 806 as seen in Figure.

4.7 (Note: a cell rotates about its longitudinal axis at about 2 Hz).

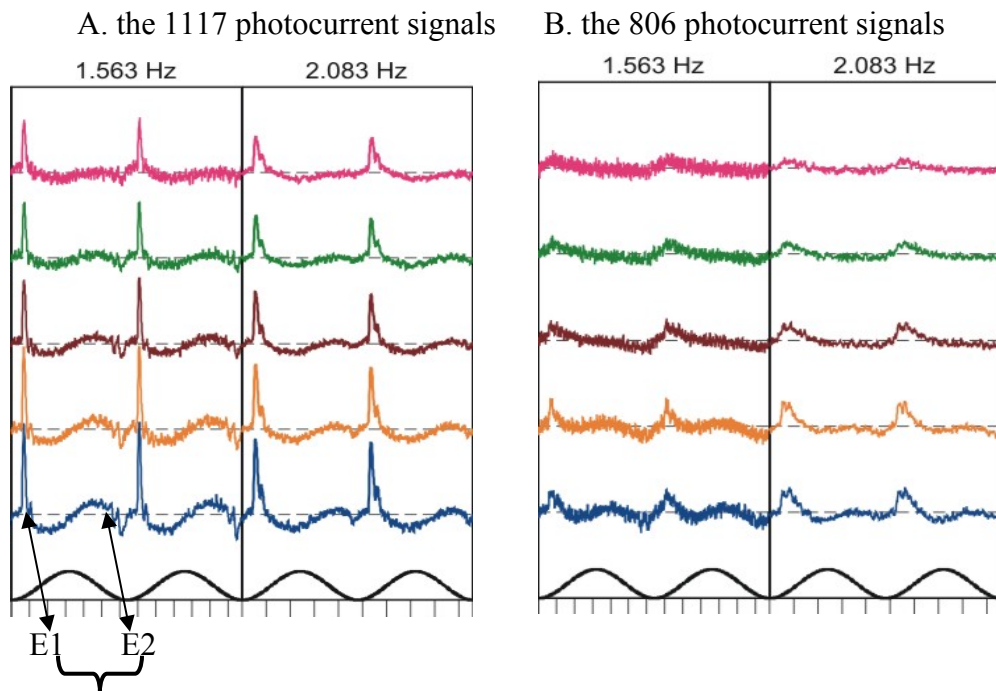


Figure 4.7. The graphs, A and B, show five repetitions of photocurrent response signals stimulated with a 500 nm laser at 1.563 Hz and 2.083 Hz with a sine-wave pattern (Capano, 2005) by using photoelectric measurement in cell suspension method (Sineshchekov and Govorunova 2001). The first record is at the bottom of the graph. Each tick on the x-axis represents the 100 ms time scale. The E1, E2, and C represent the first electric current peak, the second electric signal current peak, and the time delay between the first and the second electrical signal respectively.

We suggest that the electrical current technique could be combined with the cell tracking technique in the future in order to better answer what regulates the sign of phototaxis. The phototactic responses of *C. reinhardtii* strain 806 and 1117 (negative and positive phototaxis strain respectively) are reported here as valuable new information under specific external ion concentrations including pH 5.5 to pH 9 (0.1 mM [Ca<sup>++</sup>] and pH 6.8) and pCa 3 to pCa 9 (6.78 mM [K<sup>+</sup>] and pH 6.4). Cells were stimulated either by green light only or both green and red light.

## 4.2 Methods and materials

### 4.2.1 Cell preparation

Wild type (1117) and 806 strains of *Chlamydomonas reinhardtii* were grown either on high salt media (HSM)-agar plate or in HSM-liquid medium under constant white light (10 W/m<sup>2</sup>) at 18 °C for 2-7 days. Cells were then harvested by using a sterilized inoculation loop and resuspended in a nitrogen-deficient minimal medium or NMM (MgSO<sub>4</sub>·7H<sub>2</sub>O 81 μM, CaCl<sub>2</sub>·7H<sub>2</sub>O 0.1 or 0.05 mM, K<sub>2</sub>HPO<sub>4</sub>·3H<sub>2</sub>O 4.13 mM, KH<sub>2</sub>PO<sub>4</sub> 2.65 mM, and Trace 0.1%) in order to have cells differentiate into gametes and placed in a shaker (speed 175 rpm) under constant white light for another 10-18 h. Our cells were harvested again by centrifuging at low speed for 5 minutes. Cell pellets were resuspended in calcium or proton medium to a final concentration of about 1-2x10<sup>6</sup> cells/ml. Cells were counted by using a Hematocytometer.

### 4.2.2 Free calcium medium preparation

Desired calcium media with MOPS buffer (MOPS 10 mM, MgSO<sub>4</sub>·7H<sub>2</sub>O 81 μM, and Trace 0.1%) were adjusted and calculated by using Maxchelator software from <http://www.stanford.edu/~cpatton/maxc.html>. Ethylenediaminetetracetic (EDTA) and ethyleneglycol-bis-(β-aminoethylether)-N,N,N', N'-tetracetic acid (EGTA) were used as chelators for this medium. See Table 4.2.

Free Calcium (M)	Chelators (μM)	CaCl <sub>2</sub> (μM)	Measured free Calcium (M)
	<i>EDTA</i>		
pCa3	0	1000.0	1x10 <sup>-3</sup>
pCa4	100	199.6	8x10 <sup>-5</sup>
pCa5	100	107.0	1x10 <sup>-6</sup>
pCa6	100	77.8	-
	<i>EGTA</i>		
pCa7	200	3.4	-
pCa8	2000	3.4	-
pCa9	2000	0.3	-

Table 4.2. Show calcium concentrations, amount of chelators and CaCl<sub>2</sub> for each expected free calcium medium. Free calcium concentration were measured with the calcium selective electrode and reference electrode (Model ISE25Ca and REF251 from Radiometer Analytical company, Colorado, USA) and compare reading values with the standard curve. (Note: this calcium selective electrode has a sensitivity of 2x10<sup>-6</sup> M. Therefore, we could not measure the calcium concentration in a lower concentration than pCa6.) Then media were adjusted to pH 6.4 at room temperature (20 °C) with sodium hydroxide (NaOH).

#### 4.2.3 Free proton medium preparation

Desired proton media of 0.1 mM calcium concentration were prepared with 2 different buffers instead of MOPS buffer which are Tris-base (pK<sub>a</sub> 8.1) buffer for pH 7, 8

and 9, and MES buffer ( $pK_a$  6.1) for pH 5.5 and 6. Use NaOH and HCl to adjust medium to desired pH.

#### 4.2.4 *Cell tracking machine*

Prepared cells were loaded with the desired medium into a hollow rectangle capillary (50x 2 x 0.2 mm, VitroCom, Mountainlakes, NJ). Samples are monitored with the computerized cell population tracker (CPT), a near-IR CCD (charge-coupled device) camera (KP-F120, 30 frames/s, Hitachi) attached to a Nikon Labophot-2 with 10x phase objective lens, monochrome CCD camera (KP-F123, Hitachi, Japan). Cells were adapted in the dark for 5 minutes before stimulating with light. The 300-W tungsten lamp was filtered through a 10 nm bandpass filter 500 nm (full-width-half-maximum band interference filter, Microcoating, Westford, MA). A HeNe laser was used for red-light background (peak at 633 nm). The 500-nm wavelength was chosen because it maximally stimulates rhodopsin receptors. To vary light intensity, optical-density or OD filters were used and light intensity was measured by using photometer (88XLA, Photodyne Inc., Camarillo, CA).

#### 4.2.5 *Data collection and analysis*

A loaded capillary tube was placed on the microscope stage and the light illuminated along its length direction with a shutter between them. The shutter was controlled by an external switch that either fully opens or closes the shutter. Samples were exposed to light initially without recording data for 5-10s and then record was begun for 10s with a sampling rate at 15 frames per second. The total number of images was 150.

For the analysis, the cell tracking software calculates net displacement and net angle as the following equations.

$$Net\ displacement = \frac{1}{n} \sqrt{\left(\sum_{i=1}^n x\right)^2 + \left(\sum_{i=1}^n y\right)^2} \quad (1)$$

$$Net\ angle = \tan^{-1} \left( \frac{\sum_{i=1}^n x}{\sum_{i=1}^n y} \right) \quad (2)$$

Where x and y are the net distance traveled in 10 s in the x and y directions of each cell respectively, n is the total number of cells on focus plane and  $0 < \text{Net angle} < 360$ .

### 4.3 Results and discussions

After spinning the cells down and adding test media, cells were not active under testing media with low calcium concentrations ( $10^{-9}$  to  $10^{-7}$  M) and high hydronium concentrations (pH 5.5 and pH 6.0). In order to have at least 50% active cells, they were adapted to testing media for about 30 to 60 minutes by shaking at 120 rpm under continuous  $1\text{ W/m}^2$  standard white fluorescence lights. Cells were tested for their phototactic responses depending on many parameters such as light intensity (at 500 nm) and ion concentrations ( $\text{Ca}^{2+}$ ,  $\text{K}^+$ ,  $\text{H}^+$ ). The net displacement was calculated through a cell population tracking program.

Generally, 806 strain cells swim away from the light or have a negative phototactic response while the 1117 strain cells swim toward the light or have a positive phototactic response, both with a small net displacement at low light intensities. They had a strong negative response for 806 (positive for 1117) at intensities between 26 and 2631  $\text{mW/m}^2$  (1 to 100  $\mu\text{w}/0.38\text{ cm}^2$ ). Some cells swam in the opposite direction for a few seconds which means they swam toward the light for 806 (away from the light for 1117).

#### 4.3.1 *Varying external free calcium ion concentration*

Both 806 and 1117 strains swam respectively away and toward the light in NMM which has  $[\text{Ca}^{2+}]_{\text{ext}}$  at  $10^{-4}$  M or pCa 4. We used these as a control sample since cells were adapted to this medium before being adjusted to a new extracellular calcium concentration. We suspended cells in NMM overnight to become gametes.

Strain 806 cells reduced their negative phototaxis or went toward more positive phototaxis when  $[\text{Ca}^{2+}]_{\text{ext}}$  is low. For example, cells suspended in  $[\text{Ca}^{2+}]_{\text{ext}}$  0.1 mM taken from an agar plate and adjusted to pCa 7, pCa 8, and pCa 9 in Figure 4.8 has less negative phototaxis than pCa 3, pCa 4, pCa 5, and pCa 6. Moreover, cells suspended in  $[\text{Ca}^{2+}]_{\text{ext}}$  0.1 mM taken from a liquid HSM culture and adjusted to pCa 6 and pCa 7 were turned into a positive phototaxis under rhodopsin activation (Figure 4.9). Since cells grown in a liquid medium have thinner cell-walls than one grown in an agar medium, this might affect the amount of ion transportation across plasma membrane. There is no result for cells taken from a liquid medium and adjusted to pCa 9, because cells were not active under this condition (Figure 4.9).

According to Figure 4.1 B and extending the pCa graph to pCa 9, extracellular calcium ions in a range from pCa 9 to pCa 1 tend to influx across the cell membrane and depolarize the membrane potential. For instance, cells suspended in pCa 4 should have a higher resting membrane potential or a more positive value than pCa 6 because it has a higher driving force and increases calcium-ion flow. However, it is not true since the maximum photocurrent or the maximum ion flow rate is between pCa 6 and pCa 7 (Figure 4.3). Therefore, other ions or membrane channels could play roles in addition to this photocurrent which hypothetically is assumed to contribute to the sign of phototaxis.

A high photocurrent (PC) or early electrical current ( $E_1$ ) at pCa 6 and pCa 7 could amplify internal biochemical signals leading to the second electrical signal ( $E_2$ ). Capano (2005)'s results show that 1117 strain (positive phototactic strain) has a high integrated second electrical signal while the 806-strain (a negative phototactic strain) second electrical signal is much smaller (Figure 4.8). The ratio of the integrated first or early electrical current ( $E_1$ ) relative to the second electrical current ( $E_2$ ) may determine the sign of phototaxis. A low  $E_1/E_2$  ratio might tend to bias cells to go toward light or have a positive phototaxis such as in 1117 strain and a high  $E_1/E_2$  ratio tends to do the opposite or have a negative phototaxis as in the 806 strain. The following results and discussions were explained according to this hypothesis.

Strain 806 cells suspended in pCa 6 and pCa 7 are expected to have a lower  $E_1/E_2$  comparing to cells in other pCa since these two conditions led to a higher  $E_1$  and simultaneously triggered a higher  $E_2$  than other pCa (See Figure 4.3 for the magnitude of the  $E_1$  signal at each calcium concentration). From this Figure, pCa7 has a low  $E_1$  and this leads to a low  $E_2$  signal. Therefore, it may result in a high  $E_1/E_2$  ratio. Our prepared pCa7 based on a calculated number may not be as accurate as others because we could not measure it, because our calcium electrode has its minimum limit at pCa6. Therefore our pCa 7 could be the pCa 6.5 on Figure 4.3 where the  $E_1$  signal is at its maximum value. If our medium is actually at pCa7, another possibility that leads to a low  $E_1/E_2$  ratio is the release of internal  $Ca^{2+}$  ions from internal organelles such as endoplasmic reticulum which increases the  $E_2$  signal. Stimulated cells with a low  $E_1/E_2$  ratio tend to swim toward light more than cells in other pCa (Figure 4.8 and 4.9). Cells suspended in pCa 3 and pCa 4 have a low  $E_1$  leading to a low  $E_2$  signal than pCa 6 and pCa 7. Therefore, the  $E_1/E_2$

ratio of pCa 3 and pCa 4 may be higher than pCa 6 and pCa 7. Thus cells in these media have negative phototaxis.

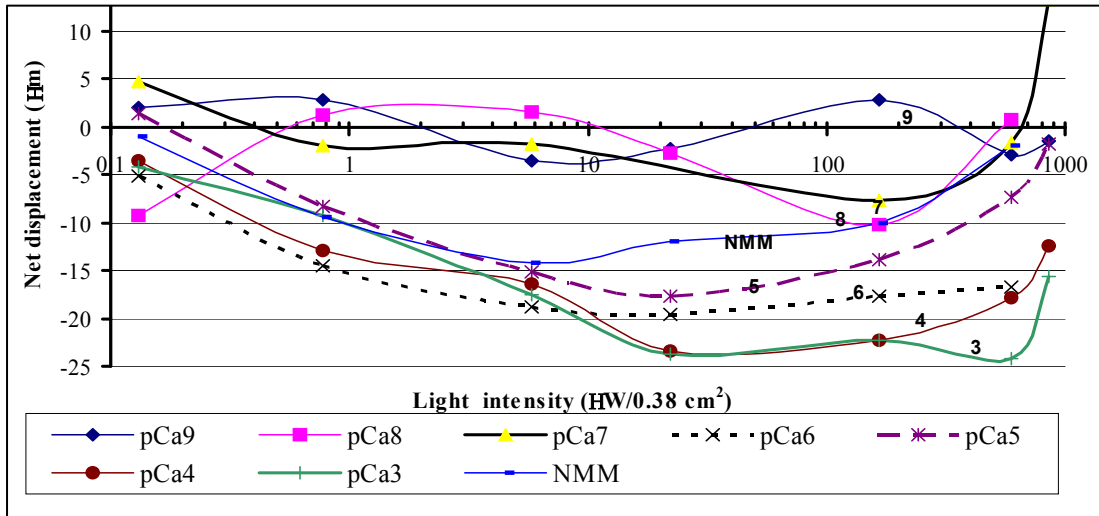


Figure 4.8. Show a net displacement response vs. green-light intensity (peak at 500 nm) of 806 strain grown on an agar plate for 7 days and suspended in 0.1 mM  $[Ca^{2+}]$  of NMM overnight. Cells were adapted to new calcium concentrations for 30 minutes.

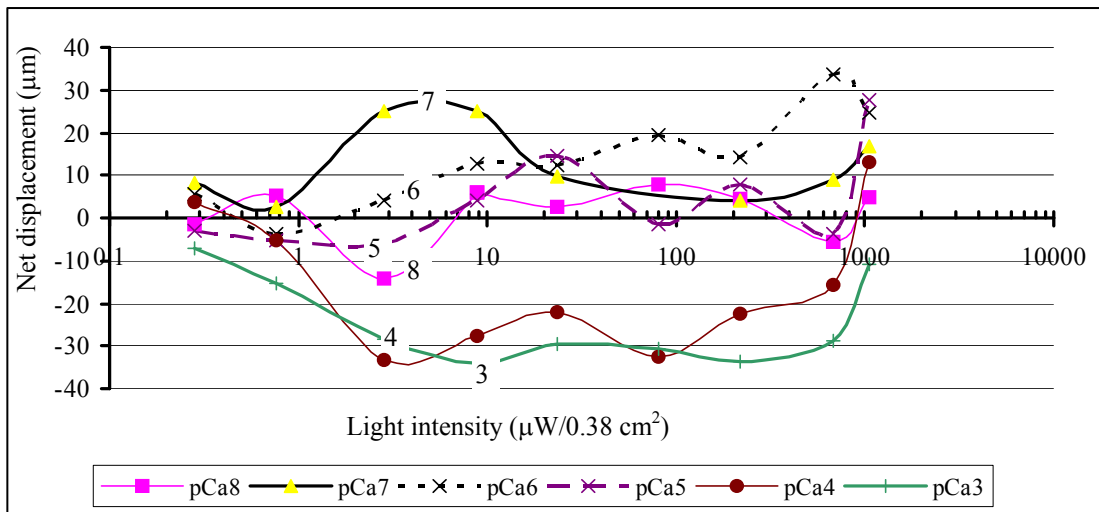


Figure 4.9. Show a net displacement response vs. green-light intensity (peak at 500 nm) of 806 strain grown in HSM liquid medium for 3 days and suspended in 0.05 mM  $[Ca^{2+}]$  of NMM overnight.

Strain *1117* cells were more sensitive to changes of extracellular calcium concentrations. Cells at pCa7 to pCa9 are non-motile. Figure 4.10 and Figure 4.11 report phototactic responses from pCa 6 to pCa 3. Strain *1117* cells took about 1 to 2 hours to recover after adding a new calcium concentration. The cAMP concentration in *1117* strain is higher than that in the *806* strain by about 5.6 times in the dark and 3 times under green light (Table 4.1). Cells suspended in pCa 3 and pCa 4 had more positive phototaxis than pCa 5 and pCa 6. Expected photocurrent or  $E_1$  signal of cells in pCa 3 and pCa 4 is lower than one of cells in pCa 5 and pCa 6 (Figure 4.3). On the other hand, its  $E_2$  signal from internal biochemical signals such as cAMP or  $IP_3$  may not change since *1117* strain has already a high intracellular concentration of cAMP. Thus, the expected  $E_1/E_2$  ratio of pCa 3 and pCa 4 should be lower than in pCa 5 and pCa 6 and should bias them to swim toward the light source. At pCa 6, cells are expected to have a high photocurrent or  $E_1$ , but the second electrical current,  $E_2$ , should not increase. Therefore, its  $E_1/E_2$  ratio is higher than pCa 3 and pCa 4 and cells swam less positively.

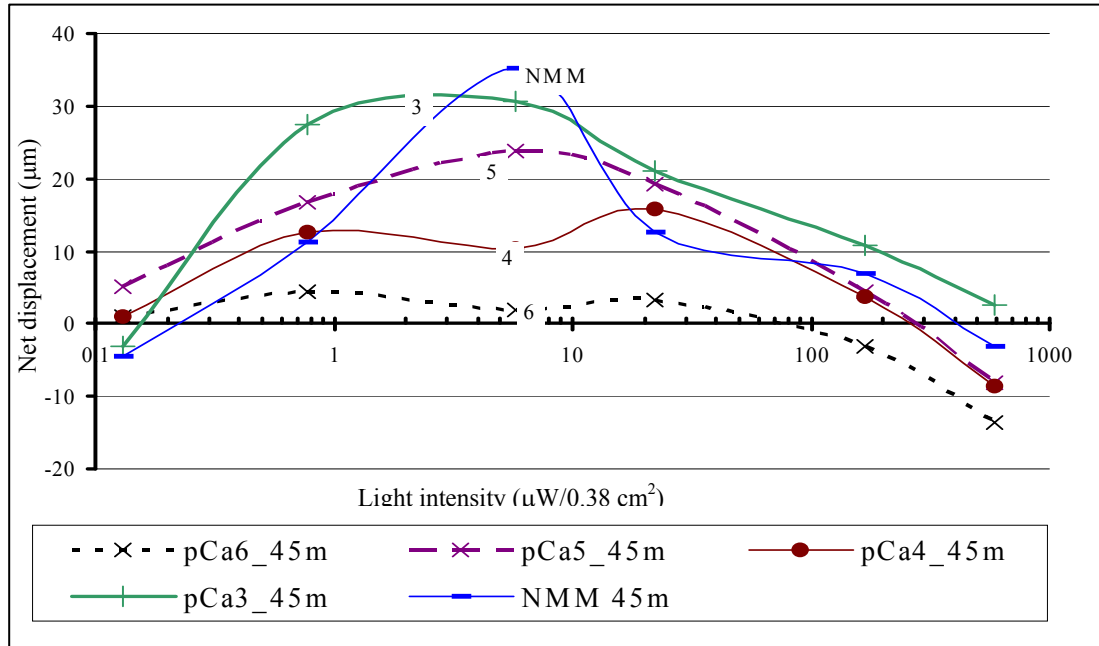


Figure 4.10. Net displacement responses due to green light (peak at 500nm) of 1117 strain grown on plate for 2 days and spin down in 0.1 mM  $[Ca^{2+}]$  NMM overnight. Cells are incubated in each medium for 45 minutes to recover at least 50%.

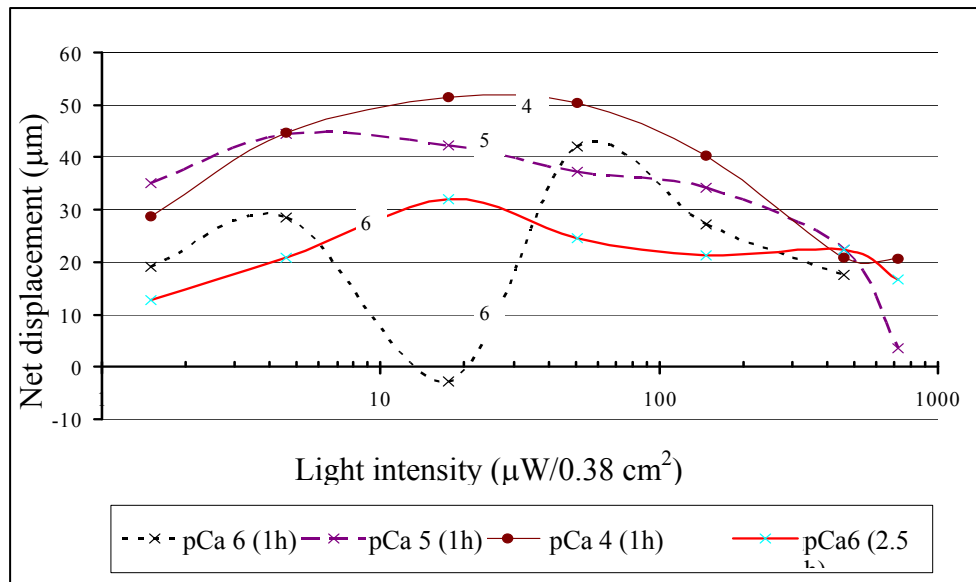


Figure 4.11. Net displacement responses vs. green-light intensity of 1117 strain grown in HSM liquid medium for 4 days and suspended in 0.05 mM  $[Ca^{2+}]$  of NMM overnight. Cells were adapted to new calcium concentrations for 1 hour at pCa 6, pCa 5 and pCa 4.

### 4.3.2 Varying external free hydronium ion concentration

Cells were suspended into two different buffers which are the MES buffer for pH 5.5 and 6.0 and the MOPS buffer for pH 7-9. Therefore these results should be considered separately. There is no reversal of phototactic direction by changing extracellular pH from pH 5.5 to 9 in both strains. Cells were adapted to new pH for 45 minutes. *806* cells had a less negative phototaxis at a higher pH or low  $[H^+]_{ext}$  such as pH 8 and 9 (Figure 4.12). The same trend toward biasing swimming toward the light was shown in *1117* strain where cells in pH 9 swam even more rapidly toward the light than one in pH 7 and pH 8 (Figure 4.13).

The photocurrent or early electrical signal ( $E_1$ ) is at its maximum magnitude at pH 7.4 if cells were adapted at pH 7.4 (Figure 4.1 C). In our case, cells were adapted to pH 6.8 before changing to a new pH. Therefore, the expected maximum photocurrent should be between pH 6 and pH 7. Cells in pH 5.5 should have both  $E_1$  and  $E_2$  signals lower than one in pH 6, but cells in pH 6 may have a higher  $E_2$  due to biochemical triggering by  $E_1$ . Therefore, the  $E_1/E_2$  ratio of cells in pH 5.5 is higher than one in pH 6. Therefore, cells in pH 5.5 show more negative phototaxis than cells in pH 6. Cells in pH 9 should have a low  $E_1$  due to a low photocurrent (Figure 4.1 C). Therefore, the  $E_1/E_2$  ratio of cells in pH 9 is lower than one in other pH which presumably leads to a decrease of negative phototaxis (*806* strain) or an increase of positive phototaxis (*1117* strain). See Figure 4.12 and 4.13 respectively.

Another explanation for an increase of positive phototaxis at pH 9 is hyperpolarization of membrane potential (more negative membrane potential comparing to a lower pH). When light triggers rhodopsins, the total number of positive charges

flowing across the cell membrane should increase and lead to a high net displacement in a positive direction. The more membrane potential is hyperpolarized, the more positive phototaxis cells have.

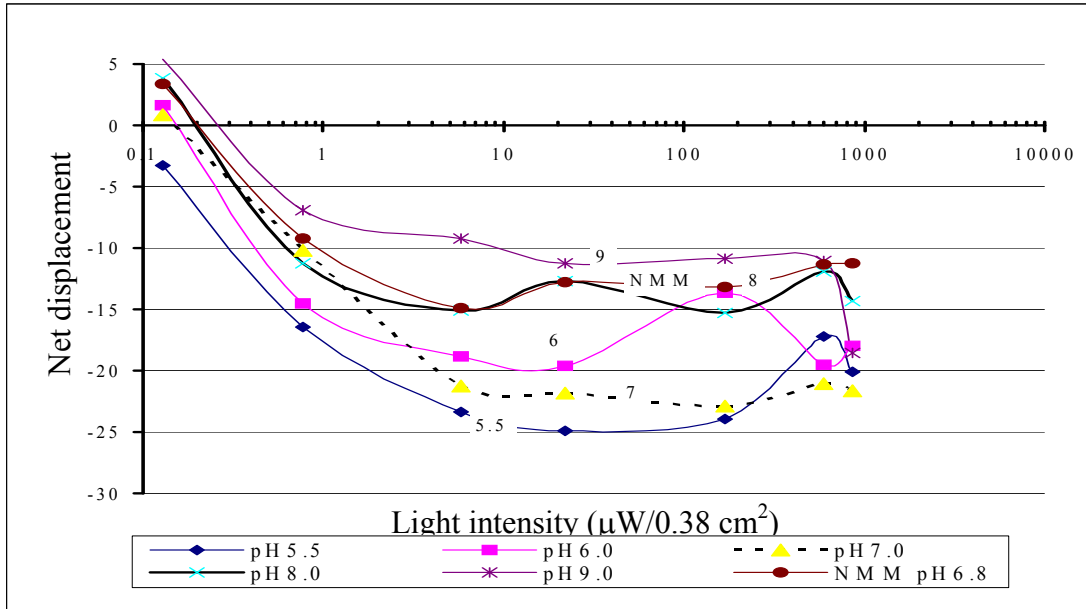


Figure 4.12. Net displacement responses vs. green-light intensity of *806* strain grown in the HSM plate for 3 days and suspended in 0.1 mM  $[\text{Ca}^{2+}]$  of NMM overnight.

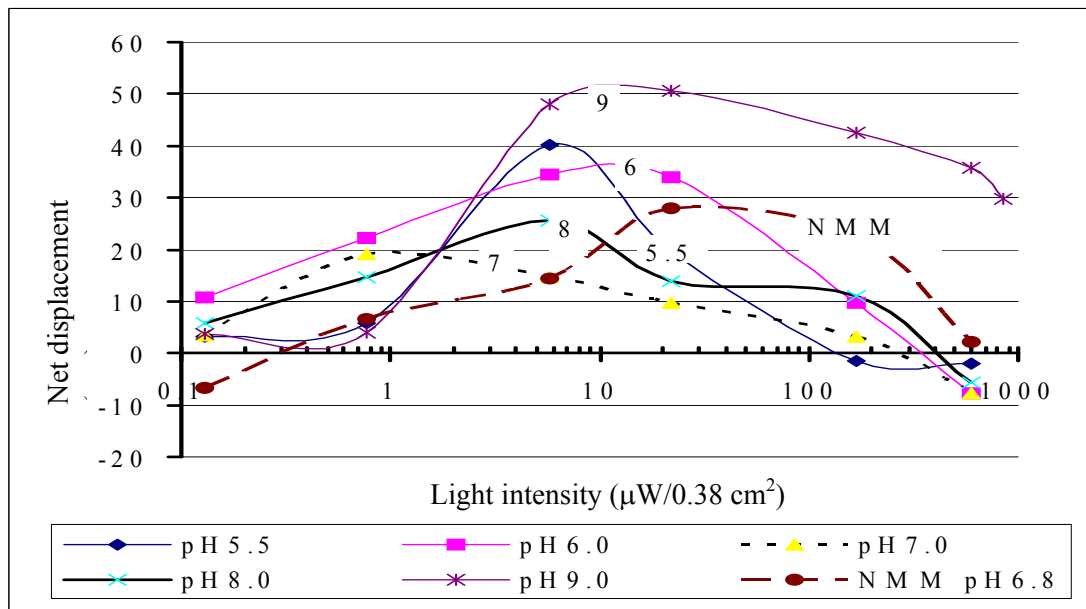


Figure 4.13. Net displacement responses vs. green-light intensity of *1117* strain grown in a HSM plate for 2 days and suspended in 0.1 mM  $[\text{Ca}^{2+}]$  of NMM overnight.

### 4.3.3 Varying external free potassium ion concentration

Increasing  $[KCl]_{ext}$  induced cells to more positive phototaxis in both 806 and 1117 strains (Figure 4.14 and 4.15 respectively). Typically the higher the concentration, the more positive the phototaxis. An exception was at 10 mM  $[KCl]_{ext}$ , 1117 cells had a less positive phototaxis than when they swam in 1 mM  $[KCl]_{ext}$ . Furthermore, 1117 cells had a negative phototaxis at low green-light intensity (0.5 to 3  $\mu W/0.38 \text{ cm}^2$ ) in 0 mM  $[KCl]_{ext}$ .

Potassium ions play an important role in setting the resting membrane potential. Usually cells maintain a high intracellular potassium concentration. According to Malhotra and Glass (1995a), the membrane potential is hyperpolarized from -137 to -157 mV by changing  $[K^+]_{ext}$  from 0.1 to 1.0 mM) and depolarized from -160 to -60 mV by changing  $[K^+]_{ext}$  from 1.0 to 300 mM (Figure 4.6). Since both strains show that a low  $[K^+]_{ext}$  bias cells to move more in positive phototaxis, it implies that the more hyperpolarized the membrane potential is, the more positively phototactic cells are.

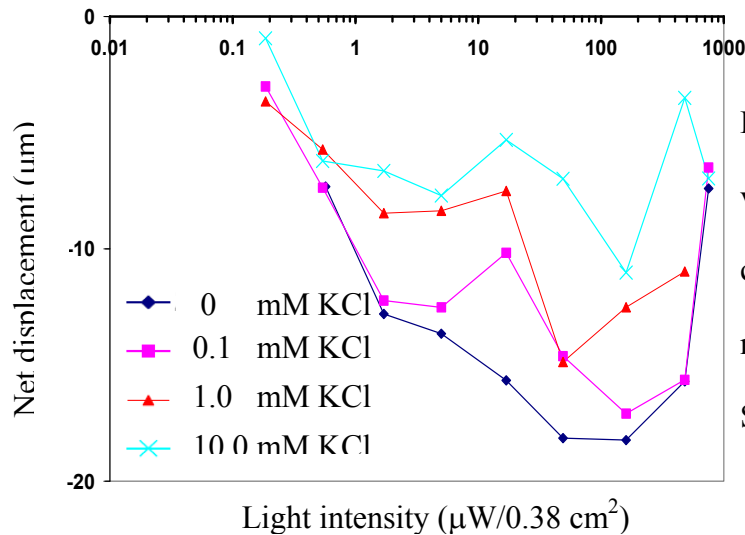


Figure 4.14. Net displacement vs. green-light intensity of 806 cells at different  $[KCl]_{ext}$  from 0 mM to 10 mM (Sims and Saranak, 2006).

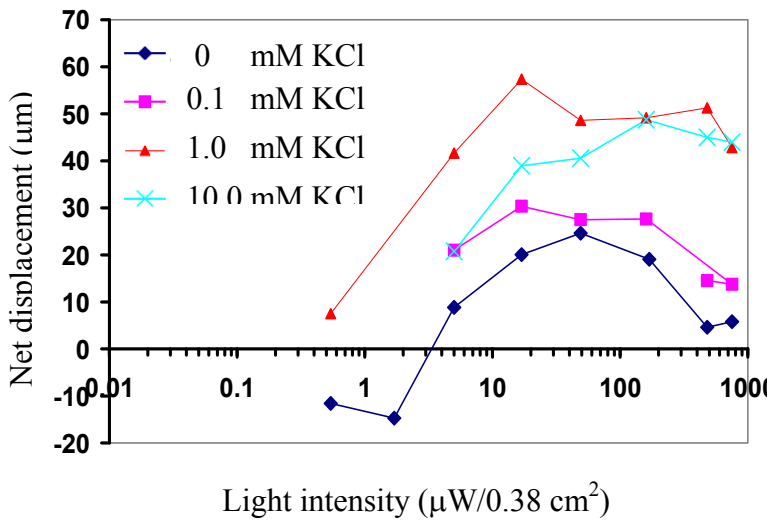


Figure 4.15. Net displacement vs. green-light intensity of *1117* cells at different  $[KCl]_{ext}$  from 0 mM to 10 mM (Sims and Saranak, 2006).

#### 4.3.4 Varying red-light intensity 633 nm

Using red light as background illumination in pCa4 and pCa5 medium, the negative phototaxis is reduced in the *806* strain (Figure 4.16 A and B). While the *806* strain in pCa 6 and 7 had reversed phototactic responses with green-light or rhodopsin excitation from negative to positive phototaxis (Figure 4.17 A and B), red-light inhibits this reversion. Increase of red-light intensity from 3.97 to 125.59  $\mu\text{w}/\text{cm}^2$  leads to a more negative phototaxis in pCa6 and 7. On the contrary, cells had lesser negative phototaxis at 500  $\mu\text{W}/0.38 \text{ cm}^2$ .

Red light (wavelength longer than 650 nm) as a background illumination hyperpolarized the membrane potential (more negative value) and increased photoreceptor potential in *Haematococcus pluvialis* (Sineschekov et al., 1990). *Haematococcus pluvialis* closely relates to *Chlamydomonas reinhardtii* and both have similar electrical characteristics. In addition, red light also reduced negative phototaxis of *806* strain in pCa4 and pCa5. This implies that hyperpolarization of cell membrane induces a reduction of negative phototaxis or an increase of positive phototaxis. The same

trend as previously seen in changes of  $[K^+]_{ext}$ . At pCa 6, the 806 strain swam toward green light without a red background (Figure 4.17 A). Adding red light as a background illumination inhibited this effect. Red light hyperpolarizing the cell membrane and further increasing the photocurrent (PC) or the  $E_1$  signal after green-light stimulation could be an explanation of this inhibition. At pCa 6 (Figure 4.17 A), the PC signal from green light without red light could be triggering the  $E_2$  signal or the chemical signal (such as cAMP) and it may already reach its maximum level due to a low cAMP level in 806. Therefore, a further increasing of the PC signal by adding red light background would not increase the  $E_2$  leading to a higher  $E_1/E_2$  ratio than one without red background or a more negative phototaxis following our hypothesis (a high  $E_1/E_2$  ratio leads to negative phototaxis).

Red light did not affect phototaxis of 1117 strain at pCa 4 and pCa 5 (Figure 4.18 A and B). Nevertheless, it increased positive phototaxis of 1117 strain at pCa 6 (Figure 4.18 C). This may be because of an increased photocurrent or first electric signal ( $E_1$ ) at pCa6 (Figure 4.3). The  $E_1$  could trigger a high  $E_2$  signal and lead to a low  $E_1/E_2$  ratio. When this ratio is low, cells tends to swim toward the light.

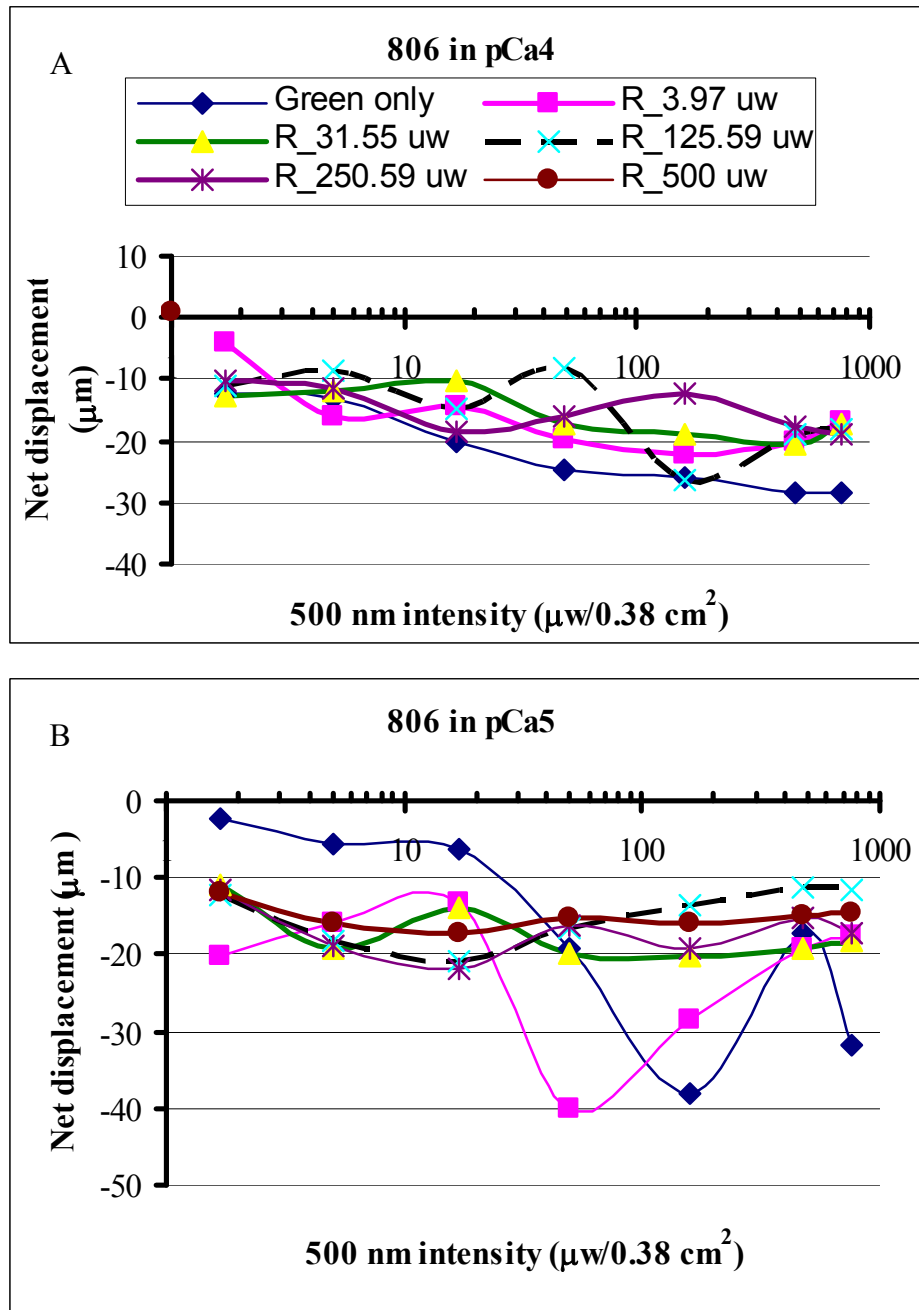


Figure 4.16 Net displacement vs. green-light intensity and red light as background illumination (633 nm) with various intensities: 0, 3.97, 31.55, 125.59 and 500  $\mu\text{w}/0.38 \text{ cm}^2$  of 806 strain in pCa 4 (A) and pCa5 (B). Cells were grown in HSM liquid media and suspended in 0.05 mM  $[\text{Ca}^{2+}]$  of NMM overnight.

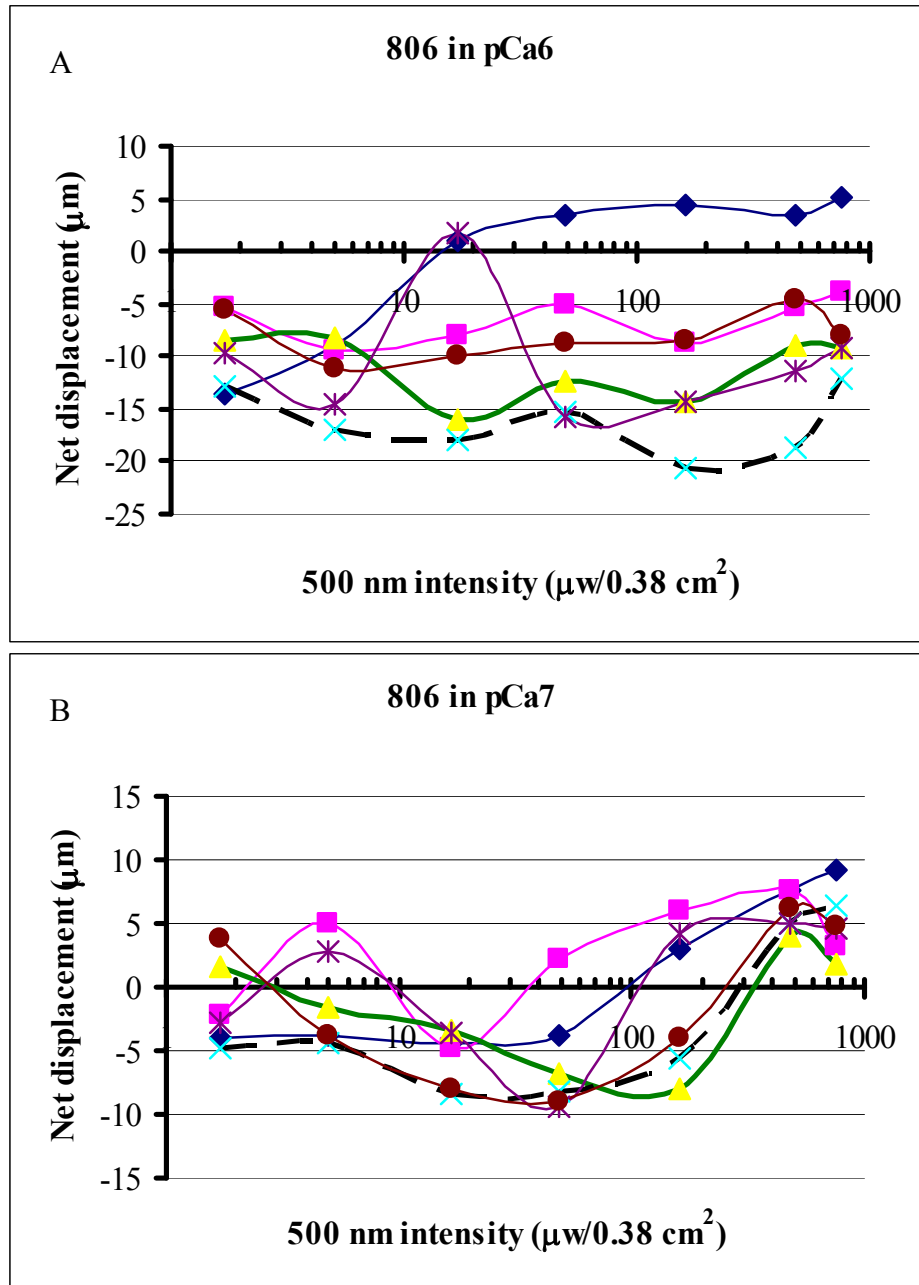


Figure 4.17 Net displacement vs. green-light intensity and red light as background illumination (633 nm) with various intensities: 0, 3.97, 31.55, 125.59 and 500  $\mu\text{w}/0.38 \text{ cm}^2$  of 806 strain in pCa 6 (A) and pCa7 (B). Cells were grown in HSM liquid media and suspended in 0.05 mM  $[\text{Ca}^{2+}]$  of NMM overnight. Note: legend is the same as Figure 4.16.

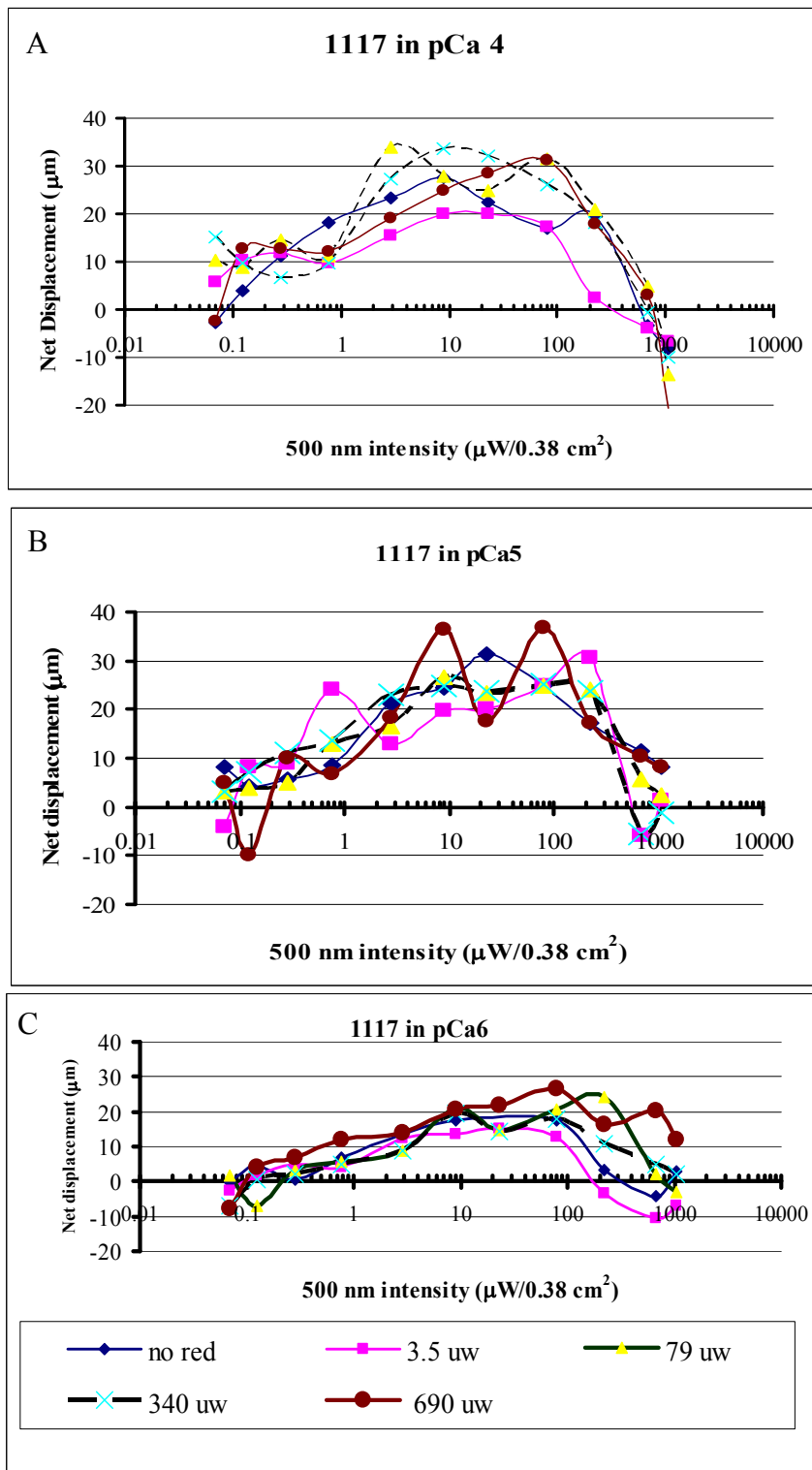


Figure 4.18 Net displacement vs. green-light intensity and red light as background illumination (633 nm) with various intensities: 0, 3.97, 31.55, 125.59 and 500  $\mu\text{w}/0.38 \text{ cm}^2$  of 1117 strain in pCa 4, pCa5, and pCa6 (A, B, and C respectively).

## 4.4 Conclusions

Photosynthetic process uses light to produce energy for the cell, increases  $H^+$  concentration in lumen compartments (inside thylakoid), and depolarizes the membrane potential. Therefore, increasing external  $H^+$ ,  $K^+$  and  $Ca^{++}$  concentration should increase the membrane potential making the cell even more depolarize, however the cells behaved differently. What is the main ion controlling phototaxis? Due to a variety of ion channels such as  $H^+/K^+$  antiport,  $2H^+/Ca^{++}$  antiport,  $H^+$  pump cross membranes which control ion transportation, each ion movement will affect another. In addition, cells have mechanism to control each ion in order to survive and keep system in equilibrium (homeostasis). All of these parameters might control only one parameter which is membrane potential either through the ion channels or pumps. This process can also be triggered by the internal or chemical signal within cells. There is a tight connection between organelle's function and control of plasma membrane's proteins such as channels and pumps.

$H^+$  and  $K^+$  drove phototactic responses of both *806* and *1117* strains in the same direction even though generally they have opposite responses to the light. Increasing of external  $H^+$  concentration decreased and increasing of external  $K^+$  concentration increased positive phototaxis to green light. On the other hand, high  $[Ca^{2+}]_{ext}$  drove each strain in the opposite direction. Increasing  $[Ca^{2+}]_{ext}$  decreased and increased positive phototaxis in *806* and *1117* strain respectively. In addition to green light, red light was used and the results depended on red-green intensity and  $[Ca^{2+}]_{ext}$ . See Table 4.3.

Level of Ion concentration or red light intensity	Positive phototactic responses in each strain	
	806	1117
Ca <sup>++</sup> ↑	↓	↑
H <sup>+</sup> ↑	↓	↓
K <sup>+</sup> ↑	↑	↑
Red (633 nm) ↑	in pCa 6-7 ↓ pCa4-5 ↑	Unclear

Table 4.3 Show the effects of the ionic concentration and red light in both *806* and *1117* strain. (Note: K<sup>+</sup> concentration results came from Olivia Sim's experiments which use KCl to vary potassium ions in media.)

Sign of phototaxis and its magnitude may be explained by using the ratio of the integral area between the first electrical current (E<sub>1</sub>) and the second electrical current (E<sub>2</sub>) or the E<sub>1</sub>/E<sub>2</sub> ratio. The higher the E<sub>1</sub>/E<sub>2</sub> ratio, the more negative the phototaxis.

To further test this suggestion, both phototactic and electrical measurement should be observed in a parallel manner. Measuring the membrane potential change will also help confirm the previous reports on hyperpolarization and depolarization at each condition such changing of extracellular ion concentration since each strain or cell behaves differently. The membrane potential regulated phototactic responses, the actual value of membrane potential in each condition should be measured as well as the internal and external ionic concentration.

# Chapter 5

## The electric field technique

---

### 5.1 Introduction

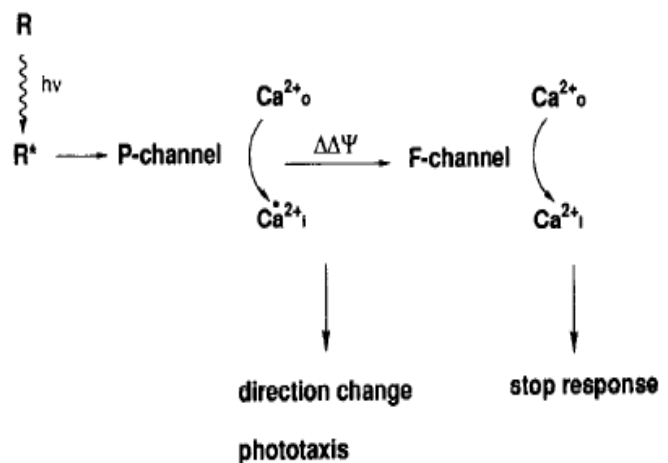
In previous chapters, we studied ciliary motility and phototaxis behaviors in order to find the response patterns triggered by rhodopsin receptors (Foster and Smyth, 1980; Kröger and Hegemann, 1994) and other photoreceptors and used them to create a model of cell decision making. In this chapter, we focus on identifying an interconnection between behavioral responses and rhodopsin excitation. We hypothesize that this interconnection is the membrane potential change.

In 1994, Kröger and Hegemann suggested a rhodopsin reaction scheme (See Figure 5.1) that the rhodopsin excitation induces the opening of the photoreceptor channel: calcium channels overlying the eyespot (P-Channel). Therefore, rhodopsin excitation causes depolarization of the membrane potential leading to cell steering and phototaxis. Their suggestions were based on photocurrent measurements using the suction pipette technique (Harz and Hegemann, 1991). Light excitation depolarizes the membrane overlying the eyespot leading to a phototaxis and also the ciliary membrane (F-Channel) leading to a “stop” or

photophobic response (Harz et al., 1992; Kröger and Hegemann, 1994).

Figure 5.1.

The rhodopsin excitation scheme of Kröger and Hegemann (1994).



Based on whole-cell clamping and measuring photocurrents, Nonnengasser et al. (1996) suggested that the rhodopsin excitation induces not only the opening of calcium channels on the eyespot, but also the opening of other monovalent channels such as  $K^+$ ,  $NH_4^+$ , and  $Na^+$  on the membrane. See Figure 5-2 for their photocurrent experiment model.

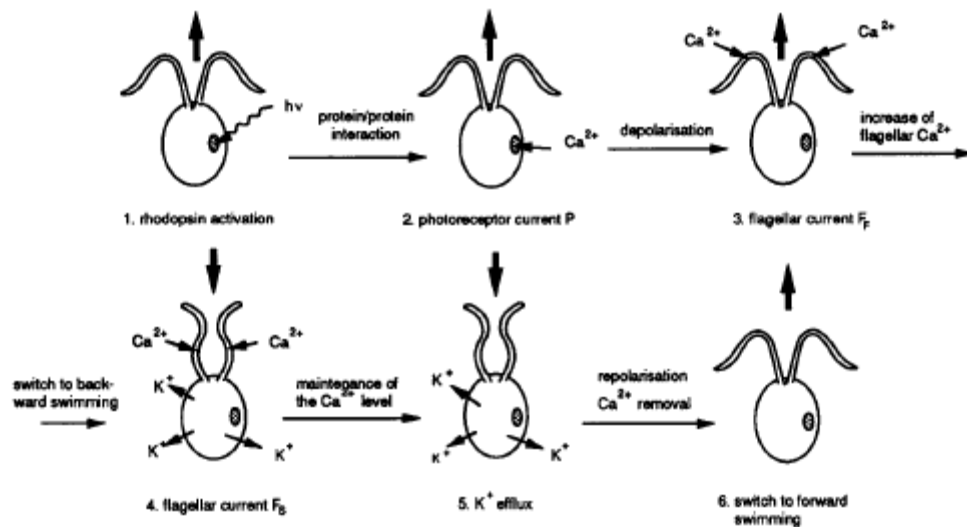


Figure 5.2. The proposed relationship among rhodopsin receptor, ion exchange, membrane potential and ciliary motility in the cell-wall-deficient mutant (CW2) of *Chlamydomonas reinhardtii* derived from experiments using whole-cell clamping. By stimulating the eyespot with the light, the  $Ca^{2+}$  channels on the eyespot are activated. This  $Ca^{2+}$  influx depolarizes the membrane potential within a few milliseconds and via a  $Ca^{2+}$  action potential initiates  $Ca^{2+}$  influx along cilia. Cells then adjust their membrane potential level by  $K^+$  efflux that brings the potential back to the resting membrane potential level (Nonnengasser et al., 1996).

Previous studies showed that membrane potential change is one of the main factors for signaling in *Chlamydomonas*, but no one has directly monitored this change dynamically due to the fast transient change of membrane potential and its small magnitude. In order to investigate this change, we decided to monitor it by using an electric field sensitive dye that intercalates into the membrane. Unlike with neurons, the microelectrode method is impractical to use with a unicellular cell green algae, because of its small size and hard wall. Sticking a microelectrode into *Chlamydomonas*'s membrane could rupture the membrane and collapse the membrane potential. In any case efforts to do this on a regular basis have proven problematic. Therefore, other methods have been suggested and the two most popular methods are whole cell clamping and fluorescence probes.

The whole cell clamping technique has been used to measure the photocurrent and its result can be related to the membrane potential change. This technique has several concerns as the following. First of all, a cell is held by a micropipette which has to apply a negative pressure in order to hold a cell in place. This can activate mechanoreceptors on the cell body (Yoshimura, 1998). Second, a cell has to be demembrated or be a wall-deficient mutant such as *Chlamydomonas* CW2 strain (not really completely wall deficient). Even though, these specific cells were chosen for experiments, getting a good seal is still very difficult. Therefore, results from this technique do not represent cells in their natural condition. Thus, using the fluorescence probes seem to be a good approach for our purpose to avoid the above problems.

A variety of fluorescence probes has been used to measure the membrane potential, but the styryl dyes are the most sensitive of the fast probes (millisecond change

with 10% fluorescence change per 100 mV as described on <http://www.invitrogen.com>). This class of dye was developed by Fluhler and colleagues (1985) and has been widely used with many kinds of cells and membrane vesicles to measure the electric field (Montana et al., 1989 and Loew et al., 1992). The advantage of this technique is that it allows long term measurement and high temporal resolution of the electric field. We chose the voltage-sensitive dye di-8-butyl-amino-naphthyl-ethylenepyridinium-propyl-sulfonate (di-8-ANEPPS) which is less susceptible to internalization than other dyes. Furthermore, this technique can be combined with a cell suspension technique (current measurement) which allows us to monitor the photoreceptor or flagellar current (PC and FC respectively) simultaneously in the future.

This chapter explains the characteristics of the di-8-anepps dye, the concept and design of electric field measurement, fluorescence stained technique, primarily results, discussion and suggestion for future improvements.

## **5.2 Characteristics of the voltage-sensitive dye di-8-butyl-amino-naphthyl-ethylenepyridinium-propyl-sulfonate (di-8-ANEPPS)**

The voltage-sensitive dye di-8-butyl-amino-naphthyl-ethylenepyridinium-propyl-sulfonate (di-8-ANEPPS) is hydrophilic. Therefore it is permeable to a lipid membrane and binds locally. See Figure 5.3 for its chemical structure and spectra. According to an electrochromic mechanism or Stark effect (Gross et al., 1994), this dye responds to the change of electric field at the binding site in the lipid bilayer by shifting both excitation

and emission wavelength (See Figure 5.3 B for its spectral shift). The spectral shift,  $\Delta\nu$ , can be calculated as the following equation (Gross et al., 1994).

$$\Delta\nu = -(1/h)\Delta\bar{\mu} \cdot \vec{E} - (1/2h)\Delta\alpha E^2 \quad (5.1)$$

where  $\Delta\bar{\mu}$  is the excitation change of electric dipole moment of chromophore,  $\Delta\alpha$  is the excitation change of polarization,  $h$  is the Planck's constant and  $\vec{E}$  is the electric field vector at the location of chromophore.

**A.**

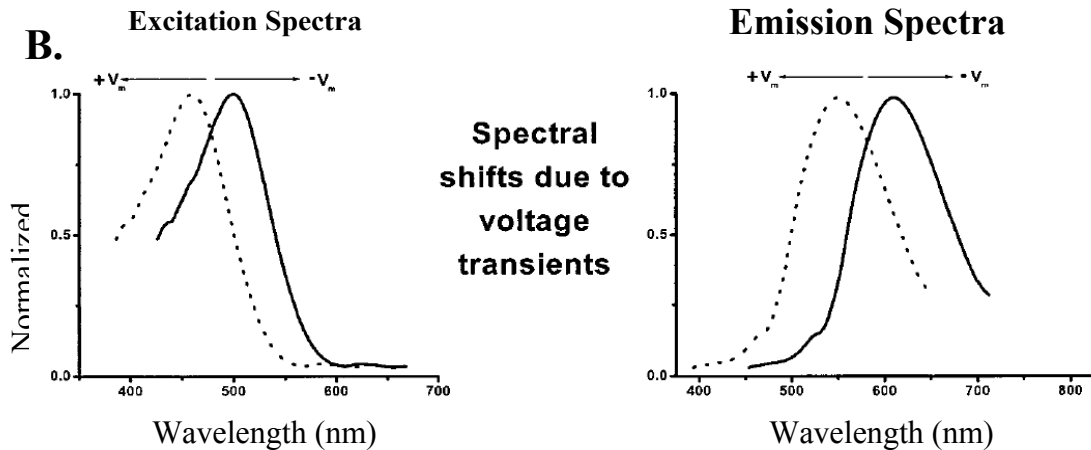
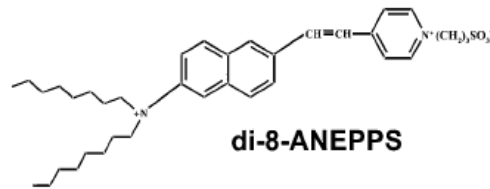


Figure 5.3. Show the structure of the voltage-sensitive dye di-8-butyl-amino-naphthyl-ethylenepyridinium-propyl-sulfonate (di-8-ANEPPS) (A) and the excitation and Emission Spectra of di-8-anepps dye dues to the electric field changes (B) by Bullen and Saggua (1999).

### 5.3 Methods and measurements

The dye characteristic allows us to monitor the relative change of the emission ratio (R) for two different wavelengths. In this project, the cell population is excited alternately at 3.2 kHz (to detect the transient change in a few milliseconds) with two excitation wavelengths which are 476 nm (avoids chlorophyll excitation) and 488 nm while the emission wavelength is recorded at 600 nm with bandwidth of 20 nm (Figure 5.4). Then we excited rhodopsin receptors with 514 nm which will change the electrical properties of cell membrane.

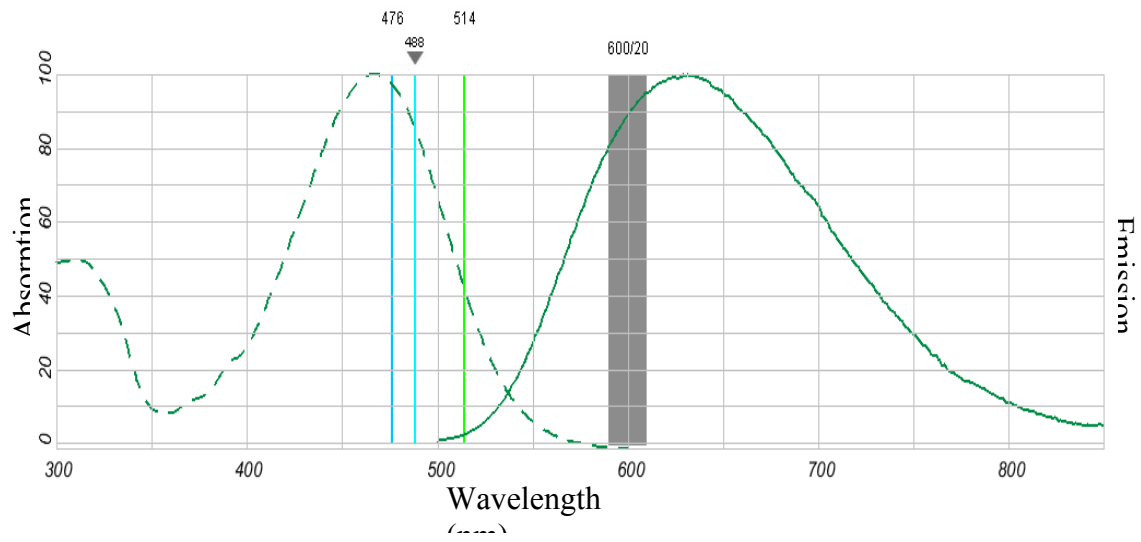


Figure 5.4. The spectra of di-8-Anepps, the dual excitation wavelength (476 nm and 488 nm) and the emission wavelength (600 nm with 20 nm bandwidth). The emission ratio ( $R=I_{476}/I_{488}$ ) is about 2.5 from this spectra. If the spectrum is shifted due to the rhodopsin excitation, this ratio should change relatively to the shift of electric field or membrane potential change. (The plot was created by using Fluorescence SpectraViewer from <http://www.invitrogen.com>.)

### 5.3.1 *Staining Method*

*C. reinhardtii* cells, both 1117 and 806, are grown in a liquid high salt media (HSM) for 3-4 days in order to get thinner cell-wall cells and they are kept under white light illumination at a controlled temperature of 18 °C. This protocol is modified from the Invitrogen company's protocol. The first step is to count cells with a hemocytometer and prepare them to a final concentration of  $3\text{-}5 \times 10^6$  cells/ml. Then the cells are spun down and resuspended in nitrogen-deficient minimal medium (NMM) and the first step is repeated. Cells were then shaken at 120 rpm while illuminating them with white light for 20 minutes. At this stage, cells shed their cell wall due to the change of medium from HSM to NMM. In order to increase the binding possibility of the dye to plasma membrane lipid bilayer, autolysin enzyme can be added at this step. Then cells were separated into 2 aliquots of 1 ml and labeled as a control sample and a stained sample. To increase the dye solubilization 5  $\mu\text{l}$  of 0.1% Pluronic F-127 and 4  $\mu\text{l}$  of Dimethyl Sulfoxide (DMSO) was added to both samples. Finally, 8  $\mu\text{M}$  or 16  $\mu\text{M}$  di-8-Anepps dye was added to the stained sample. Both the control and stained samples were then wrapped with foil to protect them from light and incubated at low temperature, 4-20 °C, for 30 to 60 minutes to inhibit internalization of the dye. The final step was to wash away the excess dye with NMM 1 ml for 2 times before the fluorescence emission or the membrane potential change was measured. See Figure 5-5 for the protocol diagram.

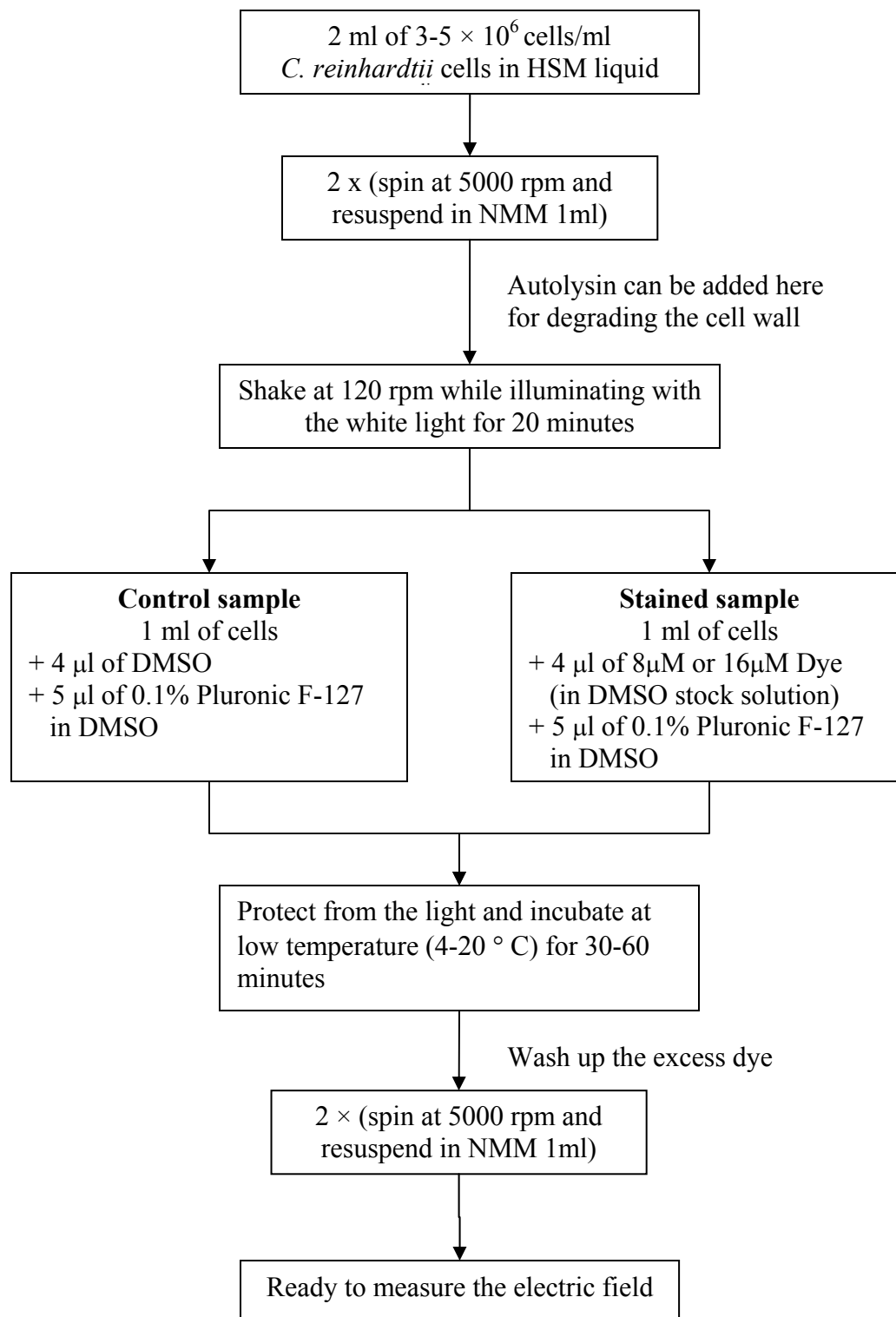


Figure 5.5. Protocol for loading the di-8-ANEPPS dye to the cells

### 5.3.2 *Experiment Setup*

We use the 210 Air-cooled argon laser (450-515nm, H210ALdiiD, National Laser Comp., Salt Lake City, UT) as our excitation light source. It has a maximum power of 500 mW and its beam diameter is  $0.67 \pm 5\%$  mm which is expanded to a uniform field and a larger diameter by using a 20×lenses expander. We control its intensity and select its wavelength by using a Polychromatic Acousto-Optic Modulator or PCAOM and its driver (AA.AOTF.nc and AA.MOD.nc respectively, Electro-Optical Product Corp., Fresh Meadows, NY) through the computer program (Ciliary Monitoring program written and developed by Ganesh Sanrinivan, Tavier Hawkins, and Suphatra Adulrattananuwat) and the digital output board (PDL-DIO 64T, United Electronic Industries, Inc., Walpole, MA). See the set up in Figure 5.6 A and B.

The excitation intensity depends on the distance from the 20×lenses expander to the cell chamber (See inside of the cell chamber in Figure 5.7). Since we do not know what the appropriate intensity is for the dye excitation intensity, we set this distance at about 50 cm which gave the maximum intensity at 476 nm. The Argon laser produces the less intensity at 476 nm than at 488 nm. The 476 nm and 488 nm intensity should be adjusted so that they give the same response amplitude on the dyed cells. This will allow us to see the effect due to the 514-nm light exciting the rhodopsin receptors. The intensity can be also adjusted by using the PCAOM remote control by adjusting its power on each line or channel. The emission light from the cells passes the sample box and is filtered with the bandwidth filter ( $600 \pm \text{nm}$ ) in front of the photomultiplier or PMT (C31034, BURLE electron tubes, Lancaster, PA) enclosing in the water-cooled chamber (TF104TSRF, Products for Research, Inc., Danvers, MA). See Figure 5.8 for schematic

of electric field measurement. The temperature controller (Products for Research, Inc., Danvers, MA), the water-flow switch (FS-4, P/N: 44729, Gems Sensors & Controls, Plainville, CT) and the solid-state relay (A1210, Crydom, San Diego, CA) control the PMT operating temperature at -20 °C. This reduces a dark noise rate of the anode dark current to 60 counts per second. The maximum DC operating voltage of PMT is **2200 V (APPROPRIATE PRECAUTIONS!!!)** supplied by the high voltage supply (PS 325/2500V-25W, Stanford Research System, Inc., Sunnyvale, CA. the operating current is about 0.25 mA) by using the **negative** voltage on the cathode. The current response signal from the anode is directly connected to the Lock-In Amplifier (SR530, Stanford Research Systems Inc.). See Figure 5.6 B.

The response signal from PMT is the current signal (I) and the Lock-In Amplifier converts it into a voltage with a gain of  $10^6$  V/A (the maximum current input of 10 mA will damage the unit). This Lock-In Amplifier is locked in to the 3.2 kHz square wave by using the same signal as the stimulus of the di-8-Anepps dye on the reference input. In order to detect the response signal, the suggested selections on the front panel of the Lock-in Amplifier are the following.

Front Panel selections of the Lock-In Amplifier:

1. Signal Inputs: Current (I)
2. Signal Filters: Bandpass, Q-of-5 Auto-tracking filter (In or Out)
3. Sensitivity: 100 - 500 mV
4. Display: Channel 1 → R (magnitude) → Output BNC ( $\pm 10$  V for  $\pm$  full scale)  
Channel 2 → Ø (Phase) → Output BNC  
Output = (X/sensitivity -offset)×Expand×10V
5. Reference Input: 3.2 kHz at 4 V (100 mV minimum)

- 6. Reference Trigger: Trigger on rising edge
- 7. Mode PLL:  $f$  ( $\times 1$  of the reference input frequency)
- 8. Phase: 0 degree
- 9. Time Constants: Pre-filter ranges from 10-300 ms (6dB/Octave)  
Post-filter is None

Note: Time Constant is  $1/(2\cdot\pi\cdot f)$  where  $f$  is the interested signal frequency (or low pass frequency). In this case, the frequency is the same as the 514 nm stimulus frequency or the rhodopsin stimulating frequency. For example, if the 514 nm stimulus is sent out at 1 Hz, then the time constant should be set to  $1/(2\cdot\pi\cdot 1\text{Hz}) = 159$  ms. On the panel, the appropriate time constant can be from 30 to 300 ms depending on the noise level. The higher the time constant, the smoother the output signal becomes.

Finally, the output signal from the Lock-in Amplifier is recorded by the analog input board (PD2-MF 16-150/16H, United Electronic Industries, Inc.) through its external pin board. We use the differential method detecting the difference voltage between two external pins. For example, the different between pin AIn0 and AIn8 is recorded as the response signal of channel 1. See Table 5.1

Channels of Lock-in Amp.		Pin No. of PD2-MF 16-150/16H
1. Magnitude (R)	BNC (+)	AIn0 (Ch1)
	BNC (-)	AIn8 (Ch1)
2. Phase ( $\phi$ )	BNC (+)	AIn1 (Ch2)
	BNC (-)	AIn9 (Ch2)

Table 5.1 Pin connections between Lock-in Amplifier and analog input board. The voltage range of magnitude signal (R) is 0 to 5 V with gain of 4 where as -10 to 10 V with gain of 1 for phase ( $\phi$ ). Note: the phase voltage is 50 mV per degree (SR530 manual of the Lock-in Amplifier.)

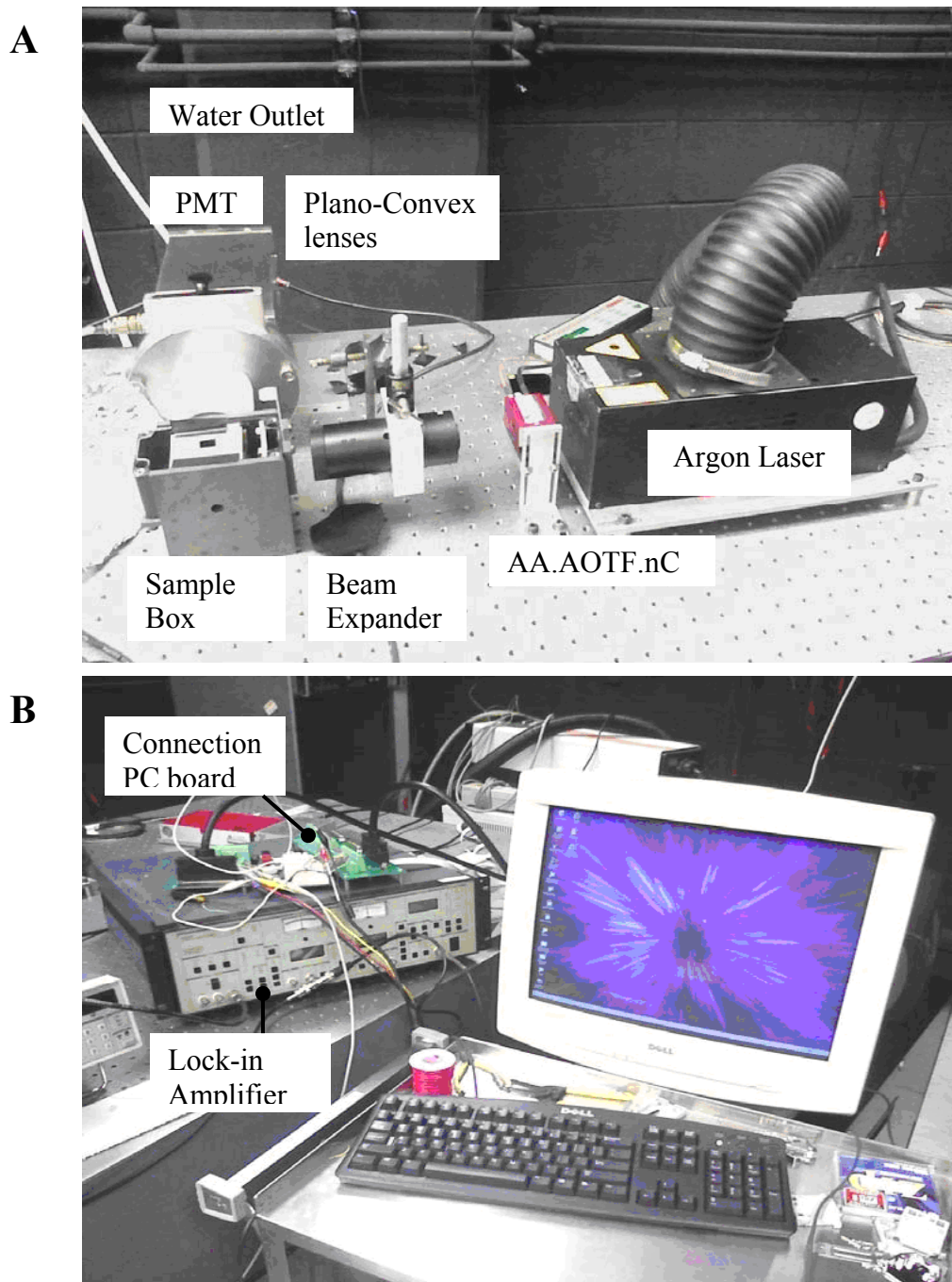
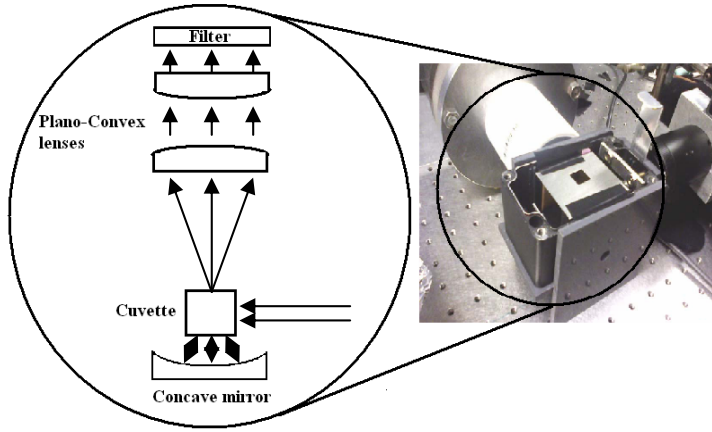


Figure 5.6. Show the electric field measurement setup which composes of A: Argon laser (H210ALdiiD), Polychromatic Acousto-Optic Modulator or PCAOM and its driver (AA.AOTF.nC and AA.MOD.nc respectively), Beam Expander, Sample Box, Plano-Convex lenses, Photomultiplier or PMT (C31034 Series), B: Lock-in Amplifier (SR530), preamplifier (SR445, not shown).

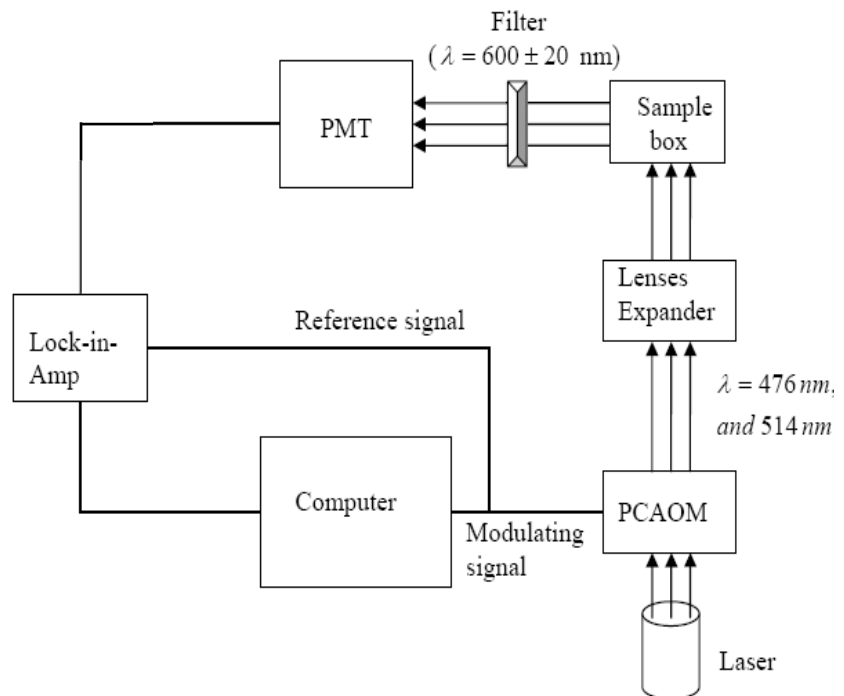
Figure 5.7. Show the inside of sample box and Plano-Convex lenses. The stimulus and modulated light pass through the small hole of sample box on the right and illuminate a cell sample within a rectangular cuvette. The emission light is then reflected by the concave



mirror, scattered to the Plano-Convex lenses and filtered with the wavelength of 600 nm.

Finally photomultiplier (PMT) receives the emission light.

Figure 5.8. Schematic of the electric field measurement. Laser is modulated by using Digital output board (PDL-DIO 64T) to obtain wavelengths at the peak of 476, 488, and 514 nm.



### 5.3.3 Operating the Ciliary Monitoring Program

The in-house software can be used for both Ciliary monitoring and Electric Field measurement, however the sampling frequency of the stimuli are different due to the high frequency square wave that we use for stimulating the dye at 3.2 kHz. Each stimulus is sent out as a digitized signal at 12.8 kHz. Figure 5.9 shows an example of stimulus files of two wavelengths.

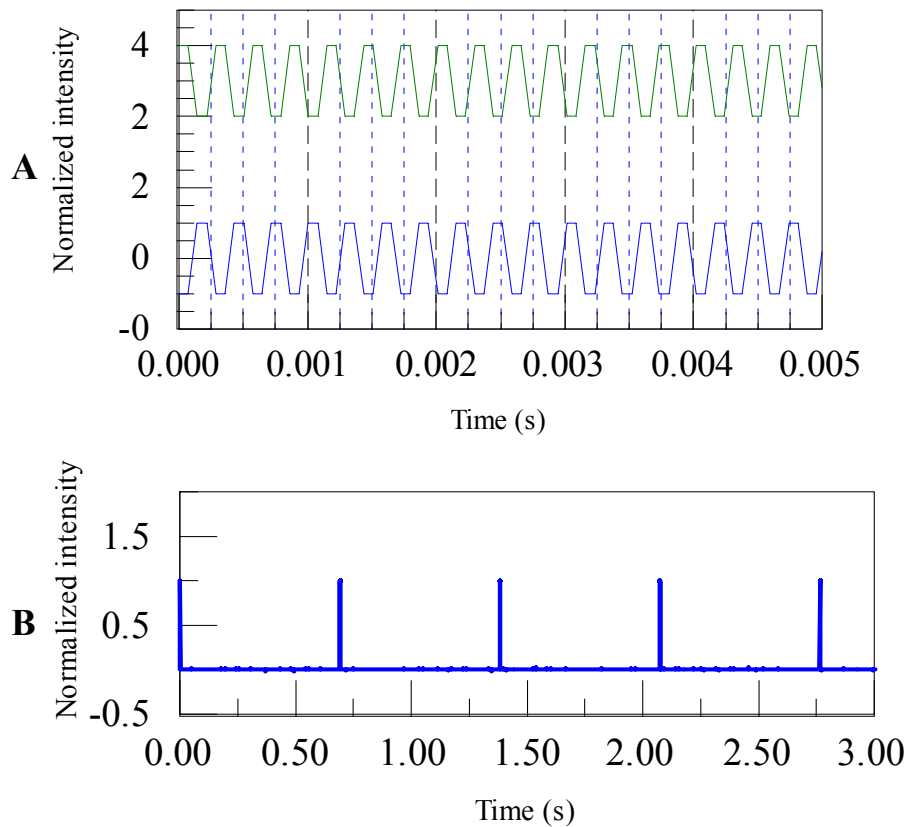


Figure 5.9. Show laser light stimulus patterns. Figure A is the two modulating signals exciting the fluorescence dye with the wavelength of 476 nm and 514 nm at frequency of 3.2 kHz. The phase difference between them is 180 degree. Figure B is the impulse stimulus pattern (514 nm) which is used to stimulate the rhodopsin receptor to initiate the change of membrane potential or an electric field.

## 5.4 Results and Discussions

- Loading of dyes on the cell membrane

After loaded the di-8-anepps dyes to cells, dyes did not completely bind to all the plasma membrane (Figure 5.10). This could be because of remaining parts of cell-wall and this dye only binds to lipid membrane. This incomplete labeling will reduce the sensitivity of our measurement. In order to get a more optimum load condition, several parameters such as dye concentration, temperature, and dye-loading time should be adjusted.

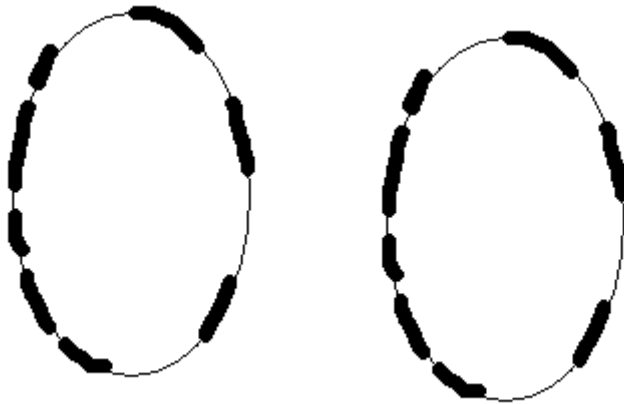


Figure 5.10. An example of a loaded single cell with the fluorescence dye (cilia are not shown).

- Recorded signals

We stimulated the loaded-cell population with 2 ms pulse-duration of green light (peak at 514 nm) with background modulation of both 514 nm and 476 nm at 3.2 kHz. Modulating light at high frequency (3.2 kHz) should not affect observation of the response of rhodopsin excitation at a lower frequency. Figure 5.11 and Figure 5.12 are examples of recorded signals from the Lock-in amplifier. According to Figures 5.11, changing dye concentrations do not show any different than the control sample or a cell without dye. Since there is no change, we further tested whether or not this is not due to our equipment sensitivity.

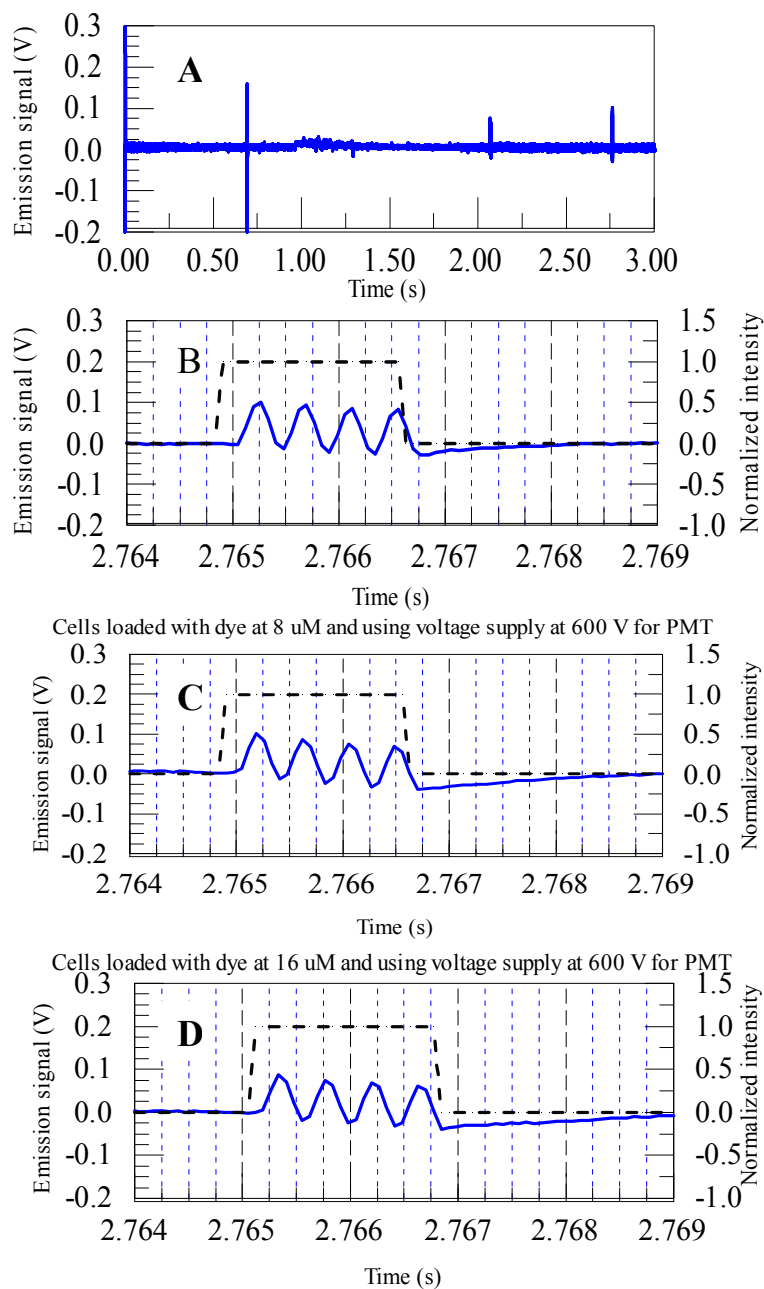


Figure 5.11. A recorded signal of different dye concentrations from Lock-in Amplifier with 600 V supplied to photomultiplier (A: a control sample on a large scale, B: a control sample on a small scale, C: a loaded sample with dye 8  $\mu\text{M}$ , C: a loaded sample with dye 16 $\mu\text{M}$ ).

Increasing the supply voltage to the photomultiplier enhanced the sensitivity to our recorded signal as seen in Figure 5.12. However, we still did not see any change of signal patterns comparing to a control sample. The fluctuating signals during the “2 ms pulse-duration” come from different emission intensity of 514 and 476 nm since it has the same frequency as our high frequency.

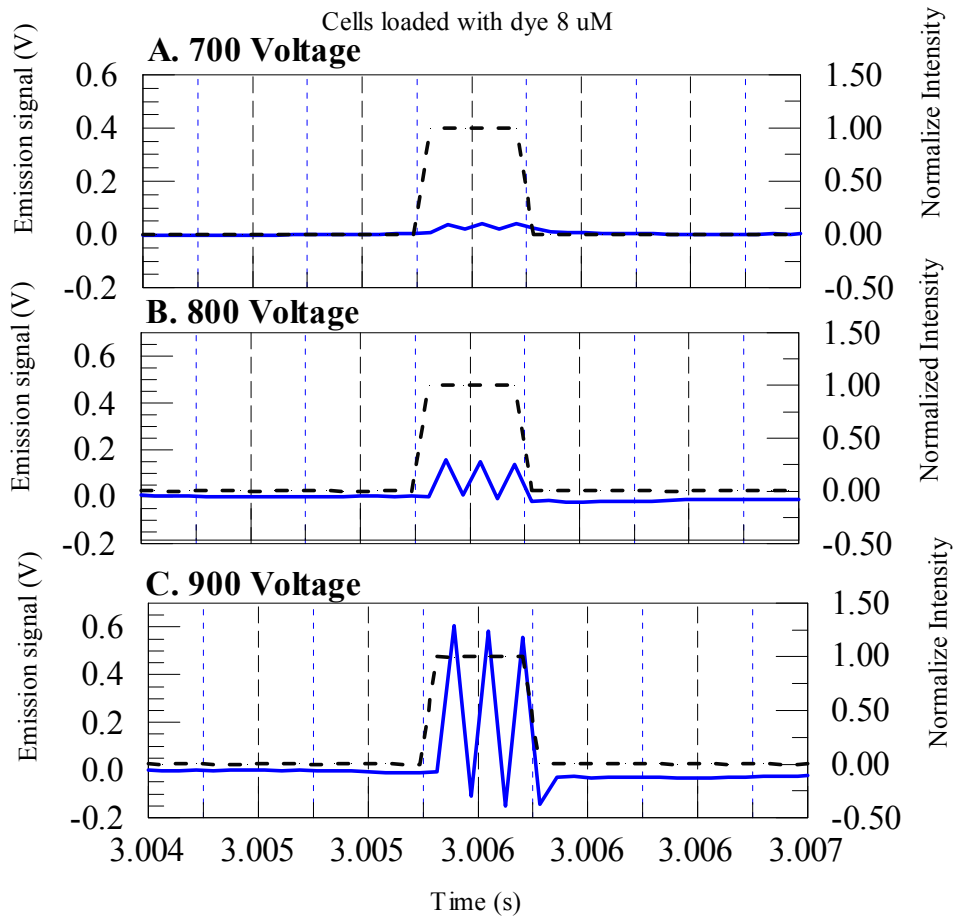


Figure 5.12. Lock-in amplifier signals of cells loaded with dye at 8  $\mu\text{M}$ . Different voltages were used on photomultiplier including A: 700, B: 800 and C: 900 V.

## 5.5 Conclusions

The primary results indicate we have not yet succeeded in measuring the electric field response and the method needs further development. Suggestions follow.

### 5.5.1 Cells

Due to its motility, observing the dye loading quantitatively is difficult. Therefore, using the paralyzed mutant of *Chlamydomonas reinhardtii* which lacks the central pair, pf18, could help in finding the optimum protocol for dye loading. The cell wall remains a barrier for dye binding to lipid membrane. The cell wall is made of high molecular carbohydrate and hydroxyproline-rich protein (glycoprotein). Therefore, finding the proper time during the cell wall shredding period to load fluorescence dyes could be crucial to incorporating the maximum amount of dye.

Use other cells that have a good loading condition to test the equipment to measure that the system is working properly.

### 5.5.2 Fluorescence dyes

Cells are autofluorescent. At this moment the di-8-Anepps is the appropriate dye to use. However, a voltage-sensitive dye with an emission wavelength that is far from the autofluorescence peak may be available in the future.

### 5.5.3 Devices and Instruments

In order to increase the signal-to-noise ratio (SNR), signal amplification and voltage supply can be adjusted to get the optimum value. Besides the SNR, we could reduce a complication for analysis and interpretation by using two photomultipliers. Currently we use only one photomultiplier to record the emission wavelength from both the 476 nm and 488 nm excitation. The recorded signal was a combination of two signals

and it was hard to identify or adjust the sensitivity of instrument in order to detect a small change.

#### *5.5.4 Auto-fluorescent emission*

*Chlamydomonas* emits the red light due to photosynthetic excitation which we do not want it to interfere with our electric field measurement. Therefore, we recorded the auto-fluorescent emission as a background and filtered it with a 600 nm-filter (Figure 5.7).

#### *5.5.5 Correction to use the in-house software at a higher sampling rate like 11 kHz*

Shifting of the stimulus for several reasons:

- The clock divider = 33 MHz/sampling frequency or refresh rate. Originally the refresh rate was set to 12800 Hz as a maximum value. However, this made the CV to be a non-integer value and it would not give the exact frequency as 12800 Hz. Therefore the sampling rate had to be changed to a number that is an integer multiple of 11 or 3. In this case, we choose 11000 Hz which is close to 12800 Hz.
- Even though changing this value reduces the shifting data point, the signal still shows unstable shifting point. A possible solution is to start filling the digital output buffer for several points before Analog-Input buffer (AI buffer). Then add the dummy value 0 at the beginning of AI buffer. At the end wrap the DO buffer tail with extra points equal to the number of dummy value.

Note: This still show a delay of 1 ms if recorded for 2 minutes.

# Chapter 6

## Summary and conclusions

---

This thesis used *Chlamydomonas reinhardtii* as a model organism to understand cell signaling pathways and their dynamics. Various techniques including the single-cell monitoring system, the cell-tracking, system and the electric field technique have been used to study cell responses such as ciliary responses, phototaxis, and electric field responses respectively.

The single-cell monitoring system was previously developed by Josef et al. (2005a and b). We improved this technique (Chapter 2) by expanding the bandwidth response to measure the beating frequency of mutant (to less than 30 Hz. See Figure 2.3 for the detector response spectrum), using up-to-date electrical components for easy replacement, increasing the recording resolution from 0.25 ms to 0.078 ms for future experiments such as white-noise experiments, and improving the recording software with C++ language.

With this technique, we further investigated red light effects on ciliary motility of both *806* and *cpc1-2* strain (Chapter 3). Red light effects on the *806* strain were previously studied with pulse-stimuli by Josef (2005). Red light excites the chloroplast and it regulates ciliary responses including beating frequency (BF) and stroke velocity (SV). We used various stimulus patterns such as continuous, pulse, and multi-sinusoidal stimuli to stimulate the cell. With the continuous red-light and pulse green-light stimuli (Figure 3.21), red light interrupts green-light phototaxis signaling pathway and possibly inhibits its responses. Using various stimulus patterns allows us to understand how the

cell processes red-light as an input and we used the output, BF and SV responses, to create a hypothesized diagram of red-light signaling pathway. The *cpc1-2* results represent how input signal is processed within the cell without 3PG conversion to ATP in ciliary compartment. With this in mind, *cpc1-2*'s multi-sinusoidal responses show a characteristic of differentiation (See Figure 3.46). Therefore, the differentiation should happen within the cell body which we hypothesize is in the chloroplast compartment. The red-light signal is differentiated and converted linearly to chemical molecules such as 3PG and NADPH. The delay time probably due mostly to diffusion is estimated to be about 400 ms (from the Bode plot of *cpc1-2* strain on Figure 3.41) and approximately linear (Figure 3.45). The *806* results represent how input signal is processed as a whole system. BF responses are non-linear (Figure 3.33) and their positive (negative) responses have a delay time of 1.18 s (0.89 s) (Figure 3.34). Therefore, the total delay time possibly due to synthesis of ATP is approximately 800 ms (the positive response delay). In addition to a delay time, we also found that the system has a tight regulation of beating frequency around 50 Hz (Figure 3.29 and 3.30). This tight regulation suggests that the system uses negative feedback control. When it breaks down, the input signal is amplified which gives us a clue that the system also has a positive feedback (Figure 3.44). In addition, it has a separate control for BF and SV responses.

We used the cell-tracking system to monitor phototaxis of both *806* and *1117* strain (negative and positive phototactic strain respectively). Phototaxis depends on various parameters including light, ions and temperature. In chapter 4, we investigated the effects of external ion concentration ( $\text{Ca}^{2+}$ ,  $\text{H}^+$ , and  $\text{K}^+$ ) and red light on phototaxis. Increasing of  $[\text{H}^+]$  and  $[\text{K}^+]$  decreased and increased positive phototaxis of both *806* and

1117 respectively. While increasing of  $[Ca^{2+}]$  decreased positive phototaxis in 806, it increased positive phototaxis in 1117. Red light tends to increase positive phototaxis in 806 under pCa4 (calcium concentration of growing solution), but red light effects are unclear in 1117. The sign of phototaxis could possibly be controlled by one parameter such as a membrane potential or a ratio of integral area between the first electrical and the second electrical current ( $E_1/E_2$  ratio) according to Capano's results (unpublished).

In order to understand the interconnection between behavioral responses such as ciliary responses and phototaxis or rhodopsin excitation, the electric field technique is developed (Chapter 5). Rhodopsin excitation changes the membrane potential, but no one monitors this change dynamically. Therefore we developed the electric field technique using the voltage-sensitive dye di-8-butyl-amino-naphthyl-ethylenepyridinium-propyl-sulfonate (di-8-ANEPPS) as an indicator and the dual excitation wavelength (476 nm and 488 nm) as stimuli. The emission wavelength (600 nm) is recorded. The technique requires further development and needs to be improved in several aspects including optimizing dye-loading conditions, reducing autofluorescence emission, and optimizing excitation intensity.

Last but not least, these techniques and results could be further investigated and integrated in order to understand cell signaling pathways of *Chlamydomonas reinhardtii* as a whole system.

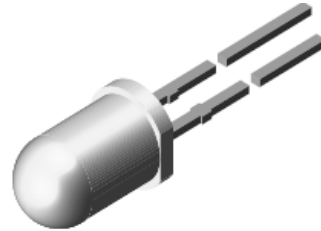
# Appendix

## A. Infrared Emitting Diode (TSFF5200)<sup>1</sup>

### Description

TSFF5200 is a high speed infrared emitting diode in GaAlAs on GaAlAs double hetero (DH) technology, molded in a clear, untinted plastic package.

The new technology combines the high speed of DH-GaAlAs with the efficiency of standard GaAlAs and the low forward voltage of the standard GaAs technology.



94 8990

### Features

- High modulation bandwidth (35 MHz)
- Extra high radiant power and radiant intensity
- Low forward voltage
- Suitable for high pulse current operation
- Standard T-1 $\frac{3}{4}$  ( $\varnothing$  5 mm) package
- Angle of half intensity  $\phi = \pm 10^\circ$
- Peak wavelength  $\lambda_p = 870$  nm
- High reliability
- Good spectral matching to Si photodetectors
- Lead-free component
- Component in accordance to RoHS 2002/95/EC and WEEE 2002/96/EC

### Applications

Infrared video data transmission between Camcorder and TV set.

Free air data transmission systems with high modulation frequencies or high data transmission rate requirements.

### Absolute Maximum Ratings

$T_{amb} = 25^\circ\text{C}$ , unless otherwise specified

Parameter	Test condition	Symbol	Value	Unit
Reverse Voltage		$V_R$	5	V
Forward current		$I_F$	100	mA
Peak Forward Current	$t_p/T = 0.5$ , $t_p = 100 \mu\text{s}$	$I_{FM}$	300	mA
Surge Forward Current	$t_p = 100 \mu\text{s}$	$I_{FSM}$	1	A
Power Dissipation		$P_V$	250	mW
Junction Temperature		$T_J$	100	$^\circ\text{C}$
Operating Temperature Range		$T_{amb}$	- 25 to + 85	$^\circ\text{C}$
Storage Temperature Range		$T_{stg}$	- 25 to + 85	$^\circ\text{C}$
Soldering Temperature	$t \leq 5$ sec, 2 mm from case	$T_{sd}$	260	$^\circ\text{C}$
Thermal Resistance Junction/ Ambient		$R_{thJA}$	300	K/W

<sup>1</sup> www.vishay.com

## Electrical Characteristics

$T_{amb} = 25\text{ }^{\circ}\text{C}$ , unless otherwise specified

Parameter	Test condition	Symbol	Min	Typ.	Max	Unit
Forward Voltage	$I_F = 100\text{ mA}$ , $t_p = 20\text{ ms}$	$V_F$		1.45	1.6	V
	$I_F = 1\text{ A}$ , $t_p = 100\text{ }\mu\text{s}$	$V_F$		2.5	3.0	V
Temp. Coefficient of $V_F$	$I_F = 100\text{ mA}$	$TK_{V_F}$		-2.4		mV/K
Reverse Current	$V_R = 5\text{ V}$	$I_R$			10	$\mu\text{A}$
Junction capacitance	$V_R = 0\text{ V}$ , $f = 1\text{ MHz}$ , $E = 0$	$C_J$		160		pF

## Optical Characteristics

$T_{amb} = 25\text{ }^{\circ}\text{C}$ , unless otherwise specified

Parameter	Test condition	Symbol	Min	Typ.	Max	Unit
Radiant Intensity	$I_F = 100\text{ mA}$ , $t_p = 20\text{ ms}$	$I_e$	80	160	400	mW/sr
	$I_F = 1\text{ A}$ , $t_p = 100\text{ }\mu\text{s}$	$I_e$	800	1600		mW/sr
Radiant Power	$I_F = 100\text{ mA}$ , $t_p = 20\text{ ms}$	$\phi_e$		40		mW
Temp. Coefficient of $\phi_e$	$I_F = 100\text{ mA}$	$TK_{\phi_e}$		-0.5		%/K
Angle of Half Intensity		$\varphi$		$\pm 10$		deg
Peak Wavelength	$I_F = 100\text{ mA}$	$\lambda_p$		870		nm
Spectral Bandwidth	$I_F = 100\text{ mA}$	$\Delta\lambda$		40		nm
Temp. Coefficient of $\lambda_p$	$I_F = 100\text{ mA}$	$TK_{\lambda_p}$		0.2		nm/K
Rise Time	$I_F = 100\text{ mA}$	$t_r$		10		ns
Fall Time	$I_F = 100\text{ mA}$	$t_f$		10		ns
Cut-Off Frequency	$I_{DC} = 70\text{ mA}$ , $I_{AC} = 30\text{ mA pp}$	$f_c$		35		MHz
Virtual Source Diameter		$\emptyset$		3.9		mm

## Typical Characteristics ( $T_{amb} = 25\text{ }^{\circ}\text{C}$ unless otherwise specified)

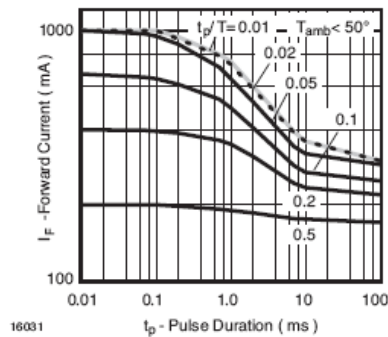


Figure 1. Pulse Forward Current vs. Pulse Duration

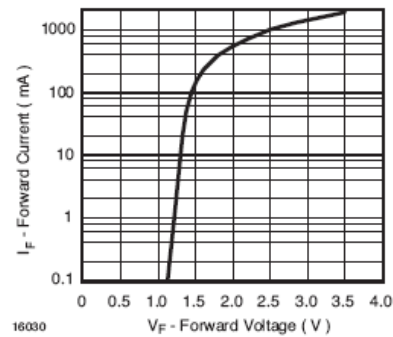


Figure 2. Forward Current vs. Forward Voltage

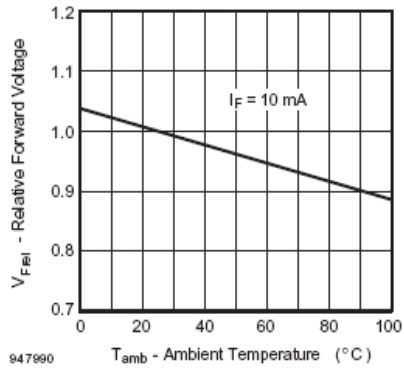


Figure 3. Relative Forward Voltage vs. Ambient Temperature

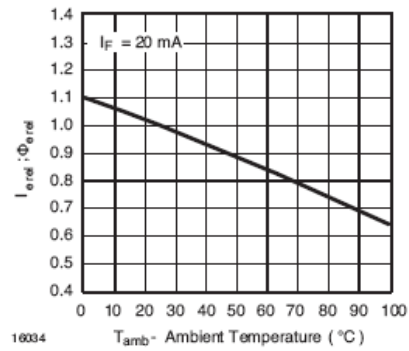


Figure 6. Rel. Radiant Intensity/Power vs. Ambient Temperature

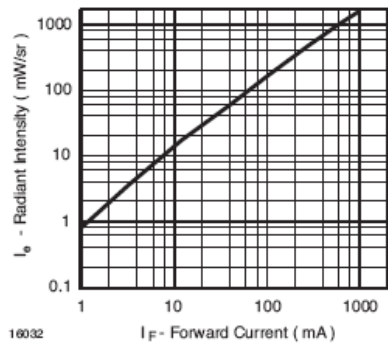


Figure 4. Radiant Intensity vs. Forward Current

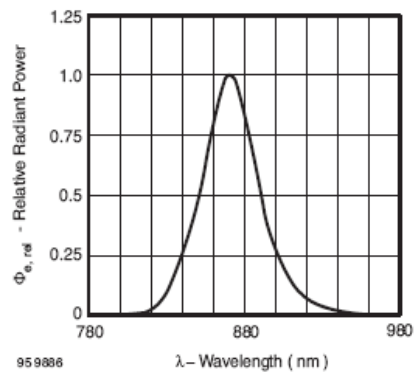


Figure 7. Relative Radiant Power vs. Wavelength

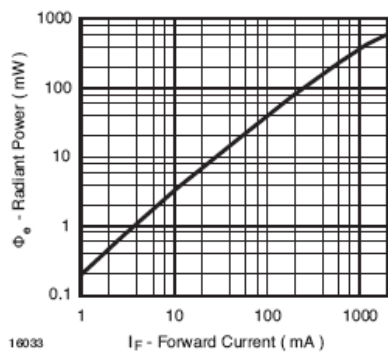


Figure 5. Radiant Power vs. Forward Current

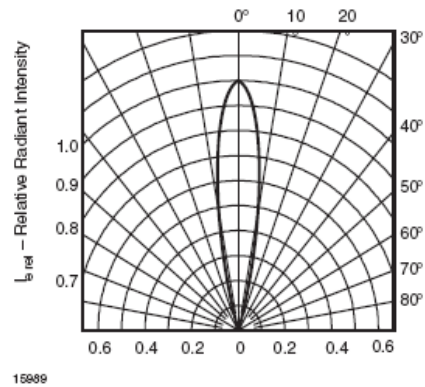


Figure 8. Relative Radiant Intensity vs. Angular Displacement

# B. Dual Low Noise Precision *Difet* OPERATIONAL AMPLIFIER<sup>2</sup>

---

## FEATURES

- LOW NOISE: 100% Tested,  $8\text{nV}/\sqrt{\text{Hz}}$  max at 10kHz
- LOW BIAS CURRENT: 4pA max
- LOW OFFSET: 500 $\mu\text{V}$  max
- LOW DRIFT: 2.8 $\mu\text{V}/^\circ\text{C}$
- HIGH OPEN-LOOP GAIN: 114dB min
- HIGH COMMON-MODE REJECTION: 96dB min

## DESCRIPTION

The OPA2111 is a high precision monolithic dielectrically isolated FET (*Difet*) operational amplifier. Outstanding performance characteristics allow its use in the most critical instrumentation applications.

Noise, bias current, voltage offset, drift, open-loop gain, common-mode rejection, and power supply rejection are superior to BIFET® amplifiers.

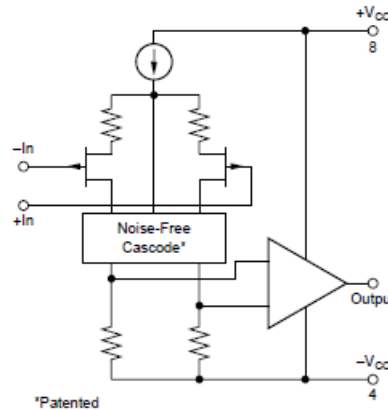
Very low bias current is obtained by dielectric isolation with on-chip guarding.

Laser trimming of thin-film resistors gives very low offset and drift. Extremely low noise is achieved with patented circuit design techniques. A cascode design allows high precision input specifications and reduced susceptibility to flicker noise.

Standard dual op amp pin configuration allows upgrading of existing designs to higher performance levels.

## APPLICATIONS

- PRECISION INSTRUMENTATION
- DATA ACQUISITION
- TEST EQUIPMENT
- PROFESSIONAL AUDIO EQUIPMENT
- MEDICAL EQUIPMENT
- DETECTOR ARRAYS



---

<sup>2</sup> Burr-Brown Corporation: [www.burr-brown.com](http://www.burr-brown.com)

# SPECIFICATIONS

## ELECTRICAL

At  $V_{CC} = \pm 15\text{VDC}$  and  $T_A = +25^\circ\text{C}$  unless otherwise noted

PARAMETER	CONDITION	OPA2111AM			OPA2111BM			OPA2111SM			OPA2111KM, KP			UNITS
		MIN	TYP	MAX	MIN	TYP	MAX	MIN	TYP	MAX	MIN	TYP	MAX	
<b>INPUT NOISE</b>														
Voltage, $f_O = 10\text{Hz}$	100% Tested		40	80		30	60		40	80		40		$\text{nV}/\sqrt{\text{Hz}}$
$f_O = 100\text{Hz}$	100% Tested		15	40		11	30		15	40		15		$\text{nV}/\sqrt{\text{Hz}}$
$f_O = 1\text{kHz}$	100% Tested		8	15		7	12		8	15		8		$\text{nV}/\sqrt{\text{Hz}}$
$f_O = 10\text{kHz}$	(1)		6	8		6	8		6	8		6		$\text{nV}/\sqrt{\text{Hz}}$
$f_B = 10\text{Hz to } 10\text{kHz}$	(1)		0.7	1.2		0.6	1		0.7	1.2		0.7		$\mu\text{Vrms}$
$f_B = 0.1\text{Hz to } 10\text{Hz}$	(1)		1.6	3.3		1.2	2.5		1.6	3.3		1.6		$\mu\text{Vp-p}$
Current, $f_B = 0.1\text{Hz to } 10\text{Hz}$	(1)		15	24		12	19		15	24		15		$\text{fAp-p}$
$f_O = 0.1\text{Hz to } 20\text{kHz}$	(1)		0.8	1.3		0.6	1		0.8	1		0.8		$\text{fA}/\sqrt{\text{Hz}}$
<b>OFFSET VOLTAGE</b> (2)														
Input Offset Voltage	$V_{CM} = 0\text{VDC}$		$\pm 0.1$	$\pm 0.75$		$\pm 0.05$	$\pm 0.5$		$\pm 0.1$	$\pm 0.75$		$\pm 0.3$	$\pm 2$	mV
Average Drift	$T_A = T_{MIN}$ to $T_{MAX}$		$\pm 2$	$\pm 6$		$\pm 0.5$	$\pm 2.8$		$\pm 2$	$\pm 6$		$\pm 8$	$\pm 15$	$\mu\text{V}/^\circ\text{C}$
Match			$\pm 1$			$\pm 0.5$			2			2		$\mu\text{V}/^\circ\text{C}$
Supply Rejection		90	110		96	110		90	110		86	110		dB
Channel Separation	100Hz, $R_L = 2\text{k}\Omega$		$\pm 3$	$\pm 31$		$\pm 3$	$\pm 16$		$\pm 3$	$\pm 31$		$\pm 3$	$\pm 50$	$\mu\text{V/V}$ dB
<b>BIAS CURRENT</b> (2)														
Input Bias Current	$V_{CM} = 0\text{VDC}$		$\pm 2$	$\pm 8$		$\pm 1.2$	$\pm 4$		$\pm 2$	$\pm 8$		$\pm 3$	$\pm 15$	pA
Match			$\pm 1$			$\pm 0.5$			$\pm 1$			2		pA
<b>OFFSET CURRENT</b> (2)														
Input Offset Current	$V_{CM} = 0\text{VDC}$		$\pm 1.2$	$\pm 6$		$\pm 0.6$	$\pm 3$		$\pm 1.2$	$\pm 6$		$\pm 3$	$\pm 12$	pA
<b>IMPEDANCE</b>														
Differential			$10^{13} \parallel 1$			$10^{13} \parallel 1$			$10^{13} \parallel 1$			$10^{13} \parallel 1$		$\Omega \parallel \text{pF}$
Common-Mode			$10^{14} \parallel 3$			$10^{14} \parallel 3$			$10^{14} \parallel 3$			$10^{14} \parallel 3$		$\Omega \parallel \text{pF}$
<b>VOLTAGE RANGE</b>														
Common-Mode Input Range	$V_N = \pm 10\text{VDC}$	$\pm 10$	$\pm 11$		$\pm 10$	$\pm 11$		$\pm 10$	$\pm 11$		$\pm 10$	$\pm 11$		V
Common-Mode Rejection		90	110		96	110		90	110		82	110		dB
<b>OPEN-LOOP GAIN, DC</b>														
Open-Loop Voltage Gain	$R_L \geq 2\text{k}\Omega$	110	125		114	125		110	125		106	125		dB
Match			3			2			3			3		dB
<b>FREQUENCY RESPONSE</b>														
Unity Gain, Small Signal			2			2			2			2		MHz
Full Power Response	20Vp-p, $R_L = 2\text{k}\Omega$	16	32		16	32		16	32			32		kHz
Slew Rate	$V_O = \pm 10\text{V}$ , $R_L = 2\text{k}\Omega$	1	2		1	2		1	2			2		V/ $\mu\text{s}$
Settling Time, 0.1%	Gain = -1, $R_L = 2\text{k}\Omega$		6			6			6			6		$\mu\text{s}$
0.01%	10V Step		10			10			10			10		$\mu\text{s}$
Overload Recovery, 50% Overdrive(3)	Gain = -1		5			5			5			5		$\mu\text{s}$
<b>RATED OUTPUT</b>														
Voltage Output	$R_L = 2\text{k}\Omega$	$\pm 10$	$\pm 11$		$\pm 10$	$\pm 11$		$\pm 10$	$\pm 11$		$\pm 10$	$\pm 11$		V
Current Output	$V_O = \pm 10\text{VDC}$	$\pm 5$	$\pm 10$		$\pm 5$	$\pm 10$		$\pm 5$	$\pm 10$		$\pm 5$	$\pm 10$		mA
Output Resistance	DC, Open-Loop		100			100			100			100		$\Omega$
Load Capacitance Stability	Gain = +1		1000			1000			1000			1000		pF
Short Circuit Current		10	40		10	40		10	40		10	40		mA
<b>POWER SUPPLY</b>														
Rated Voltage			$\pm 15$			$\pm 15$			$\pm 15$			$\pm 15$		VDC
Voltage Range, Derated Performance		$\pm 5$		$\pm 18$	$\pm 5$		$\pm 18$	$\pm 5$		$\pm 18$	$\pm 5$		$\pm 18$	VDC
Current, Quiescent	$I_O = 0\text{mADC}$		5	7		5	7		5	7		5	9	mA
<b>TEMPERATURE RANGE</b>														
Specification	Ambient Temp.	-25		+85	-25		+85	-55		+125	0		+70	$^\circ\text{C}$
Operating "M" Package	Ambient Temp.	-55		+125	-55		+125	-55		+125	-55		+125	$^\circ\text{C}$
"P" Package													+85	$^\circ\text{C}$
Storage "M" Package	Ambient Temp.	-85		+150	-85		+150	-85		+150	-85		+150	$^\circ\text{C}$
"P" Package													+85	$^\circ\text{C}$
$\theta_{JA}$ Junction-Ambient			200			200			200			200(4)		$^\circ\text{C}/\text{W}$

NOTES: (1) Sample tested—this parameter is guaranteed. (2) Offset voltage, offset current, and bias current are measured with the units fully warmed up. (3) Overload recovery is defined as the time required for the output to return from saturation to linear operation following the removal of a 50% input overdrive. (4) Typical  $\theta_{JA} = 150^\circ\text{C}/\text{W}$  for plastic DIP.

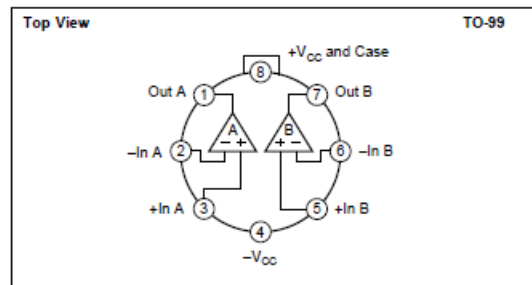
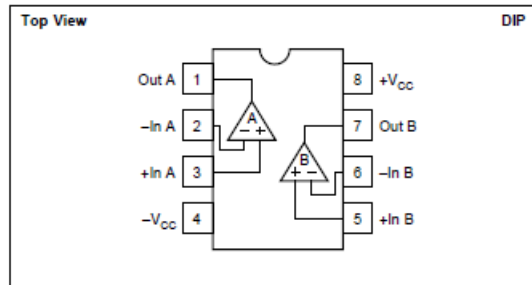
## ELECTRICAL (FULL TEMPERATURE RANGE SPECIFICATIONS)

At  $V_{CC} = \pm 15\text{VDC}$  and  $T_A = T_{MIN}$  to  $T_{MAX}$  unless otherwise noted.

PARAMETER	CONDITION	OPA2111AM			OPA2111BM			OPA2111SM			OPA2111KM, KP			UNITS
		MIN	TYP	MAX	MIN	TYP	MAX	MIN	TYP	MAX	MIN	TYP	MAX	
<b>TEMPERATURE RANGE</b> Specification Range	Ambient Temp.	-25		+85	-25		+85	-55		+125	0		+70	°C
<b>INPUT OFFSET VOLTAGE<sup>(1)</sup></b> Input Offset Voltage Average Drift Match Supply Rejection	$V_{CM} = 0\text{VDC}$		$\pm 0.22$ $\pm 2$ 1 86	$\pm 1.2$ $\pm 8$ 1 100		$\pm 0.08$ $\pm 0.5$ 0.5 90	$\pm 0.75$ $\pm 2.8$ 0.5 100		$\pm 0.3$ $\pm 2$ 2 86	$\pm 1.5$ $\pm 8$ 2 100		$\pm 0.9$ $\pm 8$ 2 100	$\pm 5$ $\pm 15$ 2 100	mV $\mu\text{V}/^\circ\text{C}$ $\mu\text{V}/^\circ\text{C}$ dB $\mu\text{V}/\text{V}$
<b>BIAS CURRENT<sup>(1)</sup></b> Input Bias Current Match	$V_{CM} = 0\text{VDC}$		$\pm 125$ 60	$\pm 1\text{nA}$		$\pm 75$ 30	$\pm 500$		$\pm 2\text{nA}$ 1nA	$\pm 16.3\text{nA}$		$\pm 125$ $\pm 500$	pA pA	
<b>OFFSET CURRENT<sup>(1)</sup></b> Input Offset Current	$V_{CM} = 0\text{VDC}$		$\pm 75$	$\pm 750$		$\pm 38$	$\pm 375$		$\pm 1.3\text{nA}$	$\pm 12\text{nA}$		$\pm 75$ $\pm 375$	pA	
<b>VOLTAGE RANGE</b> Common-Mode Input Range Common-Mode Rejection	$V_{IN} = \pm 10\text{VDC}$	$\pm 10$ 86	$\pm 11$ 100		$\pm 10$ 90	$\pm 11$ 100		$\pm 10$ 86	$\pm 11$ 100		$\pm 10$ 80	$\pm 11$ 100	V dB	
<b>OPEN-LOOP GAIN, DC</b> Open-Loop Voltage Gain Match	$R_L \geq 2\text{k}\Omega$	106 106	120 5		110 110	120 3		106 106	120 5		100 100	120 5	dB dB	
<b>RATED OUTPUT</b> Voltage Output Current Output Short Circuit Current	$R_L = 2\text{k}\Omega$ $V_O = \pm 10\text{VDC}$ $V_O = 0\text{VDC}$	$\pm 10.5$ $\pm 5$ 10	$\pm 11$ $\pm 10$ 40		$\pm 10.5$ $\pm 5$ 10	$\pm 11$ $\pm 10$ 40		$\pm 10.5$ $\pm 5$ 10	$\pm 11$ $\pm 10$ 40		$\pm 10.5$ $\pm 5$ 10	$\pm 11$ $\pm 10$ 40	V mA mA	
<b>POWER SUPPLY</b> Current, Quiescent	$I_O = 0\text{mADC}$		5	8		5	8		5	8		5	10	mA

NOTES: (1) Offset voltage, offset current, and bias current are measured with the units fully warmed up.

## CONNECTION DIAGRAMS



## ABSOLUTE MAXIMUM RATINGS

Supply	$\pm 18\text{VDC}$
Internal Power Dissipation ( $T_J \leq +175^\circ\text{C}$ )	500mW
Differential Input Voltage	Total $V_{CC}$
Input Voltage Range	$\pm V_{CC}$
Storage Temperature Range: "M" Package	$-65^\circ\text{C}$ to $+150^\circ\text{C}$
"P" Package	$-40^\circ\text{C}$ to $+85^\circ\text{C}$
Operating Temperature Range: "M" Package	$-55^\circ\text{C}$ to $+125^\circ\text{C}$
"P" Package	$-40^\circ\text{C}$ to $+85^\circ\text{C}$
Lead Temperature (soldering, 10s)	$+300^\circ\text{C}$
Output Short Circuit to Ground ( $+25^\circ\text{C}$ )	Continuous
Junction Temperature	$+175^\circ\text{C}$

## PACKAGE INFORMATION

MODEL	PACKAGE	PACKAGE DRAWING NUMBER <sup>(1)</sup>
OPA2111AM	TO-99	001
OPA2111BM	TO-99	001
OPA2111KM	TO-99	001
OPA2111SM	TO-99	001
OPA2111KP	8-Pin Plastic DIP	006

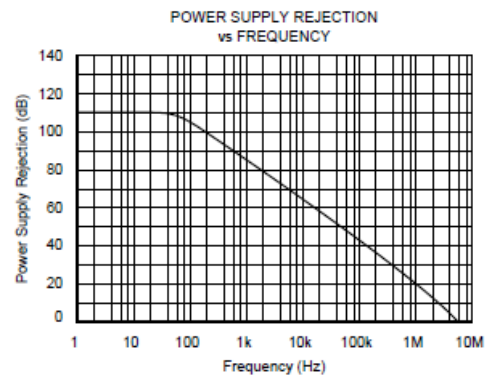
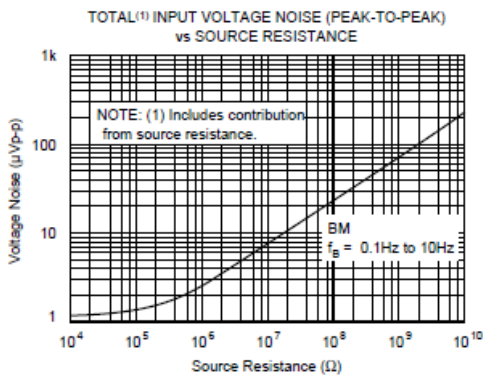
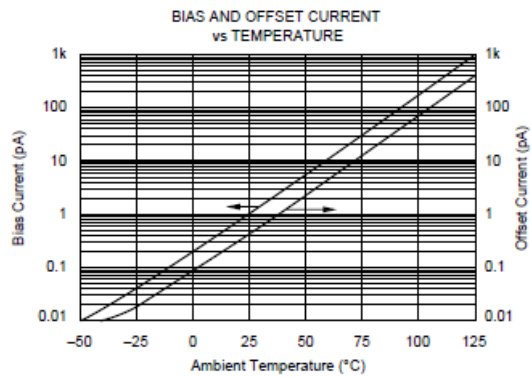
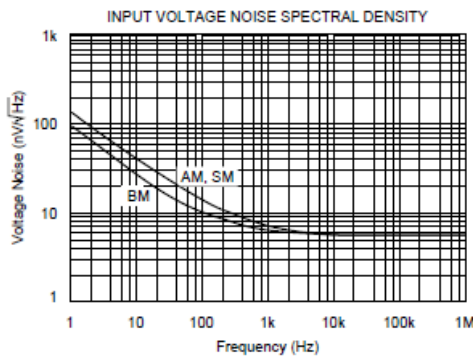
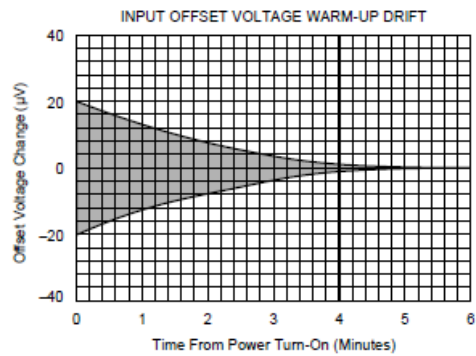
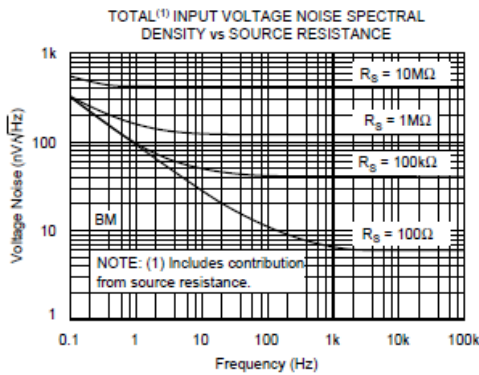
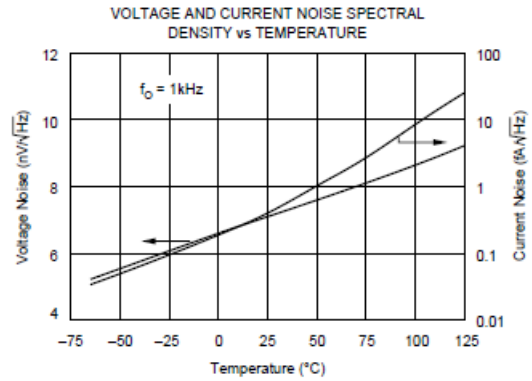
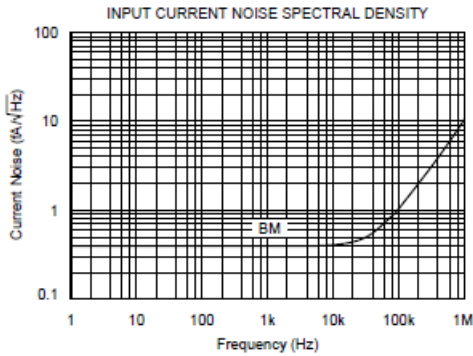
NOTE: (1) For detailed drawing and dimension table, please see end of data sheet, or Appendix D of Burr-Brown IC Data Book.

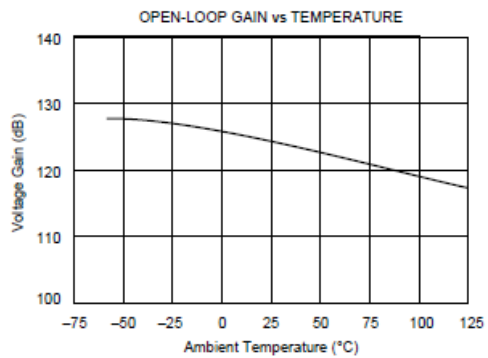
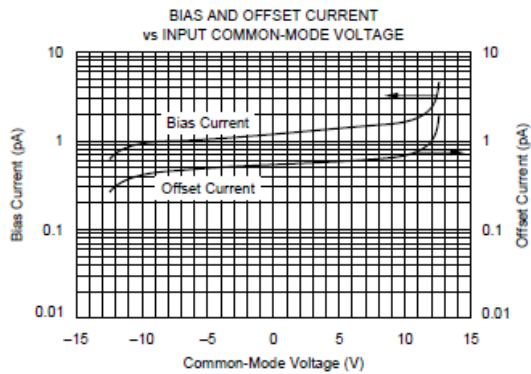
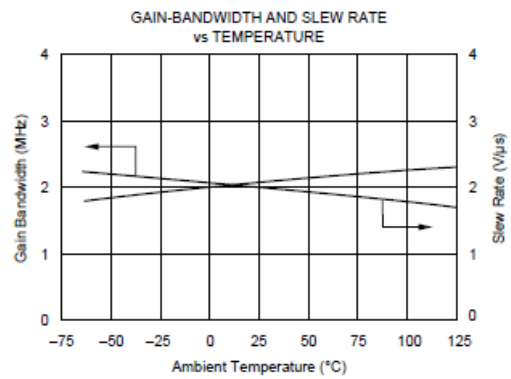
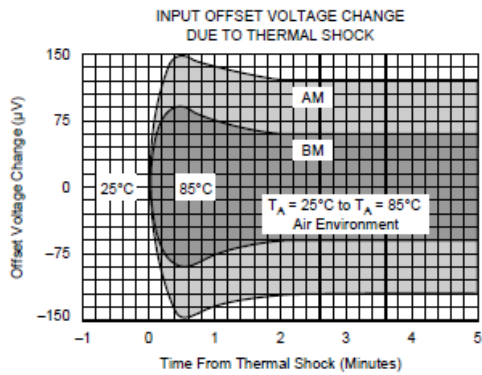
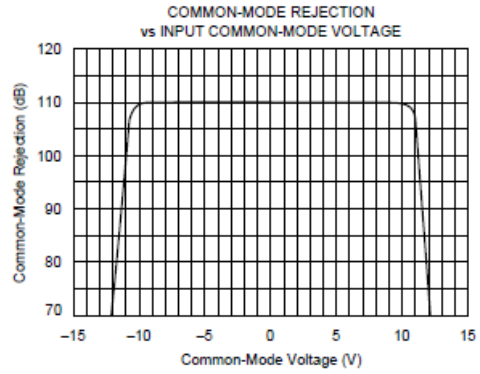
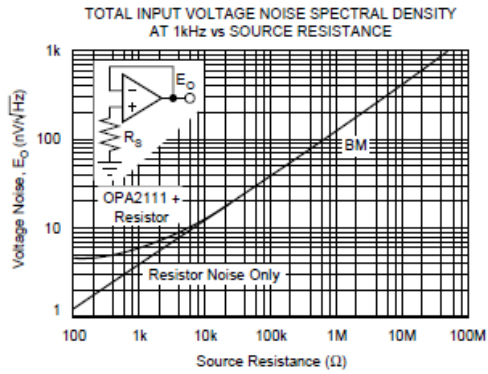
## ORDERING INFORMATION

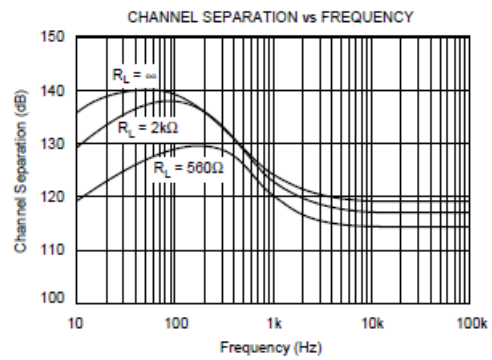
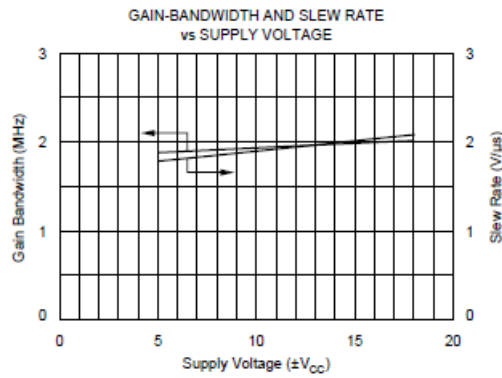
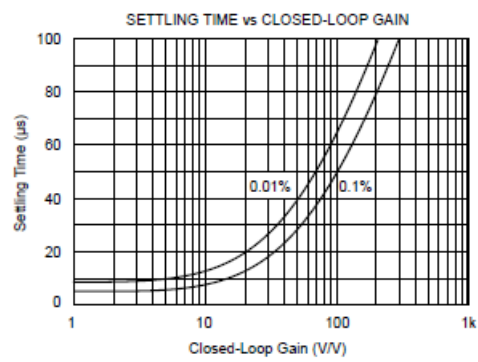
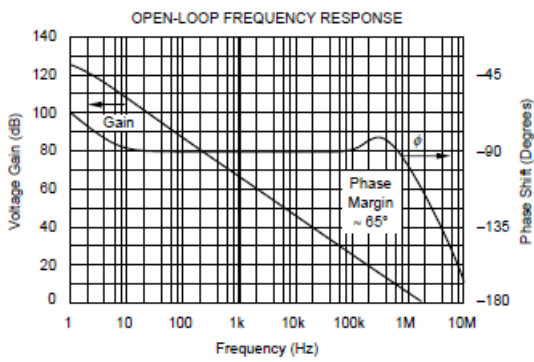
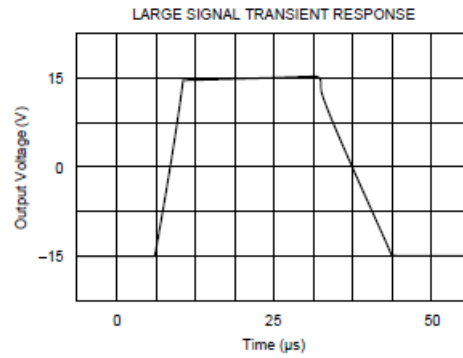
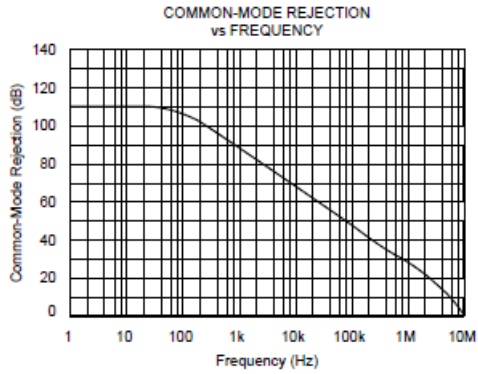
MODEL	PACKAGE	TEMPERATURE RANGE	OFFSET VOLTAGE, max (mV)
OPA2111AM	TO-99	$-25^\circ\text{C}$ to $+85^\circ\text{C}$	$\pm 0.75$
OPA2111BM	TO-99	$-25^\circ\text{C}$ to $+85^\circ\text{C}$	$\pm 0.5$
OPA2111KM	TO-99	$0^\circ\text{C}$ to $+70^\circ\text{C}$	$\pm 2$
OPA2111SM	TO-99	$-55^\circ\text{C}$ to $+125^\circ\text{C}$	$\pm 0.75$
OPA2111KP	8-Pin Plastic DIP	$0^\circ\text{C}$ to $+70^\circ\text{C}$	$\pm 2$

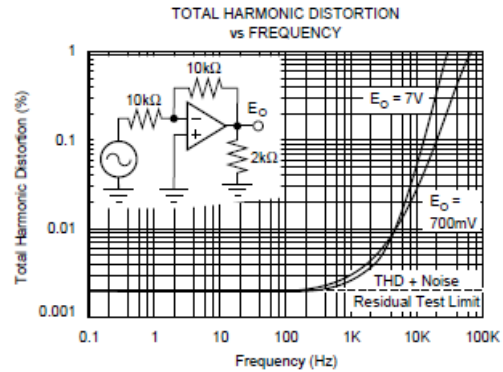
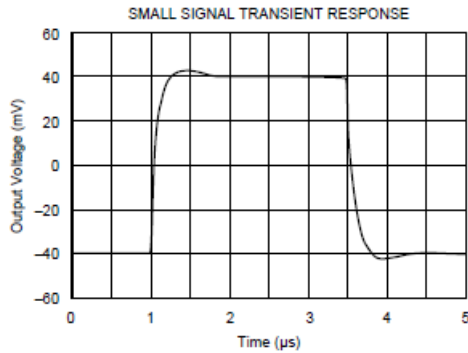
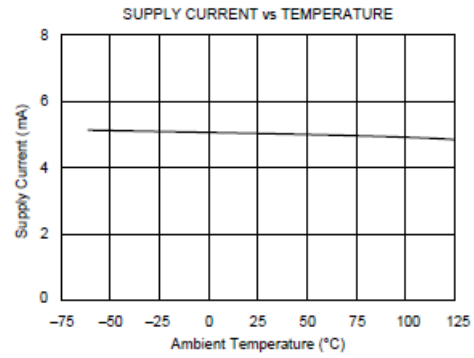
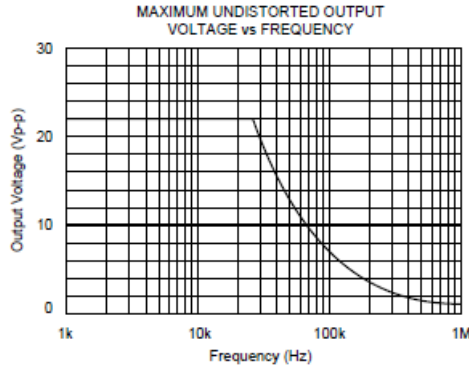
# TYPICAL PERFORMANCE CURVES

$T_A = +25^\circ\text{C}$ , and  $V_{CC} = \pm 15\text{VDC}$  unless otherwise noted.









## APPLICATIONS INFORMATION

### OFFSET VOLTAGE ADJUSTMENT

The OPA2111 offset voltage is laser-trimmed and will require no further trim for most applications.

Offset voltage can be trimmed by summing (see Figure 1). With this trim method there will be no degradation of input offset drift.

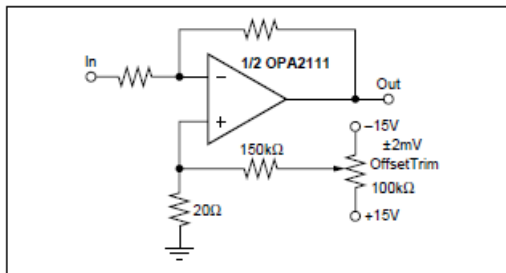


FIGURE 1. Offset Voltage Trim.

### INPUT PROTECTION

Conventional monolithic FET operational amplifiers require external current-limiting resistors to protect their inputs against destructive currents that can flow when input FET gate-to-substrate isolation diodes are forward-biased. Most BIFET amplifiers can be destroyed by the loss of  $-V_{CC}$ .

Because of its dielectric isolation, no special protection is needed on the OPA2111. Of course, the differential and common-mode voltage limits should be observed. Static damage can cause subtle changes in amplifier input characteristics without necessarily destroying the device. In precision operational amplifiers (both bipolar and FET types), this may cause a noticeable degradation of offset voltage and drift.

Static protection is recommended when handling any precision IC operational amplifier.

## GUARDING AND SHIELDING

As in any situation where high impedances are involved, careful shielding is required to reduce "hum" pickup in input leads. If large feedback resistors are used, they should also be shielded along with the external input circuitry.

Leakage currents across printed circuit boards can easily exceed the bias current of the OPA2111. To avoid leakage problems, it is recommended that the signal input lead of the OPA2111 be wired to a Teflon standoff. If the OPA2111 is to be soldered directly into a printed circuit board, utmost care must be used in planning the board layout. A "guard" pattern should completely surround the high impedance input leads and should be connected to a low impedance point which is at the signal input potential (see Figure 2).

## NOISE: FET vs BIPOLAR

Low noise circuit design requires careful analysis of all noise sources. External noise sources can dominate in many cases, so consider the effect of source resistance on overall operational amplifier noise performance. At low source impedances, the low voltage noise of a bipolar operational amplifier is superior, but at higher impedances the high current noise of a bipolar amplifier becomes a serious liability. Above about 15kΩ the OPA2111 will have lower total noise than an OP-27 (see Figure 3).

## BIAS CURRENT CHANGE vs COMMON-MODE VOLTAGE

The input bias currents of most popular BIFET® operational amplifiers are affected by common-mode voltage (Figure 4). Higher input FET gate-to-drain voltage causes leakage and ionization (bias) currents to increase. Due to its cascode input stage, the extremely low bias current of the OPA2111 is not compromised by common-mode voltage.

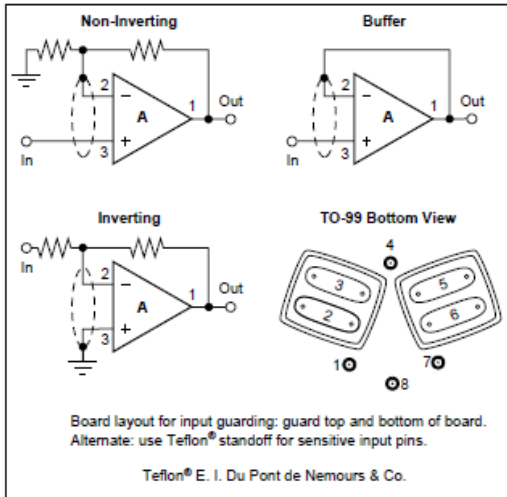


FIGURE 2. Connection of Input Guard.

## APPLICATIONS CIRCUITS

Figures 5 through 13 are circuit diagrams of various applications for the OPA2111.

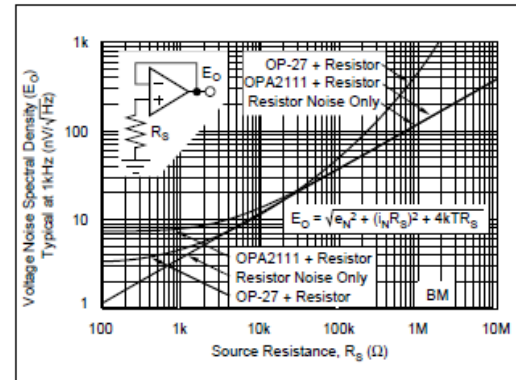


FIGURE 3. Voltage Noise Spectral Density vs Source Resistance.

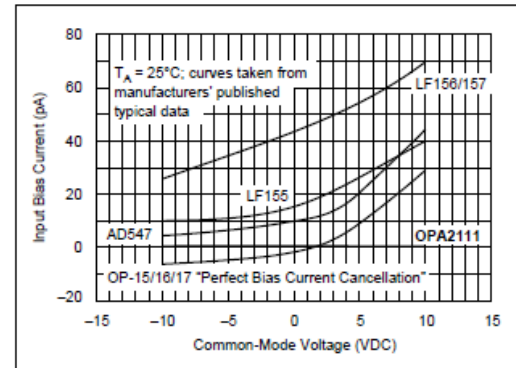


FIGURE 4. Input Bias Current vs Common-Mode Voltage.

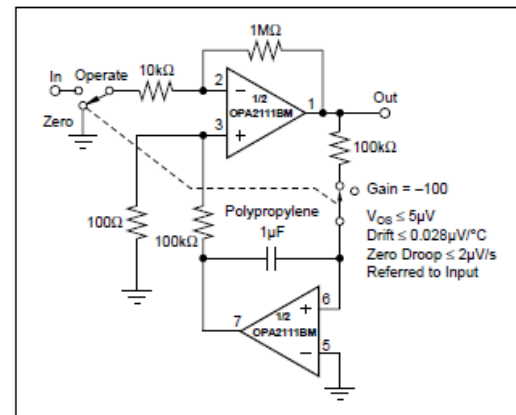


FIGURE 5. Auto-Zero Amplifier.

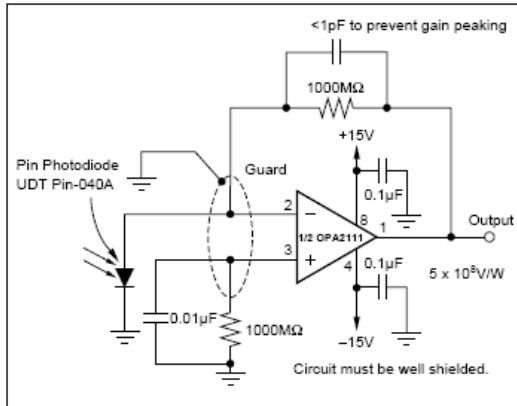


FIGURE 6. Sensitive Photodiode Amplifier.

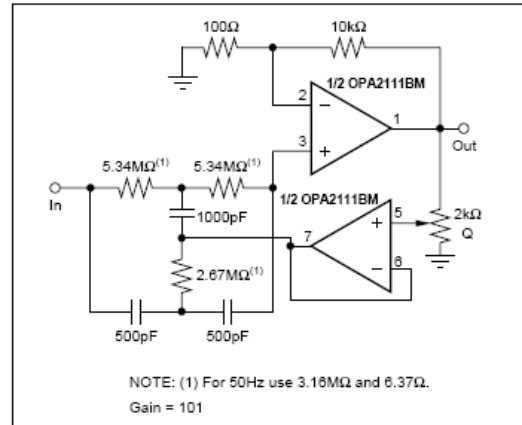


FIGURE 7. High Impedance 60Hz Reject Filter with Gain.

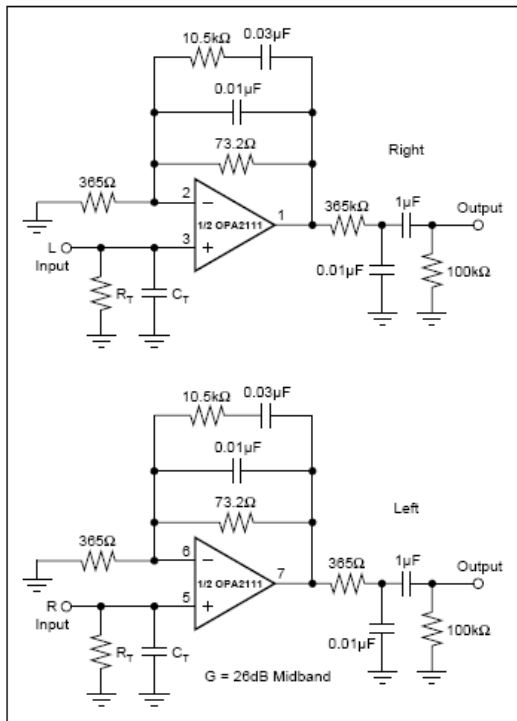


FIGURE 8. RIAA Equalized Stereo Preamplifier.

# C. Universal Active Filter (UAF42)<sup>3</sup>

## FEATURES

- **VERSATILE:**
  - Low-Pass, High-Pass
  - Band-Pass, Band-Reject
- **SIMPLE DESIGN PROCEDURE**
- **ACCURATE FREQUENCY AND Q:**
  - Includes On-Chip 1000pF  $\pm 0.5\%$  Capacitors

## APPLICATIONS

- **TEST EQUIPMENT**
- **COMMUNICATIONS EQUIPMENT**
- **MEDICAL INSTRUMENTATION**
- **DATA ACQUISITION SYSTEMS**
- **MONOLITHIC REPLACEMENT FOR UAF41**

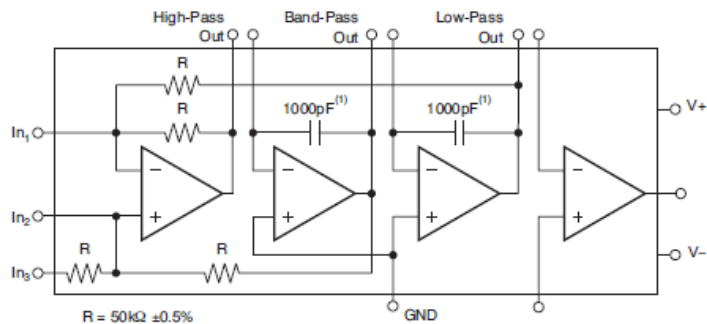
## DESCRIPTION

The UAF42 is a universal active filter that can be configured for a wide range of low-pass, high-pass, and band-pass filters. It uses a classic state-variable analog architecture with an inverting amplifier and two integrators. The integrators include on-chip 1000pF capacitors trimmed to 0.5%. This architecture solves one of the most difficult problems of active filter design—obtaining tight tolerance, low-loss capacitors.

A DOS-compatible filter design program allows easy implementation of many filter types, such as Butterworth, Bessel, and Chebyshev. A fourth, uncommitted FET-input op amp (identical to the other three) can be used to form additional stages, or for special filters such as band-reject and Inverse Chebyshev.

The classical topology of the UAF42 forms a time-continuous filter, free from the anomalies and switching noise associated with switched-capacitor filter types.

The UAF42 is available in 14-pin plastic DIP and SOIC-16 surface-mount packages, specified for the  $-25^{\circ}\text{C}$  to  $+85^{\circ}\text{C}$  temperature range.



NOTE: (1)  $\pm 0.5\%$ .

<sup>3</sup> Burr-Brown product from Texas instruments Incorporated: [www.ti.com](http://www.ti.com) (1992-2007)



This integrated circuit can be damaged by ESD. Texas Instruments recommends that all integrated circuits be handled with appropriate precautions. Failure to observe proper handling and installation procedures can cause damage. ESD damage can range from subtle performance degradation to complete device failure. Precision integrated circuits may be more susceptible to damage because very small parametric changes could cause the device not to meet its published specifications.

### ABSOLUTE MAXIMUM RATINGS<sup>(1)</sup>

Over operating free-air temperature range unless otherwise noted.

	UAF42	UNIT
Power Supply Voltage	±18	V
Input Voltage	±V <sub>S</sub> ±0.7	V
Output Short-Circuit	Continuous	
Operating Temperature	-40 to +85	°C
Storage Temperature	-40 to +125	°C
Junction Temperature	+125	°C

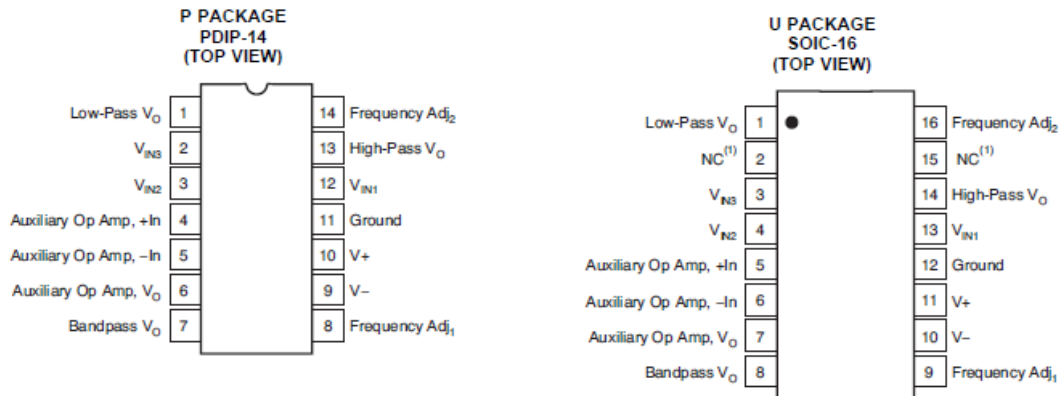
(1) Stresses above these ratings may cause permanent damage. Exposure to absolute maximum conditions for extended period may degrade device reliability. These are stress ratings only, and functional operation of the device at these or any other conditions beyond those specified is not supported.

### ORDERING INFORMATION<sup>(1)</sup>

PRODUCT	PACKAGE-LEAD	PACKAGE DESIGNATOR	PACKAGE MARKING
UAF42AP	PDIP-14	N	UAF42APS
UAF42APG4			
UAF42AU	SOIC-16	DW	UAF42AUS
UAF42AUE4			

(1) For the most current package and ordering information see the Package Option Addendum at the end of this document, or see the TI web site at [www.ti.com](http://www.ti.com).

### PIN CONFIGURATIONS



NOTE: (1) NC = no connection. For best performance connect all NC pins to ground to minimize inter-lead capacitance.

## ELECTRICAL CHARACTERISTICS

At  $T_A = +25^\circ\text{C}$ , and  $V_S = \pm 15\text{V}$ , unless otherwise noted.

PARAMETER	CONDITIONS	UAF42AP, AU			UNIT
		MIN	TYP	MAX	
<b>FILTER PERFORMANCE</b>					
Frequency Range, $f_n$			0 to 100		kHz
Frequency Accuracy vs Temperature	$f = 1\text{kHz}$		0.01	1	%/ $^\circ\text{C}$
Maximum Q			400		—
Maximum (Q • Frequency) Product			500		kHz
Q vs Temperature	$(f_o \cdot Q) < 10^4$		0.01		%/ $^\circ\text{C}$
Q Repeatability	$(f_o \cdot Q) < 10^5$		0.025		%/ $^\circ\text{C}$
Offset Voltage, Low-Pass Output	$(f_o \cdot Q) < 10^5$		2	$\pm 5$	mV
Resistor Accuracy			0.5	1	%
<b>OFFSET VOLTAGE<sup>(1)</sup></b>					
Input Offset Voltage vs Temperature			$\pm 0.5$	$\pm 5$	mV
Input Offset Voltage vs Power Supply	$V_S = \pm 6\text{V to } \pm 18\text{V}$	80	$\pm 3$	96	$\mu\text{V}/^\circ\text{C}$
<b>INPUT BIAS CURRENT<sup>(1)</sup></b>					
Input Bias Current	$V_{CM} = 0\text{V}$		10	50	pA
Input Offset Current	$V_{CM} = 0\text{V}$		5		pA
<b>NOISE</b>					
Input Voltage Noise					
Noise Density: $f = 10\text{Hz}$			25		nV/ $\sqrt{\text{Hz}}$
Noise Density: $f = 10\text{kHz}$			10		nV/ $\sqrt{\text{Hz}}$
Voltage Noise: BW = 0.1Hz to 10Hz			2		$\mu\text{V}_{PP}$
Input Bias Current Noise					
Noise Density: $f = 10\text{kHz}$			2		fA/ $\sqrt{\text{Hz}}$
<b>INPUT VOLTAGE RANGE<sup>(1)</sup></b>					
Common-Mode Input Range			$\pm 11.5$		V
Common-Mode Rejection	$V_{CM} = \pm 10\text{V}$	80	96		dB
<b>INPUT IMPEDANCE<sup>(1)</sup></b>					
Differential			$10^{13} \parallel 2$		$\Omega \parallel \text{pF}$
Common-Mode			$10^{13} \parallel 6$		$\Omega \parallel \text{pF}$
<b>OPEN-LOOP GAIN<sup>(1)</sup></b>					
Open-Loop Voltage Gain	$V_O = \pm 10\text{V}, R_L = 2\text{k}\Omega$	90	126		dB
<b>FREQUENCY RESPONSE</b>					
Slew Rate			10		V/ $\mu\text{s}$
Gain-Bandwidth Product	$G = +1$		4		MHz
Total Harmonic Distortion	$G = +1, f = 1\text{kHz}$		0.1		%
<b>OUTPUT<sup>(1)</sup></b>					
Voltage Output	$R_L = 2\text{k}\Omega$	$\pm 11$	$\pm 11.5$		V
Short Circuit Current			$\pm 25$		mA
<b>POWER SUPPLY</b>					
Specified Operating Voltage			$\pm 15$		V
Operating Voltage Range		$\pm 6$		$\pm 18$	V
Current			$\pm 6$	$\pm 7$	mA
<b>TEMPERATURE RANGE</b>					
Specified		-25		+85	$^\circ\text{C}$
Operating		-25		+85	$^\circ\text{C}$
Storage		-40		+125	$^\circ\text{C}$
Thermal Resistance, $\theta_{JA}$			100		$^\circ\text{C}/\text{W}$

(1) Specifications apply to uncommitted op amp,  $A_4$ . The three op amps forming the filter are identical to  $A_4$  but are tested as a complete filter.

## APPLICATION INFORMATION

The UAF42 is a monolithic implementation of the proven state-variable analog filter topology. This device is pin-compatible with the popular UAF41 analog filter, and it provides several improvements.

The slew rate of the UAF42 has been increased to 10V/μs, versus 1.6V/μs for the UAF41. Frequency • Q product of the UAF42 has been improved, and the useful natural frequency extended by a factor of four to 100kHz. FET input op amps on the UAF42 provide very low input bias current. The monolithic construction of the UAF42 provides lower cost and improved reliability.

### DESIGN PROGRAM

Application report [SBFA002](#) (available for download at [www.ti.com](http://www.ti.com)) and a computer-aided design program also available from Texas Instruments, make it easy to design and implement many kinds of active filters. The DOS-compatible program guides you through the design process and automatically calculates component values.

Low-pass, high-pass, band-pass and band-reject (notch) filters can be designed. The program supports the three most commonly-used all-pole filter types: Butterworth, Chebyshev and Bessel. The less-familiar inverse Chebyshev is also supported, providing a smooth passband response with ripple in the stop band.

With each data entry, the program automatically calculates and displays filter performance. This feature allows a spreadsheet-like *what-if* design approach. For example, a user can quickly determine, by trial and error, how many poles are required for a desired attenuation in the stopband. Gain/phase plots may be viewed for any response type.

The basic building element of the most commonly-used filter types is the second-order section. This section provides a complex-conjugate pair of poles. The natural frequency,  $\omega_n$ , and Q of the pole pair determine the characteristic response of the section. The low-pass transfer function is shown in [Equation 1](#):

$$\frac{V_O(s)}{V_I(s)} = \frac{A_{LP}\omega_n^2}{s^2 + s\omega_n/Q + \omega_n^2} \quad (1)$$

The high-pass transfer function is given by [Equation 2](#):

$$\frac{V_{HP}(s)}{V_I(s)} = \frac{A_{HP}s^2}{s^2 + s\omega_n/Q + \omega_n^2} \quad (2)$$

The band-pass transfer function is calculated using [Equation 3](#):

$$\frac{V_{BP}(s)}{V_I(s)} = \frac{A_{BP}(\omega_n/Q) s}{s^2 + s\omega_n/Q + \omega_n^2} \quad (3)$$

A band-reject response is obtained by summing the low-pass and high-pass outputs, yielding the transfer function shown in [Equation 4](#):

$$\frac{V_{BR}(s)}{V_I(s)} = \frac{A_{BR}(s^2 + \omega_n^2)}{s^2 + s\omega_n/Q + \omega_n^2} \quad (4)$$

The most common filter types are formed with one or more cascaded second-order sections. Each section is designed for  $\omega_n$  and Q according to the filter type (Butterworth, Bessel, Chebyshev, etc.) and cutoff frequency. While tabulated data can be found in virtually any filter design text, the design program eliminates this tedious procedure.

Second-order sections may be noninverting ([Figure 1](#)) or inverting ([Figure 2](#)). Design equations for these two basic configurations are shown for reference. The design program solves these equations, providing complete results, including component values.

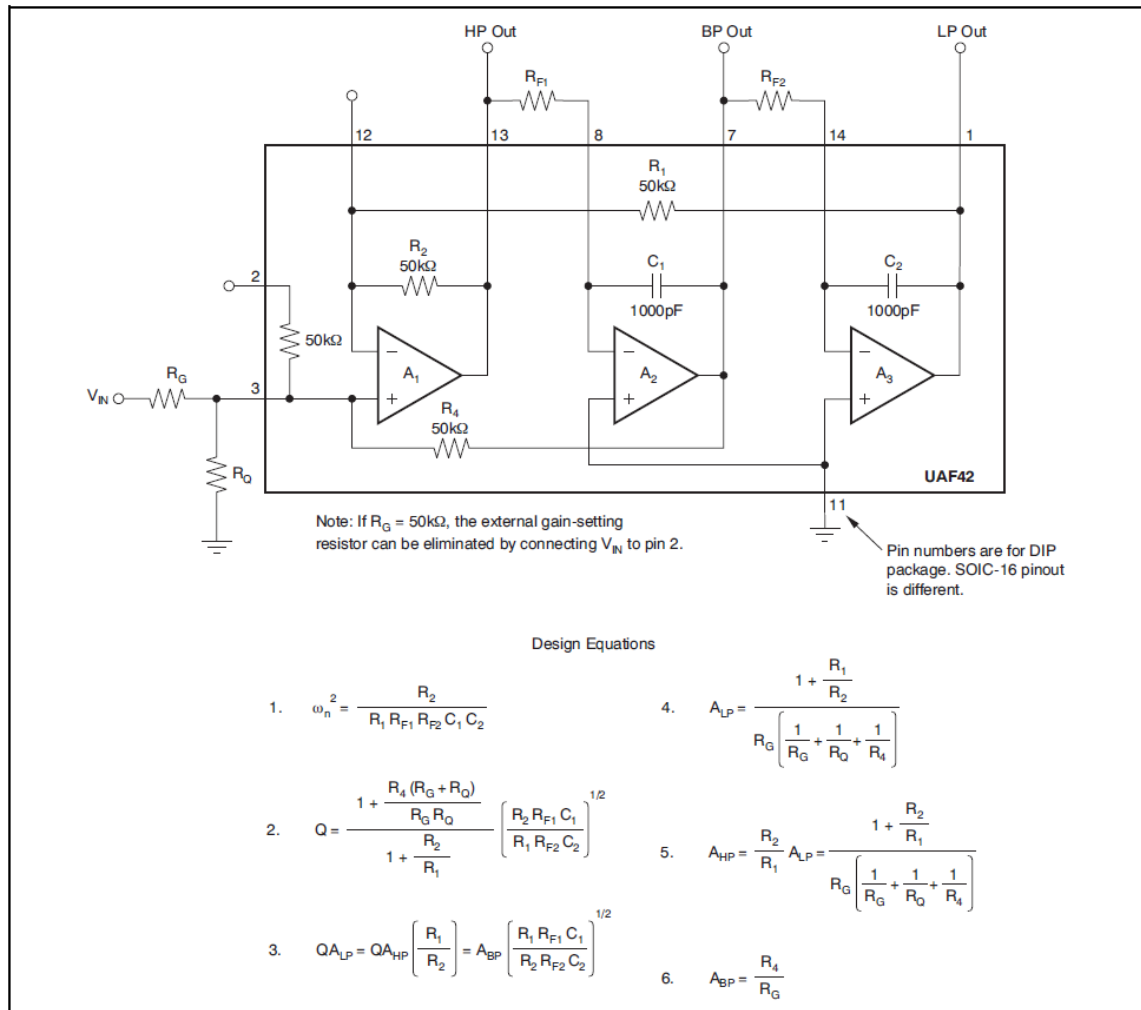


Figure 1. Noninverting Pole-Pair

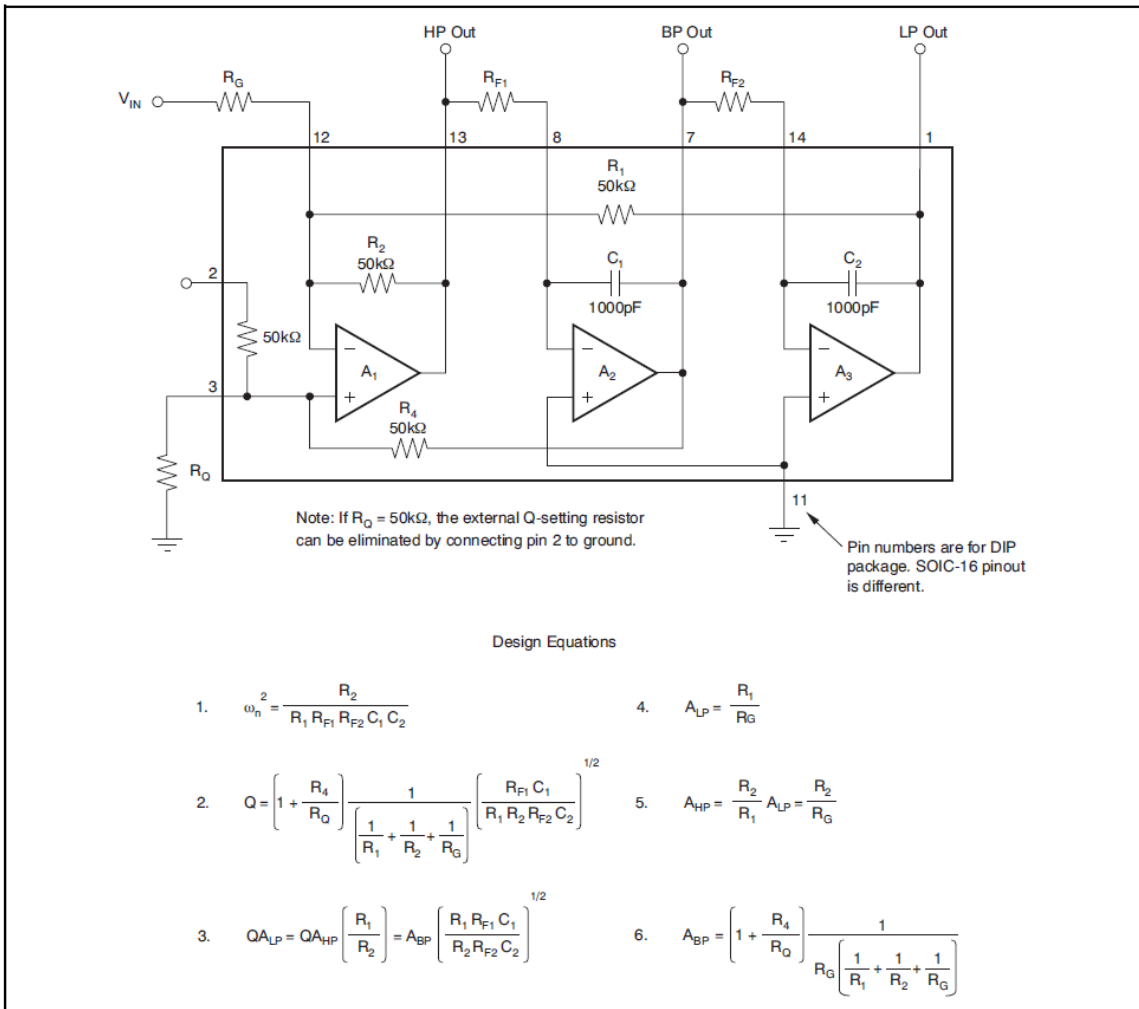


Figure 2. Inverting Pole-Pair

# D. Instrumental Amplifier (INA101HP)<sup>4</sup>

## FEATURES

- LOW DRIFT:  $0.25\mu\text{V}/^\circ\text{C}$  max
- LOW OFFSET VOLTAGE:  $25\mu\text{V}$  max
- LOW NONLINEARITY: 0.002%
- LOW NOISE:  $13\text{nV}/\sqrt{\text{Hz}}$
- HIGH CMR: 106dB AT 60Hz
- HIGH INPUT IMPEDANCE:  $10^{10}\Omega$
- 14-PIN PLASTIC, CERAMIC DIP, SOL-16, AND TO-100 PACKAGES

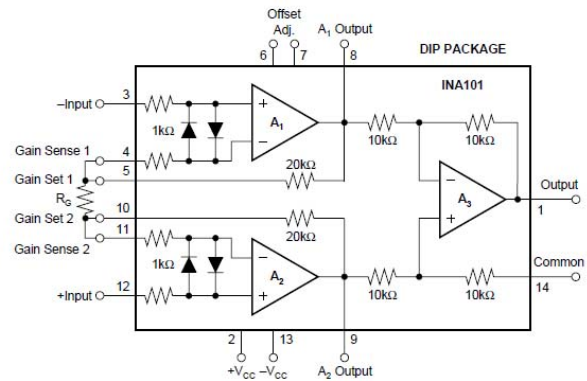
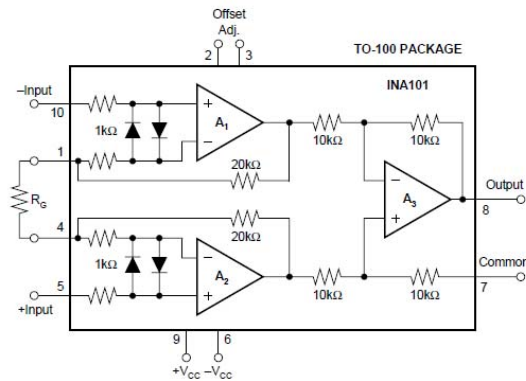
## APPLICATIONS

- STRAIN GAGES
- THERMOCOUPLES
- RTDs
- REMOTE TRANSDUCERS
- LOW-LEVEL SIGNALS
- MEDICAL INSTRUMENTATION

## DESCRIPTION

The INA101 is a high accuracy instrumentation amplifier designed for low-level signal amplification and general purpose data acquisition. Three precision op amps and laser-trimmed metal film resistors are integrated on a single monolithic integrated circuit.

The INA101 is packaged in TO-100 metal, 14-pin plastic and ceramic DIP, and SOL-16 surface-mount packages. Commercial, industrial and military temperature range models are available.



<sup>4</sup> Burr-Brown product from Texas instruments Incorporated: [www.ti.com](http://www.ti.com)

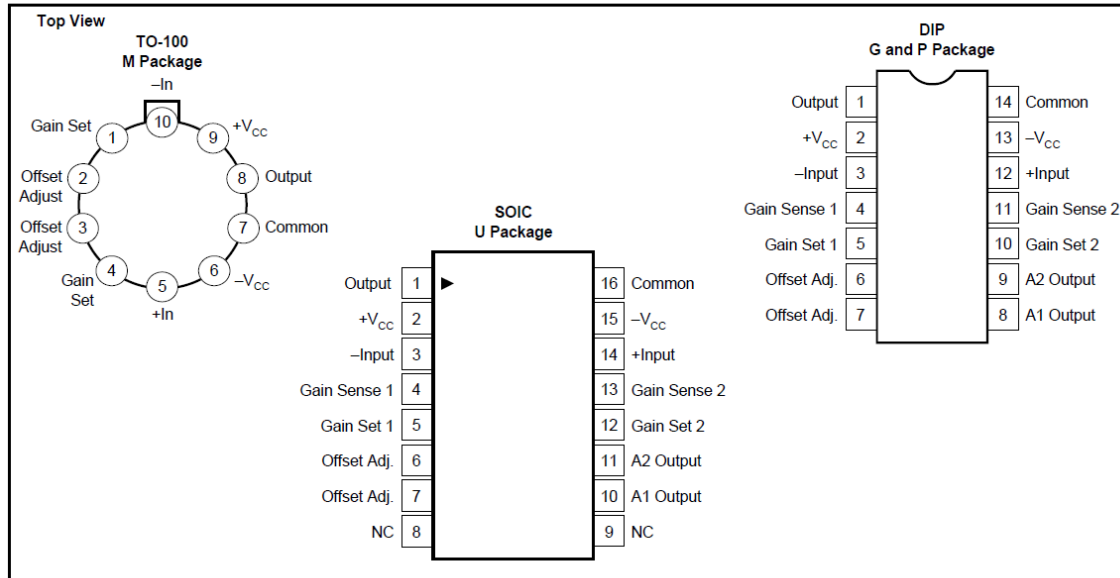
# SPECIFICATIONS

## ELECTRICAL

At +25°C with ±15VDC power supply and in circuit of Figure 1, unless otherwise noted.

PARAMETER	INA101AM, AG			INA101SM, SG			INA101CM, CG			INA101HP, KU			UNITS
	MIN	TYP	MAX	MIN	TYP	MAX	MIN	TYP	MAX	MIN	TYP	MAX	
<b>GAIN</b>													
Range of Gain	1		1000	*	*	*	*	*	*	*	*	*	V/V
Gain Equation		$G = 1 + (40k/R_G)$			*	*		*	*	*	*	*	V/V
Error from Equation, DC <sup>(1)</sup>		$\pm(0.04 + 0.00016G - 0.02/G)$	$\pm(0.1 + 0.0003G - 0.05/G)$		*	*		*	*	$\pm(0.1 + 0.00015G - 0.05/G)$	$\pm(0.3 + 0.0002G - 0.10/G)$	*	%
Gain Temp. Coefficient <sup>(3)</sup>													
G = 1		2	5		*	*		*	*	*	*	*	ppm/°C
G = 10		20	100		*	*		10	*	*	*	*	ppm/°C
G = 100		22	110		*	*		11	*	*	*	*	ppm/°C
G = 1000		22	110		*	*		11	*	*	*	*	ppm/°C
Nonlinearity, DC <sup>(2)</sup>		$\pm(0.002 + 10^{-5} G)$	$\pm(0.005 + 2 \times 10^{-5} G)$		$\pm(0.001 + 10^{-5} G)$	$\pm(0.002 + 10^{-5} G)$		$\pm(0.001 + 10^{-5} G)$	$\pm(0.002 + 10^{-5} G)$		*	*	% of p-p FS
<b>RATED OUTPUT</b>													
Voltage	±10	±12.5		*	*		*	*		*	*		V
Current	±5	±10		*	*		*	*		*	*		mA
Output Impedance		0.2			*			*			*		Ω
Capacitive Load		1000			*			*			*		pF
<b>INPUT OFFSET VOLTAGE</b>													
Initial Offset at +25°C		$\pm(25 + 200/G)$	$\pm(50 + 400/G)$		$\pm(10 + 100/G)$	$\pm(25 + 200/G)$		$\pm(10 + 100/G)$	$\pm(25 + 200/G)$		$\pm(125 + 450/G)$	$\pm(250 + 900/G)$	μV
vs Temperature			$\pm(2 + 20/G)$			$\pm(0.75 + 10/G)$			$\pm(0.25 + 10/G)$		$\pm(2 + 20/G)$		μV/°C
vs Supply		$\pm(1 + 20/G)$			*	*		*	*		*	*	μV/V
vs Time		$\pm(1 + 20/G)$			*	*		*	*		*	*	μV/mo
<b>INPUT BIAS CURRENT</b>													
Initial Bias Current (each input)		±15	±30		±10	*		±5	±20		*	*	nA
vs Temperature		±0.2			*	*		*	*		*	*	nA/°C
vs Supply		±0.1			*	*		*	*		*	*	nA/V
Initial Offset Current		±15	±30		±10	*		±5	±20		*	*	nA
vs Temperature		±0.5			*	*		*	*		*	*	nA/°C
<b>INPUT IMPEDANCE</b>													
Differential		$10^{10} \parallel 3$			*	*		*	*		*	*	Ω    pF
Common-mode		$10^{10} \parallel 3$			*	*		*	*		*	*	Ω    pF
<b>INPUT VOLTAGE RANGE</b>													
Range, Linear Response	±10	±12		*	*		*	*		*	*		V
CMR with 1kΩ Source Imbalance													
DC to 60Hz, G = 1	80	90		*	*		*	*		65	85		dB
DC to 60Hz, G = 10	96	106		*	*		*	*		90	95		dB
DC to 60Hz, G = 100 to 1000	106	110		*	*		*	*		100	105		dB
<b>INPUT NOISE</b>													
Input Voltage Noise													
$f_b = 0.01\text{Hz to }10\text{Hz}$		0.8			*	*		*	*		*	*	μV, p-p
Density, G = 1000					*	*		*	*		*	*	nV/√Hz
$f_b = 10\text{Hz}$		18			*	*		*	*		*	*	nV/√Hz
$f_b = 100\text{Hz}$		15			*	*		*	*		*	*	nV/√Hz
$f_b = 1\text{kHz}$		13			*	*		*	*		*	*	nV/√Hz
Input Current Noise													
$f_b = 0.01\text{Hz to }10\text{Hz}$		50			*	*		*	*		*	*	pA, p-p
Density					*	*		*	*		*	*	pA/√Hz
$f_b = 10\text{Hz}$		0.8			*	*		*	*		*	*	pA/√Hz
$f_b = 100\text{Hz}$		0.46			*	*		*	*		*	*	pA/√Hz
$f_b = 1\text{kHz}$		0.35			*	*		*	*		*	*	pA/√Hz
<b>DYNAMIC RESPONSE</b>													
Small Signal, ±3dB Flatness													
G = 1		300			*	*		*	*		*	*	kHz
G = 10		140			*	*		*	*		*	*	kHz
G = 100		25			*	*		*	*		*	*	kHz
G = 1000		2.5			*	*		*	*		*	*	kHz
Small Signal, ±1% Flatness													
G = 1		20			*	*		*	*		*	*	kHz
G = 10		10			*	*		*	*		*	*	kHz
G = 100		1			*	*		*	*		*	*	kHz
G = 1000		200			*	*		*	*		*	*	Hz
Full Power, G = 1 to 100		6.4			*	*		*	*		*	*	Hz
Slew Rate, G = 1 to 100		0.4		*	*	*		*	*		*	*	V/μs
Settling Time (0.1%)													
G = 1		30	40		*	*		*	*		*	*	μs
G = 100		40	55		*	*		*	*		*	*	μs
G = 1000		350	470		*	*		*	*		*	*	μs
Settling Time (0.01%)													
G = 1		30	45		*	*		*	*		*	*	μs
G = 100		50	70		*	*		*	*		*	*	μs
G = 1000		500	650		*	*		*	*		*	*	μs
<b>POWER SUPPLY</b>													
Rated Voltage		±15			*	*		*	*		*	*	V
Voltage Range	±5		±20		*	*		*	*		*	*	V
Current, Quiescent <sup>(4)</sup>		±6.7	±8.5		*	*		*	*		*	*	mA
<b>TEMPERATURE RANGE<sup>(6)</sup></b>													
Specification	-25		+85	-55		+125	*	*	*	0	+70		°C
Operation	-55		+125	*		*	*	*	*	-25	+85		°C
Storage	-65		+150	*		*	*	*	*	-40	+85		°C

## PIN CONFIGURATIONS



## ORDERING INFORMATION

PRODUCT	PACKAGE	TEMPERATURE RANGE
INA101AM	10-Pin Metal TO-100	-25°C to +85°C
INA101CM	10-Pin Metal TO-100	-25°C to +85°C
INA101AG	14-Pin Ceramic DIP	-25°C to +85°C
INA101CG	14-Pin Ceramic DIP	-25°C to +85°C
INA101HP	14-Pin Plastic DIP	0°C to +70°C
INA101KU	SOL-16 Surface-Mount	0°C to +70°C
INA101SG	14-Pin Ceramic DIP	-55°C to +125°C
INA101SM	10-Pin Metal TO-100	-55°C to +125°C

## ABSOLUTE MAXIMUM RATINGS

Supply Voltage	±20V
Power Dissipation	600mW
Input Voltage Range	±V <sub>CC</sub>
Output Short Circuit (to ground)	Continuous
Operating Temperature M, G Package	-55°C to +125°C
P, U Package	-25°C to +85°C
Storage Temperature M, G Package	-65°C to +150°C
P, U Package	-40°C to +85°C
Lead Temperature (soldering, 10s) M, G, P Package	+300°C
Lead Temperature (wave soldering, 3s) U Package	+260°C

## PACKAGE INFORMATION

PRODUCT	PACKAGE	PACKAGE DRAWING NUMBER <sup>(1)</sup>
INA101AM	10-Pin Metal TO-100	007
INA101CM	10-Pin Metal TO-100	007
INA101AG	14-Pin Ceramic DIP	169
INA101CG	14-Pin Ceramic DIP	169
INA101HP	14-Pin Plastic DIP	010
INA101KU	SOL-16 Surface-Mount	211
INA101SG	14-Pin Ceramic DIP	169
INA101SM	10-Pin Metal TO-100	007

NOTE: (1) For detailed drawing and dimension table, please see end of data sheet, or Appendix D of Burr-Brown IC Data Book.



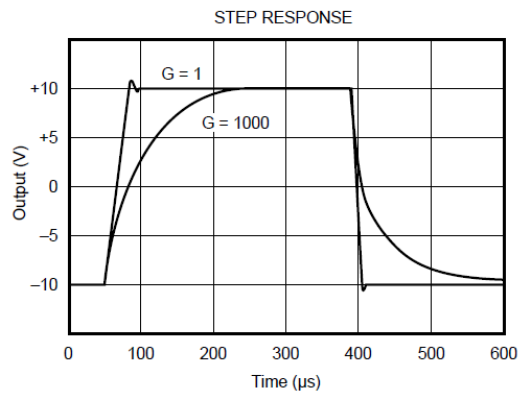
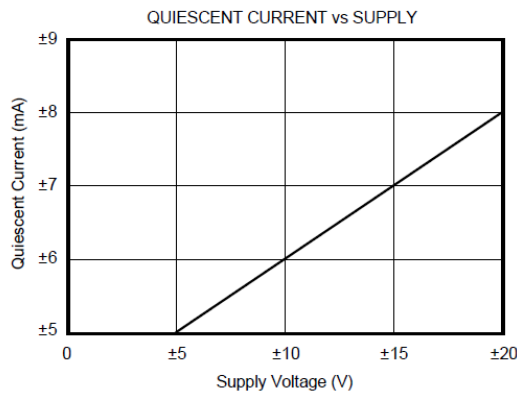
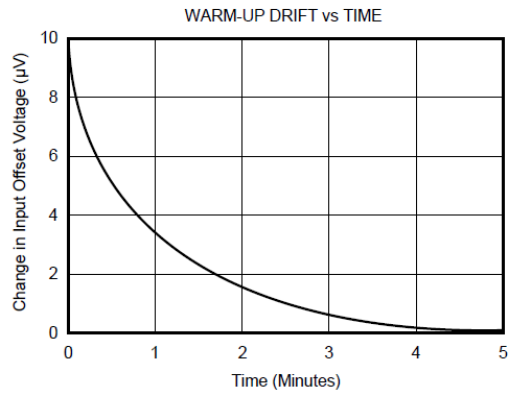
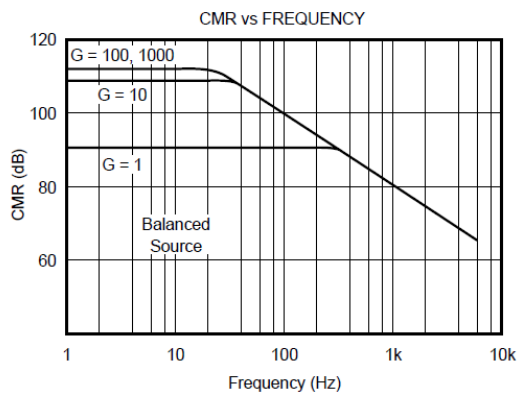
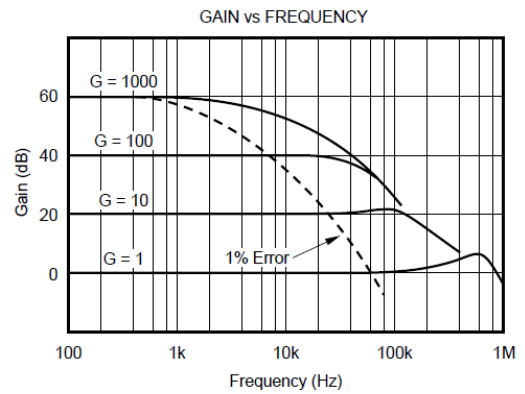
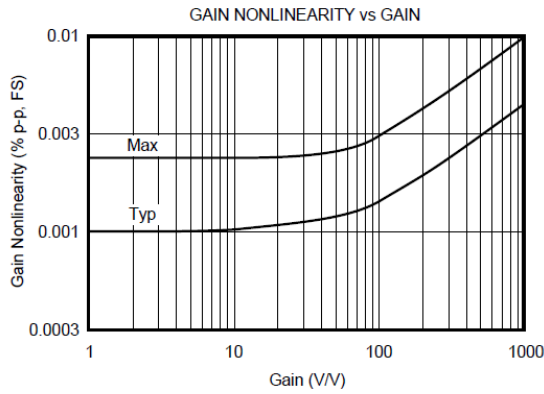
## ELECTROSTATIC DISCHARGE SENSITIVITY

This integrated circuit can be damaged by ESD. Burr-Brown recommends that all integrated circuits be handled with appropriate precautions. Failure to observe proper handling and installation procedures can cause damage.

ESD damage can range from subtle performance degradation to complete device failure. Precision integrated circuits may be more susceptible to damage because very small parametric changes could cause the device not to meet its published specifications.

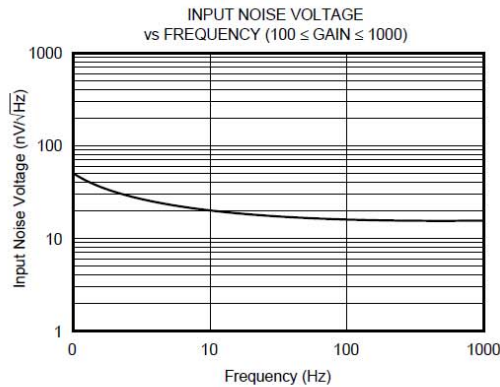
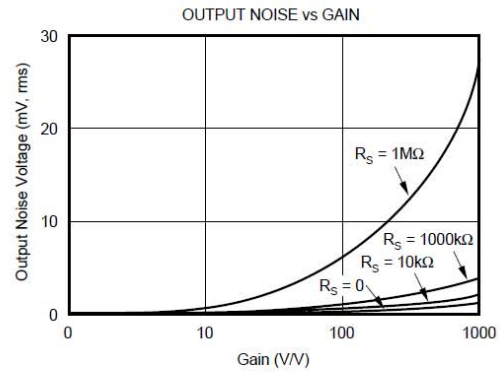
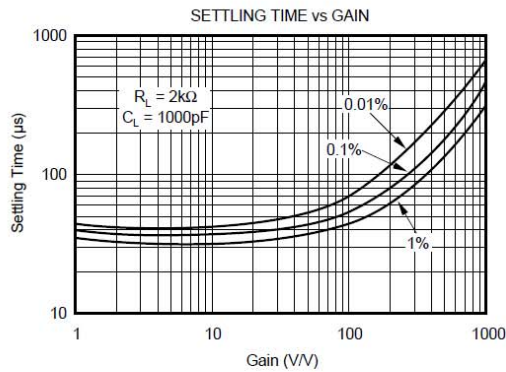
# TYPICAL PERFORMANCE CURVES

At +25°C,  $V_{CC} = \pm 15V$  unless otherwise noted.



## TYPICAL PERFORMANCE CURVES (CONT)

At +25°C,  $V_{CC} = \pm 15V$  unless otherwise noted.



## APPLICATION INFORMATION

Figure 1 shows the basic connections required for operation of the INA101. (Pin numbers shown are for the TO-100 metal package.) Applications with noisy or high impedance power supplies may require decoupling capacitors close to the device pins as shown.

The output is referred to the output Common terminal which is normally grounded. This must be a low-impedance connection to assure good common-mode rejection. A resistance greater than  $0.1\Omega$  in series with the Common pin will cause common-mode rejection to fall below 106dB.

### SETTING THE GAIN

Gain of the INA101 is set by connecting a single external resistor,  $R_G$ :

$$G = 1 + \frac{40k\Omega}{R_G} \quad (1)$$

The  $40k\Omega$  term in equation (1) comes from the sum of the two internal feedback resistors. These are on-chip metal film resistors which are laser trimmed to accurate absolute values. The accuracy and temperature coefficient of these resistors are included in the gain accuracy and drift specifications of the INA101.

The stability and temperature drift of the external gain setting resistor,  $R_G$ , also affects gain.  $R_G$ 's contribution to gain accuracy and drift can be directly inferred from the gain equation (1). Low resistor values required for high gain can make wiring resistance important. Sockets add to the wiring resistance which will contribute additional gain error (possibly an unstable gain error) in gains of approximately 100 or greater. The gain sense connections on the DIP and SOL-16 packages (see Figure 2) reduce the gain error produced by wiring or socket resistance.

### OFFSET TRIMMING

The INA101 is laser trimmed for low offset voltage and drift. Most applications require no external offset adjustment. Figure 2 shows connection of an optional potentiometer connected to the Offset Adjust pins for trimming the input offset voltage. (Pin numbers shown are for the DIP package.) Use this adjustment to null the offset voltage in high gain ( $G \geq 100$ ) with both inputs connected to ground. Do not use this adjustment to null offset produced by the source or other system offset since this will increase the offset voltage drift by  $0.3\mu\text{V}/^\circ\text{C}$  per  $100\mu\text{V}$  of adjusted offset.

Offset of the output amplifier usually dominates when the INA101 is used in unity gain ( $G = 1$ ). The output offset

voltage can be adjusted with the optional trim circuit connected to the Common pin as shown in Figure 2. The voltage applied to Common terminal is summed with the output. Low impedance must be maintained at this node to assure good common-mode rejection. The op amp connected as a buffer provides low impedance.

### THERMAL EFFECTS ON OFFSET VOLTAGE

To achieve lowest offset voltage and drift, prevent air currents from circulating near the INA101. Rapid changes in temperature will produce a thermocouple effect on the package leads that will degrade offset voltage and drift. A shield or cover that prevents air currents from flowing near the INA101 will assure best performance.

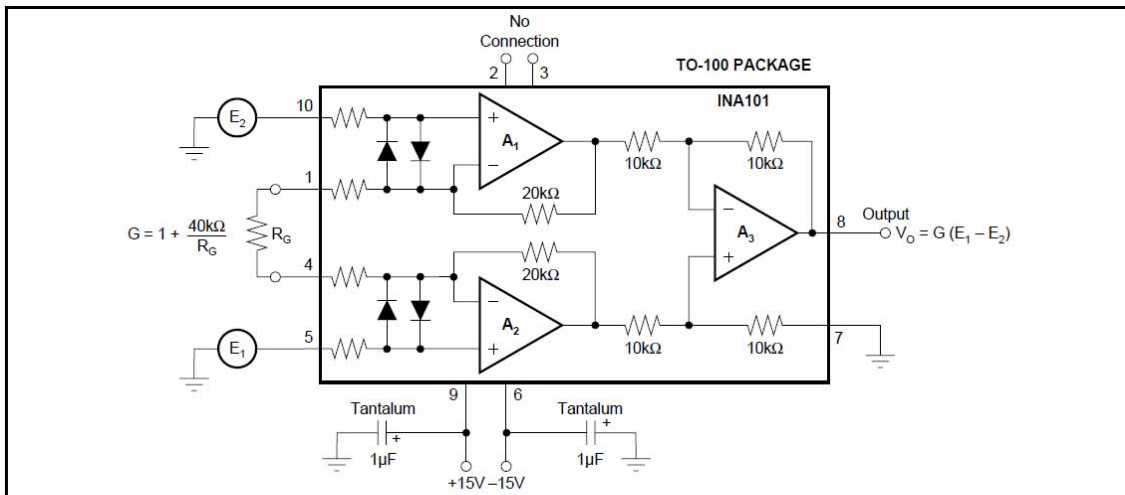


FIGURE 1. Basic Connections.

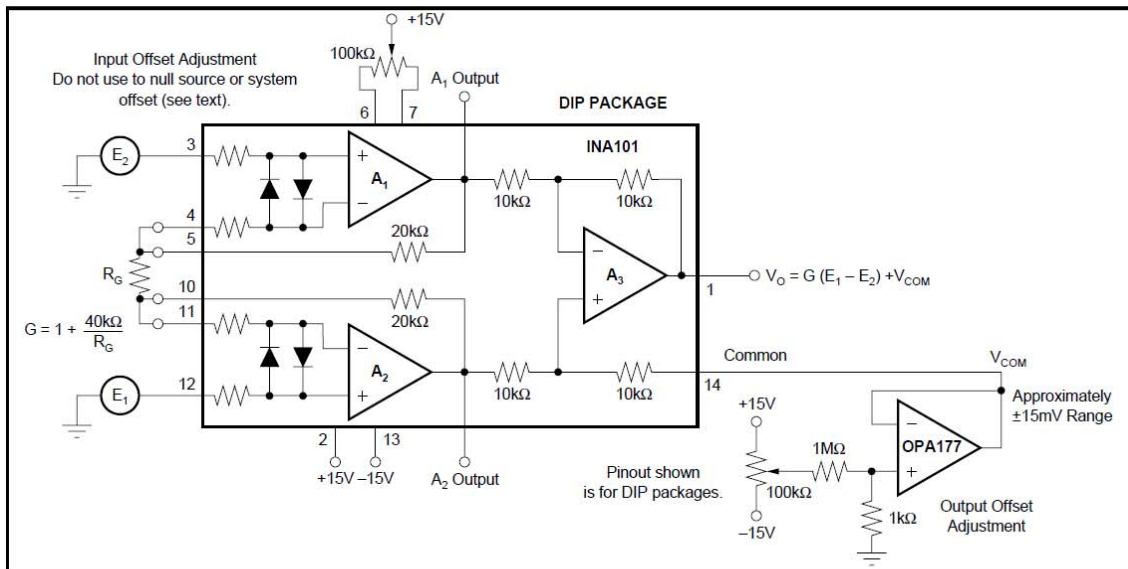
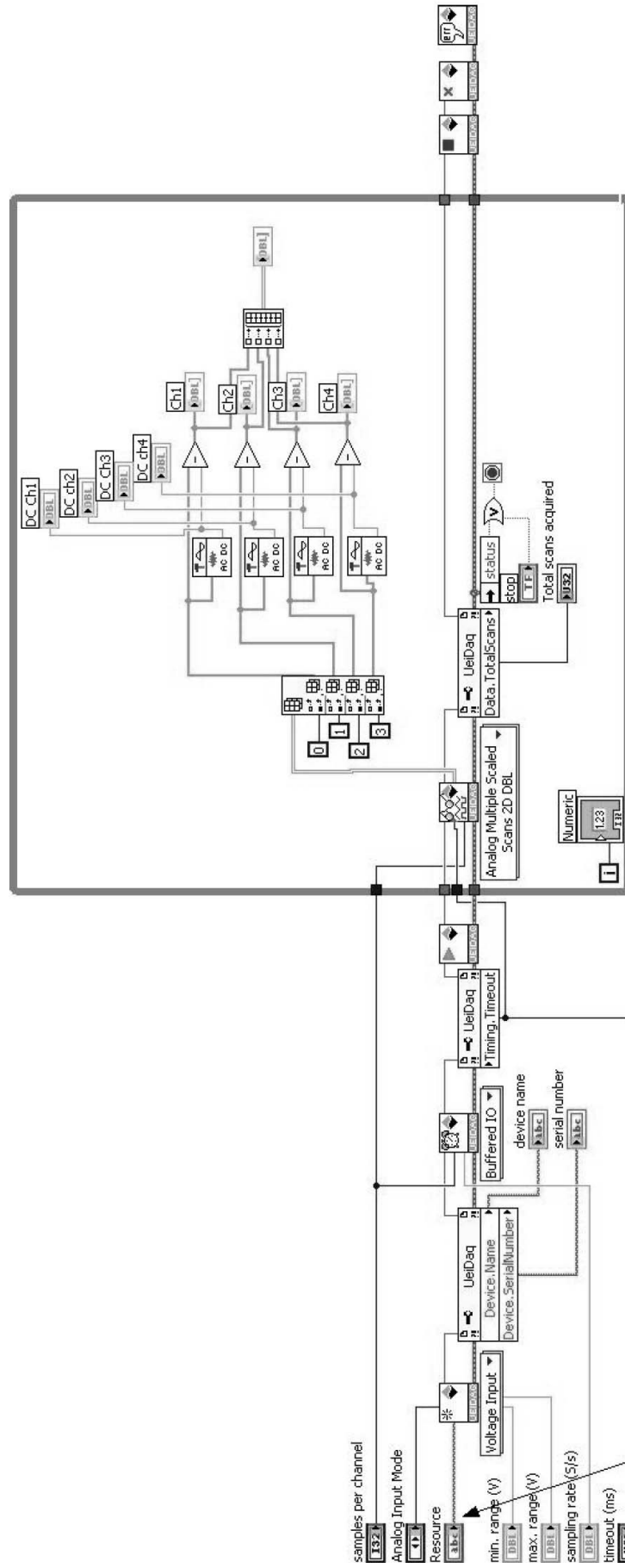


FIGURE 2. Optional Trimming of Input and Output Offset Voltage.

# E. Ciliary Monitoring Program to maneuver both cilia on 2D plane using Lab View



## BIBLIOGRAPHY

**Alric J, Lavergne J and Rappaport F.** Redox and ATP control of photosynthetic cyclic electron flow in *Chlamydomonas reinhardtii* (I) aerobic conditions. *Biochim Biophys Acta* 1797: 1: 44-51, 2010.

**Balkos KD and Colman B.** Mechanism of CO<sub>2</sub> acquisition in an acid-tolerant *Chlamydomonas*. *Plant Cell Environ* 30: 6: 745-752, 2007.

**Bendix S.** Phototaxis. *Bot Rev* 26: 2: 145-208, 1960.

**Bessen M, Fay RB and Witman GB.** Calcium Control of Waveform in Isolated Flagellar Axonemes of *Chlamydomonas*. *J Cell Biol* 86: 2: pp. 446-455, 1980.

**Berg JM, Tymoczko JL, Stryer L, Stryer L and Biochemistry.** *Biochemistry*. New York: W.H. Freeman, 2002.

**Boonyareth M, Saranak J, Pinthong D, Sanvarinda Y and Foster K.** Roles of cyclic AMP in regulation of phototaxis in *Chlamydomonas reinhardtii*. *Biologia* 64: 6: 1058-1065, 2009.

**Bothwell JH, Brownlee C, Hetherington AM, Ng CK, Wheeler GL and McAinsh MR.** Biolistic delivery of Ca<sup>2+</sup> dyes into plant and algal cells. *Plant J* 46: 2: 327-335, 2006.

**Braun FJ and Hegemann P.** Direct measurement of cytosolic calcium and pH in living *Chlamydomonas reinhardtii* cells. *Eur J Cell Biol* 78: 3: 199-208, 1999.

**Brokaw CJ.** Control of flagellar bending: a new agenda based on dynein diversity. *Cell Motil Cytoskeleton* 28: 3: 199-204, 1994.

**Brokaw CJ and Kamiya R.** Bending patterns of *Chlamydomonas* flagella: IV. Mutants with defects in inner and outer dynein arms indicate differences in dynein arm function.

*Cell Motil Cytoskeleton* 8: 1: 68-75, 1987.

**Budde RJ and Randall DD.** Light as a signal influencing the phosphorylation status of plant proteins. *Plant Physiol* 94: 4: 1501-1504, 1990.

**Buder J.** Zur Kenntnis der phototaktischen Richtungsbewegungen. *Jahrbuch wiss Botanik* 58: 105-220, 1917.

**Bullen A and Saggau P.** High-speed, random-access fluorescence microscopy: II. Fast quantitative measurements with voltage-sensitive dyes. *Biophys J* 76: 4: 2272-2287, 1999.

**Burgess SA, Walker ML, Sakakibara H, Knight PJ and Oiwa K.** Dynein structure and power stroke. *Nature* 421: 6924: 715-718, 2003.

**Campbell NA.** *Biology*. Menlo Park, California: Benjamin/Cummings Pub. Co, 1996.

**Campbell NA and Reece JB.** *Biology*. San Francisco: Pearson Benjamin Cummings, 2009, p. 1267.

**Cao W, Haig-Ladewig L, Gerton GL and Moss SB.** Adenylate kinases 1 and 2 are part of the accessory structures in the mouse sperm flagellum. *Biol Reprod* 75: 4: 492-500, 2006.

**Capano CD.** *Photo-Induced Current Measurements in Chlamydomonas Cell*

*Suspensions* (B.Sc. Project). Department of Physics, Syracuse University, Syracuse, New York: 2005.

**Deininger W, Kröger P, Hegemann U, Lottspeich F and Hegemann P.**

Chlamyrodopsin represents a new type of sensory photoreceptor. *EMBO Journal* 14: 23: 5849-5858, 1995.

**Dzeja PP, Chung S and Terzic A.** Integration of Adenylate kinase and Glycolytic and Glycogenolytic Circuits in Cellular Energetics. In *Moleculaar System Bioenergetics: Energy for Life*. Edited by V. Saks, KGaA, Weinheim, Wiley-VCH: 265-301, 2007.

**Dzeja PP and Terzic A.** Adenylate kinase and AMP signaling networks: Metabolic monitoring, signal communication and body energy sensing. *Int J Mol Sci* 10: 4: 1729-1772, 2009.

**Ehlenbeck S, Gradmann D, Braun FJ and Hegemann P.** Evidence for a light-induced H(+) conductance in the eye of the green alga *Chlamydomonas reinhardtii*. *Biophys J* 82: 2: 740-751, 2002.

**Ferris CD and Snyder SH.** IP3 receptors. Ligand-activated calcium channels in multiple forms. *Adv Second Messenger Phosphoprotein Res* 26: 95-107, 1992.

**Fliegauf M, Benzing T and Omran H.** When cilia go bad: cilia defects and ciliopathies. *Nat Rev Mol Cell Biol* 8: 11: 880-893, 2007.

**Fluhler E, Burnham VG and Loew LM.** Spectra, membrane binding, and potentiometric responses of new charge shift probes. *Biochemistry* 24: 21: 5749-5755, 1985.

**Forti G, Furia A, Bombelli P and Finazzi G.** In vivo changes of the oxidation-reduction state of NADP and of the ATP/ADP cellular ratio linked to the photosynthetic activity in *Chlamydomonas reinhardtii*. *Plant Physiol* 132: 3: 1464-1474, 2003.

**Foster KW, Josef K, Saranak J and Tuck N.** Dynamics of a sensory signaling network in a unicellular eukaryote. *Conf Proc IEEE Eng Med Biol Soc* 1: 252-255, 2006.

**Foster KW, Saranak J and Patel N.** A rhodopsin is the functional photoreceptor for phototaxis in the unicellular eukaryote *Chlamydomonas*. *Nature* 311: 5988: 756-759, 1984.

**Foster KW and Smyth RD.** Light Antennas in phototactic algae. *Microbiol Rev* 44: 4: 572-630, 1980.

**Fujiu K, Nakayama Y, Yanagisawa A, Sokabe M and Yoshimura K.** *Chlamydomonas* CAV2 Encodes a Voltage- Dependent Calcium Channel Required for the Flagellar Waveform Conversion. *Curr Biol* 19: 2: 133-139, 2009.

**Gemel J and Randall DD.** Light regulation of leaf mitochondrial pyruvate dehydrogenase complex : role of photorespiratory carbon metabolism. *Plant Physiol* 100: 2: 908-914, 1992.

**Gray J.** A New Method of Recording Ciliary Movement. *Nature* 123: 3090: 86, 1929.

**Gross E, Bedlack RS,Jr and Loew LM.** Dual-wavelength ratiometric fluorescence measurement of the membrane dipole potential. *Biophys J* 67: 1: 208-216, 1994.

**Habermacher G and Sale WS.** Regulation of dynein-driven microtubule sliding by an axonemal kinase and phosphatase in *Chlamydomonas* flagella. *Cell Motil Cytoskeleton* 32: 2: 106-109, 1995.

**Harris EH.** *Chlamydomonas* as a Model Organism. *Annu Rev Plant Physiol Plant Mol Biol* 52: 363-406, 2001.

**Harris DJ.** *Bioenergetics at a glance*. Oxford, England; Blackwell Science, 1995, p. 116.

- Harz H and Hegemann P.** Rhodopsin-regulated calcium currents in *Chlamydomonas*. *Nature* 351: 6326: 489-491, 1991.
- Harz H, Nonnengässer C and Hegemann P.** The photoreceptor current of the green alga *Chlamydomonas*. *Philos Trans R Soc Lond Ser B* 338: 39-52, 1992.
- Haupt ,Wolfgang and Bretz ,Norbert.** Short-term reactions of phytochrome in *Mougeotia*? *Planta* 1: 1-3, 1976.
- Holland EM, Braun FJ, Nonnengasser C, Harz H and Hegemann P.** The nature of rhodopsin-triggered photocurrents in *Chlamydomonas*. I. Kinetics and influence of divalent ions. *Biophys J* 70: 2: 924-931, 1996.
- Holland EM, Harz H, Uhl R and Hegemann P.** Control of phobic behavioral responses by rhodopsin-induced photocurrents in *Chlamydomonas*. *Biophys J* 73: 3: 1395-1401, 1997.
- Horst CJ and Witman GB.** ptx1, a nonphototactic mutant of *Chlamydomonas*, lacks control of flagellar dominance. *J Cell Biol* 120: 3: 733-741, 1993.
- Howard DR, Habermacher G, Glass DB, Smith EF and Sale WS.** Regulation of *Chlamydomonas* flagellar dynein by an axonemal protein kinase. *J Cell Biol* 127: 6 Pt 1: 1683-1692, 1994.
- Ianowski JP and O'Donnell MJ.** Electrochemical gradients for Na<sup>+</sup>, K<sup>+</sup>, Cl<sup>-</sup> and H<sup>+</sup> across the apical membrane in Malpighian (renal) tubule cells of *Rhodnius prolixus*. *J Exp Biol* 209: Pt 10: 1964-1975, 2006.
- Jackson MB.** *Molecular and cellular biophysics*. Cambridge ; New York: Cambridge University Press, 2006, p. 512.

- Johnson DE, Johnson J. R. and Moore HP.** *A handbook of active filters*. Englewood Cliffs, N.J.: Prentice-Hall, 1980, 244 p.
- Josef K, Saranak J and Foster KW.** Linear systems analysis of the ciliary steering behavior associated with negative-phototaxis in *Chlamydomonas reinhardtii*. *Cell Motil Cytoskeleton* 63: 12: 758-777, 2006.
- Josef K.** The nonlinear phototaxis signaling network of *Chlamydomonas* investigated by observing ciliary responses of individual cells to green and red light. Ph.D. Dissertation, Syracuse University, Syracuse, New York, 2005.
- Josef K, Saranak J and Foster KW.** Ciliary behavior of a negatively phototactic *Chlamydomonas reinhardtii*. *Cell Motil Cytoskeleton* 61: 2: 97-111, 2005a.
- Josef K, Saranak J and Foster KW.** An electro-optic monitor of the behavior of *Chlamydomonas reinhardtii* cilia. *Cell Motil Cytoskeleton* 61: 2: 83-96, 2005b.
- Josef K.** Electro-optical monitoring of the flagella of *Chlamydomonas* algae. Master's thesis, Syracuse University, 1994.
- Kagami O and Kamiya R.** Translocation and rotation of microtubules caused by multiple species of *Chlamydomonas* inner-arm dynein. *J Cell Sci* 103: 3: 653-664, 1992.
- Kamiya R, Kurimoto E and Muto E.** Two types of *Chlamydomonas* flagellar mutants missing different components of inner-arm dynein. *J Cell Biol* 112: 3: 441-447, 1991.
- Kamiya R and Okamoto M.** A mutant of *Chlamydomonas reinhardtii* that lacks the flagellar outer dynein arm but can swim. *J Cell Sci* 74: 181-191, 1985.
- Kamiya R and Witman GB.** Submicromolar levels of calcium control the balance of beating between the two flagella in demembranated models of *Chlamydomonas*. *J Cell Biol* 98: 1: 97-107, 1984.

**King SM and Kamiya.** Axonemal Dyneins: Assembly, Structure, and Force Generation. In: *The Chlamydomonas sourcebook: Cell motility and behavior*, edited by Witman GB, Burlington, Massachusetts, Academic Press, 2009, p. 131-142.

**Kondo T, Johnson CH and Hastings JW.** Action Spectrum for Resetting the Circadian Phototaxis Rhythm in the CW15 Strain of Chlamydomonas: I. Cells in Darkness. *Plant Physiol* 95: 1: 197-205, 1991.

**Kröger P and Hegemann P.** Photophobic responses and phototaxis in Chlamydomonas are triggered by a single rhodopsin photoreceptor. *Plant Physiol* 102: 1: 5-9, 1994.

**Kromer S and Heldt HW.** On the Role of Mitochondrial Oxidative Phosphorylation in Photosynthesis Metabolism as Studied by the Effect of Oligomycin on Photosynthesis in Protoplasts and Leaves of Barley (*Hordeum vulgare*). *Plant Physiol* 95: 4: 1270-1276, 1991.

**Kromer S, Malmberg G and Gardestrom P.** Mitochondrial Contribution to Photosynthetic Metabolism (A Study with Barley (*Hordeum vulgare* L.) Leaf Protoplasts at Different Light Intensities and CO<sub>2</sub> Concentrations). *Plant Physiol* 102: 3: 947-955, 1993.

**Lehtonen J and Saari J.** Illumination does not affect the membrane potential or the plasma membrane H<sup>+</sup>-ATPase activity in *Micrasterias*. *Physiol Plantarum* 110: 4: 436-442, 2000.

**Leigh RA and Jones RGW.** A Hypothesis Relating Critical Potassium Concentrations for Growth to the Distribution and Functions of this Ion in the Plant Cell. *New Phytol* 97: 1: 1-13, 1984.

**Litvin FF, Sineshchekov OA and Sineshchekov VA.** Photoreceptor electric potential in the phototaxis of the alga *Haematococcus pluvialis*. *Nature* 271: 5644: 476-478, 1978.

**Lis RV and Atteia A.** Control of Mitochondrial Function via Photosynthetic Redox Signals. *Photosynth Res* 79: 2: 133-148, 2004.

**Loew LM, Cohen LB, Dix J, Fluhler EN, Montana V, Salama G and Wu JY.** A naphthyl analog of the aminostyryl pyridinium class of potentiometric membrane dyes shows consistent sensitivity in a variety of tissue, cell, and model membrane preparations. *J Membr Biol* 130: 1: 1-10, 1992.

**Malhotra B and Glass A.** Potassium Fluxes in *Chlamydomonas reinhardtii* (I. Kinetics and Electrical Potentials). *Plant Physiol* 108: 4: 1527-1536, 1995a.

**Malhotra B and Glass A.** Potassium Fluxes in *Chlamydomonas reinhardtii* (II. Compartmental Analysis). *Plant Physiol* 108: 4: 1537-1545, 1995b.

**McAinsh MR and Pittman JK.** Shaping the calcium signature. *New Phytol* 181: 2: 275-294, 2009.

**Memon RA, Saccomani M and Glass ADM.** Efficiency of Potassium Utilization by Barley Varieties: The Role of Subcellular Compartmentation. *J Exp Bot* 36: 12: 1860-1876, 1985.

**Merchant SS, Prochnik SE, Vallon O, Harris EH, Karpowicz SJ, Witman GB, Terry A, Salamov A, Fritz-Laylin LK, Marechal-Drouard L, Marshall WF, Qu L, Nelson DR, Sanderfoot AA, Spalding MH, Kapitonov VV, Ren Q, Ferris P, Lindquist E, Shapiro H, Lucas SM, Grimwood J, Schmutz J, Cardol P, Cerutti H, Chanfreau G, Chen C, Cognat V, Croft MT, Dent R, Dutcher S, Fernandez E, Fukuzawa H, Gonzalez-Ballester D, Gonzalez-Halphen D, Hallmann A, Hanikenne**

**M, Hippler M, Inwood W, Jabbari K, Kalanon M, Kuras R, Lefebvre PA, Lemaire SD, Lobanov AV, Lohr M, Manuell A, Meier I, Mets L, Mittag M, Mittelmeier T, Moroney JV, Moseley J, Napoli C, Nedelcu AM, Niyogi K, Novoselov SV, Paulsen IT, Pazour G, Purton S, Ral J, Riano-Pachon DM, Riekhof W, Rymarquis L, Schroda M, Stern D, Umen J, Willows R, Wilson N, Zimmer SL, Allmer J, Balk J, Bisova K, Chen C, Elias M, Gendler K, Hauser C, Lamb MR, Ledford H, Long JC, Minagawa J, Page MD, Pan J, Pootakham W, Roje S, Rose A, Stahlberg E, Terauchi AM, Yang P, Ball S, Bowler C, Dieckmann CL, Gladyshev VN, Green P, Jorgensen R, Mayfield S, Mueller-Roeber B, Rajamani S, Sayre RT, Brokstein P, Dubchak I, Goodstein D, Hornick L, Huang YW, Jhaveri J, Luo Y, Martinez D, Ngau WCA, Otilar B, Poliakov A, Porter A, Szajkowski L, Werner G, Zhou K, Grigoriev IV, Rokhsar DS and Grossman AR.** The Chlamydomonas Genome Reveals the Evolution of Key Animal and Plant Functions. *Science* 318: 5848: 245-250, 2007.

**Messerli MA, Amaral-Zettler LA, Zettler E, Jung SK, Smith PJ and Sogin ML.** Life at acidic pH imposes an increased energetic cost for a eukaryotic acidophile. *J Exp Biol* 208: Pt 13: 2569-2579, 2005.

**Metzler DE and Metzler CM.** *Biochemistry: the chemical reactions of living cells*. San Diego, Calif.: Harcourt/Academic Press, 2001.

**Michelet L, Zaffagnini M and Lemaire D.** Thioredoxins and Related Proteins. In: *The Chlamydomonas sourcebook: Organellar and metabolic processes*, edited by Stern DB. London: Academic Press, 2009, p. 401-443.

- Mitchell BF, Pedersen LB, Feely M, Rosenbaum JL and Mitchell DR.** ATP Production in *Chlamydomonas reinhardtii* Flagella by Glycolytic Enzymes. *Mol Biol Cell* 16: 10: 4509-4518, 2005.
- Mitchell DR.** Orientation of the central pair complex during flagellar bend formation in *Chlamydomonas*. *Cell Motil Cytoskeleton* 56: 2: 120-129, 2003.
- Mitchell DR and Rosenbaum JL.** A motile *Chlamydomonas* flagellar mutant that lacks outer dynein arms. *J Cell Biol* 100: 4: 1228-1234, 1985.
- Mittag M, Kiaulehn S and Johnson CH.** The circadian clock in *Chlamydomonas reinhardtii*. What is it for? What is it similar to? *Plant Physiol* 137: 2: 399-409, 2005.
- Moncada S and Erusalimsky JD.** Does nitric oxide modulate mitochondrial energy generation and apoptosis? *Nat Rev Mol Cell Biol* 3: 3: 214-220, 2002.
- Montana V, Farkas DL and Loew LM.** Dual-wavelength ratiometric fluorescence measurements of membrane potential. *Biochemistry* 28: 11: 4536-4539, 1989.
- Moon YJ, Park YM, Chung YH and Choi JS.** Calcium is involved in photomovement of cyanobacterium *Synechocystis* sp. PCC 6803. *Photochem Photobiol* 79: 1: 114-119, 2004.
- Morand LZ, Kidd DG and Lagarias JC.** Phytochrome levels in the green alga *Mesotaenium caldariorum* are light regulated. *Plant Physiol* 101: 1: 97-104, 1993.
- Morel-Laurens N.** Calcium control of phototactic orientation in *Chlamydomonas reinhardtii*: sign and strength of response. *Photochem Photobiol* 45: 1: 119-128, 1987.
- Movassagh T, Bui KH, Sakakibara H, Oiwa K and Ishikawa T.** Nucleotide-induced global conformational changes of flagellar dynein arms revealed by in situ analysis. *Nat Struct Mol Biol* 17: 6: 761-767, 2010.

- Murphy E, Imahashi K and Steenbergen C.** Bcl-2 regulation of mitochondrial energetics. *Trends Cardiovasc Med* 15: 8: 283-290, 2005.
- Murrill PW.** *Automatic control of processes*. Scranton: International Textbook Co, 1967, p. 467.
- Nagel G, Ollig D, Fuhrmann M, Kateriya S, Musti AM, Bamberg E and Hegemann P.** Channelrhodopsin-1: a light-gated proton channel in green algae. *Science* 296: 5577: 2395-2398, 2002.
- Nagel G, Szellas T, Huhn W, Kateriya S, Adeishvili N, Berthold P, Ollig D, Hegemann P and Bamberg E.** Channelrhodopsin-2, a directly light-gated cation-selective membrane channel. *Proc Natl Acad Sci U S A* 100: 24: 13940-13945, 2003.
- Nelson DL and Cox MM.** *Lehninger principles of biochemistry*. New York: Worth Publishers, 3<sup>rd</sup> Edition, 2000.
- Nonnengasser C, Holland EM, Harz H and Hegemann P.** The nature of rhodopsin-triggered photocurrents in *Chlamydomonas*. II. Influence of monovalent ions. *Biophys J* 70: 2: 932-938, 1996.
- Nultsch ,W.** Effect of external factors on phototaxis of *Chlamydomonas reinhardtii*. *Arch Microbiol* 1: 93-99, 1979.
- Nultsch W and Häder D.** Photomovement of motile microorganisms. *Photochem Photobiol* 29: 2: 423-437, 1979.
- Nultsch W and Throm G.** Effect of external factors on phototaxis of *Chlamydomonas reinhardtii*. I. Light. *Arch Microbiol* 103: 2: 175-179, 1975.

- Okita N, Isogai N, Hirono M, Kamiya R and Yoshimura K.** Phototactic activity in *Chlamydomonas* 'non-phototactic' mutants deficient in Ca<sup>2+</sup>-dependent control of flagellar dominance or in inner-arm dynein. *J Cell Sci* 118: 3: 529-537, 2005.
- Patel-King RS, Benashski SE and King SM.** A bipartite Ca<sup>2+</sup>-regulated nucleoside-diphosphate kinase system within the *Chlamydomonas* flagellum. The regulatory subunit p72. *J Biol Chem* 277: 37: 34271-34279, 2002.
- Pazour GJ, Agrin N, Leszyk J and Witman GB.** Proteomic analysis of a eukaryotic cilium. *J Cell Biol* 170: 1: 103-113, 2005.
- Petridou S, Foster K and Kindle K.** Light induces accumulation of isocitrate lyase mRNA in a carotenoid-deficient mutant of *Chlamydomonas reinhardtii*. *Plant Mol Biol* 33: 3: 381-392, 1997.
- Pfeffer W.** *Pflanzenphysiologie*. Leipzig, 1904.
- Pittman JK, Edmond C, Sunderland PA and Bray CM.** A cation-regulated and proton gradient-dependent cation transporter from *Chlamydomonas reinhardtii* has a role in calcium and sodium homeostasis. *J Biol Chem* 284: 1: 525-533, 2009.
- Puntoni S, Marangoni R, Gioffré D and Colombetti G.** Effects of Ca<sup>2+</sup> and K<sup>+</sup> on motility and photomotility of the marine ciliate *Fabrea salina*. *J Photochem Photobiol B* 43: 3: 204-208, 1998.
- Racey TJ, Hallett R and Nickel B.** A quasi-elastic light scattering and cinematographic investigation of motile *Chlamydomonas reinhardtii*. *Biophys J* 35: 3: 557-571, 1981.
- Ray J.** *Historia Plantarum*. 1693.

**Reisdorph NA and Small GD.** The CPH1 gene of *Chlamydomonas reinhardtii* encodes two forms of cryptochrome whose levels are controlled by light-induced proteolysis.

*Plant Physiol* 134: 4: 1546-1554, 2004.

**Rüffer U and Nultsch W.** Flagellar photoresponses of ptx1, a nonphototactic mutant of *Chlamydomonas*. *Cell Motil Cytoskeleton* 37: 2: 111-119, 1997.

**Rüffer U and Nultsch W.** Flagellar photoresponses of *Chlamydomonas* cells held on micropipettes: III Shock response. *Bot Acta* 108: 169-276, 1995.

**Rüffer U and Nultsch W.** Flagellar photoresponses of *Chlamydomonas* cells held on micropipettes: II. Change in flagellar beat pattern. *Cell Motil Cytoskeleton* 18: 4: 269-278, 1991.

**Rüffer U and Nultsch W.** Flagellar photoresponses of *Chlamydomonas* cells held on micropipettes: I. Change in flagellar beat frequency. *Cell Motil Cytoskeleton* 15: 3: 162-167, 1990.

**Rüffer U and Nultsch W.** Comparison of the beating of cis- and trans-flagella of *Chlamydomonas* cells held on micropipettes. *Cell Motil Cytoskeleton* 7: 1: 87-93, 1987.

**Sanders D, Brownlee C and Harper JF.** Communicating with calcium. *Plant Cell* 11: 4: 691-706, 1999.

**Saks VA.** *Molecular system bioenergetics :energy for life*. Weinheim: Wiley-VCH, 2007, p. 604.

**Schaller K, David R and Uhl R.** How *Chlamydomonas* keeps track of the light once it has reached the right phototactic orientation. *Biophys J* 73: 3: 1562-1572, 1997.

- Siedow JN and Day DA.** *Respiration and photorespiration*, in *Biochemistry and Molecular Biology of Plants*, edited by B. B. Buchanan, W. Gruissem and R. L. Jones, Eds. American Society of Plant Physiologists: 676-728, 2000.
- Sims OL and Saranak J.** Effects of external potassium concentrations and green light on phototaxis in *Chlamydomonas*. Undergraduate project (BIO 460), Syracuse University, Syracuse, New York. 2006.
- Sineshchekov OA, Govorunova EG and Spudich JL.** Photosensory functions of channelrhodopsins in native algal cells. *Photochem Photobiol* 85: 2: 556-563, 2009.
- Sineshchekov OA and Govorunova EG.** Chapter 9 Electrical events in photomovement of green flagellated algae. In: *Comprehensive Series in Photosciences*, edited by Donat-P. Häder and A.M. BreureElsevier Science B.V., 2001, p. 245-280.
- Sineshchekov OA and Govorunova EG.** Rhodopsin-mediated photosensing in green flagellated algae. *Trends Plant Sci* 4: 2: 58-63, 1999.
- Sineshchekov OA.** Photoreception in unicellular flagellates: Bioelectric phenomena in phototaxis. In: *Light in Biology and Medicine II*, edited by Douglas RH. New York: Plenum Press, 1991, p. 523-532.
- Sineshchekov OA, Litvin FF and Keszthelyi L.** Two components of photoreceptor potential in phototaxis of the flagellated green alga *Haematococcus pluvialis*. *Biophys J* 57: 1: 33-39, 1990.
- Sineshchekov OA and Litvin FF.** The mechanisms of phototaxis in microorganisms. In: *Molecular Mechanisms of Biological Action of Optic Radiation*, edited by Rubin AB. Nauka, Moscow, 1988, p. 412-427.

- Sineshchekov OA.** The investigation of the photoelectric processes in phototaxis of a green alga. *Ph D Thesis Moscow State University, Moscow* 1978.
- Smith E, Howard L, and Dymek E.** Image series: Algae TEM. E.M. Lab image gallery, Electron microscope facility, Dartmouth College [Public Domain, last modified on 6 April 2001]. <http://remf.dartmouth.edu/images/algaeTEM/source/4.html> [retrieved on 31 December 2009].
- Smith E, Howard L, and Dymek E.** Image series: Algae SEM. E.M. Lab image gallery, Electron microscope facility, Dartmouth College [Public Domain, last modified on 6 April 2001]. <http://remf.dartmouth.edu/images/algaeSEM/source/1.html> [retrieved on 02 July 2010].
- Smyth RD and Berg HC.** Change in flagellar beat frequency of *Chlamydomonas* in response to light. *Cell Motil 2*: S1: 211-215, 1982.
- Snell WJ, Buchanan M and Clausell A.** Lidocaine Reversibly Inhibits Fertilization in *Chlamydomonas*: A Possible Role for Calcium in Sexual Signalling. *J Cell Biol* 94: 3: pp. 607-612, 1982.
- Stavis RL and Hirschberg R.** Phototaxis in *Chlamydomonas reinhardtii*. *J Cell Biol* 59: 2 Pt 1: 367-377, 1973.
- Takahashi T and Watanabe M.** Photosynthesis modulates the sign of phototaxis of wild-type *Chlamydomonas reinhardtii*: Effects of red background illumination and 3-(3',4'- dichlorophenyl)-1,1-dimethylurea. *FEBS Letters* 336: 3: 516-520, 1993.
- Takao D and Kamimura S.** FRAP analysis of molecular diffusion inside sea-urchin spermatozoa. *J Exp Biol* 211: Pt 22: 3594-3600, 2008. **Tcherkez G, Cornic G, Bligny R,**

- Gout E and Ghashghaie J.** In vivo respiratory metabolism of illuminated leaves. *Plant Physiol* 138: 3: 1596-1606, 2005.
- Teramoto H, Ishii A, Kimura Y, Hasegawa K, Nakazawa S, Nakamura T, Higashi S, Watanabe M and Ono TA.** Action spectrum for expression of the high intensity light-inducible Lhc-like gene Lhl4 in the green alga *Chlamydomonas reinhardtii*. *Plant Cell Physiol* 47: 3: 419-425, 2006.
- Togashi T and Cox PA.** Phototaxis and the evolution of isogamy and 'slight anisogamy' in marine green algae: insights from laboratory observations and numerical experiments. *Bot J Linn Soc* 144: 3: 321-327, 2004.
- Treviranus LC.** Vermischte. Schriften anatomischen und physiologischen inhalts von G. R. und L. C. *Treviranus Bnd II* 79-87, 1817.
- Uematsu-Kaneda H and Furuya M.** Effects of Calcium and Potassium Ions on Phototaxis in *Cryptomonas*. *Plant Cell Physiol* 23: 8: 1377-1382, 1982.
- Wakabayashi K, Misawa Y, and Kamiya R.** Redox poise determines the sign of phototaxis in *Chlamydomonas*. The 14<sup>th</sup> International Conference on the Cell and Molecular Biology of *Chlamydomonas*, Wheaton College, Norton, Massachusetts. 2010.
- Weissig H and Beck CF.** Action Spectrum for the Light-Dependent Step in Gametic Differentiation of *Chlamydomonas reinhardtii*. *Plant Physiol* 97: 1: 118-121, 1991.
- Wirschell M, Pazour G, Yoda A, Hirono M, Kamiya R and Witman GB.** Oda5p, a novel axonemal protein required for assembly of the outer dynein arm and an associated adenylate kinase. *Mol Biol Cell* 15: 6: 2729-2741, 2004.
- Wratten SD.** *Video techniques in animal ecology and behaviour*. London ; New York: Chapman & Hall, 1994, p. 211.

**Yagi T, Uematsu K, Liu Z and Kamiya R.** Identification of dyneins that localize exclusively to the proximal portion of Chlamydomonas flagella. *J Cell Sci* 122: Pt 9: 1306-1314, 2009.

**Yagi T, Minoura I, Fujiwara A, Saito R, Yasunaga T, Hirono M and Kamiya R.** An axonemal dynein particularly important for flagellar movement at high viscosity. Implications from a new Chlamydomonas mutant deficient in the dynein heavy chain gene DHC9. *J Biol Chem* 280: 50: 41412-41420, 2005.

**Yoshimura K.** Mechanosensitive channels in the cell body of Chlamydomonas. *J Membr Biol* 166: 2: 149-155, 1998.

**Zhang H and Mitchell DR.** Cpc1, a Chlamydomonas central pair protein with an adenylate kinase domain. *J Cell Sci* 117: Pt 18: 4179-4188, 2004.

## **BIOGRAPHICAL DATA**

**AUTHOR:** Suphatra Adulrattananuwat

**PLACE OF BIRTH:** Bangkok, Thailand

**DATE OF BIRTH:** April 16, 1977

### **GRADUATE AND UNDERGRADUATE SCHOOLS ATTENDED:**

- Chulalongkorn University, Bangkok, Thailand
- Prince of Songkhla University, Songkhla, Hatyai, Thailand

### **DEGREES AWARDED:**

- Master of Science, physics, Chulalongkorn University, 2003
- Bachelor of Science, physics, Prince of Songkhla University, 1999

### **AWARDS AND HONORS:**

- Traveling award, the 14<sup>th</sup> International Conference on the Cell and Molecular Biology of *Chlamydomonas*, Norton, Massachusetts, 2010
- Henry Levinstein Fellowship, Syracuse University, Syracuse, New York summer, 2008
- Development and Promotion of Science and Technology (DPST) Scholarship, Thailand, 1994-2007

### **PROFESSIONAL EXPERIENCE:**

- Research Assistant, Department of Physics, Syracuse University, New York 2003-2010
- Teaching Assistant, Department of Physics, Syracuse University, New York 2005-2009